THESIS FOR THE DEGREE OF DOCTOR OF PHILOSOPHY

Beyond Virtual Synchronous Machine Control

Grid-Forming Converter Control Providing
Intrinsic Support in Sustainable Power Grids

Paul Imgart

Department of Electrical Engineering
Chalmers University of Technology
Gothenburg, Sweden, 2025

Beyond Virtual Synchronous Machine Control

Grid-Forming Converter Control Providing
Intrinsic Support in Sustainable Power Grids

Paul Imgart
ISBN 978-91-8103-274-1

Acknowledgements, dedications, and similar personal statements in this thesis reflect the author's own views.

Doktorsavhandlingar vid Chalmers tekniska högskola
Ny serie nr 5732
ISSN 0346-718X

Department of Electrical Engineering
Chalmers University of Technology
SE-412 96 Gothenburg, Sweden
Phone: +46 (0)31 772 1000

Printed by Chalmers Digital Printing
Gothenburg, Sweden, September 2025

Beyond Virtual Synchronous Machine Control

Grid-Forming Converter Control Providing
Intrinsic Support in Sustainable Power Grids

Paul Imgart
Department of Electrical Engineering
Chalmers University of Technology

Abstract

Grid-forming converter control is considered one of the most important contributions to handle the challenges of converter-dominated power grids. This is due to its advantages over classic grid-following control structures, such as more robust operation in weak grids and the ability to intrinsically provide grid-supporting services like fast fault-current contribution and inertial support. Nevertheless, grid-following converters show superior properties in some areas such as dynamic performance in strong grids and effective converter current limitation, in particular in comparison to those grid-forming control structures that are limited to the emulation of synchronous machines, i.e. virtual synchronous machines.

The aim of this thesis is to investigate the possibilities to combine the advantages of both grid-forming and grid-following converter control through the development of a grid-forming control approach that combines robustness and intrinsic grid support with the dynamic performance and fault-ride through capability of grid-following control. Through a study of existing control designs and grid-connection requirements for converter-interfaced generation as well as power electronic applications within transmission systems such as high voltage direct current (HVDC) transmission systems or flexible alternating current transmission systems (FACTS), gaps in the existing strategies are identified.

A voltage-based current-limitation strategy that maintains grid-forming behaviour even during current limitation is presented. In concurrence, the transient stability of grid-forming converters during current limitation due to voltage dips and frequency disturbances is studied and improved through the development of an inertia emulation loop. The focus is then moved to the behaviour of the converter in the frequency domain to ensure sufficient damping provision as well as prevent adverse control interactions. This is

addressed by developing a decoupled grid-forming control structure, in which individual control parameters influence different parts of the frequency response, enabling an effective shaping of the converter's behaviour. Finally, a tuning approach that is based on performance requirements is presented for the virtual admittance control parameters.

Through these results, this thesis contributes to the development of converter control strategies that intrinsically provide grid support and enable the operation of sustainable, converter-dominated power grids.

Keywords: Grid-connected converters, power-electronic converter control, grid-forming converters, grid codes, connection requirements, current limitation, transient stability, inertia support, frequency behaviour, power decoupling, virtual admittance.

To my grandparents Gerd and Irene,
who inspired me to remain curious and
showed me what a wonderful place this world is,
and to those who dedicate their lives to preserving it.

List of Publications

This thesis is based on the following publications:

[A] **Paul Imgart**, Mebtu Beza, Massimo Bongiorno, Jan R. Svensson, "An Overview of Grid-Connection Requirements for Converters and Their Impact on Grid-Forming Control". Published in 24th European Conference on Power Electronics and Applications, EPE 2022 ECCE Europe.

[B] Anant Narula, **Paul Imgart**, Massimo Bongiorno, Mebtu Beza, Jan R. Svensson, Jean-Philippe Hasler, "Voltage-based Current Limitation Strategy to Preserve Grid-forming Properties Under Severe Grid Disturbances". Published in IEEE Open Journal of Power Electronics, Feb. 2023.

[C] **Paul Imgart**, Anant Narula, Massimo Bongiorno, Mebtu Beza, Jan R. Svensson, "A Cascaded Power Controller for Robust Frequency Ride-Through of Grid-Forming Converters". Published in 2022 IEEE Energy Conversion Congress and Exposition (ECCE).

[D] **Paul Imgart**, Anant Narula, Massimo Bongiorno, Mebtu Beza, Jan R. Svensson, "External Inertia Emulation to Facilitate Active-Power Limitation in Grid-Forming Converters". Published in IEEE Transactions on Industry Applications, Nov. 2024.

[E] **Paul Imgart**, Massimo Bongiorno, Jan R. Svensson, Mebtu Beza, "Stability Limits and Improved Robustness of Grid-Forming Converters With External Inertia-Emulation Loop". Published in 25th European Conference on Power Electronics and Applications (EPE'23 ECCE Europe), Sep. 2023.

[F] **Paul Imgart**, Anant Narula, Massimo Bongiorno, Mebtu Beza, Jan R. Svensson, Jean-Phillipe Hasler, Paolo Mattavelli, "Decoupled PQ Grid-Forming Control with Tunable Converter Frequency Behaviour". Submitted to IEEE Transactions for consideration..

Other publications by the author, not included in this thesis, are:

[G] **P. Imgart**, P. Chen, "Effective Inertia Constant: A Frequency-Strength Indicator For Converter-Dominated Power Grids". *2023 IEEE Belgrade PowerTech*, Belgrade, Serbia, Jun. 2023.

[H] A. Narula, **P. Imgart**, M. Bongiorno, M. Beza, "Empowering Offshore Wind with ES-STATCOM for Stability Margin Improvement and Provision of Grid-Forming Capabilities". *Electric Power Systems Research vol. 234*, Paris, France, Sep. 2024.

[I] A. Narula, **P. Imgart**, M. Bongiorno, P. Mattavelli, M. Beza, J. R. Svensson, "Power-Response Matrix-Based Modeling of Converter Systems for Small-Signal Analysis". *2024 IEEE Energy Conversion Congress and Exposition (ECCE)*, Phoenix, USA, Oct. 2024.

Contents

Acknowledgments

During my PhD studies, I had the incredible privilege to receive support from many people, and I am convinced that I would not have been able to finish this thesis without them. First of all, I would like to thank my supervisors. My main supervisor, Professor Massimo Bongiorno, has not only gone out of his way to support and guide me, he also knew when to challenge me. I have always had the impression that my education was a top priority for him, and I am deeply thankful for that. I am not sure if I was the kind of student you deserved, but I am sure you were the supervisor I needed. Thank you!

I would like to thank my assistant supervisor Associate Professor Mebtu Beza for his expertise and support. Your knowledge in power system control has been immensly valuable. I am also thankful for the guidance I have received from my assistant supervisor Adjunct Professor Jan R. Svensson. Our regular discussions have helped me to keep the big picture in mind, and to learn to motivate and contextualise the chosen direction.

My reference group has been important in guiding me through the research project, and I am grateful for the support I have received and the interesting and helpful discussions I had with Jean-Philippe Hasler from Hitachi Energy and Dr. Robert Eriksson from Svenska kraftnät. The dialogue with them and their colleagues has been stimulating and helped me to understand the practical applications of my research better.

The financial support as part of the SamspEl program from Energimyn-

digheten and from Svenska kraftnät have made this project possible and are greatly acknowledged, as is the support provided by Hitachi Energy.

I would also like to thank my colleagues at Chalmers Electrical Power Engineering. Dr. Anant Narula, who I had the honour to share the office with, has been a big help and a great companion. I am extremely grateful for the countless times I could ask you for help and discuss questions and ideas for you, as well as for the great memories we share. The lunches I shared with my fellow PhD student Kristoffer Fürst have been a great help in getting settled in Sweden and at Chalmers, and I am happy that your children now have taken over my role in asking you for the meaning of Swedish words. I am extremely grateful that Associate Professor Peiyuan Chen gave me the possibility to come to Chalmers as an exchange student and to return again later. It is difficult to overstate the impact this opportunity has had on my life. I would also like to thank Nima, Lluc and Lazar, as well as my other colleagues, for the interesting and fun conversations as well as for supportive and welcoming atmosphere in our division. I am specifically thankful for the work Sara Fogelström has put into improving our division's work environment.

The time in the board of the doctoral student guild has been educational and inspiring, and I would like to thank my colleagues Elin, Daniel, Francisco, Fredrik, Christina, Yan, Angelica and Michail in particular for their tireless efforts. I am also thankful for the invaluable work DrGenie is doing, and am particularly thankful for the great and uplifting collaboration with Georgia and Vi. I extend my thanks also to the senior faculty members that deeply care about research education and PhD students' situations, your work makes a difference.

It would be impossible to mention and thank all the great friends who have supported me throughout these years, but it feels important to thank Nelly, Gustav and Sara, who have had to endure the side-effects of writing this thesis first hand. I am also deeply grateful for the support from my parents Ina and Hartmut, who have always encouraged and believed in me, but also given me the freedom to explore and find my own way. I am always able to count on my siblings Clara and Vincent, and I am immensely grateful for the relation we have.

Paul Imgart
Göteborg, Sweden
August 2025

Acronyms

ac alternating current

ACER European Union Agency for the Cooperation of Energy Regulators

AEMO Australian Energy Market Operator

APC active-power controller

AVC ac-voltage controller

BESS battery energy storage system

CC current controller

dc direct current

EMF electromotive force

EMT electro-magnetic transients

ENTSO-E European Network of Transmission System Operators for Electricity

FACTS Flexible Alternating-Current Transmission Systems

FRT fault ride-through

GFL grid-following

GFM grid-forming

HVAC High-Voltage Alternating Current

HVDC High-Voltage Direct Current

IEL inertia-emulation loop

LCC line-commutated converter

NC HVDC Network Code for HVDC and DC-connected generation

NC RfG Network Code Requirements for Generators

NFP network frequency pertubation

PCC point of common coupling

PI proportional-integral

PLL phase-locked loop

PSC power-synchronisation control

PV photovoltaics

RLS recursive least squares

RoCoF rate of change of frequency

RPC reactive-power controller

SC synchronous condenser

SFR synchronous-frequency resonance

SM synchronous machine

SRF synchronous reference frame

STATCOM static compensator

TSO transmission system operator

UPS uninterruptible power source

VA virtual admittance

VCC vector current controller

VI virtual impedance

VSC voltage source converter

VSM virtual synchronous machine

Part I

Overview

CHAPTER 1

Introduction

1.1 Background

In 2024, the average global temperature has for the first time in history exceeded 1.5 °C above its pre-industrial level, thereby surpassing the threshold set in the Paris Agreement for a significant reduction of the risks and impacts of climate change [1]–[3]. This increase in temperature has been mainly caused by anthropogenic greenhouse gas emissions, and has consequences such as the increased frequency and intensity of extreme weather events such as heatwaves, droughts, floods and storms, the accelerating loss of polar and alpine ice as well as an increasingly threatening impact on biodiversity [1], [4]. These effects demonstrate that the need to mitigate this human-made climate crisis by a decisive and swift radical reduction of greenhouse gas emissions is now more urgent than ever [5].

Since a notable part of the global greenhouse gas emissions causing the observed climate change are related to the production of electricity[1], the transformation to renewable and sustainable energy sources is a crucial component

[1] In 2022, approximately one third of greenhouse gas emissions were caused by the heat and electricity sector [6].

of climate action. In addition to supplying the existing loads from renewable energy sources, these also need to cover additional loads as the decarbonization of the heat and transportation sectors are expected to mainly rely on electrification [7]. In its long term market analysis, the Swedish transmission system operator (TSO) Svenska kraftnät expects a large increase in electricity consumption, in some scenarios up to more than 340 TWh/year in 2045 compared to 155 TWh/year in 2025 [7]. The vast majority of this increased consumption is expected to be covered by converter-interfaced renewable generation [7].

Hand in hand with this rapid and massive increase in electricity consumption and production from renewable energy sources, the transition towards sustainable energy grids poses a number of unprecedented challenges for safe operation of electrical power systems [8], [9]. Some of the causes for these challenges include increased loads, the successive replacement of synchronous machines with converter-interfaced generation such as wind power or solar photovoltaics, increased share of fluctuating and intermittent power generation, as well as increased demands on flexibility and utilization of power grid assets [8], [10], [11]. Denmark, Ireland and Australia are examples for countries with a high instantaneous share of renewables. In Denmark's western transmission grid, which forms part of the large Central Europe synchronous area, renewable generation exceeded consumption for 14 % of the year's hours already in 2014 [12]. The islanded Irish power grid will explore the possibility to increase the upper limit for converter-interfaced generation from currently 75 % to 80 % [13], and in 2024, the Australian power system saw a maximum share of converter-interfaced renewable generation of 73 %, with South Australia currently surpassing 100 % nearly every day[2] [14], [15].

In parallel to the growing amount of power-electronic converters due to the increasing share of renewable generation, power electronics are also more commonly deployed to enhance utilization and flexibility in power systems, or to address some of the aforementioned challenges, e.g. in the form of High-Voltage Direct Current (HVDC) transmission systems or Flexible Alternating-Current Transmission Systems (FACTS) devices such as a static compensator (STATCOM) [16], [17]. In particular offshore wind power is commonly combined with either an HVDC transmission system for grid connection, or, in the case

[2]Generation exceeding local consumption orted to other parts of the Australian power system.

of a High-Voltage Alternating Current (HVAC) connection to shore, a STATCOM to ensure grid code compliance [18], [19].

Among the challenges that system operators connect to the increasing penetration of power-electronic converters are reduced system inertia and fault current levels (sometimes expressed instead as reduced system frequency and voltage strength) as well as increased risk of adverse control interaction [8], [20]–[22]. As a consequence of these challenges, the requirements for converter-interfaced generation have become increasingly strict. This can be exemplified with the evolution of grid-connection requirements for wind power: about 40 to 30 years ago, wind power plants were in many systems treated as pure energy suppliers without notable responsibility for stable operation of the power system. In consequence, connection requirements were mostly limited to power quality issues, in particular those related to harmonic pollution [23]. As the share of wind power increased, these plants started to have an impact on the stability of power grids in countries such as Denmark, Ireland or Germany. In response to this, new connection requirements were introduced which aimed at reducing possible negative impacts on the power system, such as rules on frequency and voltage support as well as regarding fault ride-through (FRT) capability[3]. These require wind-turbines to participate in basic active and reactive power regulation for frequency and voltage control and to remain connected even during large disturbances [17], [19], [24]–[29].

As wind power in some power grids began to provide at some instants the majority of energy generation, the role continued to shift: instead of connecting to a stiff and stable system, renewables are progressively becoming a defining part of that system, which comes with their share of responsibility for system stability and robustness [30]. This change is in concrete terms expressed in discussions about requirements covering areas such as inertial response, contribution to fault current level, black start capability, survival of system splits, stable operation in weak grids[4], prevention of adverse control

[3] Depending on the power system and its share of wind power, these requirements may have been introduced earlier or later.

[4] There exists a variety of definitions for the concept of grid strength, typically related to the short-circuit power. More generally, and more suitable for converter-dominated power systems, the Australian TSO Australian Energy Market Operator (AEMO) defines grid strength as *the ability of the power system to maintain and control the voltage waveform at any given location in the power system, both during steady state operation and following a disturbance.* In a grid modelled as a Thévenin equivalent, this relates to the Thévenin impedance, with a stronger grid having a smaller impedance [31]. If not

interactions and provision of sinks for harmonics and unbalances [8], [20], [32], [33].

This shift of power-electronic devices from mere background characters towards protagonists with systemic importance has driven the continued investigation and development of converter control [30]. The majority of existing power electronic devices in generation and transmission systems are voltage source converters (VSCs) controlled as grid-following (GFL) controlled converters, which in essence adjust and follow changes in the grid, instead of counteracting them. In practice, this typically implies synchronization to a grid voltage and injecting controllable active and reactive power, typically by means of a vector current controller (VCC) [20], [31]. In concurrence with the increasing need for converter-interfaced resources to contribute to system stability, and more expansive connection requirements, the concept of grid-forming (GFM) converter control has received the attention of the power electronic and power system communities [8], [20], [30], [31], [34], [35].

The large variety of GFM converter control concepts originates mainly from two different, but related goals: To enable efficient load-sharing of parallel inverters in microgrid, leading to droop-based GFM control [36]–[40], and to use the properties of synchronous machines (SMs) to ensure stable converter operation in weak grids [41]–[45]. It has subsequently been shown in [45], [46] that the control concepts resulting from both approaches are equivalent to each other, and converters with GFM control have come to be commonly described as acting as a (slowly varying) voltage source behind an impedance, which allows them to form a voltage that other devices can synchronise to and that counteracts grid disturbances. They are more robust than GFL converters when connected to weak grids and typically provide grid-supporting functionalities such as inertial support, frequency control and black-start capability intrinsically, without the need for explicit control action [8], [20], [31].

While GFL converters do not intrinsically provide grid services such as inertial response or fault-current contribution, they still have some advantageous properties when compared to GFM control schemes. GFL converters allow for straight-forward current limitation and typically have a dynamic performance when connected to strong grids with faster tracking of power-reference setpoints [47]–[49]. Moreover, it is relevant to question if replication of the SM's behaviour is the best way for converter systems to support the power grid,

stated otherwise, this definition will be used in this thesis.

or if this wastes the potentials enabled due to the much faster and precise controllability of converter systems. SM behaviour is dictated by the SM's physical properties instead of being a design choice, and in consequence SMs can cause stability issues such as power oscillations or transient instability.

Consequently, this thesis explores the possibilities to combine the advantages of GFL and GFM converter control, and aims to develop an converter control structure that intrinsically supports the power grid without being limited to the emulation of SM behaviour.

1.2 Aim and Scope

The aim of this thesis is to propose and investigate control solutions for grid-connected converters that intrinsically support the power grid.

In particular, the thesis investigates if it is possible to combine the intrinsic grid-support and robustness that characterise existing GFM converter control like the virtual synchronous machine, with the improved dynamic performance and FRT capability of GFL converters. To achieve this aim, the thesis intends to provide a thorough understanding of the principle of GFM converter control as well as its definitions proposed in regulation and academic literature. It reviews GFL and GFM control strategies as well as their strengths and weaknesses. Based on a study of grid-connection requirements, an overview of necessary grid-support functionalities is provided. On this base, it is identified in which areas existing GFM control strategies have a need for improvement. Particular focus is put on the ability to provide GFM behaviour even during large system disturbances, which can cause the converter current to saturate. Furthermore, the ability to shape the converter's input admittance is addressed.

The studies in this thesis are conducted using analytical methods in time and frequency domain, electro-magnetic transients (EMT) simulations as well as validation through laboratory experiments. The simulations have been carried out using MATLAB Simulink and PSCAD. The thesis covers some aspects of varying grid conditions and multi-converter setups, but focuses on generic single-converter setups for the exploration of new concepts. Since the focus in this thesis is on the control of the grid-side converter and the impact it has on the grid, a simplified, application-agnostic system consisting of a two-level VSC with a stiff direct current (dc) voltage and an L-filter is

studied as the standard case in this work. Where applicable, i.e. for general calculations and simulations, the converter is modelled as a controllable voltage source[5], while detailed simulations are conducted with a switching model. Laboratory experiments have been carried out with a two-level VSC with a stiff dc voltage. If not specified differently, the grid has been modelled as a Thévenin equivalent. The choice of the simplest converter topology and filter design allows to focus on the impact of the controller instead of the specifics of the chosen converter system [50].

1.3 Contributions

To the best of the author's knowledge, the thesis and its included papers present the following scientific contributions:

- An overview of grid-connection requirements for converters and the implications for GFM control. In **Paper A**, a categorization of requirements is developed, different grid codes and related documents are compared, and specific requirements for converters with GFM control are listed.

- An analysis of the transient stability of GFM controllers during current saturation. **Papers B - E** show analytical, simulation and experimental results of the stability and observations of instability related to the combination of frequency disturbances, inertia provision and current limitation.

- A current limitation scheme maintaining the grid-forming behaviour by acting on the GFM controller's internal voltage source. **Paper B** presents and investigates the performance of this voltage-based current limitation during voltage dips and frequency disturbances.

- A robust way to provide inertia in GFM controllers preventing instability. The developed inertia-emulation loop is presented in **Paper C**, its robustness is investigated and improved in **Paper E** and the results are expanded and validated with laboratory experiments in **Paper D**.

[5] Also known as average converter model.

- A decoupled GFM converter control that decouples active and reactive power while allowing free choice of virtual resistance and inductance, enabling effective tuning of the converter's frequency behaviour. If so desired, the controller can be tuned to be symmetric. In **Paper F**, this controller is derived, presented and studied, with experimental results demonstrating the controller's performance.

- A tuning method for the virtual admittance in GFM converter control based on the converter's desired frequency behaviour. In Chapter 5, a previously unpublished method is proposed to tune the virtual admittance that is present in many GFM control strategies. The parameters are selected to fulfil requirements regarding desired properties such as damping provision. This is achieved by relating the properties to the converter's frequency behaviour. Furthermore, the impact of the chosen parameters on the converter's response to disturbances such as voltage dips and angle jumps is studied.

1.4 Thesis Outline

The thesis is a compilation thesis consisting of two parts: Part one, the overview, containing introduction, context and in some cases additional material for the topics touched upon in the included publications, and part two, the included papers. Please note that the included publications are not listed chronologically, but to follow the structure of the thesis.

This introductory chapter is followed by Chapter 2, which gives an introduction into the principles of GFL and GFM converter control, gives some examples for both control principles and discusses disadvantages and advantages of both. Chapter 3 gives an overview of grid-connection requirements for grid-connected converters, their implications for converter control as well as recent development. This is followed by Chapter 4, which discusses the operation of GFM controllers during current limitation. In Chapter 5, methods to shape the frequency response of GFM controllers are presented. The conclusions of this work as well as suggestions for future work are given in Chapter 6.

CHAPTER 2

Grid-Following and Grid-Forming Converter Control

This chapter contains an introduction and overview into grid-connected converters and the main categories of their control, including the discussion of definitions of grid-forming control (Section 2.1). This is followed by the fundamentals of grid-following (Section 2.2) and grid-forming control (Section 2.3) as well as their main properties and features.

2.1 Control of Grid-Connected Converters

Power-electronic converters have become a key technology in most parts of the electric power system and fill a large variety of roles in generation, transmission and consumption of electric energy. They come in a large span of voltage and power ratings and can range in size from phone chargers up to the imposing valve stacks of HVDC substations. The focus of this thesis is on medium- and high-voltage grid-connected VSCs in bulk power systems, with main applications being renewable power generation technologies like wind and solar photovoltaics (PV) or in some cases even hydro power [17], [19],

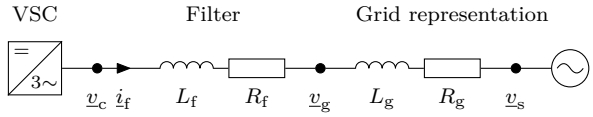

Figure 2.1: Single-line diagram of an exemplary converter system.

[25], [51]–[55], HVDC transmission systems[1] [56], VSC-based FACTS such as STATCOMs [57], [58] and grid-connected battery energy storage systems (BESSs) [59]–[61]. Large parts of the converter design are application-specific, e.g. the choice of the converter topology, DC-link control or filter design [17], [29], [50], [62]–[67]. This thesis focuses on the control of the grid-side converter and its impact on the grid. For this reason, the application-agnostic system consisting of a two-level VSC with a stiff dc voltage and an L-filter as shown in Fig. 2.1 is studied as the standard case in this work.

As mentioned in Chapter 1, the evolution of the role of converter-interfaced resources in power grids, innovation in power-electronic technology and increasingly strict requirements have caused a continuous development of new converter-control structures. This results in a vast number of publications and variations of controllers, which would make a complete review, classification and comparison of those control structures challenging. For overviews with different focus and from different years, the reader is referred to [63], [68]–[72]. To facilitate comparison and development of converter-control structures, it is crucial to have an understanding of the components that typically form the control system. Based on the guide presented in [17], [73], the following parts can be identified (see Fig. 2.2 for a diagrammatic representation)[2]:

- *Modulation stage:* The modulation stage and all sub-ordinated control layers are responsible for enabling the switched source behaviour of the power-electronic device. The modulation stage is topology- and hardware-dependent, while all outer control layers can be common for different VSC topologies under the assumption of sufficiently fast switching and transient capabilities. Most types of outer control layers operate

[1] Note that only some HVDC systems use VSCs, sometimes called *HVDC light*. This work is not relevant for HVDC systems based on line-commutated converters (LCCs), typically named *HVDC classic* in contrast.

[2] The structure presented here forms part of a more complex system. According to the subject of the thesis, the *converter control layer* [73] is highlighted here.

independent from the modulation, with the exception of control structures that directly generate switching signals, e.g. some dead-beat and model-predictive controllers [68].

- *Inner control:* The inner control loops are responsible of generating the reference for the modulation stage, in the case of a VSC the reference voltages for each phase. It is possible to have several parallel control loops, e.g. separate controllers for positive and negative sequence whose outputs are added to generate the reference. The most common type of inner control for VSCs is a current control.

- *Outer control:* The outer control, if present, generates reference values for the inner control from setpoints in other quantities. A common control cascade are power or voltage controller as outer control loops and a current controller as inner control loop. To prevent undesired interaction between outer and inner control their closed-loop bandwidths are typically separated by at least a decade [74]. The distinction between inner and outer control loop is arbitrary when only one of them is present, and is in this thesis based on the speed of the controller: The inner control has a closed-loop bandwidth of about a decade slower than the converter's switching frequency, i.e. a couple hundred up to 500 Hz for a switching frequency of 5 kHz, while the outer control is typically two decades slower, i.e. up to 50 Hz for the same switching frequency. There also exist control strategies with three control loops in cascade, even though two or one are more common.

- *Filtering/decoupling layer:* In some control structures there is a layer between inner and outer control loop designed to filter the reference for the inner control or to shape the converter's properties as seen from the grid. Examples for this layer can be a virtual impedance (VI) or virtual admittance (VA).

- *Synchronisation loop:* To be able to synchronise to an existing grid and connect to other sources, the converter system needs to synchronise to the voltage at its connection point. In some control structures this is realized with a specialised control loop, typically a phase-locked loop (PLL), while in others the synchronisation is realized through other control loops, e.g. the active-power controller.

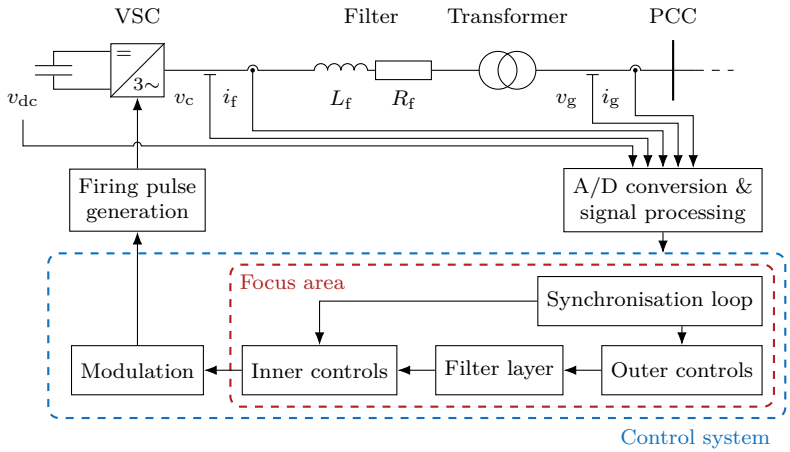

Figure 2.2: Simplified single-line diagram of a converter system with important measurement signals and control system components. The part of the control system this thesis focuses on is indicated in red.

This separation of the controllers into common components allows to identify different parts of control structures by their function and compare them.

The fundamental task for the control system in most grid-connected converters[3] is to control the flow of active and reactive power between the converter and the grid. As a consequence of this shared goal, the steady-state behaviour at the fundamental frequency is the same for all converter-control structures discussed here: the converter behaves as a controllable power source.

The different ways control structures implement this behaviour have however an impact on the dynamics and the behaviour at other frequencies, i.e. regarding subharmonic and harmonic phenomena. The differences between control structures are therefore visible in the converter's frequency response at other frequencies than the fundamental[4]. Based on these differences, converter-control structures can fundamentally be separated into grid-following and grid-forming controllers [70].

To understand the basic differences between these categories, it can be help-

[3] With the exception of power-electronic loads like drive systems, chargers, etc.

[4] Note that depending on the quantity and reference frame, the fundamental can be located either at 0 Hz or fundamental frequency.

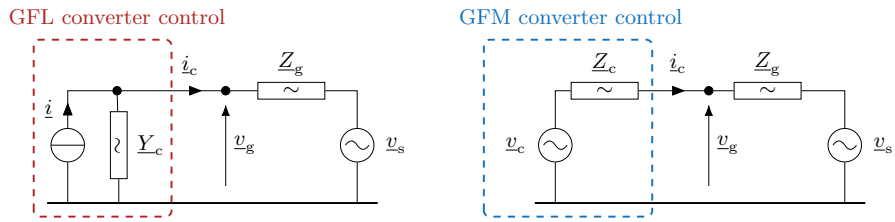

Figure 2.3: Electrical representation of a converter with GFL, represented as a current source parallel to an admittance (left), and a converter with GFM control, represented as a voltage source in series with an impedance (right).

ful to put them into the historic context they were developed in. When VSC converters started to appear in the grid, they were few and far in between, and had relatively low impact on the power grid [23]. The control of these grid-connected converters was largely inspired by drive-system control structures, with a focus on decoupling of active and reactive power and very fast current control. Because the converter aims to keep its current constant and a control action from the outer loops is required to change the current, converters controlled in this manner are represented as a controllable current source with a parallel admittance, as shown in Fig. 2.3. To keep the current constant, the converter voltage[5] has to follow any eventual change in the grid voltage, which is why this type of control came to be coined as grid-following (GFL) control.

As the number of converters in the grid increased, their dynamic behaviour also started to have an impact on the grid. Converters were placed in positions with weaker grids, and control interactions began to appear [75]–[77]. As a consequence, academia and industry turned their attention towards alternative control structures with a different dynamic behaviour. The emerging idea was to replicate the behaviour of a SM: a slowly varying voltage source behind an impedance. In this way, the converter's reaction to a disturbance in the grid voltage would be a changing current – the slowly changing converter voltage intrinsically[6] acts stabilising. Examples for this are the immediate

[5] Even when modelled as a current source, a VSC acts as a voltage source, which in this case is controlled with a very high closed-loop bandwidth to keep the current constant.
[6] Here, intrinsic is used to describe an reaction that occurs without the need for any control

contribution of current during short-circuit faults and voltage dips as well an inertial response during grid-frequency disturbances. Due to this behaviour and because of their ability to operate independently of other voltage sources, this type of control structures is called GFM control.

The exact understanding of what constitutes GFL and GFM control has undergone changes over time, and even today there is no universally accepted, precise definition of what constitutes GFM behaviour and how to demonstrate it [20]. In Table A.1 in Appendix A, some older and recent definitions of GFM converter control are listed. Appendix A of [78] contains a more in-depth comparison of definitions from the literature. Even though the definitions compared in Table A.1 are rather vague and distinct, there is agreement in that GFM behaviour means to act as a grid-frequency voltage source behind an impedance. To achieve the steady-state goal of controlling power, the voltage source is allowed to change, but with a limited speed[7]. The following sections use some example control structures to illustrate how these different key aspects of GFL and GFM control are realised.

2.2 Grid-Following Converter Control

To be able to provide the fast and accurate current control that characterises GFL converter control, the controller needs to track and synchronise to the (ideally strong) grid voltage at the point of common coupling (PCC) [20], [40], [51], [58], [70], [79]. The control of exchanged active and reactive power is typically achieved by using outer power control loops[8] in cascade with an inner current controller [51]. An example for this control structure, here implemented in the rotating synchronous reference frame (SRF), is shown in Fig. 2.4. Synchronisation to the grid voltage is in this and similar GFL control structures typically achieved by the usage of a PLL like the one shown in Fig. 2.5 [51], [65], [70], [79].

The tuning procedure for the control parameters depends on the specific

action. Some other terms used in the literature to describe this property of GFM control are natural, passive or automatic.

[7] Where this speed limit lies depends on the application and the system operator's specification. In [33], 5 Hz is specified as the upper limited for the loop bandwidth of control loops that change the GFM controller's internal voltage.

[8] These are in some cases replaced or complemented by alternating current (ac) and dc voltage controllers.

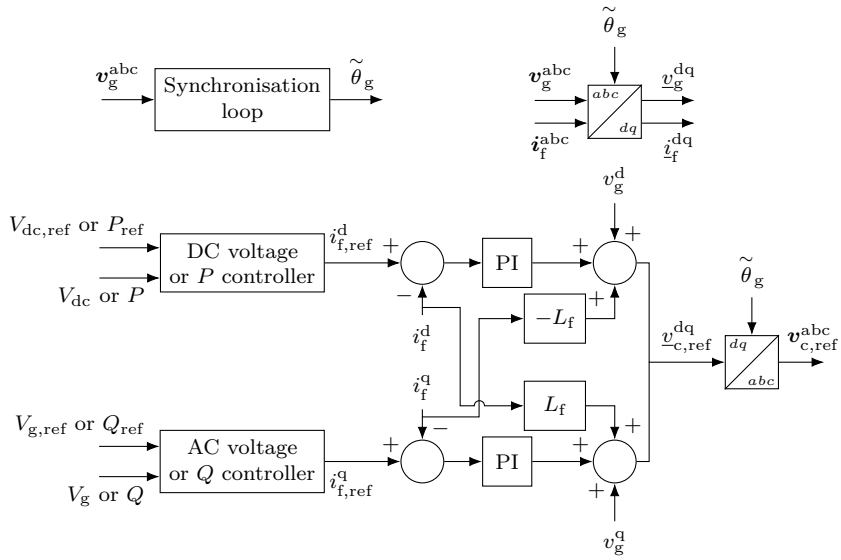

Figure 2.4: Example of a control structure for a cascaded GFL converter control.

structure and the system the converter is connected to. For the example system shown here a loop-shaping approach is typically used [80]. To prevent interaction of the cascaded control loops, their closed-loop bandwidths should be separated by at least a decade [80]. Nevertheless, with modern grid-connected VSC converters switching at frequencies of 5 kHz and above, very accurate and fast power control can be achieved. Fast control does however require that the voltage at the PCC is strong, i.e. not affected by the converter.

2.3 Grid-Forming Converter Control

As mentioned earlier, GFM converter control implies behaving as a slowly varying voltage source. This typically implicitly includes the ability to synchronise to an existing grid voltage, but also operate independently – to "form

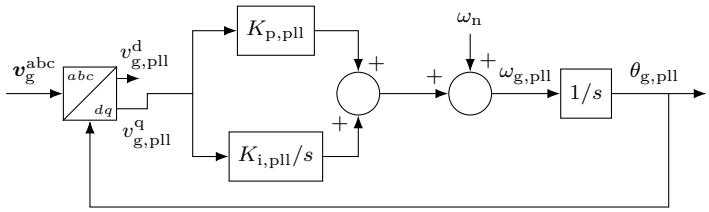

Figure 2.5: Block diagram of a PLL as it is typically used for synchronisation in GFL converters.

a grid"[9]. GFM control concepts originated in different contexts, mainly related from two different intentions.

The first context is distributed renewables or energy storages in microgrids [37]. The GFM control that has been developed in this context is typically called droop controller and is a response to the challenge of sharing the load of frequency and voltage control between several distributed, parallel converters in islanded microgrids [81]–[83]. Already in 1993, a control based on frequency and voltage droop was proposed to solve this question [81]. While this control still relies on a filtered estimation of the AC voltage angle, later implementations of the droop control successively place more emphasis on the ability to create a system voltage [38], [39], [84]–[87].

The second context is the previously introduced observation that the fast control actions of converters with GFL control can destabilize weak grids [77]. Based on this, converter control structures were proposed that replicated the behaviour of a SM. Some of the earliest examples for control structures based on this principle are the virtual synchronous machine (VSM) [41], [44], [45], [88]–[91], the power-synchronisation control (PSC) [92]–[94], and the synchronverter [42], [95]–[98].

In [45], [46], it has been shown that droop control and virtual synchronous machine are, under certain circumstances, equivalent to each other. In consequence, the development efforts on GFM controllers, even tough originating from separate intentions, have become mostly unified. One common aspect among most GFM control structures is the way how the active power transfer is used for synchronisation: Most GFM controllers adjust the frequency of the

[9] In [8], this ability is called "create system voltage". Similar to a SM, islanded operation might require the addition or activation of a frequency controller that is deactivated when operated synchronously to other sources.

internal voltage source based on the active-power control error, thereby delegating the synchronisation task to the active-power controller (APC). This principle resembles the synchronising torque known from SMs [92].

There exist numerous alternatives, refinements and improvements to the previously mentioned GFM control structures, and a complete review of these is outside the scope of this thesis[10]. Instead, based on the comparisons in [18], [45], [100], a selection of the most common GFM control structures is presented below. To emphasize that the majority of GFM controllers consist of different parts that tend to reappear even in other GFM control structures, the following overview is separated by outer and inner control.

Outer Control Loops

Generally, the GFM converter control's defining internal voltage source[11] is generated by the outer control loop(s), which also typically take care of the synchronisation to the grid voltage. Three commonly used outer control loops are presented below.

Droop Control

As mentioned before, droop control is one of the earliest types of GFM control structures and had originally the aim to share the load of controlling frequency and voltage magnitude between parallel inverters. Figure 2.6 shows a block diagram of a typical GFM droop controller, based on [103], [104].

At the core of the droop controller is the frequency-droop-based APC, which uses the active-power control error to provide synchronisation with the grid-voltage angle. Most commonly, the controller is designed in the SRF and the dq-frame is aligned with the converter-voltage vector.

Due to the droop characteristic, the active power injected to the grid, P, deviates from the reference P_{ref} in steady state if the grid frequency differs from the frequency reference value ω_{ref}. A lower frequency increases the power and viceversa, with m_{p} denoting the droop constant. This control design resembles the governor of a SM and its primary frequency control [105]. To ensure stability, the measured active power is low-pass filtered with the bandwidth ω_{fp}. The filter time constant determines the controller's speed of response.

[10] Refer to [31], [45], [64], [66], [69], [72], [99]–[102] for reviews of GFM control structures.
[11] Sometimes also denoted as the converter's *virtual back electromotive force (EMF)*.

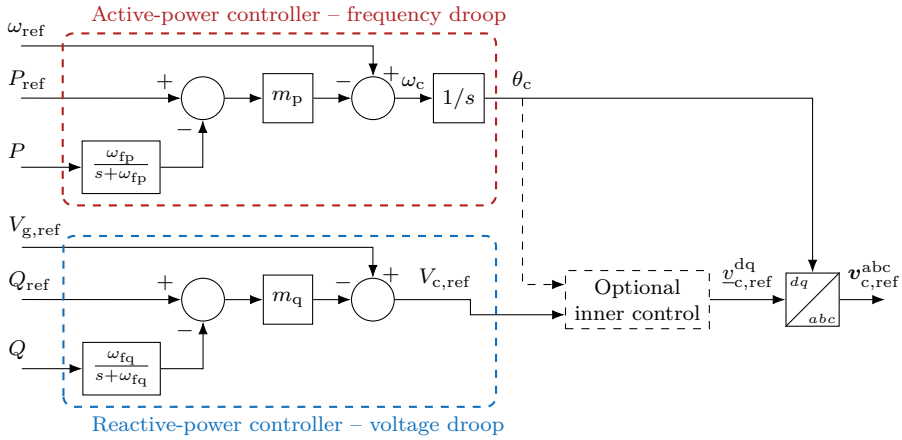

Figure 2.6: Block diagram of a typical GFM droop controller.

The reactive-power controller (RPC) is responsible for determining the magnitude of the internal voltage based on the voltage droop m_{q}. Inner control loops such as a VI, current controller (CC) etc. can optionally be used, otherwise the converter voltage is formed as

$$\underline{v}^{\text{dq}}_{\text{c,ref}} = V_{\text{c,ref}} \tag{2.1}$$

in the SRF aligned with the angle generated by the APC.

Virtual Synchronous Machine

The VSM implements the equations describing the SM behaviour into the converter controller [41], [44], [45]. The detail of the emulated model and the controlled variable (voltage or current) varies between implementations [103], with the second-order (purely mechanical) model being the most common in recent publications. If desired, a more accurate emulation of the SM behaviour can be achieved by addition of flux linkage equations. These higher-order models do however not tend to provide any additional benefits for the grid [45]. If a second- or first-order representation is chosen, an additional RPC or ac-voltage controller (AVC) is needed to regulate the magnitude of the GFM controller's internal voltage source.

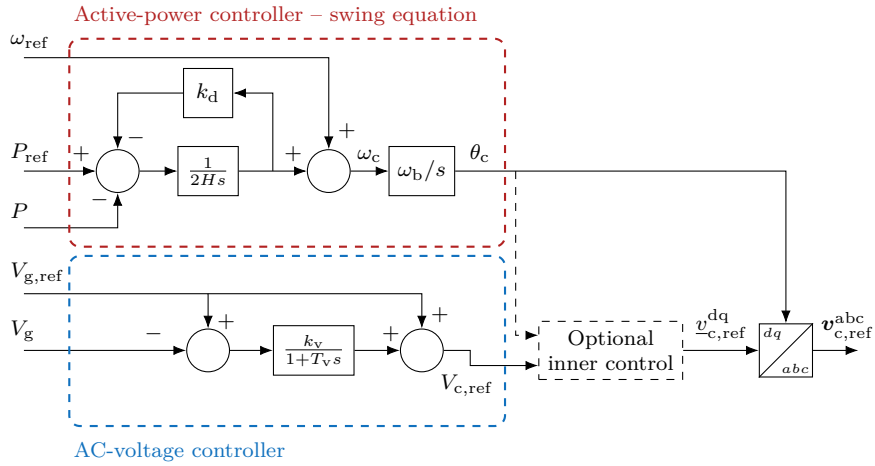

Figure 2.7: Block diagram of a typical VSM controller.

Figure 2.7 shows the block diagram of a second-order VSM. The APC implements the swing equation, the set of differential equations describing the mechanical behaviour of the SM in per-unit:

$$2H\omega_{\text{c}}s = P_{\text{ref}} - P - k_{\text{d}}(\omega_{\text{c}} - \omega_{\text{g}}), \tag{2.2}$$

where H is the machine's inertia time constant (expressed in seconds), k_{d} the damping constant and ω_{g} the angular grid frequency [105]. To avoid the need to include a grid-frequency estimation, instead of the actual grid frequency ω_{g} often the rated or reference angular frequency ω_{ref} is used in the damping term, as shown in Fig. 2.7 [72], [106]. This will cause a steady-state droop effect if the grid frequency varies from the reference [107], [108]. Similar to the droop controller, the VSM control depicted here provides an internal voltage in the SRF aligned to it, and the controller can be combined with additional inner control loops [103]. For a constant grid frequency, the VSM has been shown to be equivalent to the droop controller [45], [46].

PI-Based Grid-Forming Controller

To eliminate the frequency droop that is present in both droop and VSM control by other means than by addition of a grid-frequency estimation, a

PI-based APC has been proposed [108]. This controller, depicted in Fig. 2.8, can be tuned to give equivalent active-power reference tracking as the VSM controller [108], while also allowing a more straight-forward tuning process using a loop shaping approach [109]. Here, the PI-based GFM controller is only shown for the APC, while the AVC from the previous structure is kept unchanged. The PI-controller can be combined with additional inner control loops, alike the other outer loops.

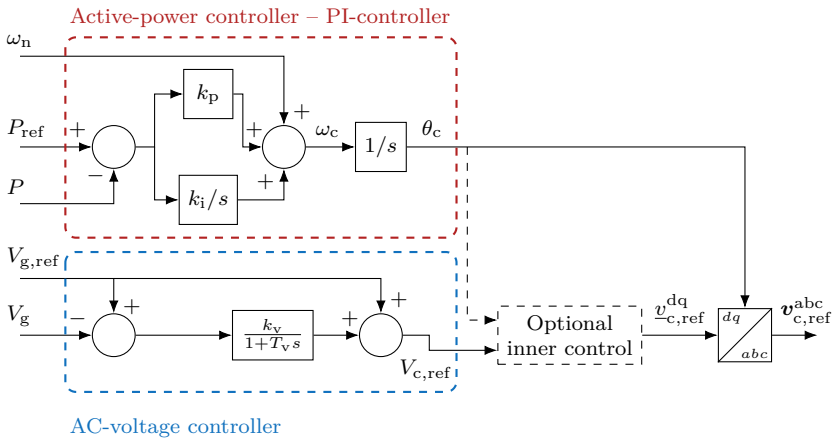

Figure 2.8: Block diagram of a PI-based GFM controller.

The special case of integral gain $k_i = 0$ is called power-synchronisation control (PSC) and predates other proposals of the PI-controller in the literature [92]. In the PSC, typically an active resistance acts on a high-pass filtered current measurement to improve damping (not depicted here, see also Chapter 5) [93]. Due to the lack of a second integrator, the PSC provides a frequency droop of k_p [93].

Filter Layers and Inner Control Loops

The presented GFM outer loop controllers generate an internal voltage source. Some authors suggest to directly pass this voltage as a reference to the modulation stage, letting it become the converter terminal voltage reference [45]. It can be advisable or necessary to instead use additional filter layers or inner

control loops to add or alter control functions and behaviour, deal with hardware limits (e.g. current limits) or take specifics of the converter topology, power system or converter filter into account [45], [72]. In this case, the inner controls will generate a new terminal-voltage reference based on the internal voltage created by the outer GFM controllers. Below, some examples are given for filter layers and inner control loops that are commonly used in GFM control structures.

Virtual Impedance and Virtual Admittance

As described earlier in this chapter, converters with GFM control are commonly expected to behave as a slowly varying voltage source behind an impedance. It can be desirable to use this impedance between the internal voltage source and the PCC as a degree of freedom in the controller design. This can be achieved by the addition of a virtual impedance (VI), effectively increasing the electrical distance between the internal voltage source and the PCC. The VI can be implemented either through a transient or a steady-state representation of the impedance [110]. The transient representation requires either a high-pass filter or derivative term, which can be related to instability, and therefore the steady-state representation shown in Fig. 2.9 is commonly used [88], [111], [112].

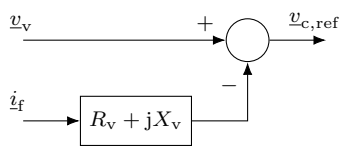

Figure 2.9: Block diagram of a steady-state implementation of the virtual impedance in SRF. $\underline{v}_{\mathrm{v}}$ is the voltage vector generated by the outer loops, R_{v} the virtual resistance and X_{v} the virtual reactance.

There exist a variety of motivations for the addition of a VI in the literature, and the realization of the VI depends on the purpose. The additional impedance can be used to decrease the R/X ratio of the total impedance, which decouples active and reactive power from each other and improves the performance of APC and RPC [113]. Furthermore, increasing the impedance between the internal voltage and the PCC decreases the coupling of the converter to the grid voltage, which reduces reactions to small variations in grid

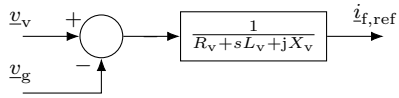

Figure 2.10: Block diagram of a transient implementation of the virtual admittance in SRF. $\underline{v}_\mathrm{v}$ is the voltage vector generated by the outer loops, and X_v can be generated using the converter's frequency ω_c or approximated with ω_b.

voltage magnitude and frequency [88]. A VI can also be employed to influence the load sharing of parallel converters, e.g. in a microgrid with varying feeder impedances [86], [114], [115]. Different VIs can be used for the fundamental and individual harmonics to achieve a desired filtering effect [116]. More generally, the VI can be used to shape the frequency response of the converter.

Different from these applications, but also widespread in the literature is the usage of a (typically non-constant) VI for current limitation in the case of voltage dips and faults [110], [117]. This additional, adaptive VI is activated when an overcurrent is detected. The usage of VI for current limitation is discussed more in details in Chapter 4, **Paper C** as well as [117], [118].

Instead of calculating the voltage drop over the VI, the admittance form can be used to calculate the resulting converter current:

$$\underline{i}_\mathrm{f,ref} = \underline{Y}_\mathrm{v}(\underline{v}_\mathrm{v} - \underline{v}_\mathrm{g}), \tag{2.3}$$

with $\underline{v}_\mathrm{v}$ denoting the internal voltage generated by the outer loops [111]. In the SRF, the transient representation of the virtual admittance (VA) $\underline{Y}_\mathrm{v}$ is given as

$$\underline{Y}_\mathrm{v} = \frac{1}{R_\mathrm{v} + sL_\mathrm{v} + \mathrm{j}\omega_\mathrm{c}L_\mathrm{v}}, \tag{2.4}$$

where R_v and L_v are the virtual resistance and inductance, respectively [111]. A block diagram of this implementation is shown in Fig. 2.10. It is important to note that in this expression R_v and L_v cannot both be zero, and should include all physical impedances located between the two voltages $\underline{v}_\mathrm{v}$ and $\underline{v}_\mathrm{g}$. Instead of multiplying the varying converter frequency ω_c, the last term is typically approximated with $X_\mathrm{v} = \omega_\mathrm{b}L_\mathrm{v}$, which in per-unit is equal to L_v. As can be seen from (2.3) and (2.4), the derivative action of a transient VI representation has been replaced by an integrative action. A consequence of

this implementation is that a current reference is generated, which results in the obligatory inclusion of a current controller.

In this thesis, only control structures which contain a VA are investigated in detail. Because of this, the terms *virtual admittance* and *virtual impedance* are used interchangeably (with the exception of discussing references). In this terminology, which is common also in the literature, VI does not denote a different implementation, but the inverse of the VA's numerical value: $\underline{Z}_\mathrm{v} = \underline{Y}_\mathrm{v}^{-1}$.

Current Control

A current controller (CC) is often needed to protect the converter hardware from overcurrent. As the CC requires current references to track, the outer loops presented above can not be used directly with a CC, but require an intermediate control loop that generates current references from the internal voltage. Examples for these are the VA described above and the voltage controller described below.

There exists a large variety of CCs that are used in GFM controllers, with the VCC presented as part of the cascaded GFL controller in the previous section being a common choice [72]. The matter of current limitation in GFM converter controllers will be discussed in detail in Chapter 4.

Voltage Control

In some cases, a voltage controller is included to regulate the voltage at the filter capacitor or the PCC to the internal voltage of the GFM controller[12] [74], [103]. To maintain the slowly varying character at the capacitor voltage, any grid disturbance requires control action. Because of this, the behaviour of this type of control is closer to the GFL controllers. This is also visible in the the frequency response of this type of controllers, which varies notably from other GFM controllers [100]. To prevent undesired interactions between the cascaded controllers, the cascaded GFM controller needs to be tuned carefully [100], [119], [120].

[12] This type of control structure is typically called cascaded GFM control.

Table 2.1: Comparison of GFL and GFM converter control.

GFL converter control	GFM converter control
Fast power-reference tracking	Slow power-reference tracking
Active and reactive power are decoupled	Coupling of active and reactive power can occur (e.g. during transients)
Dedicated synchronisation loop needed (e.g. PLL)	Dedicated synchronisation loop not needed
High performance in strong grids (high short-circuit power, stiff grid frequency)	High performance in weak grids (low short-circuit power, varying grid frequency)
Issues in weak grids: interactions between PLL and CC	Issues in strong grids: slow controller causes low performance and can result in oscillatory step response.
Grid support during disturbances requires control action from outer loops	Immediate, intrinsic grid support
Trivial current limitation	Challenging current limitation
Dominating technology in grid-connected VSCs	Emerging technology

2.4 Discussion

The fundamental difference between GFL and GFM converter control lies in their dynamic and harmonic behaviour. When faced with a disturbance in the grid voltage, the GFL control quickly adapts to maintain a constant current, while the GFM control only slowly follows the changes. The consequences of this fundamental difference on the converter behaviour are summarised in Table 2.1.

In particular at locations with a low grid strength, converters with GFL control can cause oscillations and instability [77], [121]–[125]. A weaker grid is

synonymous with a larger grid impedance, which in turn means an increasing variation in the PCC voltage for a given change in converter current. As a result, the dynamics of the synchronisation loop have in these situations a dominant impact on the performance of the complete system, which can lead to undesirable interactions between converters and cause instability. This means that GFL controllers are not a suitable control choice at particularly weak connection points. Furthermore, due to their current-source character, GFL converters require control action from the outer loops to provide support during grid disturbances, e.g. reactive power during voltage dips. This means that the provision of grid-support services not only can require additional control loops and increased complexity, but in essence has to counteract the underlying behaviour of the controller. Converters with GFM control on the other hand excel at weak grid locations due to the intrinsic character of their grid support.

Considering the conclusions from [18], [100], a VA-based GFM controller with a PI-based APC has been chosen as the starting point for the work in this thesis. The VA-based control structure has been selected since the VA allows to shape the converter's input admittance to provide filtering (through virtual inductance) and damping (through virtual resistance), as well as it makes the converter less sensitive to changes in grid strength. The PI-based outer loop has been chosen as it does not couple its damping provision with a steady-state frequency droop[13], and due to the availability of the effective loop-shaping tuning method. The control structure is depicted in Fig. 2.11 and is discussed in detail, including the tuning of its control parameters, in [109] as well as in **Paper C**. In **Paper F**, a different controller is suggested, which is introduced in Chapter 5.

[13] As is the case e.g. in the VSM [107].

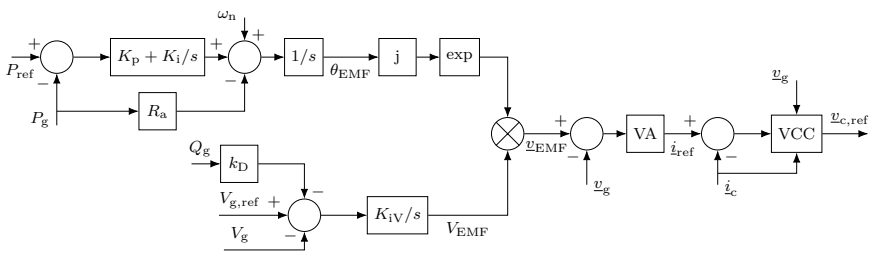

Figure 2.11: Block diagram of the chosen control structure.

CHAPTER 3

Connection Requirements for Grid-Connected Converters

In this chapter, an introduction and overview of grid connection requirements for grid-connected converters is given. A detailed study has been published in 2022 as **Paper A**, which is discussed and contextualized to this thesis in this chapter. As converter-dominated power grids in general and GFM converter control in particular are subjects of current research and the knowledge about these topics is continuously evolving, there has been development in grid-connection requirements since the original study. An overview of these recent developments in converter connection requirements concludes the chapter.

3.1 Types and Impact of Requirement Documents

Connection requirements for grid-connected converters are given in different types of documents that can vary in scope, stringency, and detail. Often several documents apply for a single application. Examples for different types of documents containing requirements are legal regulation (e.g. international [126] and national [127]), industry standards (e.g. [32], [128]), connection rules and grid codes (e.g. [129]), specifications for particular (ancillary) services (e.g. [33], [130]), and finally customer- and application-specific requirements. While

most requirement documents are publicly available, some require purchase, or, as for example some customer requirements, can even be confidential.

Grid-connection requirements can have a large impact on the design of a converter system in general and its control structure in particular, which might need to be altered to follow specific requirements. The requirements impacting the control structure can in some cases be mandatory, while they are optional in other cases, e.g. when enabling the provision of specific ancillary services such as fast-frequency response or power oscillation damping [130]. An explicit pre- or proscription of specific control implementations is however quite atypical, as requirements are typically given to the extent possible as technology- and implementation-agnostic performance requirements. Refer to the rest of this chapter, **Paper A** and [19], [24], [26], [31], [131]–[137] for examples on how grid connection requirements impact converter control structures and particularly GFM control.

High-power converter systems are very development- and testing-intense, and for the converter system to be commercially viable, as much of the system as possible should be reusable independent of the power system which the converter is connecting to. Even though the amount of case-specific design and adaption increases with the power rating, meaning that e.g. HVDC systems and FACTS are typically tailor-made, re-using parts of the system such as the control structure is common and required for economic viability. Due to this, specifications can have an impact beyond their formal scope of validity. This can be illustrated with the explicit ban of the use of a VI in converters with GFM controllers in the British power system, which was published by the British TSO National Grid in 2021 [33]. In control structures that contain a VI, the VI typically forms a central, non-optional part of the overall control structure. Those manufacturers using a VI in their converter control would have been left with the choice to either develop a new control structure lacking a VI, or to forgo the British market. As maintaining two different control structures typically is unfeasible, this ban would have had effects on other markets as well, even though the VI has a number of advantageous properties. The VI-restriction has been removed by the British TSO in 2024 [138].

For the study published in **Paper A**, the following documents have been selected for comparison to provide a representation of different types of requirement documents: The European network codes on Requirements for Generators (NC RfG) and HVDC transmission systems and dc-connected

generation (NC HVDC) [126], [139], their Swedish national implementations [127], [140], the VDE industrial norm VDE-AR-N 4131 for HVDC and dc-connected generation, which is the German national implementation of NC HVDC [32], the IEEE draft standard for converter-interfaced resources P2800 [128], and the final grid code modification report on GFM capability by the British TSO National Grid (NG GC0137) [33]. As most available documents did not contain requirements on GFM-capability at the point of the study, the European Network of Transmission System Operators for Electricity (ENTSO-E) report on this matter has been included in the comparison as an indication on expected future developments [8].

3.2 Categories of Requirements

As outlined in Chapter 1, grid-connection requirements for converters have evolved and become more complex over time [19], [24]. While three to two decades ago converter-interfaced generation still led a niche existence without notable impact on system stability, requirements mainly aimed to prevent negative impact on the rest of the grid by regulating power quality and permissible harmonic content. As the penetration of power electronics increased, they started to have an impact on the power system, which led to the requirement to participate in steady-state voltage control (by means of reactive power) and prevention of overfrequency (by reduction of active power). Also, with increasing amount and size of renewable generation size, disconnection in case of nearby faults was not acceptable any more, causing the introduction of low-voltage and fault ride through requirements [24]. With converter-interfaced generation providing the majority of generation in some power systems, new challenges such as low system inertia, converter-induced instability, and lack of black-start capability came into focus and were reflected in newer requirement documents published around 2016 - 2020.

Requirement documents of different type, but even within the same type, can be extremely different in their structure, rigour, definitions and extent, even though the previously delineated trends apply in general. Some grid codes deal with specific topics in great detail, while others relegate them to appendices, supplemental material, industrial norms or do not take them up at all. To enable a qualitative comparison of the requirements posed on grid-connected converters, it is therefore instrumental to establish categories of

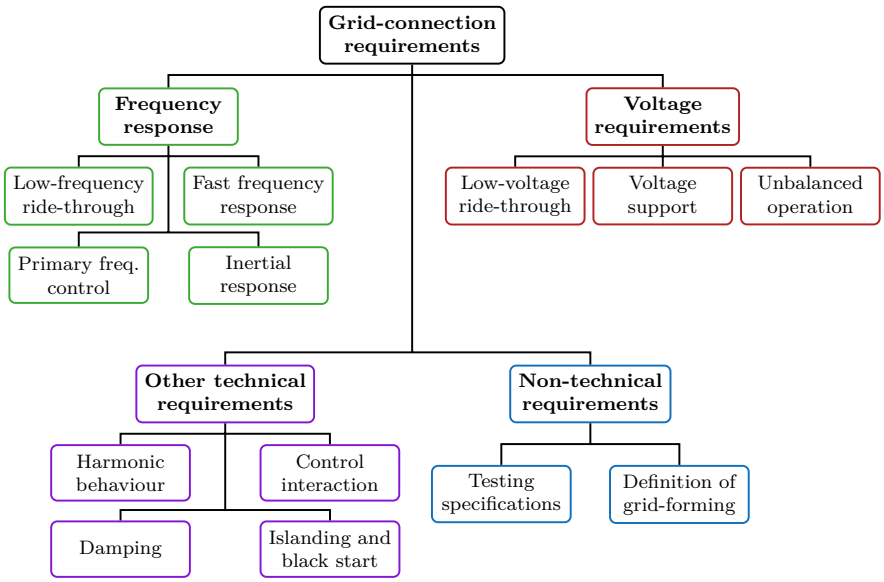

Figure 3.1: The categories used for comparison of requirements in **Paper A**.

requirements. The choice of the categories shown in Fig. 3.1 is motivated and clarified further in **Paper A**.

3.3 Conclusions from the Study of Requirements

A general comparison of requirements from all categories is challenging, as the specifications are often given in different formats between documents, and the level of detail can vary greatly. Important differences often hide in details, definitions etc., which makes a generalization difficult. There are however some conclusions to be drawn from the overview on requirements in the documents selected for comparison shown in Table 3.1. A more detailed, per-category analysis is available in **Paper A**.

Typically, requirements depend on the application, and the majority of regulations regarding grid-connected converters treat for converter-interfaced generation (e.g. [126]–[128]). While there also exist documents for HVDC transmission systems and dc-linked generation such as offshore wind-parks [32],

Table 3.1: Overview of requirement categories included in the documents compared in **Paper A**. ✓: explicitly specified, required by standard or on demand of the TSO; ○ : unspecific/implicitly specified; ✗: not mentioned.

Type of requirement	NC RfG & HVDC [126], [139]	SE RfG & HVDC [127], [140] *	VDE-AR-N 4131 [32]	IEEE P2800 [128]	NG GC0137 [33]	ENTSO-E report [8]
Frequency response						
Frequency deviation	✓	✓	✓	✓	○	○
Primary frequency control	✓	✓	✓	✓	✗	✗
Fast frequency response	✗	✗	✓	✓	✗	✗
Inertial response	✓	✗	✓	✗	✓	✓
Voltage requirements						
Voltage deviation	✓	✓	✓	✓	○	○
Voltage support	✓	✗	✓	✓	○	○
Unbalanced operation	✗	✗	✓	○	✗	✓
Other technical requirements						
Harmonic behaviour	✗	✗	✓	✓	○	✓
Damping	✓	✓	✓	○	✓	✓
Control interaction	○	○	✓	○	✓	✓
Islanding and black start capability	✓	✗	✓	✗	✗	○
Non-technical requirements						
Testing specifications	✓	✗	✓	✓	✓	○
Definition of grid-forming capability	✗	✗	✗	○	✓	✓

*: As SE RfG & SE HVDC are national implementations of NC RfG & NC HVDC, respectively, they include the requirements mentioned there. Here is indicated where these documents contain substantial concretizations or additions.

[139], [140], general requirements for other devices such as grid-supporting or grid-forming BESSs and STATCOMs are still rare [78], [136], [141], [142]. In those cases technical specifications given by the customer often contain the bulk of requirements. Despite this application-specific character of the requirements it has been observed in the study that the difference in requirements tends to be mostly gradual or quantitative. Bigger qualitative differences are typically rather to be found for varying converter system power and voltage ratings, e.g. ENTSO-E's power park module classes. A consequence of this is that the technical requirements do not obligate to design application-specific GFM control structures.

The overview in Table 3.1 asserts the previously mentioned variation in detailedness. A reason for this lies in different philosophies from TSO-side regarding requirements: Some TSOs prefer to specify many capabilities as requirements to be fulfilled by all connected devices, thereby prioritizing reliability [32], while others tend to be much more restrained in the amount of obligatory requirements and aim to handle the system needs primarily through market-based instruments such as new ancillary-service products, which prioritizes affordability [130], [140], [143]. These differences are induced by power system properties such as size, interconnectedness, generation mix and control philosophy, as well as legal culture and similar factors. This means that also non-obligatory specifications like [33], [130] should be taken into account for the design of requirement-compliant control structures.

The study in **Paper A** concludes that, at the time of publishing, none of the compared regulations requires GFM control, and only the British grid code defines GFM capability (through [33]). It can however be seen that some documents, e.g. [32], require capabilities that are typically associated with GFM control, such as inertial response and black start capability. Based on this study it can be concluded that there are few concrete restrictions and requirements to follow in the development of GFM control structures, with the previously mentioned bandwidth-limitation and subsequently retracted VI-restriction in the British grid code modification being the only exceptions.

3.4 Recent Developments in Requirements for GFM Capabilities

Since this study of requirements in has been conducted and published as **Paper A** in 2022, several new documents dealing with requirements for GFM converter control have been published [78], [142], [144], [145]. Furthermore, the European Union Agency for the Cooperation of Energy Regulators (ACER) has recommended the European Commission to amend, among others, the existing regulations NC RfG and NC HVDC [146]–[149]. In the proposed amendment all converter-interfaced generation[1] above a certain power and voltage rating [2] is required to provide GFM capability, with the TSOs being allowed to require the same even for smaller units and HVDC stations[3]. Based on this, ENTSO-E has published a first interim report containing technical requirements for GFM behaviour of converter-interfaced generation, which will serve as the base for further discussions [151]. A selection of testing scenarios for the corresponding regulations can be found in [152], [153]. Additionally, these recent documents have been discussed in the literature by academia and industry [19], [30], [135]–[137]. A comprehensive overview of the recently published requirements can be found in [137], as well as an introduction to the European regulation framework and the reasoning behind its proposed compliance assessment, which aims to define performance indicators to assess GFM behaviour independently of the grid or testing environment.

In contrast to the conclusions of the earlier study, due to these documents there is now a large amount of detailed technical specifications for GFM behaviour available. All of the recent specifications reiterate that the converter with GFM controller should behave as a voltage source behind an impedance, and that the voltage magnitude and frequency shall remain constant during the period immediately following a grid disturbance – as long as the converter's current, energy or voltage limits are not exceeded. The consequences of this intrinsic behaviour are then discussed mainly for grid voltage angle jumps, frequency transients and grid-voltage magnitude changes. An overview of the

[1] Called power park modules in the European regulation.

[2] Generation connected to 110 kV or above of class B or higher, i.e. rated at least at 1 MW in Continental Europe, 1.5 MW in the Nordic region, 0.5 MW in the Baltic, and 0.1 MW on Ireland, or alternatively generation above 10 MW [147].

[3] Nonwithstanding strong indications that a much smaller share of GFM-controlled converters of about 20 % might be enough to ensure system stability [8], [150].

requirement areas contained in the recent specifications[4] are shown in Table 3.2.

These recent specifications on GFM converters make some of the conclusions from **Paper A** obsolete. The documents contain detailed definitions and requirements of GFM behaviour and allow for detailed compliance studies. In case the regulation suggestion [146] is accepted, GFM behaviour even becomes mandatory for all larger converter-interfaced generation. References between the specification documents are common and the documents appear more uniform when compared to the ones in the first study, which testifies to an active exchange and collaboration between the system operators on this topic. And finally, several of the documents explicitly formulate the goal to be technology- and implementation agnostic, while the previous study remarked on the British VI-restriction as an exception to this rule.

Even though the GFM control structures studied in this work have not been tested explicitly for compliance with the recently published GFM specifications, they follow the basic principle of creating a slowly varying voltage source behind an impedance, and the voltage magnitude and frequency remains constant during the period immediately following a grid disturbance[5]. It is therefore expected that these controllers are able to also fulfil the core requirements of the recent specifications, provided that the control parameters are tuned accordingly.

[4]The areas chosen here are more specific to GFM control than the categories used in Table 3.1. It is important to keep in mind that the previous requirements, e.g. on steady-state voltage regulation, still apply to GFM converters.

[5]With the exception of the need for current limitation, which is recognized by the studied grid codes and discussed in the following chapter.

Table 3.2: Overview of GFM requirement categories included in recent documents.
✓: explicitly specified, required; ○ : unspecific/implicitly specified; ✗: not mentioned.

Type of requirement	AEMO [144], [153]	Fingrid [142]	NERC [78]	UNIFI [145]	ENTSO-E [151]
Active power response to grid voltage angle jumps and frequency transients (inertial response)	✓	✓	✓	✓	✓
Reactive power response to grid voltage magnitude changes	✓	✓	✓	✓	✓
Response time specification	○	✓	○	○	✓
Behaviour under current saturation	✓	✗	○	✓	✓
Weak grid operation	✓	✓	✓	✓	✓
Islanded operation	✓	✓	✓	✓	✓
Power system oscillation damping	✓	✓	✗	✓	○
Unbalanced operation	○	✓	✓	✓	✓
Frequency response characteristics & passivity	✓	✗	✓	✗	✗
Testing specifications	✓	✓	✓	✗	✓

CHAPTER 4

Grid-Forming Converter Operation During Current Saturation

This chapter will discuss some of the challenges of current limitation in GFM controllers as well as the transient stability problem for those controllers during current limitation. It will also introduce the solutions to these challenges proposed in **Papers B - E**.

4.1 Grid-Forming Converter Current Limitation

The review of grid-connection requirements in the previous chapter has shown that fault-ride through capability (summarized in the category voltage deviation) is a central requirement. Power-electronic converters only possess very limited overcurrent capability due to the low thermal capacity and high temperature sensitivity of the semiconductors, which means that current limitation is crucial, in particular during large system events, such as short-circuit faults. As indicated earlier, GFM converters should behave as a slowly varying voltage source. If this behaviour is to be preserved even during conditions that cause current saturation, current limitation becomes non-trivial [71], [118].

At the same time, disturbances such as faults pose the largest risk for instability in the grid, with the consequence that the stabilizing properties associated with GFM converter control are most advantageous during those occurrences. Consequently, it is desirable to retain the GFM behaviour as much as possible even during current saturation. Recognizing the necessity for current limitation, requirements for GFM converters typically allow the converter to change its dynamic properties for up to a few fundamental frequency cycles before returning to its voltage-source behaviour [144], [154], [155], or to retain the GFM behaviour only for disturbance counteracting the current saturation [147]. An effective current-limitation strategy for GFM converters consequently needs to ensure not only that the current does not exceed the set limits, but also that the converter remains in stable operation and retains the GFM properties to the degree possible.

This section will give an overview of existing current limitation strategies for GFM controllers and discuss some of their shortcomings. It will then give an introduction into the study of GFM controllers' transient stability during current saturation. Finally, it will present the basic principle and some central parts of the voltage-based current limitation presented in **Paper C**.

Review of Existing Current-Limitation Strategies

The large number of current-limitation methods for GFM converters that have been reported in the literature in recent years is testament of the importance and challenging character of current limitation in GFM controllers. A comprehensive review of existing limitation methods, which can be classified into the following four main categories, is available in [118]. The categories can be summarized as:

- *Immediate current limitation*: Methods of this category require an explicit current reference, which is – at least during limitation – tracked by a CC. It is therefore commonly applied in cascaded voltage and current vector controllers [74], [103], [156] and in virtual admittance control [108], [109], [111]. This method can lead to stability problems during severe grid disturbances [157], as will be discussed more in detail in the following section.
  Some control structures do not rely on a CC during normal operation, but activate it during current saturation only (e.g. PSC [92], [93]). This

can imply switching the synchronisation task from the APC to a PLL, and changing the converter behaviour from a voltage source to a current source, i.e. to a GFL characteristic [158], [159].

- *Indirect current limitation by virtual impedance*: This category utilizes the fact that GFM controllers behave as a voltage source behind an impedance, and a manipulation of the (virtual) impedance can be used to change the current exchanged with the grid without altering the voltage source. A shortcome of the VI-based limitation approach [110], [113], [117], [160], [161] is that it requires knowledge of system parameters to appropriately select the VI parameters. System conditions differing from those assumptions can result in overcurrent or low utilization of the converter's fault current contribution capability [118]. An adaptive VI, which is commonly used to address this problem, can on the other hand deteriorate the converter's transient stability [162].

- *Indirect current limitation by voltage limitation*: Also based on the characteristic of GFM control to behave as a voltage source behind an impedance, this category of methods aims to limit the current by manipulating the converter's internal voltage source. Some methods limit both voltage magnitude and angle using an estimate of the grid voltage angle [163], [164], which in practice can mean a switch to PLL-based synchronisation. If only the voltage magnitude is limited, a different limitation strategy is needed for the active current – typically a power limiter [165].

- *Indirect current limitation by power limitation*: Methods of this category rely on limitation of the inputs to the active- and reactive-power control loops to prevent overcurrent [108], [166], [167]. They commonly require fault detection, which can be unreliable for e.g. overcurrents caused by frequency disturbances. Furthermore, as the outer control loops are typically relatively slow in GFM controllers (up to 5 Hz), relying solely on this type of method can fail to reliably prevent transient overcurrents [118].

The reviewed methods are not able to satisfy the goal of effective current limitation that keeps the converter stable even under disturbed and weak grid conditions while retaining as much of the GFM properties as possible. This is

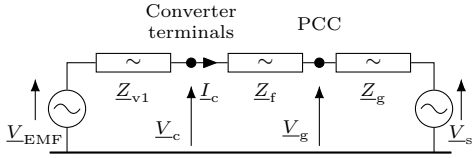

Figure 4.1: Equivalent circuit representation of a converter with GFM control approach with virtual-back EMF and virtual impedance.

in particular the case as the majority of current limitation studies is designed with voltage-dip induced overcurrent in mind [108], [117], [168]–[174]. As shown in **Paper B, C** and the following section, large frequency disturbances can also cause overcurrent and result in instability if the current limitation method is not designed with this disturbance type in mind, in particular if the converter is supposed to provide inertial support.

Transient Stability of Converters with GFM Control

To analyse the transient stability of a generic GFM-controlled converter, the system depicted in Fig. 4.1 is studied. It consists of a converter with GFM control, modelled as its internal voltage source $\underline{V}_{\mathrm{EMF}}$ and the tunable part of the VI $\underline{Z}_{\mathrm{v1}}$, the filter impedance $\underline{Z}_{\mathrm{f}}$, and the Thévenin equivalent representing the grid with the grid impedance $\underline{Z}_{\mathrm{g}}$ and the voltage $\underline{V}_{\mathrm{s}}$.

The transient stability of this system can be studied with the help of the quasi-steady state active-power transfer between converter and grid. Neglecting the resistive elements[1], the converter current $\underline{I}_{\mathrm{c}}$ is given as

$$\underline{I}_{\mathrm{c}} = \frac{\underline{V}_{\mathrm{EMF}} - \underline{V}_{\mathrm{s}}}{\mathrm{j}X} = \frac{V_{\mathrm{s}} \sin\delta + \mathrm{j}(V_{\mathrm{s}} \cos\delta - V_{\mathrm{EMF}})}{X}, \tag{4.1}$$

where $\delta = \angle\underline{V}_{\mathrm{EMF}} - \angle\underline{V}_{\mathrm{s}}$ is the angle difference between the voltage sources, and X is the total reactance between them. This allows to calculate the active power P as

$$P = \mathfrak{Re}\left(\underline{V}_{\mathrm{EMF}}\ \mathrm{conj}(\underline{I}_{\mathrm{c}})\right) = \frac{V_{\mathrm{s}} V_{\mathrm{EMF}}}{X} \sin\delta, \tag{4.2}$$

which is the $P - \delta$ curve shown as a solid blue line in Fig. 4.2.

[1] This is done for simplicity of the derivation, and is allowable as the resistance only has a small impact due to its typically small value in power grids.

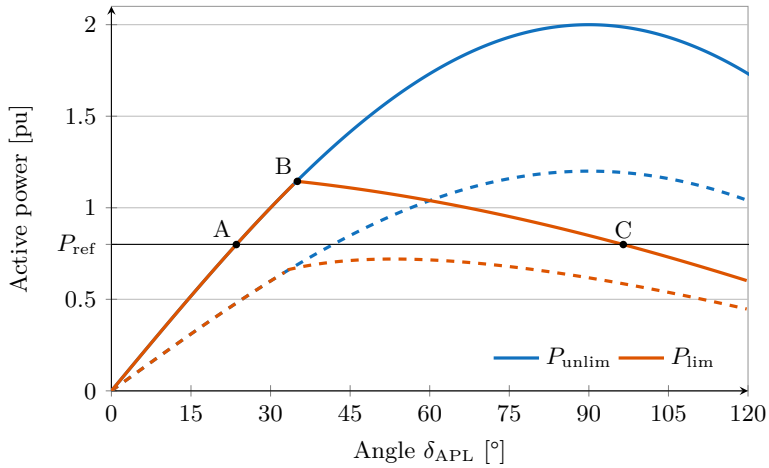

Figure 4.2: P-δ_{APL}-curve illustrating the converter angle stability problem for a current limit of 1.2 pu. A: pre-disturbance operating point; B: current limit reached; C: transient stability limit. Solid lines: $V_{\text{EMF}} = V_{\text{s}} = 1\,\text{pu}$. Dashed lines: $V_{\text{EMF}} = 1\,\text{pu}$ & $V_{\text{s}} = 0.6\,\text{pu}$.

The impact of current limitation on transient stability is studied by applying an immediate current limitation, the so-called magnitude or circular-current limiter that scales the current reference to the maximum magnitude without altering the angle [108], [118]. With $\underline{I}_{\text{ref}}$ being the current reference and I_{max} the current limit, the limited current reference is described as

$$\underline{I}_{\text{ref,lim}} = \underline{I}_{\text{ref}} \frac{I_{\text{max}}}{I_{\text{ref}}} \quad \forall\, I_{\text{ref}} > I_{\text{max}}. \tag{4.3}$$

This manipulation of the current reference is equivalent to changing the internal voltage source's magnitude and angle, illustrated as $\underline{V}'_{\text{EMF}}$ in Fig. 4.3. From the figure it can be seen that the load angle δ resulting from the limitation is reduced when compared to the unlimited load angle generated by the APC, denoted as δ_{APL}. Even though the load angle is altered, angle and magnitude of the unlimited internal voltage source still have an impact as they determine the angle of the resulting (unlimited as well as limited) current reference. Based on this, (4.1)-(4.3) can be used to determine the relation between the current-limited active power P_{lim} and the APL output angle δ_{APL}

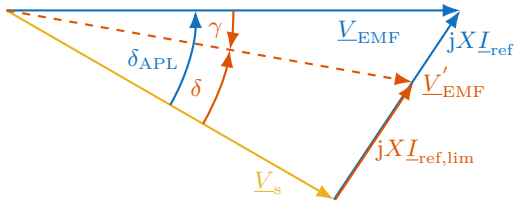

Figure 4.3: Phasor diagram illustrating the impact of the circular current limitation strategy on the back EMF.

as

$$P_{\mathrm{lim}} = \mathfrak{Re}\left(\underline{V}_{\mathrm{s}}\ \mathrm{conj}(\underline{I}_{\mathrm{ref,lim}})\right) \tag{4.4}$$
$$= \frac{V_{\mathrm{s}} V_{\mathrm{EMF}} I_{\mathrm{max}} \sin\delta_{\mathrm{APL}}}{\sqrt{V_{\mathrm{s}}^2 + V_{\mathrm{EMF}}^2 - 2V_{\mathrm{s}}V_{\mathrm{EMF}}\cos\delta_{\mathrm{APL}}}}, \qquad I_{\mathrm{ref}} > I_{\mathrm{max}}.$$

This relationship is illustrated as a solid red line in Fig. 4.2. The current limit is reached at operating point B, and a further increase δ_{APL} results in a decreasing power transfer, which is in contrary to the unlimited case presented in blue. The effect of a voltage dip, here from 1 pu to 0.6 pu, is shown as the dashed lines in the same figure.

From this, two instability mechanisms can be observed, which are explored more in detail in **Paper B** and are in principle similar to a SM's instability mechanisms. The first is caused by the maximum active-power transfer becoming smaller than the active-power reference, e.g. due to a voltage dip (see dashed line in Fig. 4.2). The second is caused by the downward sloping of the power-angle curve as soon as current limitation is reached. This condition can be reached as part of a fault ride-through (in case the active-power reference has not been adapted), or caused by a temporal increase of the load angle e.g. due to a phase jump or frequency disturbance of the grid voltage. The speed of the APC determines how vulnerable the converter is to this instability mechanism, which results in a higher risks for converters whose APC are tuned to a slow speed to provide an inertial response. While the first, voltage-dip-induced instability has been studied widely in the literature [108], [117], [168], [170]–[172], [174], the latter has been rarely regarded in existing publications [175].

Voltage-Based Current Limitation

To address the shortcomings of the existing current limitation strategies and the risk of instability, a voltage-based current limitation is proposed that aims to retain as much of the voltage-source characteristics as possible by adapting the converter's internal voltage to limit the current. The method is based on a voltage-magnitude limitation together with limitation of the active-power reference. It is presented in detail in **Paper B**, but the core principles are summarized below.

Principle

The principle of the voltage-based current limitation is based on the idea that to limit the current of a converter with GFM controller while retaining as much of the voltage source characteristics as possible, as much of the original control principle should remain unaltered. To achieve this, the approach focuses on adjusting the converter's internal voltage source instead of the current reference.

The converter current is determined by both angle and magnitude of the internal and the PCC voltage:

$$\underline{I}_{\mathrm{c}} = \frac{\underline{V}_{\mathrm{EMF}} - \underline{V}_{\mathrm{g}}}{R_{\mathrm{v}} + \mathrm{j}X_{\mathrm{v}}}. \tag{4.5}$$

Due to the predominantly reactive nature of the grid, the angle of the internal voltage is in GFM converters typically determined by the APC, and the magnitude is set by the RPC or AVC. While it is straightforward to limit the difference in magnitude between V_{EMF} and V_{g}, limiting the angle difference requires knowledge of the angle of V_{g}, which is difficult to acquire. Moreover, relying on an grid-angle estimation method such as a PLL to limit the angle difference is equivalent to switching to the PLL for synchronisation, as the APC's angle output would be disregarded. Switching to PLL-based synchronisation also raises stability concerns, as the PLL typically is relatively slow, in particularly in the case of weak grids.

The suggested approach solves this problem by applying a limit on the active-power reference at the APC's input, while relying on a relatively fast APC to track this reference effectively. The limit is dynamic and adapted based on the grid-voltage magnitude to prevent instability due to too high power reference during voltage dips. The magnitude of the internal voltage is

determined by the AVC, and is subsequently limited dynamically based on the grid-voltage magnitude. To prevent overvoltage after the fault, an anti-windup loop with the gain k_{AW} is included for the AVC. The complete block diagram of the proposed controller including the voltage-based current limitation scheme is shown in Fig. 4.4. As can be seen from the diagram, an immediate current limitation[2] is kept between the VA and VCC. This limitation is only a backup and is activated for a couple of milliseconds following a large disturbance at maximum. To ensure that the voltage-based limitation can provide the limitation, the current limit for that method should be chosen slightly lower than that of the immediate current limiter.

During limitation, it is necessary to prioritise active or reactive-power injection from the converter. Often, this is specified in grid-code requirements, typically prioritising reactive power to support the grid-voltage magnitude [176]. The proposed method is here shown with prioritisation of reactive power, but can be adapted according to the requirements. The estimation of the active-power and voltage-magnitude limits based on this is described below.

Calculation of Active-Power Limits

Prioritizing reactive power transfer, the upper limit for the active-power reference, P_{ul}, is calculated as

$$P_{\mathrm{ul}} = \sqrt{S_{\mathrm{avail}}^2 - Q_{\mathrm{g}}^2}, \tag{4.6}$$

where S_{avail} denotes the available apparent power of the converter, and Q_{g} is the reactive power injected from the converter (or, eventually, the reactive power demanded by the grid codes). The available apparent power of the converter is dynamically calculated based on the PCC-voltage magnitude V_{g} as $S_{\mathrm{avail}} = \frac{S_{\mathrm{N}} V_{\mathrm{g}}}{V_{\mathrm{N}}}$, where S_{N} and V_{N} denote the rated power and voltage of the converter, respectively. If $Q_{\mathrm{g}} \geq S_{\mathrm{avail}}$ (this condition can appear during the first instants of a deep voltage dip for instance, when the converter current momentarily rises above its rated value), the upper limit for the active-power reference is set to zero.

[2]Denoted as *hard current limiter* in **Paper B**.

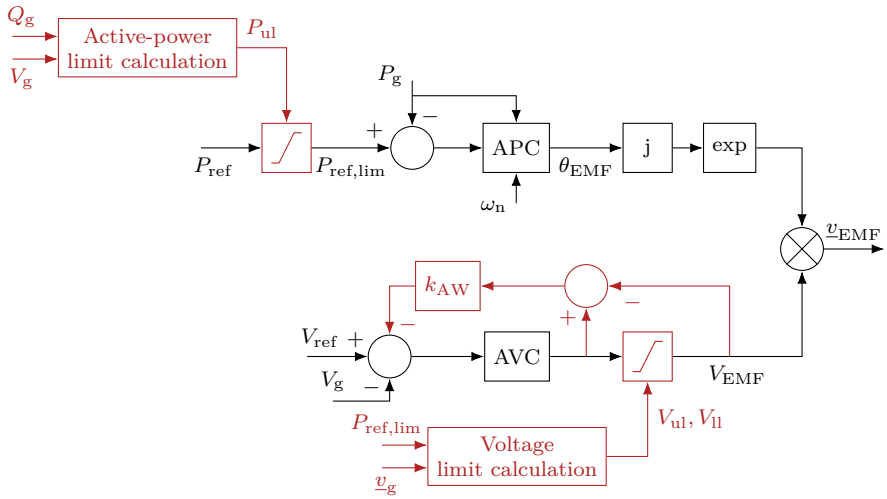

(a) Outer control loops with the proposed current-limitation method.

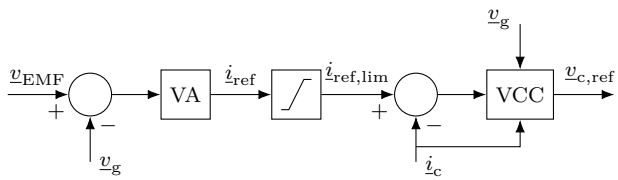

(b) Inner control loops to be used with the proposed current-limitation method.

Figure 4.4: Block diagram of the proposed controller including the voltage-based current limitation scheme. Limiters added by the proposed method shown in red.

Calculation of Voltage-Magnitude Limits

Based on the equations describing the power transfer, the upper and lower limits for the magnitude of the internal voltage can be estimated. The signs of active and reactive power are based on the current direction in Fig. 4.1. Denoting the limited active-power reference as $P_{\mathrm{ref,lim}}$ and the available reactive power as $Q_{\mathrm{avail}} = \sqrt{S_{\mathrm{avail}}^2 - P_{\mathrm{ref,lim}}^2}$, the upper limit for the magnitude of the internal voltage, V_{ul}, is calculated as

$$V_{\mathrm{ul}} = \left| \underline{v}_{\mathrm{g}} + \frac{P_{\mathrm{ref,lim}} - \mathrm{j}Q_{\mathrm{avail}}}{\mathrm{conj}(\underline{v}_{\mathrm{g}})} (R_{\mathrm{v}} + \mathrm{j}X_{\mathrm{v}}) \right|. \tag{4.7}$$

The lower limit for the internal voltage, V_{ll}, which is relevant e.g. during voltage swells, can be calculated accordingly:

$$V_{\mathrm{ll}} = \left| \underline{v}_{\mathrm{g}} + \frac{P_{\mathrm{ref,lim}} + \mathrm{j}Q_{\mathrm{avail}}}{\mathrm{conj}(\underline{v}_{\mathrm{g}})} (R_{\mathrm{v}} + \mathrm{j}X_{\mathrm{v}}) \right|. \tag{4.8}$$

Laboratory Verification

To verify that the proposed limitation strategy is able to limit the current as intended, it has been verified in laboratory experiments. All laboratory experiments reported in this thesis have been conducted using the setup in illustrated in Fig. 4.5. The device under testing is a two-level VSC with a stiff DC link voltage. It is connected through an L-filter to a shunt capacitor, which stabilises the PCC voltage. The grid is represented by a REGATRON controllable ac voltage source and physical reactors modelling the line impedance to provide the desired grid strength. Both converters are controlled using dSPACE hardware-in-the-loop platforms. The parameters for the laboratory setup are reported in Table 4.1.

In **Paper B**, results from several different grid disturbances are shown to demonstrate the effectiveness of the proposed voltage-based current limitation. Figure 4.6 reproduces the response to a voltage dip and frequency disturbance here. It can be seen that the converter current is limited and reactive power is prioritized during the dip as intended.

The reader can refer to **Paper B** for more experimental results and suggested additions to the controller for unbalanced faults.

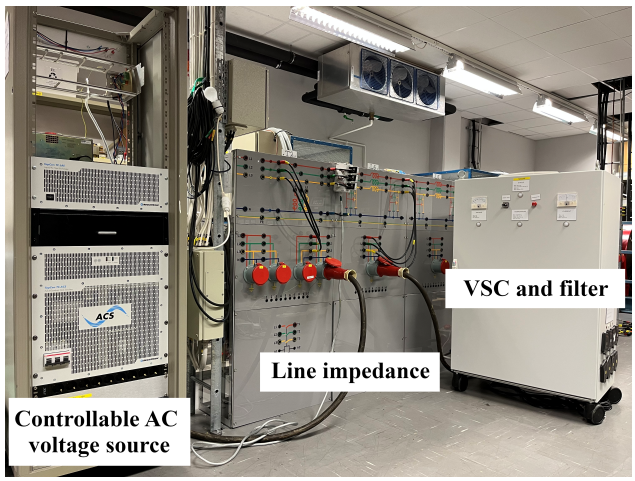

(a) Photograph of the laboratory setup.

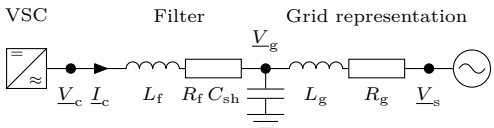

(b) Single-line diagram of the laboratory setup.

Figure 4.5: Laboratory setup used for the experiments in this thesis.

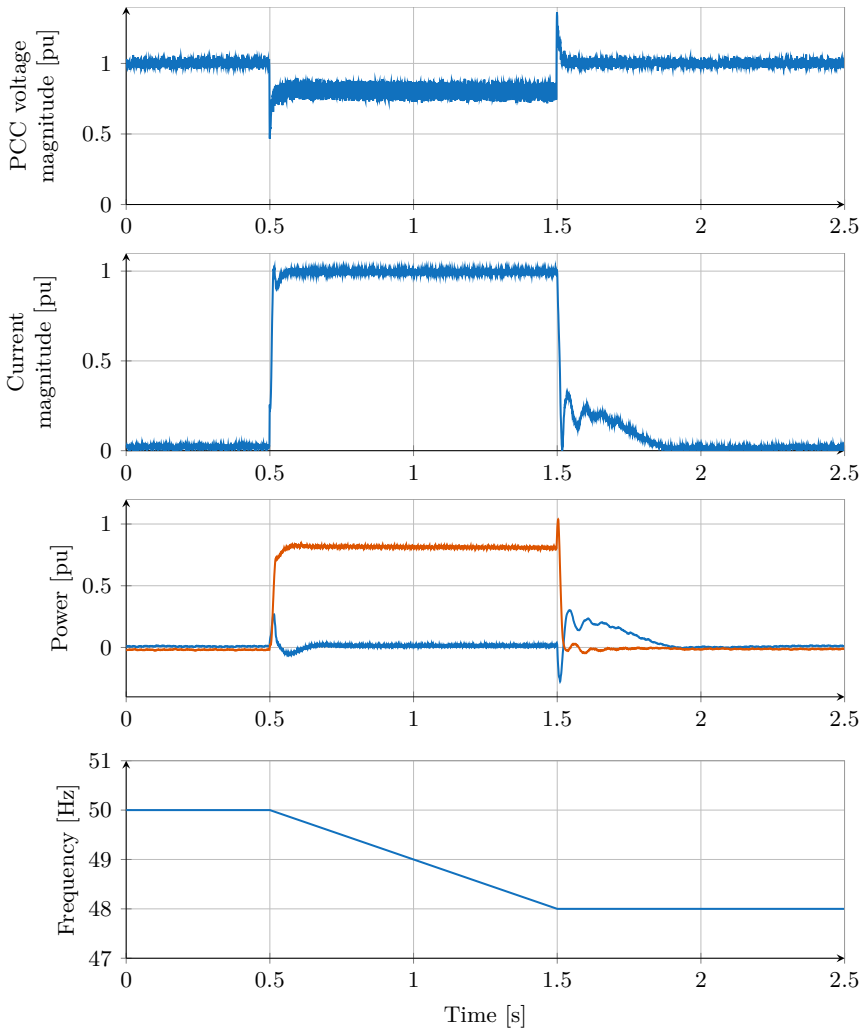

Figure 4.6: Dynamic response of converter with proposed voltage-based current limitation to a balanced three-phase voltage dip accompanied by a frequency disturbance. Third plot from top: blue curve is active power, red curve is reactive power. Bottom plot: frequency disturbance imposed by the controllable ac power source.

4.2 Inertia-Emulation Loop

A converter with GFM control acts as a slowly varying voltage source. This means that the converter will resist a change in the grid frequency by providing an inertial response. The speed of the APC determines the inertia constant characterising the response, with a faster APC having a smaller inertia constant. However, tuning the speed of the APC primarily with the desired inertial response in mind can be undesirable, as the APC also is responsible for the synchronisation of the GFM controller and a slow APC is more prone to the frequency-induced instability during current saturation that has been described above. Due to this reason, a relatively fast APC with a closed-loop bandwidth of 5 Hz has been used in the voltage-based current limitation in the previous section. The inertial response of an APC with this speed is negligible, so an inertia-emulation loop (IEL) is proposed in the following to be able to provide an inertial response when required which is independent of the APC's speed. The IEL adds the emulated inertial power to the converters' active-power reference, which allows it to be limited by the active-power limiter described previously. Due to this, the IEL can also be used to provide an inertial response with GFL controllers.

The IEL has first been presented in **Paper C** and been studied more in detail and tested in the laboratory for **Paper D**. The IEL's stability limits and possibilities to further improve them for extreme conditions are discussed in **Paper E**.

Working Principle

The IEL's basic principle is to estimate an inertial-response power P_{H}, which is then added to the APC's reference. The inertial response should be proportional to the frequency derivative, which is here estimated by a PLL-like structure. The structure is similar to the approaches proposed in [177], [178], which suggest to use a PLL for inertial response in GFL controllers. It is important to note that the IEL does not interfer with the synchronisation of the converter, as it only alters the APC's active-power reference. As the frequency derivative is implicitly determined in the IEL, it avoids the noise-sensitive derivation step known from other methods to provide an inertial response proportional to the frequency derivative. Furthermore, the estimate of the rate of change of frequency (RoCoF) is immediately available, minimis-

ing delays in the converter's inertial response [177]. To further minimize the impact of negative sequence and harmonics in the grid voltage on the generated inertial-response power, a sequence separation and harmonic filtering method based on a recursive least squares (RLS) algorithm is applied on the IEL inputs. The proposed IEL is depicted in Fig. 4.7, and its position in the GFM controller is shown in Fig. 4.4.

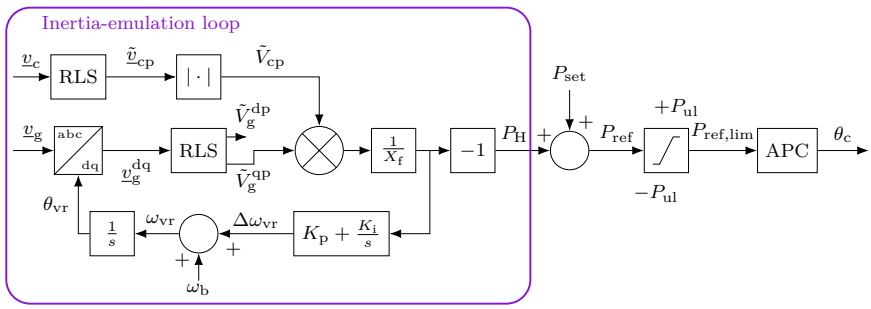

Figure 4.7: Proposed inertia-emulation loop. $\tilde{x}_p$ denotes the positive sequence component of quantity $\underline{x}$ as estimated by the RLS.

Tuning

The goal in tuning the IEL is that the converter's inertial response should be equivalent to a SM with a selected inertia constant H. The output of the IEL is the pure inertial response P_H, which is equivalent to a lossless synchronous condenser (SC), where the mechanical power $P_m = 0$. The fundamental idea is that both SC and IEL track the phase angle of the grid voltage with a given speed, which corresponds to their inertia. A notable difference to the SM is that the IEL is not limited to replicating the SM's inertial response, but offers the possibility to freely tune the response's damping, which in a SM typically would cause additional losses.

The relation between a change in rotor speed of the SM and an active-power imbalance is given by the swing equation:

$$2H\frac{\mathrm{d}\omega_r}{\mathrm{d}t} = P_m - P_e - K_d(\omega_r - \omega_s). \tag{4.9}$$

Here, H denotes the inertia constant in seconds, ω_r is the angular rotor frequency, ω_g the angular frequency of the grid voltage, P_e the electrical power

injected to the grid and K_d the damping coefficient of the machine, with all quantities but H in pu. For a SM operating in a stable steady-state operating point, electrical and mechanical power must be equal. During a grid disturbance, the power imbalance in such a machine will be its inertial response $P_\mathrm{H,SM} = P_\mathrm{m} - P_\mathrm{e}$. Based on the previous equation and the derivations in **Paper C**, it can be shown that the SC's inertial power is given as

$$P_\mathrm{H,SM} = -\frac{V_\mathrm{EMF}}{X} V_\mathrm{s}^\mathrm{q}, \tag{4.10}$$

where V_s^q denotes the source voltage q-component in the SRF aligned with the SC's internal voltage, and X the sum of reactances between the back EMF and source voltage. The SC's change in rotor speed is then in Laplace-domain determined by

$$\omega_\mathrm{r} s = -\left(\frac{K_\mathrm{d}}{2HP_\mathrm{smax}} s + \frac{1}{2H}\right) P_\mathrm{H}, \tag{4.11}$$

where ω_r is the machines' rotor speed and $P_\mathrm{smax} = \frac{V_\mathrm{EMF} V_\mathrm{s}}{X}$ is the machine's maximum transferable active power.

To achieve an equivalent behaviour, the inertial-response power is generated based on the q-component of the PCC voltage in the IEL's SRF, V_g^q:

$$P_\mathrm{H} = -\frac{V_\mathrm{c}}{X_\mathrm{f}} V_\mathrm{g}^\mathrm{q}, \tag{4.12}$$

with the converter voltage magnitude V_c and the filter reactance X_f[3]. Due to the selected PLL-like structure of the IEL, the derivative of the loop's frequency estimate ω_vr is given as

$$\omega_\mathrm{vr} s = -(K_\mathrm{p} s + K_\mathrm{i}) P_\mathrm{H}, \tag{4.13}$$

where K_p and K_i are the proportional and integral gain, respectively. Equivalent frequency tracking behaviour for SM and IEL, given in (4.11) and (4.13), respectively, can be established by selecting the IEL's parameters as

$$K_\mathrm{i} = \frac{\omega_\mathrm{b}}{2H}, \quad K_\mathrm{p} = \zeta \sqrt{\frac{2\omega_\mathrm{b}}{HP_\mathrm{max}}}, \tag{4.14}$$

[3]Instead of V_c and X_f, V_EMF and X_v could be chosen. Here, the converter voltage and filter reactance are selected to avoid the power coupling dynamics introduced by R_v and to couple the emulated inertia closer to the grid voltage. Furthermore, the grid's Thévenin voltage $\underline{V}_\mathrm{s}$ is replaced with the PCC voltage $\underline{V}_\mathrm{g}$, as the latter can be directly measured.

with $P_{\max} = \frac{V_c V_g}{X_f}$ and $\zeta = \sqrt{\frac{\omega_b}{2HP_{\max}}} K_d$ the desired damping ratio of the inertial response. Refer to **Paper D** for a detailed discussion of the selection of damping.

Laboratory Verification

The inertial response provided by a controller with GFM control containing the proposed IEL has been verified in the laboratory using the previously presented setup. In Fig. 4.8, the inertial response to a relatively large frequency disturbance of 2 Hz/s for a duration of 1.5 s is shown. The converter is tuned to provide an inertial response corresponding to $H = 5$ s with a damping ratio of $\zeta = 0.707$. In both cases, an immediate current limiter limits the current at 1.2 pu. The blue curve shows the results for a controller providing inertia exclusively with the APC. As can be seen from the figure, the frequency disturbance causes the current to saturate, and the converter loses stability. If the inertia instead is provided by the IEL, as shown in red, the controller can limit the current at 1 pu using the active-power limiter described above and maintain stability while providing the maximum possible amount of inertia.

Stability Limits

Since the IEL is designed to track the grid-voltage angle with a limited loop bandwidth, instability can occur if the frequency derivative becomes to large, as would be the case for a SM. This instability is investigated in detail in **Paper E**. The resulting instability conditions are illustrated in Fig. 4.9 for four different simulated inertia constants. In the top graph, it can be seen how long a given RoCoF needs to be sustained for the IEL to become unstable. An IEL emulating 10 s of inertia becomes unstable if subject to a RoCoF exceeding 16 Hz/s for at least 0.6 s. From the bottom figure it can be seen, that this would correspond to a grid frequency of 40 Hz. Both the critical RoCoF as well as the resulting frequency deviation are about an order of magnitude above the limits required for generation in current grid codes.

Apart from the stability limits of the IEL, **Paper E** also studies a more realistic concern. If the inertial-response power estimated by the IEL is capped by the converter's active-power limit, the limited power will not be reduced immediately when the frequency disturbance subsides. In the paper, three different modifications of the IEL are investigated, and the addition of an aux-

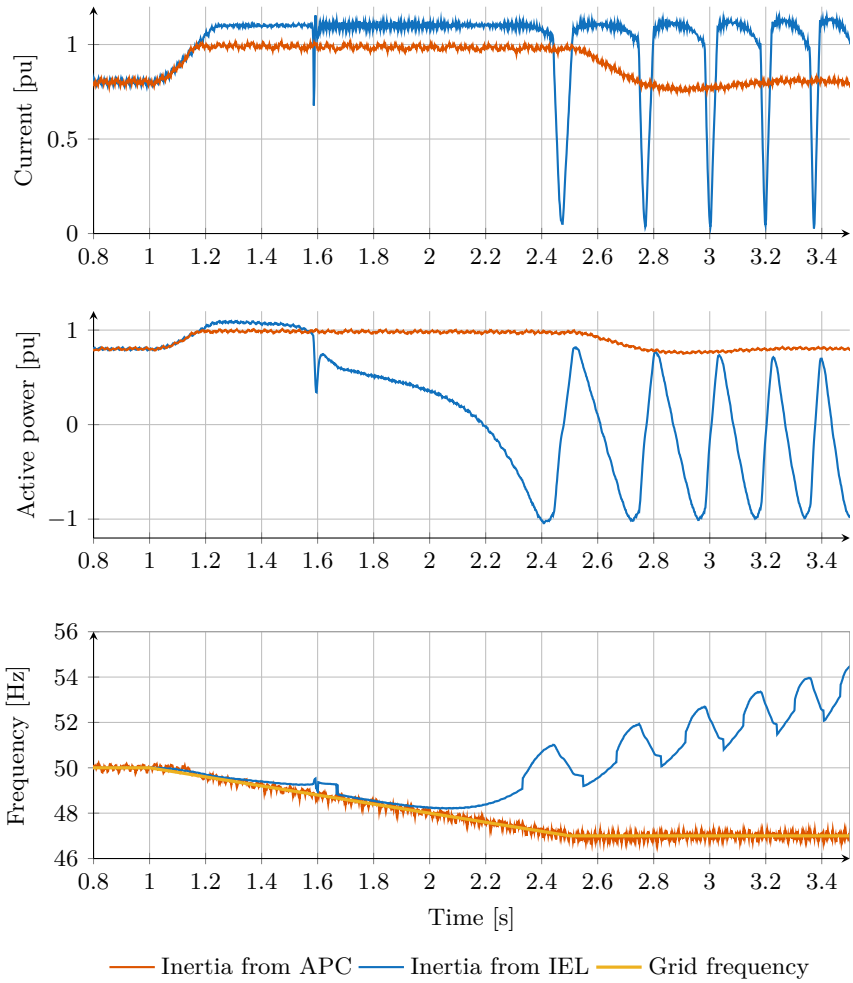

Figure 4.8: Inertial response from APC and IEL to a grid-frequency disturbance of 2 Hz/s during $t = 1\,\mathrm{s}$ to 2.5 s. Top: Grid and internal converter frequency. Middle: Positive sequence active power. Bottom: Converter-current magnitude I_c.

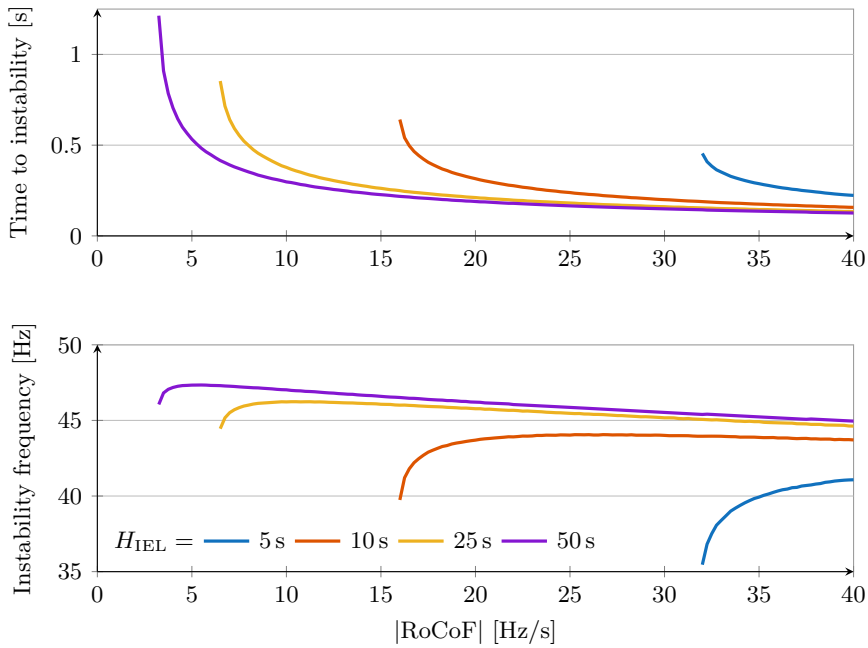

Figure 4.9: Top: Estimated critical ROCOF and time to occurence of IEL instability, depending on the inertia constant. Bottom: Estimated critical ROCOF and frequency at occurence of IEL instability.

iliary PI-controller shown in Fig. 4.10 is suggested to prevent this behaviour. The auxiliary PI-controller has a notably larger gains than the PI-controller included in the IEL and its input is multiplied by the portion of the inertial-response power that is cut by the limiter. Its output is added to the output of the IEL's PI-controller, and it effectively reduces the IEL's inertia constant so that the inertial-response power remains close to the limit.

4.3 Discussion

The proposed current-limitation strategy is able to effectively limit the converter current without relying on the immediate current limiter. The result

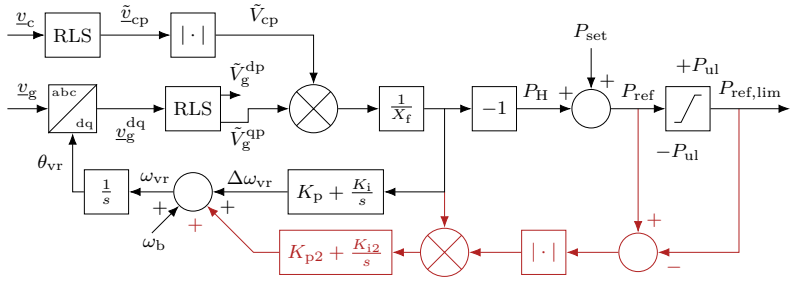

Figure 4.10: IEL modification suggestion in red: Addition of an auxiliary PI-controller.

of the application of voltage limits is that the magnitude of internal voltage source might change suddenly. This is necessary to keep within the current limits. As far as possible, the strategy maintains the GFM behaviour. This is achieved by keeping the dynamics of the APC unchanged, and by applying the limiters before the VA, which means that the converter's frequency response for higher frequencies remains unchanged.

The IEL has been suggested to provide inertia without having to slow down the APC to match the desired inertia constant, which is the typical implementation of inertia in the VSM and similar GFM control strategies and can cause instability during large disturbances. The IEL offers a number of key advantages compared to the VSM implementation of inertia. Separating synchronisation and active-power reference tracking in the APC from inertia provision allows to choose the APC's speed independent from the desired inertia, which protects against instability caused by current saturation due to frequency-disturbances and phase-jumps. It also allows for faster and more efficient power-reference tracking. Furthermore, the separation enabled by the IEL makes it possible to select different damping ratios for active-power reference tracking and inertial response. It also enables for greater flexibility such as adapting or disabling of the inertial response, e.g. based on a connected energy storage's charging state, without manipulation of the APC. Finally, it should be mentioned that this method is suited for inertia provision in GFL converters as well, as adding the inertial-response power to the active-power reference makes it independent of the rest of the controller[4].

[4]Provided the controller can track the active-power reference sufficiently fast for the inertial

The main disadvantage of the IEL lies in the way the inertial response is achieved. Providing the inertial response with the APC, as is commonly the case in GFM converters, means that inertial response becomes a disturbance rejection: The changing grid angle requires the APC to change its frequency to eliminate the power control error caused by the frequency disturbance. As the inertial response is caused by the internal voltage lagging behind in following the changing grid frequency, the inertial response becomes an intrinsic response which does not require any control action. In the IEL on the other hand, the faster APC is able to track the changing grid angle more efficiently, and the inertial response is provided by an intentional control action. Depending on the exact interpretation of GFM behaviour this might be undesired. It is however a way to enable a freely tunable inertial response in a robust GFM controller that retains as much GFM behaviour as possible even during large disturbances that cause the converter current to saturate.

response.

Table 4.1: System and control parameters of the laboratory setup.

System parameters		Control parameters	
S_N	1 kVA	L_v1	0.343 pu
V_N	100 V	R_v1	0.9843 pu
ω_b	314.16 rad/s	$\alpha_\mathrm{P} = \alpha_\mathrm{Q}$	2π 5 rad/s
L_f	0.157 pu	$\zeta_\mathrm{P} = \zeta_\mathrm{Q}$	1
R_f	0.0157 pu	α_CC	2π 200 rad/s
SCR	3.18		
C_sh	0.0942 pu		

CHAPTER 5

Frequency-Response Shaping of Grid-Forming Controllers

As established earlier, GFM behaviour manifests itself through the converter supporting the grid without active control effort, but as an intrinsic reaction to disturbances. Methods based on the frequency-domain response of the converter, such as impedance-based analysis [80], [179], [180], passivity [181], [182], network frequency pertubation (NFP) plots [183], [184], as well as the power-response matrix [185], are among the preferred ways to investigate, demonstrate and create this desired characteristic [8], [33], [144], [154], [186]. This chapter will discuss the desired frequency behaviour of a converter with GFMcontrol, in particular using the converter's input admittance. It will then present the concept of decoupled GFM control, a GFM control strategy that decouples active and reactive power and allows to shape sections of the converter's frequency response independently from each other by tuning separate control parameters. The controller is presented and investigated in detail in **Paper F**. Finally, a previously unpublished method for tuning of the VA's parameters to achieve the desired frequency response is presented.

5.1 Desired Grid-Forming Frequency Response

GFM behaviour means for the converter to act as a slowly varying voltage source behind an impedance. It is important to stress that the slow variation is not only permissible, but actually required, since the converter has to adapt magnitude and angle of its terminal voltage to control its active- and reactive-power transfer. This is not specific for converter-based generation, but applies to SMs as well – with the difference that converters can be controlled much faster, which is why some system operators choose to specify an upper limit for how fast the internal voltage can be changed, e.g. 5 Hz in the case of the British Grid Code [33], [129]. This means that the converter, up to the speed of its outer (power) control loops, shows constant power behaviour, which displays itself as an input admittance that in SRF decreases asymptotically towards a fixed, setpoint-dependent negative resistance as the frequency decreases[1] [80].

At higher frequencies, i.e. in the harmonic range, the converter should act as an impedance with inductive or inductive-resistive behaviour, which manifests as a decreasing input admittance [8]. This behaviour enables the converter to provide passive damping by acting as a sink for harmonic currents, which improves voltage quality and grid strength at the PCC. Furthermore, acting as a constant impedance means that the converter is passive and will not negatively contribute to adverse control interactions within the controllable frequency range [8]. It is important to note that the presence of any fast-acting inner control loop such as a CC poses the risk of deteriorating the passivity of the converter in the frequency range close to its loop bandwidth [182]. To focus on the impact of the rest of the controller, the impact of the fast CC and modulation stage is neglected in this chapter. The desired behaviour of the converter is illustrated in Fig. 5.1.

With the desired behaviour in the low-frequency range (constant power, input admittance decreasing towards 0 Hz) and the high-frequency range (constant inductive-resistive impedance, input admittance decreasing towards higher frequencies) established, this poses the question in which frequency range the behaviour should transition and what behaviour is desirable in that range. To understand this, the input admittance of the voltage source behind an impedance shown in Fig. 5.2 is analysed.

[1] In a stationary reference frame, this would instead be the case at fundamental frequency, with the input admittance increasing for both lower and higher frequencies. To avoid confusion, this chapter will solely use SRF where not explicitly stated differently.

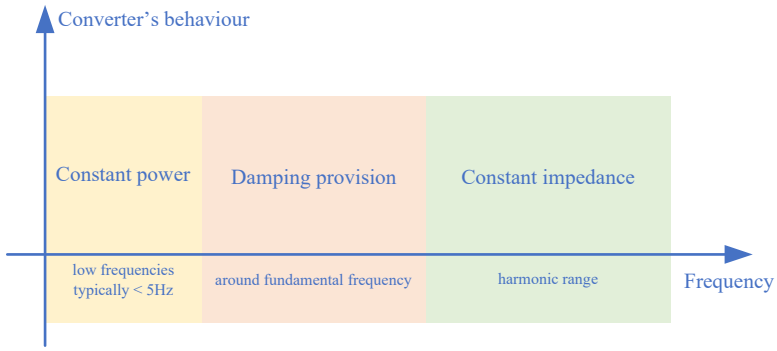

Figure 5.1: Desired GFM control behaviour at different frequencies.

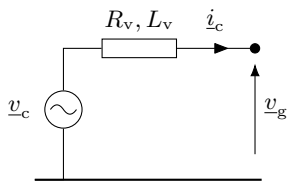

Figure 5.2: Single-line diagram of a model consisting of a voltage source behind an impedance.

In a SRF rotating with ω_b, this input admittance is given as

$$\boldsymbol{Y}(s) = \frac{1}{(R_\mathrm{v} + sL_\mathrm{v})^2 + (\omega_\mathrm{b} L_\mathrm{v})^2} \begin{bmatrix} R_\mathrm{v} + sL_\mathrm{v} & \omega_\mathrm{b} L_\mathrm{v} \\ -\omega_\mathrm{b} L_\mathrm{v} & R_\mathrm{v} + sL_\mathrm{v} \end{bmatrix}, \quad \text{where} \tag{5.1}$$

$$\Delta \boldsymbol{i_c} = -\boldsymbol{Y} \Delta \boldsymbol{v_g} \tag{5.2}$$

with $\Delta \boldsymbol{i_c} = [i_\mathrm{c}^\mathrm{d} \quad i_\mathrm{c}^\mathrm{d}]^\mathrm{T}$ and $\Delta \boldsymbol{v_g} = [v_\mathrm{g}^\mathrm{d} \quad v_\mathrm{g}^\mathrm{d}]^\mathrm{T}$. The Bode diagram of $\boldsymbol{Y}(1,1) = \boldsymbol{Y}(2,2) = \underline{Y}_\mathrm{dd} = \underline{Y}_\mathrm{qq}$, shown in Fig. 5.3, reveals a resonance close to ω_b. Due to the rotating reference frame, this resonance corresponds to a direct current – the dc component known from changing the ac voltage over an inductance. The resistance in the impedance dampens the resonance by letting the dc component decay faster. This phenomenon is well known and described in the literature as synchronous-frequency resonance (SFR) [187]. The dc component has to be damped out quickly, as direct currents can damage transformers and other equipment in the ac grid.

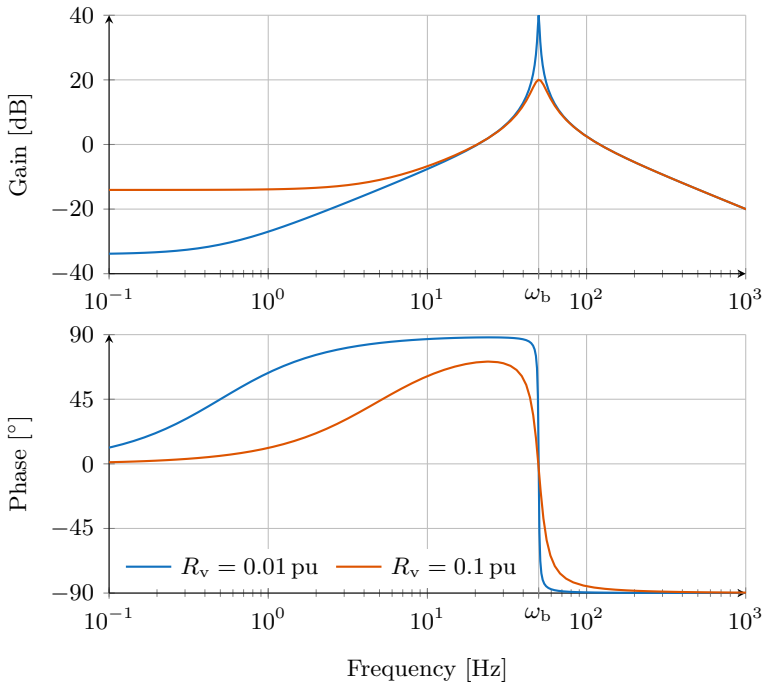

Figure 5.3: Bode diagram of $\underline{Y}_{dd} = \underline{Y}_{qq}$ of the setup shown in Fig. 5.2, with $X_v = 1$ pu and $\omega_b = 2\pi\ 50$ rad/s. Blue: $R/X = 0.01$. Red: $R/X = 0.1$.

As a consequence of this, there are conflicting design goals for the VA. A low R/X ratio is desirable, as it decouples active and reactive power in the converter control. At the same time a low R/X ratio causes a significant SFR, which has to be prevented. Being centred at ω_b, the SFR is positioned in the frequency range between low frequency (up to approximately the outer controllers' loop bandwidths) and the harmonic range. Furthermore, due to the frequency shift, it is also in this range that the converter's response to subsynchronous phenomena (such as power system oscillations) is revealed. This means that the converter should provide damping in this transition range [32], [188].

5.2 Decoupled Grid-Forming Control

This section will introduce the decoupled GFM controller, a GFM control strategy that decouples active- and reactive-power reference tracking to enable free choice of virtual resistance and inductance. The section contains a brief description of the overall control structure and the VA phase compensation, which is the component ensuring decoupling. Finally, it will be shown how this control design enables to shape the frequency response of the GFM controller. A detailed description of the controller is given in **Paper F**.

Motivation

The coupling of active and reactive power is a well-known challenge of GFM controllers [189], [190]. The cause for the coupling lies in the basic principle of using the active power to control the angle of the internal voltage source, and the reactive power to control its magnitude. This separation is based on the following power-flow equations:

$$\underline{S} = P + \mathrm{j}Q = \frac{V_1^2 - \underline{V}_1 \mathrm{conj}(\underline{V}_2)}{\underline{Z}}, \tag{5.3}$$

where $\underline{V}_1$ and $\underline{V}_2$ are two generic voltage sources, $\underline{Z}$ is the impedance connecting them, and $\underline{S}$ is the apparent power flow, consisting of active power P and reactive power Q at $\underline{V}_1$ coming from $\underline{V}_2$. Assuming that the resistive part of the impedance is negligible, $\underline{Z} \approx \mathrm{j}X$, allows to separate active and reactive power by

$$\underline{S} = P + \mathrm{j}Q = \frac{V_1 V_2 \sin\delta}{X} + \mathrm{j}\frac{V_1 V_2 \cos\delta - V_1^2}{X}, \tag{5.4}$$

where δ is the angle between the two voltage sources: $\delta = \angle\underline{V}_2 - \angle\underline{V}_1$. This is typically linearized for small changes in voltage magnitude and angle changes as $\sin\Delta\delta \approx \delta$ and $\cos\Delta\delta \approx 1$ at an operating point with a small angle δ_0, which allows the assumption of $\sin\delta_0 \approx 0$ and $\cos\delta_0 \approx 1$. This results in

$$\Delta P = \frac{V_{1,0} V_{2,0}}{X}\Delta\delta \tag{5.5}$$

$$\Delta Q = \frac{V_{2,0} - 2V_{1,0}}{X}\Delta V_1. \tag{5.6}$$

From this linearization it can be seen that under inductive conditions, the active power changes with the voltage angle, and the reactive power with the voltage magnitude.

The idealised conditions assumed above do however not apply everywhere. Converters connected to distribution grids often are connected to R/X ratios that are not negligible. Furthermore, for large load angles, which in particular can appear under weak grid conditions, the assumptions for decoupling active and reactive power become less accurate. This has the consequence that a control action of the APC also impacts the converters reactive power, and vice versa, a phenomenon commonly described as power coupling.

One method to improve the decoupling for high R/X ratios is to use the VI or VA to reduce the R/X ratio experienced by the converter. This however deteriorates the problem of the SFR, as an increased inductance causes a larger resonance. To mitigate this, a high-pass filtered active resistance as in [93] or the virtual resistance can be used. This however re-introduces power coupling, and only addresses the SFR without unlocking the potential to independently select the VA parameters.

To mitigate this, the decoupled GFM controller in Fig. 5.4 is suggested. Here, an identical PI-based structure is chosen for the APC and RPC. This allows for control symmetry if the corresponding parameters are selected to be equal, which facilitates system analysis by making single-input single-output representation of the converter possible. The decoupling of active and reactive power is achieved by applying the VA phase compensation explained below to the output of the outer loops instead of directly using their output to form the internal voltage source. The phase compensation is based on [38], [191], [192], and it assumes that the output of the outer loops is the complex logarithm of the uncompensated voltage [192]. Both phase and magnitude of this voltage are manipulated by the phase compensation to account for the coupling introduced by the VA. As a result, a purely resistive[2] system model is obtained, which allows independent design of the outer loops.

[2]The direction of the compensation is arbitrary and could be chosen to be purely inductive instead, if the real and imaginary part of the phase compensation input are switched accordingly. This choice does not have a notable impact on the converter's terminal behaviour, as it only has an impact on the virtual voltage generated by the outer loops, but not beyond the phase compensation.

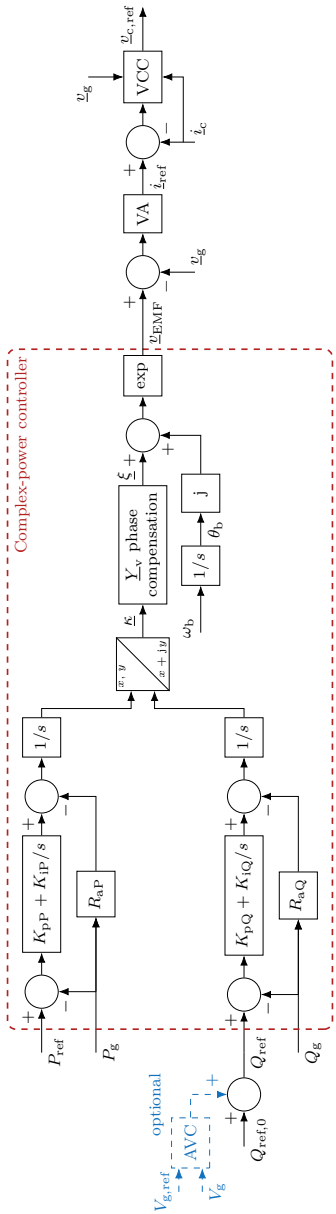

Figure 5.4: Block diagram of the suggested decoupled GFM controller.

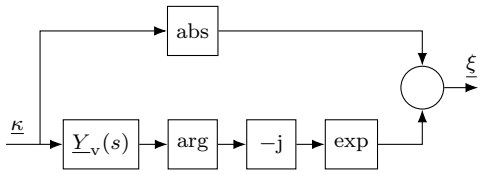

Figure 5.5: Suggested compensation of the virtual impedance angle.

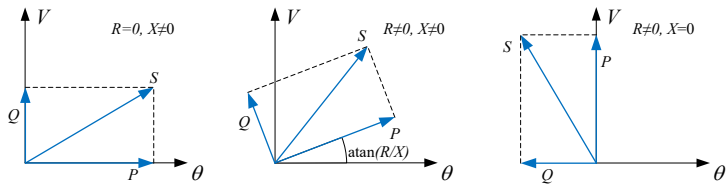

Figure 5.6: Impact of impedance angle on relation between voltage's amplitude and angle and active and reactive power.

Virtual Admittance Phase Compensation

The VA-phase compensation is responsible for decoupling active and reactive power, making them independent of the R/X ratio of the VA and grid connection. Conceptually, the decoupling is achieved by dynamically rotating the complex output signal of the outer loops $\underline{\kappa}$ by the frequency-dependent virtual-impedance angle, $\varphi_{\mathrm{Y}}(s)$. This is achieved through the structure depicted in Fig. 5.5.

In consequence, from the virtual internal voltage source, the resulting power flow appears as if governed by a purely resistive network, where voltage magnitude controls active power and voltage-phase angle controls reactive power (see Fig. 5.6). The concept of the VA-phase compensation proposed here is similar to the method proposed in [38], [191], as it rotates the complex-apparent power vector to remove the coupling introduced by an admittance with both resistive and inductive elements. However, it is important to note that the dynamic implementation proposed here is applicable for a wide frequency range well beyond the fundamental frequency. An in-depth analysis of the phase compensation can be found in **Paper F**.

The impact of the phase compensation can be seen from the simulation results in Fig. 5.7. The figure shows simulated PCC voltage magnitude, filter

Table 5.1: System and control parameters for the simulation, in accordance with the laboratory setup used for **Paper F**.

System parameters		Control parameters	
S_N	100 MVA	L_v1	0.343 pu
V_N	400 kV	R_v1	0.9843 pu
ω_b	314.16 rad/s	$\alpha_\mathrm{P} = \alpha_\mathrm{Q}$	2π 5 rad/s
L_f	0.157 pu	$\zeta_\mathrm{P} = \zeta_\mathrm{Q}$	1
R_f	0.0157 pu	α_CC	2π 200 rad/s
SCR	6.6		
C_sh	0.0942 pu		

current, active, and reactive power at the PCC for a series of reference steps in active and reactive power. In red, the figure shows the response of the suggested decoupled GFM controller, while in blue the response of an identical controller with equal parameters, but with a deactivated phase compensation is shown. The phase compensation's impact on the power coupling can be observed in the power plots: without the phase compensation, steps in active power cause a large disturbance in the reactive power transfer, and vice versa, as can be seen from the blue curves. With the phase compensation, only a minimal impact can be observed, mainly caused by the finite grid strength.

Shaping of Frequency Response in Decoupled GFM Control

A detailed analysis of the frequency response of the decoupled GFM controller is given in **Paper F**, both using simplified analytical expressions with a quasi-steady state VA model as well as with the dynamical VA implementation. The analysis shows that the proposed design addresses both the problem of SFR as well as power coupling. It demonstrates furthermore how different control parameters can be used to influence the controller response in different frequency ranges. These findings are summarized in Fig. 5.8, which shows the *dd*-element of the converter's input admittance as a comparison to the desired converter behaviour shown in Fig. 5.1. For comparison, the response of the pure virtual admittance, without controller, is also shown in black.

From Fig. 5.8, it can be seen that the main difference to the pure admit-

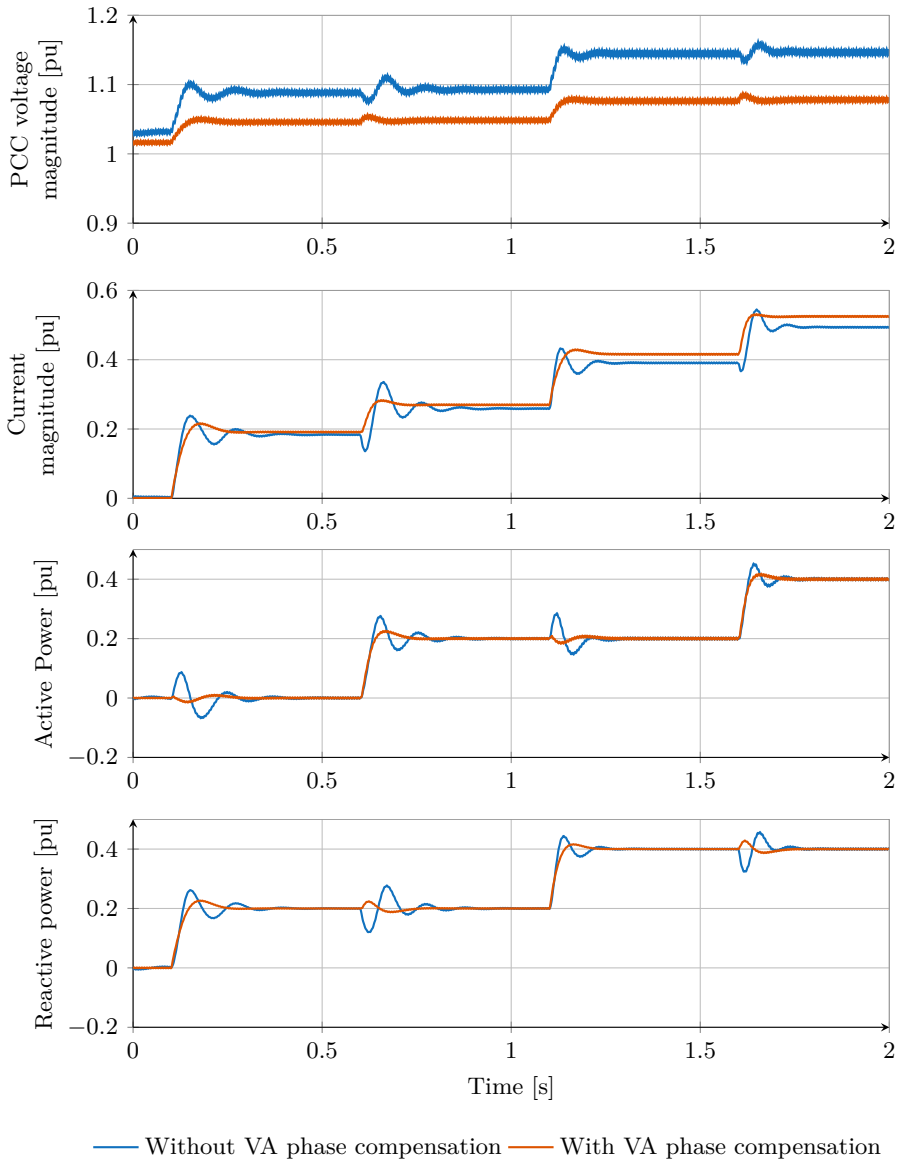

Figure 5.7: Results of steps in the power references of the proposed controller with inactive and active phase compensation. Blue curves: Phase compensation inactive. Red curves: Phase compensation active.

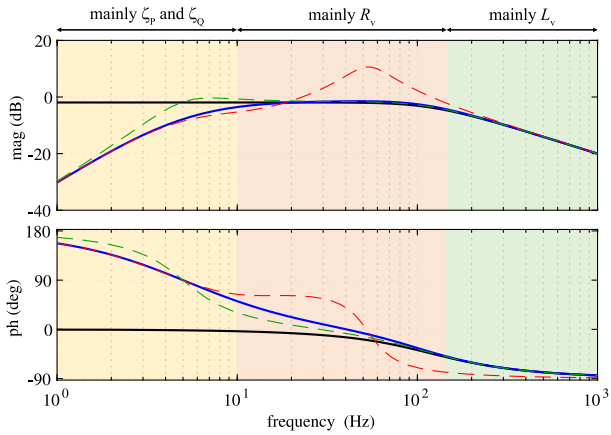

Figure 5.8: Comparison of $\underline{Y}_{\mathrm{dd}}$ of virtual admittance and decoupled GFM controller. Virtual reactance is 0.5pu. Solid black curves: virtual admittance response, with $R_{\mathrm{v}} = 1$ pu; Solid blue curves: GFM controller response, with $R_{\mathrm{v}} = 1$ pu and $\zeta_{\mathrm{P}} = \zeta_{\mathrm{Q}} = \zeta = 1$. Dashed green curves: GFM controller response, with $R_{\mathrm{v}} = 1$ pu and $\zeta = 0.7$; Dashed red curves: GFM controller response, with $R_{\mathrm{v}} = 0.25$ pu and $\zeta = 1$.

tance appears for frequencies around and below the APL's and RPL's loop bandwidth, as the converter shows a constant power behaviour in this range. As can be seen from the dashed green curve, the main way to impact the controller's response at frequencies around the power controller's loop bandwidth (apart from tuning the outer loops to a different bandwidth) is the power controller damping ratio[3] ζ. At higher frequencies (here up to about 100 Hz) and in particular around the fundamental, the virtual resistance R_{v} becomes the dominant factor. This parameter also plays the main role in the damping of the SFR. For frequencies above this, the main impact on the input admittance gradually shifts from R_{v} to the virtual inductance L_{v}.

[3] As shown in detail in **Paper F**, due to the chosen tuning of the power controllers, the closed-loop transfer function is a second-order system with the damping ratio ζ.

5.3 Virtual-Admittance Tuning

In Section 5.2 it has been demonstrated that the VA plays a central role in shaping the frequency response of the converter. This is principally the case for frequencies above the bandwidth of the outer power control loops. This can be illustrated with the help of the understanding that the GFM converter should behave as a voltage source behind an impedance, as shown in Fig. 2.3: At frequencies different to the fundamental frequency, the converter ideally appears as an impedance to the grid, and this impedance corresponds in this control structure to $\underline{Y}_\mathrm{v}^{-1}$. In consequence, the VA largely defines the converter's behaviour, in particular during transients and in the harmonic range. In addition to this, the decoupled GFM controller allows to freely choose the VA's parameters without the need to keep a small R/X ratio. This gives rise to the question how the parameters of the VA should be determined, which will be discussed in this section.

First, tuning methods available in the literature are discussed and goals for the tuning process are established. Next, a tuning method based on these goals is suggested, before the impact of the parameters on the response to transient disturbances in the grid is discussed. A software implementation of the tuning method proposed below is available online [193]. The results in this section are to be published in a paper that is under preparation at the time of writing this thesis.

Tuning Methods in the Literature and Tuning Goals

Reviewing the existing literature reveals a large number of tuning approaches and recommendations for VIs and VAs in GFM control structures. Naturally, the approaches differ greatly depending on the intended purpose of the VA. A large group of publications, e.g. [116], [194]–[199], employs an adaptive VA to ensure (typically reactive or harmonic) power sharing. A different large group applies a typically adaptive VI to limit the converter current [110], [113], [117], [160], [161]. Other publications study through eigenvalue analysis the impact of the VA parameters on the converter's stability [113], [200]–[207], with the generalised result that larger values for L_v and R_v tend to improve stability. For the purpose of the VA in the control structure discussed in this work, these aforementioned approaches are either irrelevant or offer little support in terms of actual tuning method.

Some publications utilizing a VA in a comparable function to the controller studied here give a value of 0.3 pu to 0.5 pu for the virtual inductance, motivating this by the similarity to typical SM transient reactances [108], [111], [208]. Publications following this approach typically suggest to select R_v based on the desired time constant of the VA, which should fall between the outer and inner control loop's bandwidth. As apparent from these references, the approach can produce a satisfactory closed-loop step response, but does at most indirectly take the VA's impact on the converter's behaviour and frequency response into account. A tuning approach that fully considers the impact of the VA parameters on the desired GFM converter behaviour is therefore required.

To the author's knowledge, only very few publications discuss a VA parameter tuning approach in the context of the VA's impact on the converter's frequency behaviour. Reference [209] considers how a low-pass filtered VI can improve stability and damping in a microgrid. The presented tuning approach requires knowledge of the complete system to conduct an eigenvalue analysis, which is often impossible to acquire in real applications, and is difficult to generalise. In [210], the impact of virtual inductance and resistance on stability and damping is discussed in relative terms, but no tuning procedure is suggested to motivate the parameter selection for the simulations in the paper.

Based on the previously described understanding of the impact of the VA on the converter's behaviour and this literature review, a meaningful tuning approach should determine the VA parameters based on the desired behaviour. The reaction to grid voltage transients, e.g. phase angle jumps or magnitude dips, depends on the disturbance, which impedes the possibility to give general tuning recommendations. Instead, the converter's desired frequency response is chosen as the primary tuning goal, which relates to the damping in the subsynchronous frequency range (including the SFR) as well as acting as a sink for harmonics.

Suggested Tuning Method

The basic idea of the suggested tuning method is to select two frequencies and define upper limits for the gain of the converter's input admittance at these frequencies. As discussed further below, these gain limits can be informed by performance requirements such as damping or settling time.

As demonstrated in **Paper F**, if the power setpoints are zero, the impact of the decoupled GFM controller's outer loops on the converter's input admittance can be modelled as a second order high-pass filter of the form $s^2/(s+\alpha)^2$, where α is the closed-loop bandwidth of the respective outer loop. If the power setpoints differ from zero, the converter's frequency response will not approach zero for a decreasing frequency (in SRF), but will approach a fixed, setpoint-dependent small value, reflecting the constant power behaviour of the outer loops. Furthermore, the high-pass filter representation assumes that the outer loops' damping ratio is equal to one. Since the frequency range of interest is above the power controllers' closed-loop bandwidth, a more accurate representation is not pursued here. Together with (5.1) and neglecting the current controller, this results in

$$\boldsymbol{Y}_\mathrm{c} = \begin{bmatrix} \frac{R_\mathrm{v}+sL_\mathrm{v}}{(R_\mathrm{v}+sL_\mathrm{v})^2+(\omega_\mathrm{c}L_\mathrm{v})^2}\frac{s^2}{(s+\alpha_\mathrm{P})^2} & \frac{\omega_\mathrm{c}L_\mathrm{v}}{(R_\mathrm{v}+sL_\mathrm{v})^2+(\omega_\mathrm{c}L_\mathrm{v})^2}\frac{s^2}{(s+\alpha_\mathrm{P})^2} \\ \frac{-\omega_\mathrm{c}L_\mathrm{v}}{(R_\mathrm{v}+sL_\mathrm{v})^2+(\omega_\mathrm{c}L_\mathrm{v})^2}\frac{s^2}{(s+\alpha_\mathrm{Q})^2} & \frac{R_\mathrm{v}+sL_\mathrm{v}}{(R_\mathrm{v}+sL_\mathrm{v})^2+(\omega_\mathrm{c}L_\mathrm{v})^2}\frac{s^2}{(s+\alpha_\mathrm{Q})^2} \end{bmatrix} \tag{5.7}$$

for the converter's input admittance, where α_P and α_Q are the active- and reactive-power controllers' closed-loop bandwidths, respectively, and ω_c is the angular frequency of the converter's internal voltage source. As the grid frequency, and the internal voltage source's frequency accordingly, only show small variations, $\omega_\mathrm{c} \approx \omega_\mathrm{b}$ is assumed for the input admittance formulation. For the following visualisations, the speed of the two power control loops is assumed to be equal: $\alpha_\mathrm{p} = \alpha_\mathrm{Q} = 5\ 2\pi$ rad/s, which results in a Hermitian input admittance:

$$\underline{Y}_\mathrm{dd} = \underline{Y}_\mathrm{qq} \qquad \text{and} \qquad \underline{Y}_\mathrm{dq} = -\underline{Y}_\mathrm{qd}, \tag{5.8}$$

where $\underline{Y}_\mathrm{dd} = \boldsymbol{Y}_\mathrm{c}(1,1)$, $\underline{Y}_\mathrm{qq} = \boldsymbol{Y}_\mathrm{c}(2,2)$, $\underline{Y}_\mathrm{dq} = \boldsymbol{Y}_\mathrm{c}(1,2)$ and $\underline{Y}_\mathrm{qd} = \boldsymbol{Y}_\mathrm{c}(2,1)$.

In the proposed tuning method, an upper limit is established for the gain of the virtual admittance at two frequencies to tune the two VA parameters, R_v and L_v. The first frequency should be the location of the SFR, as this is the frequency where the gain of the input admittance reaches its maximum. For higher R/X ratios, this resonance becomes more damped and the natural frequency, where the input admittance has the highest gain, moves towards higher frequencies. The natural frequency, neglecting the impact of the outer loops, is given as

$$\omega_\mathrm{n} = \sqrt{\omega_\mathrm{b}^2 + \frac{R_\mathrm{v}^2}{L_\mathrm{v}^2}}. \tag{5.9}$$

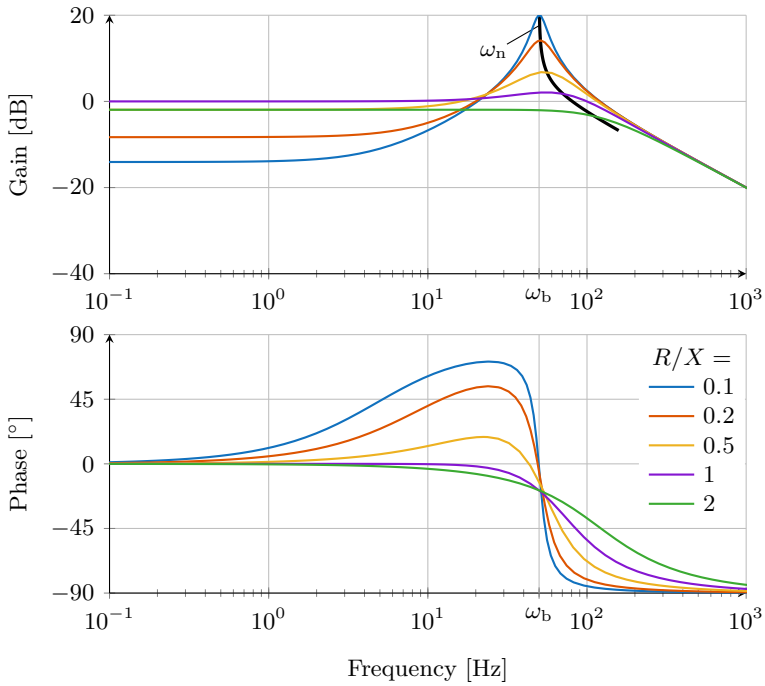

Figure 5.9: Bode diagram of the diagonal elements of the input admittance for $L_v = 0.5\,\text{pu}$ and varying resistance. Impact of the outer loops is neglected. In black: trajectory of the gain at natural frequency.

In Fig. 5.9, a Bode diagram of the input admittance for $L_v = 0.5\,\text{pu}$ and $R_v \in \{0.05, 0.1, 0.2, 0.5, 1\}\text{pu}$ is shown, with the curve in black marking the trajectory of the gain at natural frequency. It can be seen that for $R/X > 1$, i.e. damping ratios approaching 1, the highest gain moves from the natural frequency to lower frequencies. Since the filtering properties of the virtual inductance typically are important, a predominantly resistive tuning of the VA is not to be expected. This means that the natural frequency remains a good choice for the location of the first maximum gain requirement. As the natural frequency depends on the chosen R/X ratio, the tuning process becomes iterative.

The second frequency can be chosen more freely. Commonly, the lowest

harmonics present in the grid are the fifth and seventh harmonic[4]. Since the fifth harmonic is a negative sequence, and the seventh is a positive sequence, both appear at $6\omega_\mathrm{b}$ in the SRF. This makes this frequency a sensible choice for the second gain maximum, choosing a required attenuation at the lowest harmonics present in the grid.

Using (5.7), the input admittance's gain is computed at the two selected frequencies and shown in Figures 5.10 and 5.11. To maintain readability, the plots have been limited to a gain of 5 pu and 1 pu, respectively. The figures illustrate that for most of the area of interest, the gain of the off-diagonal elements of the input-admittance matrix[5] is lower than the diagonal elements'[6] gain, which based on the analysis of the frequency response in **Paper F** was expected. Only for a very poorly damped SFR, the off-diagonal elements have a higher gain around the natural frequency (see Fig. 5.10)[7]. As a parameter combination with a poorly damped SFR is not expected to be desirable, the tuning process is based on the gain of the diagonal elements. The change of the contour lines' slope between Fig. 5.10 and Fig. 5.11 demonstrates how the impact of the virtual inductor on the gain increases with the frequency: around the natural frequency, the VA's resistive component is dominant, while the inductive component is mainly responsible for the behaviour at higher frequencies.

The maximum gain requirement at the two selected frequencies can be formulated as

$$|\underline{Y}_\mathrm{dd}(\mathrm{j}\omega_\mathrm{n})| \leq m_1 \quad \text{and} \tag{5.10}$$

$$|\underline{Y}_\mathrm{dd}(\mathrm{j}6\omega_\mathrm{b})| \leq m_2, \tag{5.11}$$

where m_1 and m_2 are the chosen gain limits. As can be seen in Figures 5.10 and 5.11, the gain off the VA's diagonal elements is monotonously decreasing in both variables, i.e. an increase in either parameter leads to a reduced gain. As a consequence, minimum values for the parameters that observe the gain requirements in (5.10) and (5.11) can be estimated by replacing the inequality with an equality. This allows to estimate an R_v for each L_v so that the

[4] Neglecting negative sequence, which appears at 100 Hz in the SRF.

[5] $\underline{Y}_\mathrm{dq}$ and $\underline{Y}_\mathrm{qd}$.

[6] $\underline{Y}_\mathrm{dd}$ and $\underline{Y}_\mathrm{qq}$

[7] A significantly slower APC could change this and would require a reevaluation of the impact of the off-diagonal elements based on their response in the subsynchronous frequency range.

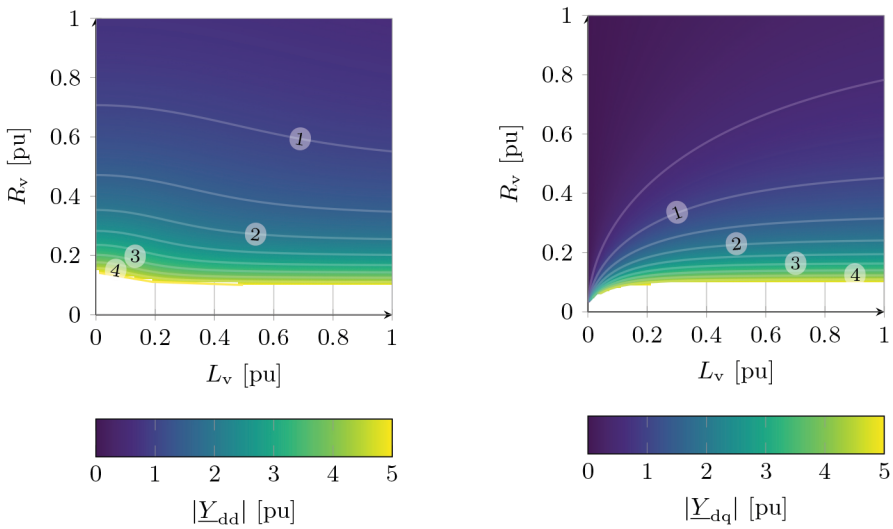

Figure 5.10: Gain of the input admittance at natural frequency ω_n.

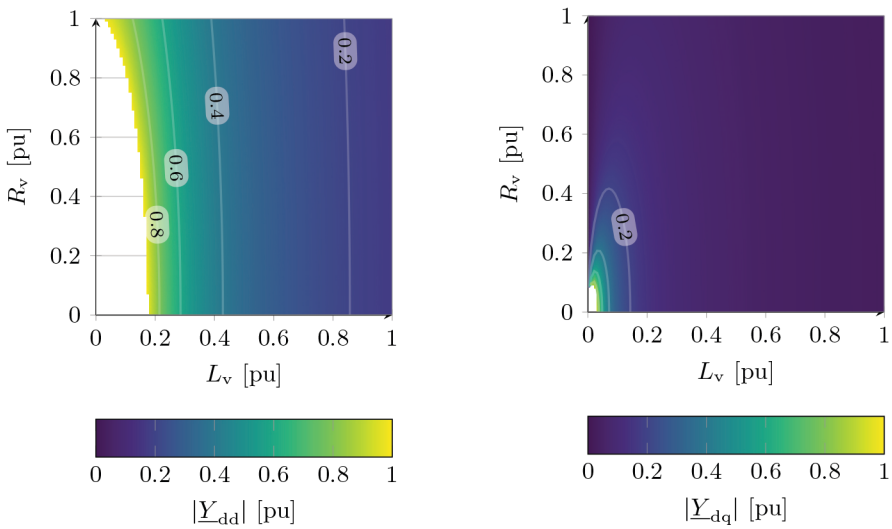

Figure 5.11: Gain of the input admittance at fifth and seventh harmonic ($6\omega_b$).

gain requirement is exactly fulfilled. For illustration purposes, the resulting functions $R_\mathrm{v}(L_\mathrm{v}, m_i)$ (where m_i is either of the maximum gain requirements m_1 or m_2) are plotted for both a strict and a loose gain requirement over the range $L_\mathrm{v} \in (0.1\,\mathrm{pu}, 1\,\mathrm{pu})$. The pair of strict requirements is $m_1 = 1\,\mathrm{pu}$ and $m_2 = 0.25\,\mathrm{pu}$, while the loose requirements are $m_1 = 2\,\mathrm{pu}$ and $m_2 = 0.5\,\mathrm{pu}$. The resulting plots are shown in Fig. 5.12 for the requirement at natural frequency (i.e. m_1), and in Fig. 5.13 for the fifth and seventh harmonic (i.e. m_2). The blue curves correspond to the respective contour lines in Figures 5.10 and 5.11[8]. As a consequence of the previously stated monotonously decreasing characteristic, all combinations of R_v and L_v above the plotted curves follow the respective requirement.

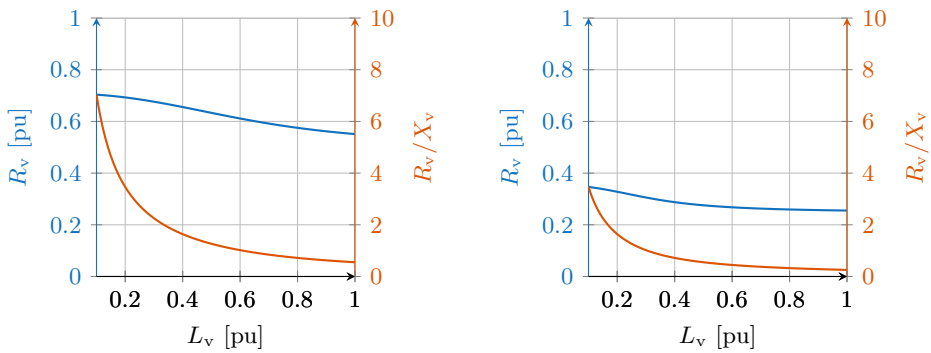

(a) $m_1 = 1\,\mathrm{pu}$.

(b) $m_1 = 2\,\mathrm{pu}$.

Figure 5.12: Combinations of R_v and L_v precisely following the gain requirement for ω_n as given in (5.10).

To complete the tuning process, both requirements are combined as illustrated in Fig. 5.14. At the intersection of both curves, the set of parameters exactly matches both requirements. In Fig. 5.15, the area covered by both surfaces contains the set of VA parameters that fulfil both maximum gain requirements. The parameters corresponding to the intersection of both curves are given in Table 5.2. Since the ratio m_2/m_1 is equal in both the strict and the loose case, the R/X ratio of the resulting parameters is constant. To illustrate the consequence of a change in this ratio, a mixed case with $m_1 = 2\,\mathrm{pu}$

[8] Observe the difference in axis limits.

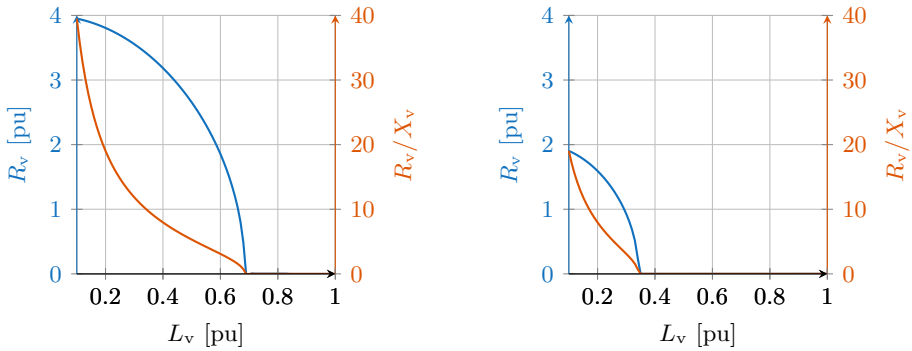

(a) $m_2 = 0.25\,\text{pu}$.

(b) $m_2 = 0.5\,\text{pu}$.

Figure 5.13: Combinations of R_v and L_v precisely following the gain requirement for $6\omega_b$ as given in (5.11).

Table 5.2: Minimum parameters following gain requirements.

Requirement	L_v	R_v	R_v/X_v
Strict	0.676 pu	0.596 pu	0.882
Loose	0.338 pu	0.298 pu	0.882
Mixed	0.684 pu	0.26 pu	0.38

and $m_2 = 0.25\,\text{pu}$ has been defined as well, with a more dominant inductive component.

In Fig. 5.16, a Bode diagram of the frequency response of the resulting input admittance's diagonal elements is shown for all three cases. As the minimum parameters for the strict and loose requirements have the same R/X ratio, the resulting frequency response is just shifted vertically. The mixed requirement illustrates how a relatively large inductive component, here dictated by the stricter high-frequency gain requirement, causes a resonance at the natural frequency if the resistive component is not increased as well.

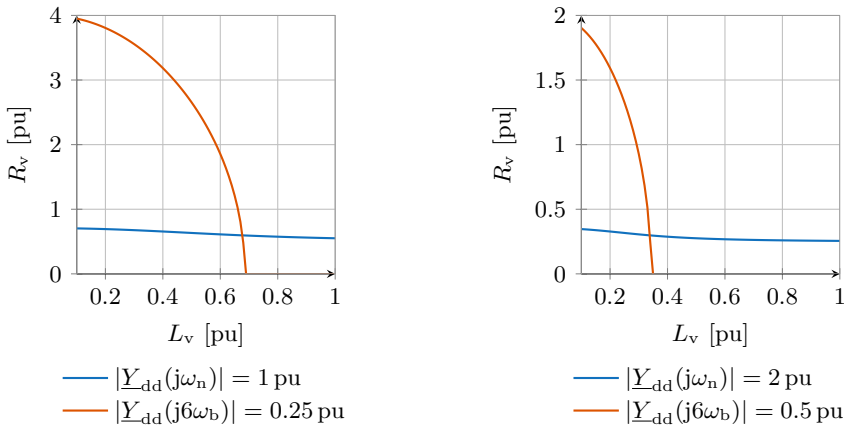

(a) Combination of the strict maximum gain requirements.

(b) Combination of the loose maximum gain requirements.

Figure 5.14: Graphical combination of the parameter combinations exactly following the gain requirements. Observe rescaled y-axis.

Relation to Decay Time Constant

The maximum gain requirements formulated above relate the VA parameters to the resulting input admittance, but performance requirements in e.g. grid codes might be formulated differently. A common requirement can instead be that a dc component caused by the SFR has to decay within a certain time. The amplitude of a damped oscillation decays with the decay time constant τ following

$$\hat{x}(t) = \hat{x}_0 \, \mathrm{e}^{-\frac{t}{\tau}}, \tag{5.12}$$

where t is the time, $\hat{x}_0$ is the amplitude of the oscillation at $t = 0$ and $\hat{x}(t)$ is the oscillation amplitude at time t. After time corresponding to the time constant has passed, the oscillation amplitude has reduced to $1/\,\mathrm{e} \approx 36.8\,\%$. If the grid code requires the oscillation to decay to a ratio of $\xi = \hat{x}(t_{\max})/\hat{x}_0$ within time $t_{\max}$, the time constant can be determined by rearranging (5.12) to

$$\tau = \frac{-t_{\max}}{\ln \xi}. \tag{5.13}$$

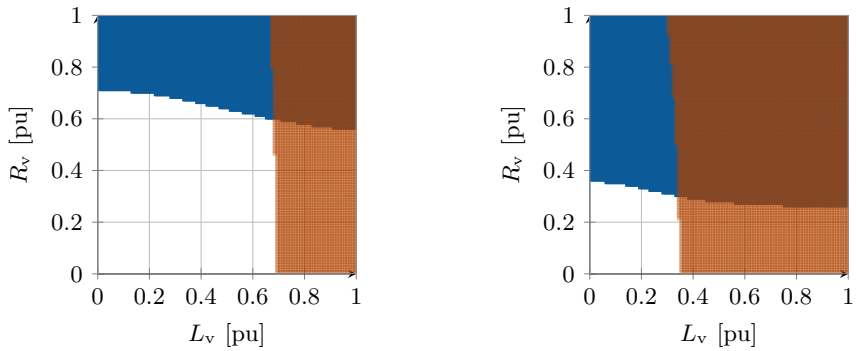

(a) Strict requirements.

(b) Loose requirements.

Figure 5.15: Set of parameters fulfilling maximum gain requirements. Blue: requirement at ω_n. Red: requirement at $6\omega_b$.

Neglecting the impact of the outer control loops, the damping ratio ζ is related to the time constant by $\zeta = (\omega_n \tau)^{-1}$. From (5.1), the damping ratio can be related to the VA parameters by

$$\zeta = \sqrt{\frac{R_v^2}{R_v^2 + \omega_b^2 L_v^2}}. \tag{5.14}$$

Together with (5.9) for ω_n, this results in[9]

$$R_v = \frac{L_v}{\tau}. \tag{5.15}$$

Consequently, the R/X ratio can be expressed as $T_b/(2\pi\tau) \approx 0.16 T_b/\tau$, with T_b being one cycle or period of the fundamental frequency, i.e. 20 ms at 50 Hz. This requirement is illustrated for two cases in Fig. 5.17: for a time constant of $\tau = 20$ ms, and for the requirement that the dc component should decay to 10 % of its initial amplitude within one cycle, which corresponds to a time constant of $\tau = 8.7$ ms. Similar to the gain-requirement-based tuning combinations shown previously, (5.15) shows that all tuning combinations lying above the indicated line perform better than required, i.e. have a shorter time constant.

[9] It is important to note that all quantities in this equation need to either be in SI units or per-unit. The conversion for the time constant is $[\tau]_{pu} = \omega_b [\tau]_s$.

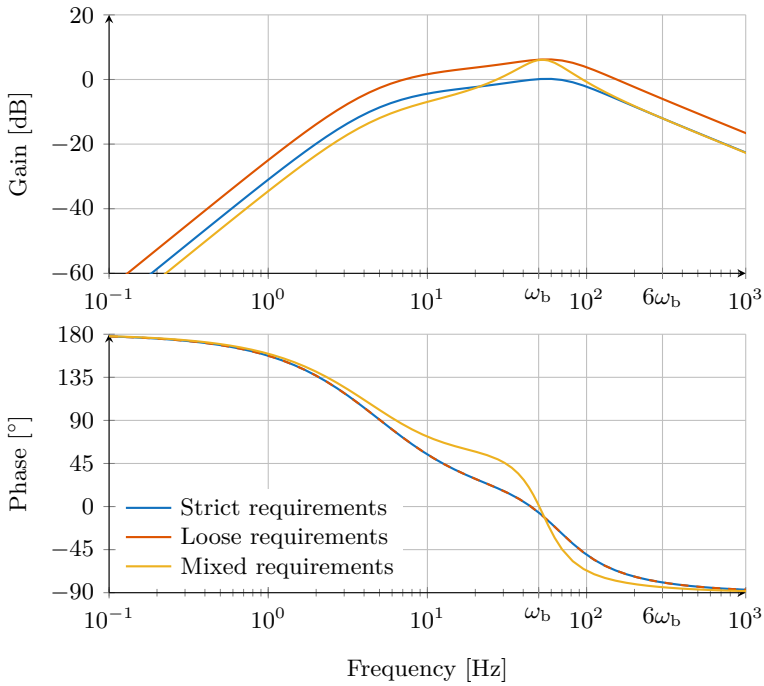

Figure 5.16: Bode diagram of the diagonal elements of the input admittance for the parameter combinations in Table 5.2.

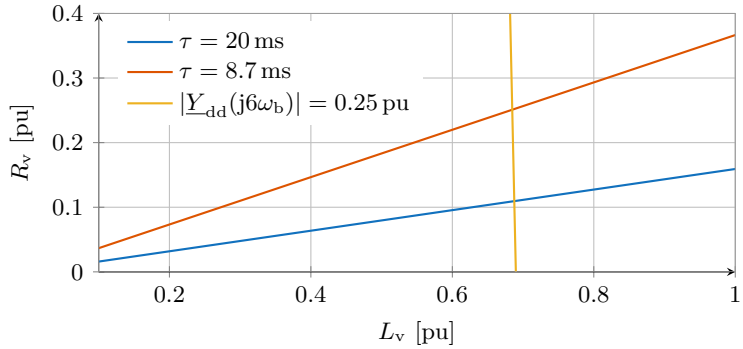

Figure 5.17: Combinations of Rv and Lv providing the required decay time constant. The yellow curve reproduces one of the gain requirements from the previous section for reference.

As shown in Fig. 5.17, the tuning combinations complying with the time-constant requirement have a different character than the maximum gain requirements due to their fixed R/X ratio. While the gain requirements call for a minimum value of the virtual impedance $Z_v = Y_v^{-1} = \sqrt{R_v^2 + \omega_b^2 L_v^2}$, the decay ratio is only depending on the R/X ratio. Consequently, a larger virtual inductance requires a larger virtual resistance to keep the time constant unchanged. To illustrate this, the tuning combination that fulfils the strict maximum gain requirement in the harmonic range, $|\underline{Y}_{dd}(j6\omega_b)| = 0.25\,\mathrm{pu}$, is shown in in yellow in Fig. 5.17. Similar to before, a pair of requirements is needed to tune the VA parameters. To achieve this, the time constant-based tuning according to (5.15) can be combined with a single maximum gain requirement, for example the one shown in yellow in Fig. 5.17.

The time-constant-based tuning is verified using time-domain simulations with parameter sets providing $\tau = 8.7\,\mathrm{ms}$: A strict case that also fulfils $m_2 = 0.25$ (as shown in the figure), and a loose case that also fulfils $m_2 = 0.5$. The parameters for the simulation follow Table 5.1, apart from the shunt capacitor, which is removed, and the VA parameters, which are shown in Table 5.3. The simulation results are shown in Fig. 5.18. The decay of the dc component is studied following a 30° phase jump in the grid Thévenin voltage $\underline{v}_s$. To facilitate estimation of the dc component and remove the impact of the outer loops from the simulation result, additionally to the simulation model used

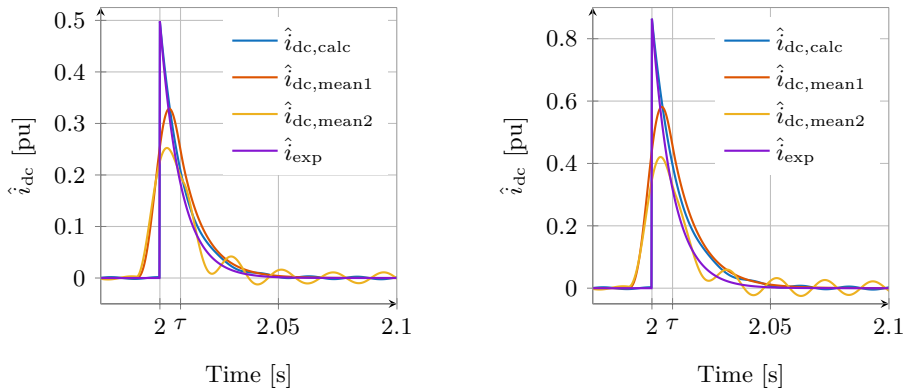

(a) Strict requirement: $m_2 = 0.25\,\text{pu}$. **(b)** Loose requirement: $m_2 = 0.5\,\text{pu}$.

Figure 5.18: Verification of the damping of the dc component by simulation for $\tau = 8.7\,\text{ms}$. VA parameters chosen to also provide $|\underline{Y}_{dd}(j6\omega_b)| = m_2$. Observe rescaled y-axis.

for the converter system in **Paper F**, a second model has been simulated implementing the converter's internal voltage as a fixed voltage source and the virtual admittance as physical inductance and resistance. Due to the absence of all controllers, the simplified model allows to estimate the ac current resulting from the phase jump and thereby isolate the dc component as $\hat{i}_{dc,calc}$. As this method cannot be applied in the full simulation model containing the decoupled GFM controller, the dc component is also estimated based on a moving average[10] with a sliding window length corresponding to T_b. This estimation is denoted $\hat{i}_{dc,mean1}$ for the simplified model and $\hat{i}_{dc,mean2}$ for the full simulation model containing all controllers. The decay time constant is then verified by comparing these to the decay function with the selected time constant, which is scaled to the correct initial value and named $\hat{i}_{exp}$.

From Fig. 5.18 it can be seen that $\hat{i}_{dc,calc}$, the isolated dc-component from the simplified model, shows a good match with the expected exponential decay. Comparison with $\hat{i}_{dc,mean1}$ demonstrates that the moving average is able to reproduce the shape of the decay despite the expected differences to the exact

[10]The moving average approximates the dc bias $\overline{x} = T^{-1} \int_{t_0}^{t_0+T} x(t)\,\mathrm{d}t$ for sampled data.

Table 5.3: Minimum parameters following combination of time constant and gain requirements.

Requirement	L_v	R_v	$R_\mathrm{v}/X_\mathrm{v}$
Strict	0.685 pu	0.251 pu	0.37
Loose	0.345 pu	0.126 pu	0.37
Slow	0.687 pu	0.109 pu	0.16

dc-component estimation. The shape of the moving average of the current in the simulation model containing the complete controller, $\hat{i}_{\mathrm{dc,mean2}}$, generally follows the expected decay as well. There is however a small low-frequency oscillation, which is likely caused by the outer control loops. Comparing the shape of dc-component decay between the strict and loose case, it can be observed that the match in the strict case is notably better. This is the case because the grid impedance has been neglected in the derivation, and the smaller value of $Z_\mathrm{v} = Y_\mathrm{v}^{-1}$ in the loose case means that the finite grid impedance of $Z_\mathrm{g} = 0.159\,\mathrm{pu}$ has a larger impact in this case. As the R/X ratio of the grid is 0.1, the R/X gets reduced and the resulting time constant increases. As a consequence of this, it is important to take the grid impedance into account in cases where the VI is not much larger than the grid impedance, i.e. weak grids or converters with a small VI.

While the decay time constant remains the same for both the strict and the loose case, Fig. 5.18 also reveals that the maximum amplitude of the calculated dc component is nearly twice as high in the loose case. Even though the relative reduction happens with the same speed, in terms of absolute value of the dc-component the stricter requirement performs notably better. To give an example, the reduction of $\hat{i}_{\mathrm{dc,calc}}$ to 0.1 pu takes approximately 16 ms in the strict requirement case, while it takes 24 ms in the loose case. This difference is due to the different size of the VI, caused by the distinct maximum gain requirements. A smaller VI results in larger currents in response to a given disturbance.

To study the interaction of decay time and input-admittance gain, the frequency response of the input admittance of both time-constant-based tuning examples is shown in Fig. 5.19. Additionally, a third example is included in

yellow, which keeps the stricter maximum gain requirement of $m_2 = 0.25\,\text{pu}$, but increases the permissible decay time constant to one cycle of the fundamental (20 ms). This third combination of requirements, denoted as *slow* in Table 5.3, has a very different R/X ratio than the other two cases, which is reflected in the resulting frequency response: While the frequency responses of both the strict and loose requirements have the same shape, just shifted in gain, the slow case shows a much more pronounced resonance around the SRF. The peak value of $\hat{i}_{\text{dc,calc}}$ (not shown here) is with 0.56 pu located slightly higher than the strict case (which shares the same gain requirement of m_2), but it takes 37 ms for the dc-component to decay to 0.1 pu due to the larger time constant.

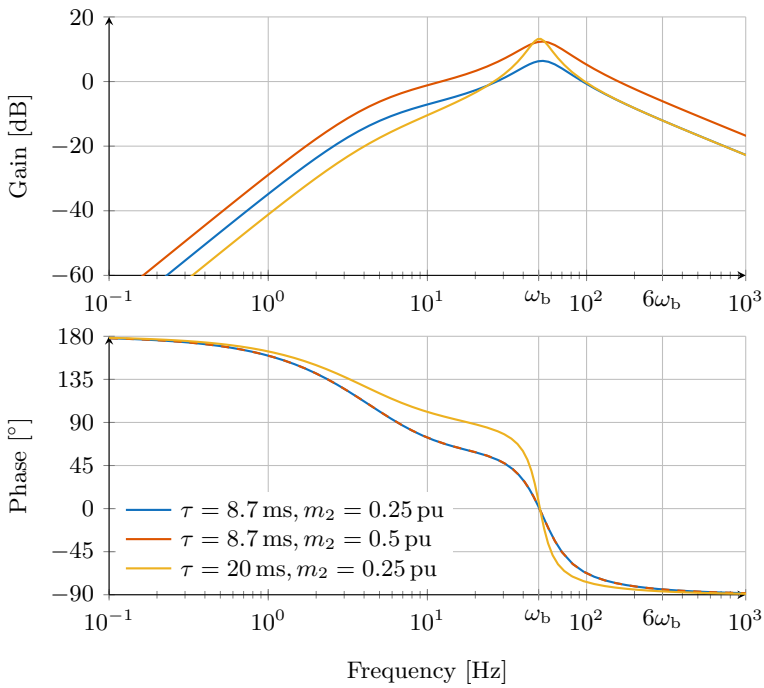

Figure 5.19: Bode diagram of the diagonal elements of the input admittance for the parameter combinations in Table 5.3. Blue: strict requirements. Red: loose requirements. Yellow: slow requirements.

These observations show that the time constant can be a meaningful addition to the previously presented maximum gain requirements, but it needs to be paired with a gain requirement to limit the dc-component in absolute terms.

VA Parameter Impact on Transient Disturbance Response

Given how the preceding analysishas established that the gain of the input admittance is monotonously decreasing for increasing R_v and L_v, one might be led to conclude that the VA parameters should simply be chosen as large as possible to maximise the provision of damping. To understand why this reasoning is erroneous, the response of the decoupled GFM controller is simulated for two grid disturbances: a 25 % voltage dip and a 10° phase jump. To underline the differences, the parameter sets with the largest difference in Z_v are used: the strict gain requirement[11], and the combination of the low decay time constant and loose gain requirement in the harmonic frequency range[12].

The simulation results are shown in Fig. 5.20 for the phase jump and in Fig. 5.21 for the voltage dip. For the voltage dip, an AVC with a droop has been activated, which changes the reactive-power reference. Since the outer loops and their parameters are the same in both the strict and loose case and only the VA parameters are changed, the results from both simulated disturbances demonstrate how the VA parameters impact the dynamic behaviour of the converter. The impact of the VA is in particular visible at the couple of cycles after the disturbance, before the outer control loops have had time to react to the disturbance. In both cases, the parameter set based on the loose requirements shows a dynamic response with a higher current peak and a larger dc-component, visible as a 50 Hz oscillation in active and reactive power.

As explained above, the dc-component should be kept as small as possible. But this can not be generalised to assume that the converter's reaction to a grid disturbance should be as small as possible, i.e. that Z_v should be chosen to be big: The larger the VI, the larger the electrical distance between PCC and the converter's internal voltage source. As a consequence, the grid support and contribution to grid strength from the converter reduces as the impedance increases. Put in simple terms, VA parameters that are too large let the

[11] $L_\mathrm{v} = 0.676\,\mathrm{pu}$, $R_\mathrm{v} = 0.596\,\mathrm{pu}$. See strict case in Table 5.2.
[12] $L_\mathrm{v} = 0.345\,\mathrm{pu}$, $R_\mathrm{v} = 0.126\,\mathrm{pu}$. See loose case in Table 5.3.

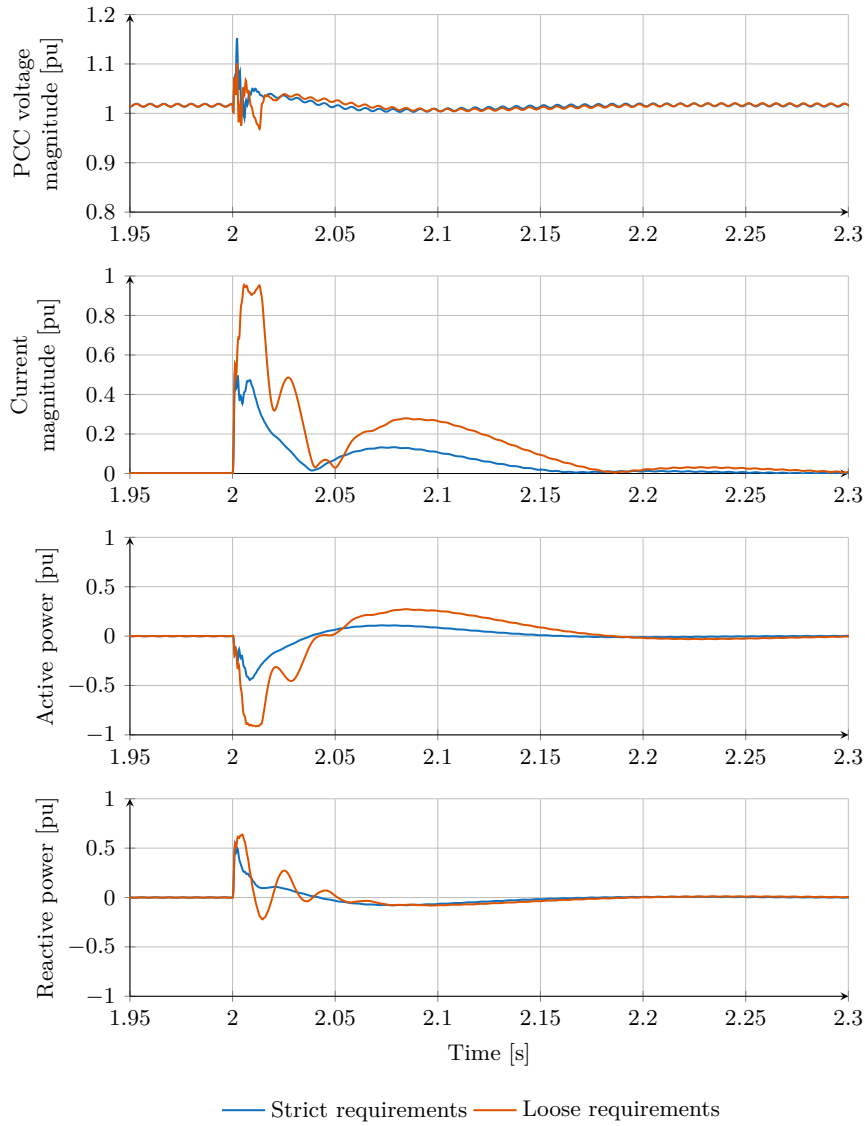

Figure 5.20: Simulated response to a 10° phase jump at the grid's Thévenin voltage for the decoupled GFM controller with two different VA tunings.

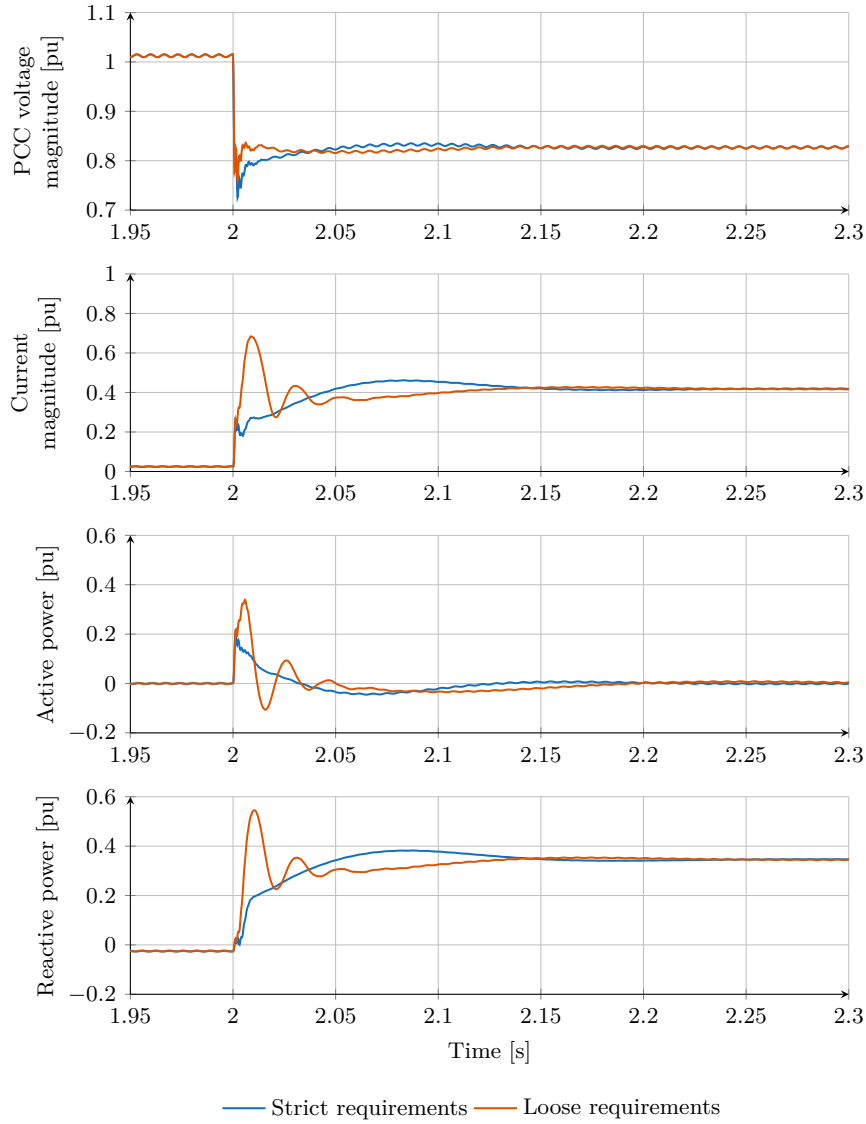

Figure 5.21: Simulated response to a 25 % voltage dip at the grid's Thévenin voltage for the decoupled GFM controller with two different VA tunings.

converter become a passive bystander – it does not negatively contribute to any control interactions, but it does not positively contribute to the stability of the grid during disturbances either.

Based on this, it could be assumed that the VA parameters should instead be selected to be as small as possible. But this would mean that even small disturbances in the grid would cause the converter's current or energy limiters[13] to saturate, and that the converter's linear control range would be very limited. It is therefore necessary to find a compromise between the advantages of large and small VA parameters. This compromise needs to take the conditions at the PCC, the system operator's requirements and the constraints of the converter system in question into account. Nevertheless, the tuning method presented above is an effective way to establish minimum values for the VA parameters that fulfil given performance requirements.

5.4 Discussion

The basic analysis of the frequency response of a voltage source behind an impedance has served as an introduction to the SFR and to illustrate the frequency response that is expected of a GFM controller.

The decoupled GFM controller offers the freedom to tune the parameters of both the outer control and the VA independently of each other without introducing power coupling in the outer controllers' active range. This enables free selection of the virtual resistance and inductance in particular, where the latter now can be used to effectively provide damping for the SFR and in the subsynchronous range. The frequency response of the decoupled controller's input admittance is studied to delineate which control parameters have a dominant impact for different frequency ranges.

Due the possibility to freely select the VA parameters, a tuning method was required to determine these parameters according to the desired frequency response. The method presented in the last part of this chapter approaches this by proposing the usage of maximum gain requirements for the input admittance at selected frequencies. This approach is extended with the option for selecting a time constant. While the proposed tuning method cannot capture

[13] As the energy stored in the capacitor on the converter's dc side is very limited in most applications, many converters are equipped with an energy limiter that prevents the dc voltage from varying too much [67].

all aspects that can have an impact on the selection of the VA parameters, it provides an effective way for basing the tuning of the virtual resistance and inductance on the impact they have on the converter's frequency behaviour.

CHAPTER 6

Concluding Remarks

6.1 Conclusions

In this thesis, a GFM converter control structure that provides intrinsic grid support and at the same time overcomes those aspects that typically are challenging for GFM controlled converters has been developed and studied.

To understand the context in which the development of GFM control is discussed by system operators and the requirements converters with GFM control have to fulfil, a study of grid codes and similar requirement documents has been conducted in 2022. The study came to the conclusion that at this point in time only the British grid code contained a definition of what constitutes GFM behaviour, and that none of the investigated documents required GFM control. There were however several grid codes that either required or gave the TSO the authority to require behaviours that are typically associated with GFM converter control, such as contribution to fault current, inertial response, and black start capability.

Chapter 3 discusses the results of the study and also gives an overview of the developments that have occurred since the study has been carried out. Several system operators have since updated their grid codes to include definitions of

GFM converter control, and ACER plans to update the European network codes, which are binding to member states of the European Union, and include obligatory GFM capability for all newly installed MW-class converters.

Based on the investigation of existing GFM control structures and grid code requirements, the capability to limit the converter current has been identified as an important challenge for GFM control. The existing current limitation strategies lack the ability to maintain the converter's GFM behaviour when the current saturates, and can even cause instability during large system disturbances. This has been addressed with the proposal of a voltage-based current limitation strategy in Chapter 4. The limitation strategy prevents overcurrents by limiting the converter's internal voltage. It has been verified in laboratory experiments, which demonstrate that the strategy is able to effectively limit the current, prevent the previously mentioned instability and preserve the GFM behaviour as much as possible.

As part of the limitation strategy, an IEL has been developed which separates inertial response from the APC. This decoupling of the active-power reference tracking and synchronisation tasks of the APC from inertial support increases robustness, as it facilitates limitation of active power. Furthermore it enables to tune inertial response and active-power reference tracking independently of each other. A study of the stability limits of the IEL concluded that the IEL is stable even under extreme conditions, but that the addition of a second, faster PI-controller not only improves robustness, but also provides improved inertial support if active-power limitation is required. The IEL enables to use the available current headroom to provide inertial support without the risk of overcurrent or instability. It also gives the flexibility to dynamically limit the inertial support, e.g. based on available energy, without changing the dynamics of the APC.

The converter dynamics are further studied in Chapter 5, which introduces the SFR and discusses the desired frequency behaviour of the converter. Increasing the virtual resistance improves damping in the subsynchronous frequency range and of the SFR, but introduces undesirable coupling of active and reactive power. To solve this a decoupled GFM controller is introduced, which allows to tune both parameters of the VA freely without introducing power coupling. Furthermore, the control structure can be designed to be symmetric if required to facilitate stability studies of the converter system. The performance of the decoupled controller has been verified by laboratory

experiment.

Based on a study of the controller's frequency response, three frequency ranges with different dominant control parameters are identified. In the low frequency range, up to the closed-loop bandwidth of the outer control loops, the outer control loops' damping ratio is dominant in determining the frequency response. Around synchronous frequency, the virtual resistance is the principal parameter, while the virtual inductance becomes predominant for higher frequencies.

Based on the important role the VA has in shaping the converter's frequency response, a previously unpublished tuning method for the VA parameters is suggested in Chapter 5. The method determines the VA parameters virtual resistance and virtual inductance based on maximum gain requirements. This allows to tune the VA according to the desired converter behaviour, i.e. based on the required damping capability for SFR and chosen harmonics. The method is extended to also include specification of a decay time constant requirement.

This work has made contributions to the design of GFM control structures which intrinsically provide grid support without requiring control action from outer control loops. As such, the thesis is useful for researchers and engineers working in development of converter control. As it highlights challenges and possible solutions both in power grid and GFM converter control, it is relevant even to system operators and power system engineers.

6.2 Recommendations for Future Work

As illustrated by this thesis, grid-connection requirements for converters are ever-evolving. Continuing and intensifying the dialogue between regulators, system operators, manufacturers and academia is of importance to ensure that new regulations enable continued development and improvement of GFM converter control while at the same time ensuring safe operation of the power systems. A study of the evolution of requirements related to GFM converter control could provide valuable insights into the interactions between regulation and innovation at the frontier of power system research.

The investigations in this work have primarily been carried out using simple grid representations. Studying more complex systems, e.g. those including resonances or providing unbalanced or distorted voltages, can improve the

practical relevance of the results. The study of a multi-converter system would also provide further insights into the requirements regarding prevention of control interactions and provision of damping.

To apply the findings of this work, it is necessary to study the interdependence of application- and topology-specific hardware limitations and the proposed control solutions. This requires choosing specific applications to study. Of special interest would be to study the application of the decoupled GFM controller in a STATCOM, possibly with integrated BESS, as this configuration enables optimal utilization of the grid-supporting capabilities.

Both GFM converter-control structures investigated in this work, the PI-based VA GFM controller from Chapter 4 and the decoupled GFM controller from Chapter 5, rely on a CC. Due to its limited closed-loop bandwidth, the CC dominates the converter response for high frequencies. Together with the impact of signal and control delays it can deteriorate the converter's passivity. Based on this, it would be beneficial to investigate possibilities to remove the CC.

It can be of interest to study alternatives to the IEL which give the same improvement in robustness without requiring control action from the outer loops for the inertial response. The auxiliary PI-controller suggested as an improvement for the IEL might be an alternative to reduce the risk of instability in inertia-providing APCs.

The proposed tuning method for the VA parameters has not been verified by experimentyet and should be refined to take possible constraints into account, e.g. from hardware ratingsm which requires quantifying the relation between VA parameters and transient disturbance response. Other details that could be explored further are the impact of the off-diagonal elements of the input admittance as well as the phase of the frequency response.

CHAPTER 7

Summary of included papers

This chapter provides a summary of the included papers and an indication of the author contributions.

Paper A: An Overview of Grid-Connection Requirements for Converters and Their Impact on Grid-Forming Control

Paul Imgart, Mebtu Beza, Massimo Bongiorno, Jan R. Svensson
An Overview of Grid-Connection Requirements for Converters and Their Impact on Grid-Forming Control
Published in 24th European Conference on Power Electronics and Applications, EPE 2022 ECCE Europe.

Summary

In this paper, existing standards for grid-connected converters are analysed and compared. It highlights commonalities and differences, and investigates the requirements for GFM converter control in particular. Finally, the impact of the studied standards on the selection of the most suitable grid-forming control structures is discussed.

Author Contributions

Paul Imgart contributed with conceptualization, investigation, methodology, visualization, and writing. Mebtu Beza, Massimo Bongiorno and Jan R. Svensson contributed with conceptualization, funding acquisition, methodology, supervision, and writing – review and editing.

Paper B: Voltage-based Current Limitation Strategy to Preserve Grid-forming Properties Under Severe Grid Disturbances

Anant Narula, **Paul Imgart**, Massimo Bongiorno, Mebtu Beza, Jan R. Svensson, Jean-Philippe Hasler
Voltage-based Current Limitation Strategy to Preserve Grid-forming Properties Under Severe Grid Disturbances
Published in IEEE Open Journal of Power Electronics, vol. 4, pp. 176–188, Feb. 2023.

Summary

This paper discusses the transient angle stability of grid-connected converters with GFM control, and which impact the need for current limitation has on it. It demonstrates why the intrinsic voltage-source behaviour makes current limitation during large grid disturbances challenging for GFM controllers. As a solution, the paper presents a novel limitation strategy that preserves the GFM properties of the converter and at the same time effectively limits the converter current to the desired value. Through the limitation of the converter's internal voltage, stable operation is achieved even during faults and large frequency disturbances in the grid. The paper also shows how the suggested controller and limitation strategy can be extended to address unbalances in the grid, e.g. due to single-phase faults. A variety of experimental results show the effectiveness of the proposed current limitation strategy in case of various grid disturbances such as balanced and unbalanced faults as well as frequency disturbances.

Author Contributions

Anant Narula contributed with conceptualization, formal analysis, investigation, methodology, software, validation, visualization and writing. Paul Im-

gart contributed with conceptualization, formal analysis, investigation, methodology, software, visualization, and writing. Massimo Bongiorno and Mebtu Beza contributed with conceptualization, funding acquisition, methodology, resources, supervision, and writing – review and editing. Jan R. Svensson contributed with funding acquisition, supervision, and writing – review and editing. Jean-Philippe Hasler contributed with conceptualization and methodology.

Paper C: A Cascaded Power Controller for Robust Frequency Ride-Through of Grid-Forming Converters

Paul Imgart, Anant Narula, Massimo Bongiorno, Mebtu Beza, Jan R. Svensson

A Cascaded Power Controller for Robust Frequency Ride-Through of Grid-Forming Converters

Published in 2022 IEEE Energy Conversion Congress and Exposition (ECCE).

Summary

In this paper, the inertia-emulation loop (IEL) has been presented for the first time. The paper introduces a GFM control structure that enables limitation of active power while at the same time retaining maximum available inertial support. This is achieved by decoupling the inertial support from the APC's other duties. The former is provided by the dedicated IEL, which calculates an active-power reference based on the desired inertial response. This is then added to the APC's reference, which can easily be limited. The proposed method is demonstrated through time-domain simulations including frequency transients of varying size and under unbalanced operating conditions.

Author Contributions

Paul Imgart contributed with conceptualization, formal analysis, investigation, methodology, software, visualization, and writing. Anant Narula contributed with conceptualization, formal analysis, investigation, methodology, software, and validation. Mebtu Beza and Massimo Bongiorno contributed with conceptualization, funding acquisition, methodology, resources, supervision, and writing – review and editing. Jan R. Svensson contributed with funding acquisition, supervision, and writing – review and editing.

Paper D: External Inertia Emulation to Facilitate Active-Power Limitation in Grid-Forming Converters

Paul Imgart, Anant Narula, Massimo Bongiorno, Mebtu Beza, Jan R. Svensson

External Inertia Emulation to Facilitate Active-Power Limitation in Grid-Forming Converters
Published in IEEE Transactions on Industry Applications, vol. 60, pp. 9145-9156, Nov. 2024.

Summary

This paper extends the previous publication on the IEL. The tuning of the APC and IEL parameters is shown in detail and the choice of damping for the inertial response is discussed. An alternative, inertia-less implementation of the APC is shown, which allows to improve the accuracy of the inertia emulation and active-power limitation. The effectiveness of the proposed method is demonstrated through laboratory experiments including frequency transients of varying size and unbalanced operating conditions.

Author Contributions

Paul Imgart contributed with conceptualization, formal analysis, investigation, methodology, software, validation, visualization, and writing. Anant Narula contributed with conceptualization, formal analysis, investigation, methodology, software, and validation. Massimo Bongiorno and Mebtu Beza contributed with conceptualization, funding acquisition, methodology, resources, supervision, and writing – review and editing. Jan R. Svensson contributed with funding acquisition, supervision, and writing – review and editing.

Paper E: Stability Limits and Improved Robustness of Grid-Forming Converters With External Inertia-Emulation Loop

Paul Imgart, Massimo Bongiorno, Jan R. Svensson, Mebtu Beza
Stability Limits and Improved Robustness of Grid-Forming Converters With External Inertia-Emulation Loop
Published in 25th European Conference on Power Electronics and Applications (EPE'23 ECCE Europe).

Summary

This paper investigates the stability limits of the IEL, which can be generalised to the large-disturbance angle-stability limits of a GFM. It compares three alternatives to improve IEL performance under power limitation. Simulations confirm the IEL's robustness and the effectiveness of the proposed solution in avoiding undesired active-power injection at the disturbance end.

Author Contributions

Paul Imgart contributed with conceptualization, formal analysis, investigation, methodology, software, visualization and writing. Massimo Bongiorno and Mebtu Beza contributed with conceptualization, funding acquisition, methodology, supervision, and writing – review and editing. Jan R. Svensson contributed with funding acquisition, supervision, and writing – review and editing.

Paper F: Decoupled PQ Grid-Forming Control with Tunable Converter Frequency Behaviour

Paul Imgart, Anant Narula, Massimo Bongiorno, Mebtu Beza, Jan R. Svensson, Jean-Phillipe Hasler, Paolo Mattavelli
Decoupled PQ Grid-Forming Control with Tunable Converter Frequency Behaviour
Submitted to IEEE Transactions for consideration..

Summary

This manuscript demonstrates how poor damping of SFR and power coupling challenge GFM converter controllers. It proposes a decoupled power controller that combines a complex-power control loop with a virtual-admittance phase compensation. This allows to provide freely tunable damping at subsynchronous and synchronous frequency as well as decoupling of active and reactive power in the power controllers' active frequency range. The control parameters can be selected to achieve a symmetric controller, which aids system analysis through single-input single-output representation. The controller's performance is evaluated in both frequency domain (by simulation) and time domain (by laboratory experiment).

Author Contributions

Paul Imgart contributed with conceptualization, formal analysis, investigation, methodology, software, validation, visualization, and writing. Anant Narula contributed with conceptualization, formal analysis, investigation, software, and validation. Massimo Bongiorno contributed with conceptualization, formal analysis, funding acquisition, methodology, resources, software, supervision, and writing – review and editing. Mebtu Beza and Jan R. Svensson contributed with funding acquisition, supervision, and writing – review and editing. Jean-Philippe Hasler and Paolo Mattavelli contributed with conceptualization, formal analysis and methodology.

APPENDIX A

Definitions of GFM Behaviour in the Literature

Table A.1: Definitions of grid-forming converter control (continued on next pages).

Source	Definition
[40]: J. Rocabert *et al.*, "Control of Power Converters in AC Microgrids," *IEEE Transactions on Power Electronics*, vol. 27, no. 11, pp. 4734–4749, Nov. 2012, ISSN: 0885-8993	"A grid-supporting power converter is controlled as a voltage source with a link impedance [...], or alternatively, as a current source with a parallel impedance [...]. In any case, its main objective is to participate in the regulation of the ac grid voltage amplitude E^* and frequency ω^* by controlling the active and reactive power delivered to the grid." *In the referenced publication, grid-forming control denotes the ability of the converter to control voltage and frequency of the grid voltage on its own, as is the case in an islanded grid with a single power source like a uninterruptible power source (UPS). Therefore, the publication's definition of grid-supporting converters is reproduced here, as this is closer to how the term grid-forming is used today.*
[20]: J. Matevosyan *et al.*, "Grid-Forming Inverters: Are They the Key for High Renewable Penetration?" *IEEE Power and Energy Magazine*, vol. 17, no. 6, pp. 89–98, Nov. 2019, ISSN: 1558-4216	"For the purpose of this article, a GFM IBPS broadly refers to an IBPS that is capable of supporting the operation of an ac power system under normal, disturbed, and emergency conditions without having to rely on services from SGs or SCs. This includes system conditions when 100 % of the electricity demand is supplied from IBPSs and situations with very low IBPS penetration as well as transitions between the two."

Table A.1 – continued from previous page

Source	Definition
[8]: ENTSO-E, "High Penetration of Power Electronic Interfaced Power Sources and the Potential Contribution of Grid Forming Converters," 2020	"In addition to capabilities of PPMs or HCSs of Classes 1 and 2, Class 3 may in future provide PPM or HCSs controls with single cycle support services allowing 100 % power electronic penetration including in headline terms [...]: • Creates system voltage (does not rely on being provided with firm clean voltage) • Contributes to Fault Level (PPS & NPS within first cycle) • Contributes to TSI (limited by energy storage capacity) • Supports system survival to allow effective operation of LFDD for rare system splits • Controls act to prevent adverse control system interactions • Acts as a sink to counter harmonics & interharmonics in system voltage • Acts as a sink to counter unbalance in system voltage A description of one practical implementation is as follows: The control strategy of grid forming PPMs or HCSs provides an inherent performance resulting from presenting to the system at the connection point a voltage behind an impedance, in effect a true voltage source."
[128]: IEEE, *P2800/D6.0 (March 2021) - Draft Standard for Interconnection and Interoperability of Inverter-Based Resources Interconnecting with Associated Transmission Systems*, Mar. 2021	"Enhanced future control strategies where the IBR still utilizes a synchronizing mechanism (like a PLL) to lock onto and keep synchronism with the grid, but may employ additional supplemental control loops and features to better stabilize its response in weak grid conditions. Here, the IBR control provides a constant voltage angle and magnitude behind an impedance in the period following a change in terminal quantities."

Table A.1 – continued from previous page

Source	Definition
[155]: NERC, "Grid Forming Technology - Bulk Power System Reliability Consideration," Nov. 2021	"The primary objective of grid-forming (GFM) controls for BPS-connected IBRs is to maintain an internal voltage phasor that is constant or nearly constant in the sub-transient to transient time frame. This allows the IBR to immediately respond to changes in the external system and maintain IBR control stability during challenging network conditions. The voltage phasor must be controlled to maintain synchronism with other devices on the grid and must also regulate active and reactive power appropriately to support the grid."

Table A.1 – continued from previous page

Source	Definition
[33]: National Grid ESO, *Final Modification Report GC0137: Minimum Specification Required for Provision of GB Grid Forming (GBGF) Capability*, Nov. 11, 2021	"[Grid Forming Capability is] (but not limited to) the capability a Power Generating Module, HVDC Converter (which could form part of an HVDC System), Generating Unit, Power Park Module, DC Converter, OTSDUW Plant and Apparatus, Electricity Storage Module, Dynamic Reactive Compensation Equipment or any Plant and Apparatus (including a smart load) whose supplied Active Power is directly proportional to the difference between the magnitude and phase of its Internal Voltage Source and the magnitude and phase of the voltage at the Grid Entry Point or User System Entry Point and the sine of the Load Angle. As a consequence, Plant and Apparatus which has a Grid Forming Capability has a frequency of rotation of the Internal Voltage Source which is the same as the System Frequency for normal operation, with only the Load Angle defining the relative position between the two. In the case of a GBGF-I, a Grid Forming Unit forming part of a GBGF-I shall be capable of sustaining a voltage at its terminals irrespective of the voltage at the Grid Entry Point or User System Entry Point for normal operating conditions. For GBGF-I, the control system, which determines the amplitude and phase of the Internal Voltage Source, shall have a response to the voltage and System Frequency at the Grid Entry Point or User System Entry Point) with a bandwidth that is less than a defined value as shown by the control system's NFP Plot."

Table A.1 – continued from previous page

Source	Definition
[78]: NERC, "White Paper: Grid Forming Functional Specifications for BPS-Connected Battery Energy Storage Systems," Sep. 2023	"Most definitions agree that at a minimum, GFM controls tend to hold their voltage magnitude and angle at the device terminals constant in the period immediately following a system event."
[147]: European Union Agency for the Cooperation of Energy Regulators (ACER), *Recommendation No 03/2023 of the European Union Agency for the Cooperation of Energy Regulators – Annex 1: Amended RfG Regulation*, Dec. 19, 2023	(a) Within the power park module's current and energy limits, the power park module shall be capable of behaving at the terminals of the individual unit(s) as a voltage source behind an internal impedance (Thevenin source), during normal operating conditions (non-disturbed network conditions) and upon inception of a network disturbance (including voltage, frequency and voltage phase angle disturbance). The Thevenin source is characterized by its internal voltage amplitude, voltage phase angle, frequency and internal impedance. (b) Upon inception of a network disturbance and while the power park module capabilities and current limits are not exceeded, the instantaneous AC voltage characteristics of the internal Thevenin source according to paragraph (a) shall be capable of not changing its amplitude and voltage phase angle while positive-sequence voltage phase angle steps or voltage magnitude steps are occurring at the connection point. The current exchanged between the power park module and the network shall flow naturally according to the main generating plant and converter impedances and the voltage difference between the internal Thevenin source and the voltage at the connection point.

References

[1] Copernicus Climate Change Service, "Global Climate Highlights 2024," Jan. 17, 2024.

[2] United Nations Framework Convention on Climate Change, "Adoption of the Paris Agreement - 21st Conference of the Parties," Paris, 2015.

[3] "Summary for Policymakers," in *Global Warming of 1.5°C: IPCC Special Report on Impacts of Global Warming of 1.5°C above Pre-industrial Levels in Context of Strengthening Response to Climate Change, Sustainable Development, and Efforts to Eradicate Poverty*, Intergovernmental Panel on Climate Change (IPCC), Ed., Cambridge: Cambridge University Press, 2022, pp. 1–24, ISBN: 978-1-00-915795-7.

[4] European Environment Agency., *European Climate Risk Assessment*. LU: Publications Office, 2024.

[5] S. Kuthunur. "'Ambitious climate action is more urgent than ever:' 3 Climate records broken in 2024," Space. (Dec. 31, 2024), [Online]. Available: `https://www.space.com/the-universe/climate-change/ambitious-climate-action-is-more-urgent-than-ever-3-climate-records-broken-in-2024` (visited on 06/16/2025).

[6] World Resources Institute, *Climate Watch Historical Greenhouse Gas Emissions*, 2025.

[7] Svenska kraftnät, "Långsiktig marknadsanalys - Scenarier för kraftsystemets utveckling fram till 2050," Sundbyberg, Sweden, Jan. 26, 2024.

[8] ENTSO-E, "High Penetration of Power Electronic Interfaced Power Sources and the Potential Contribution of Grid Forming Converters," 2020.

[9] Svenska kraftnät, "Grid development plan 2024–2033," Feb. 21, 2024.

[10] Svenska kraftnät, "Balancing market outlook 2030," Dec. 19, 2024.

[11] H. Holttinen, J. Kiviluoma, D. Flynn, *et al.*, "System Impact Studies for Near 100% Renewable Energy Systems Dominated by Inverter Based Variable Generation," *IEEE Transactions on Power Systems*, vol. 37, no. 4, pp. 3249–3258, Jul. 2022, ISSN: 1558-0679.

[12] Ea Energy Analyses, "The Danish Experience with Integrating Variable Renewable Energy.," Copenhagen, Denmark, Sep. 2015.

[13] M. I. Santaella. "Ireland: How to run an electricity system on high shares of wind energy," WindEurope. (Jun. 4, 2025), [Online]. Available: `https://windeurope.org/newsroom/news/ireland-how-to-run-an-electricity-system-on-high-shares-of-wind-energy/` (visited on 06/25/2025).

[14] G. Parkinson. "Share of renewables hits record high on Australia's main grid, sends coal to new low," RenewEconomy. (Sep. 9, 2024), [Online]. Available: `https://reneweconomy.com.au/share-of-renewables-hits-record-high-on-australias-main-grid-pushes-coal-to-new-low/` (visited on 06/25/2025).

[15] G. Parkinson. ""Our largest load is now our largest generator:" The path to world's first 100 pct variable renewable grid," RenewEconomy. (Jun. 19, 2025), [Online]. Available: `https://reneweconomy.com.au/our-largest-load-is-now-our-largest-generator-the-path-to-worlds-first-100-pct-variable-renewable-grid/` (visited on 06/25/2025).

[16] N. G. Hingorani and L. Gyugyi, *Understanding FACTS: Concepts and Technology of Flexible AC Transmission Systems*. New York: IEEE Press, 2000, 432 pp., ISBN: 978-0-7803-3455-7.

[17] B. K. Bose, Ed., *Power Electronics in Renewable Energy Systems and Smart Grid: Technology and Applications*, 1st ed. Wiley, Jul. 15, 2019, ISBN: 978-1-119-51562-3 978-1-119-51566-1.

[18] A. Narula, "Grid-forming wind power plants," Chalmers University of Technology, 2023.

[19] F. Blaabjerg, M. Chen, and L. Huang, "Power electronics in wind generation systems," *Nature Reviews Electrical Engineering*, vol. 1, no. 4, pp. 234–250, Apr. 2024, ISSN: 2948-1201.

[20] J. Matevosyan, B. Badrzadeh, T. Prevost, *et al.*, "Grid-Forming Inverters: Are They the Key for High Renewable Penetration?" *IEEE Power and Energy Magazine*, vol. 17, no. 6, pp. 89–98, Nov. 2019, ISSN: 1558-4216.

[21] ENTSO-E, "High Penetration of Power Electronic Interfaced Power Sources (HPoPEIPS)," 2017, p. 37.

[22] C. Collados-Rodriguez, M. Cheah-Mane, E. Prieto-Araujo, and O. Gomis-Bellmunt, "Stability Analysis of Systems With High VSC Penetration: Where Is the Limit?" *IEEE Transactions on Power Delivery*, vol. 35, no. 4, pp. 2021–2031, Aug. 2020, ISSN: 1937-4208.

[23] P. Sorensen, N. A. Cutululis, T. Lund, *et al.*, "Power Quality Issues on Wind Power Installations in Denmark," in *2007 IEEE Power Engineering Society General Meeting*, Jun. 2007, pp. 1–6.

[24] R. Zavadil, N. Miller, A. Ellis, and E. Muljadi, "Making connections [wind generation facilities]," *IEEE Power and Energy Magazine*, vol. 3, no. 6, pp. 26–37, Nov. 2005, ISSN: 1558-4216.

[25] J. Carrasco, L. Franquelo, J. Bialasiewicz, *et al.*, "Power-Electronic Systems for the Grid Integration of Renewable Energy Sources: A Survey," *IEEE Transactions on Industrial Electronics*, vol. 53, no. 4, pp. 1002–1016, Jun. 2006, ISSN: 1557-9948.

[26] I. M. de Alegría, J. Andreu, J. L. Martín, P. Ibañez, J. L. Villate, and H. Camblong, "Connection requirements for wind farms: A survey on technical requierements and regulation," *Renewable and Sustainable Energy Reviews*, vol. 11, no. 8, pp. 1858–1872, Oct. 1, 2007, ISSN: 1364-0321.

[27] M. Tsili and S. Papathanassiou, "A review of grid code technical requirements for wind farms," *IET Renewable Power Generation*, vol. 3, no. 3, pp. 308–332, Sep. 8, 2009, ISSN: 1752-1416, 1752-1424.

[28] International Renewable Energy Agency (IRENA) and Global Wind Energy Council (GWEC), "30 Years of Policies for Wind Energy - Lessons from 12 Wind Energy Markets," Abu Dhabi, UAE, 2013.

[29] B. Jain, S. Jain, and R. K. Nema, "Control strategies of grid interfaced wind energy conversion system: An overview," *Renewable and Sustainable Energy Reviews*, vol. 47, pp. 983–996, Jul. 1, 2015, ISSN: 1364-0321.

[30] B. Bahrani, M. H. Ravanji, B. Kroposki, *et al.*, "Grid-Forming Inverter-Based Resource Research Landscape: Understanding the Key Assets for Renewable-Rich Power Systems," *IEEE Power and Energy Magazine*, vol. 22, no. 2, pp. 18–29, Mar. 2024, ISSN: 1558-4216.

[31] C. Cardozo, T. Prevost, S.-H. Huang, *et al.*, "Promises and Challenges of Grid Forming: Transmission System Operator, Manufacturer and Academic View Points," *Power Systems Computation Conference*, 2024.

[32] Verband der Elektrotechnik Elektronik Informationstechnik e. V., *Technical requirements for grid connection of high voltage direct current systems and direct current-connected power park modules (VDE-AR-N 4131 TAR HVDC)*, Mar. 2019.

[33] National Grid ESO, *Final Modification Report GC0137: Minimum Specification Required for Provision of GB Grid Forming (GBGF) Capability*, Nov. 11, 2021.

[34] G. Denis, T. Prevost, P. Panciatici, X. Kestelyn, F. Colas, and X. Guillaud, "Review on potential strategies for transmission grid operations based on power electronics interfaced voltage sources," in *2015 IEEE Power & Energy Society General Meeting*, Jul. 2015, pp. 1–5.

[35] A. Tayyebi, F. Dörfler, F. Kupzog, Z. Miletic, and W. Hribernik, "Grid-Forming Converters – Inevitability, Control Strategies and Challenges in Future Grids Application," *CIRED Workshop*, no. 0236, p. 5, 2018.

[36] A. Tuladhar, H. Jin, T. Unger, and K. Mauch, "Parallel operation of single phase inverter modules with no control interconnections," in *Proceedings of APEC 97 - Applied Power Electronics Conference*, vol. 1, Feb. 1997, 94–100 vol.1.

[37] R. H. Lasseter, "MicroGrids," in *2002 IEEE Power Engineering Society Winter Meeting. Conference Proceedings (Cat. No.02CH37309)*, vol. 1, Jan. 2002, 305–308 vol.1.

[38] K. De Brabandere, B. Bolsens, J. Van den Keybus, A. Woyte, J. Driesen, and R. Belmans, "A Voltage and Frequency Droop Control Method for Parallel Inverters," *IEEE Transactions on Power Electronics*, vol. 22, no. 4, pp. 1107–1115, Jul. 2007, ISSN: 1941-0107.

[39] R. Majumder, B. Chaudhuri, A. Ghosh, R. Majumder, G. Ledwich, and F. Zare, "Improvement of Stability and Load Sharing in an Autonomous Microgrid Using Supplementary Droop Control Loop," *IEEE Transactions on Power Systems*, vol. 25, no. 2, pp. 796–808, May 2010, ISSN: 0885-8950.

[40] J. Rocabert, A. Luna, F. Blaabjerg, and P. Rodríguez, "Control of Power Converters in AC Microgrids," *IEEE Transactions on Power Electronics*, vol. 27, no. 11, pp. 4734–4749, Nov. 2012, ISSN: 0885-8993.

[41] H.-P. Beck and R. Hesse, "Virtual synchronous machine," in *2007 9th International Conference on Electrical Power Quality and Utilisation*, Barcelona, Spain: IEEE, Oct. 2007, pp. 1–6, ISBN: 978-84-690-9441-9.

[42] Q. Zhong and G. Weiss, "Synchronverters: Inverters That Mimic Synchronous Generators," *IEEE Transactions on Industrial Electronics*, vol. 58, no. 4, pp. 1259–1267, Apr. 2011, ISSN: 1557-9948.

[43] Y. Chen, R. Hesse, D. Turschner, and H. Beck, "Improving the grid power quality using virtual synchronous machines," in *2011 International Conference on Power Engineering, Energy and Electrical Drives*, May 2011, pp. 1–6.

[44] Y. Chen, R. Hesse, D. Turschner, and H.-P. Beck, "Comparison of methods for implementing virtual synchronous machine on inverters," *Renewable Energy and Power Quality Journal*, pp. 734–739, Apr. 2012, ISSN: 2172038X, 2172038X.

[45] S. D'Arco and J. A. Suul, "Virtual synchronous machines — Classification of implementations and analysis of equivalence to droop controllers for microgrids," in *2013 IEEE Grenoble Conference*, Jun. 2013, pp. 1–7.

[46] S. D'Arco and J. A. Suul, "Equivalence of Virtual Synchronous Machines and Frequency-Droops for Converter-Based MicroGrids," *IEEE Transactions on Smart Grid*, vol. 5, no. 1, pp. 394–395, Jan. 2014, ISSN: 1949-3053, 1949-3061.

[47] D. Pattabiraman, R. H. Lasseter., and T. M. Jahns, "Comparison of Grid Following and Grid Forming Control for a High Inverter Penetration Power System," in *2018 IEEE Power & Energy Society General Meeting (PESGM)*, Aug. 2018, pp. 1–5.

[48] X. Gao, D. Zhou, A. Anvari-Moghaddam, and F. Blaabjerg, "A Comparative Study of Grid-Following and Grid-Forming Control Schemes in Power Electronic-Based Power Systems," *Power Electronics and Drives*, vol. 8, no. 1, pp. 1–20, Jan. 1, 2023, ISSN: 2543-4292.

[49] A. Cakiroglu, H. Akdemir, M. Altın, and C. Kasnakoglu, "A Comparative Analysis of Grid Forming and Grid Following Control Methodologies for Power Inverters Under Fault Ride Through Events," in *2024 International Conference on Smart Energy Systems and Technologies (SEST)*, Sep. 2024, pp. 1–6.

[50] G. V. Hollweg, S. A. Khan, S. Chaturvedi, Y. Fan, M. Wang, and W. Su, "Grid-Connected Converters: A Brief Survey of Topologies, Output Filters, Current Control, and Weak Grids Operation," *Energies*, vol. 16, no. 9, p. 3611, Apr. 22, 2023, ISSN: 1996-1073.

[51] F. Blaabjerg, R. Teodorescu, M. Liserre, and A. V. Timbus, "Overview of Control and Grid Synchronization for Distributed Power Generation Systems," *IEEE Transactions on Industrial Electronics*, vol. 53, no. 5, pp. 1398–1409, Oct. 2006, ISSN: 1557-9948.

[52] V. Yaramasu, B. Wu, P. C. Sen, S. Kouro, and M. Narimani, "High-power wind energy conversion systems: State-of-the-art and emerging technologies," *Proceedings of the IEEE*, vol. 103, no. 5, pp. 740–788, May 2015, ISSN: 1558-2256.

[53] T. Jimichi, M. Kaymak, and R. W. De Doncker, "Design and Experimental Verification of a Three-Phase Dual-Active Bridge Converter for Offshore Wind Turbines," in *2018 International Power Electronics Conference (IPEC-Niigata 2018 -ECCE Asia)*, May 2018, pp. 3729–3733.

[54] T. Holzer and A. Muetze, "Full-Size Converter Operation of Large Hydro Power Generators: Generator Design Aspects," in *2018 IEEE Energy Conversion Congress and Exposition (ECCE)*, Sep. 2018, pp. 7363–7368.

[55] M. Vasiladiotis, R. Baumann, C. Häderli, and J. Steinke, "IGCT-Based Direct AC/AC Modular Multilevel Converters for Pumped Hydro Storage Plants," in *2018 IEEE Energy Conversion Congress and Exposition (ECCE)*, Sep. 2018, pp. 4837–4844.

[56] N. Flourentzou, V. G. Agelidis, and G. D. Demetriades, "VSC-Based HVDC Power Transmission Systems: An Overview," *IEEE Transactions on Power Electronics*, vol. 24, no. 3, pp. 592–602, Mar. 2009, ISSN: 1941-0107.

[57] Z. Yang, C. Shen, L. Zhang, M. Crow, and S. Atcitty, "Integration of a StatCom and battery energy storage," in *2001 Power Engineering Society Summer Meeting. Conference Proceedings (Cat. No.01CH37262)*, Jul. 2001.

[58] M. Bongiorno, "On Control of Grid-connected Voltage Source Converters - Mitigation of Voltage Dips and Subsynchronous Resonances," Chalmers University of Technology, 2007, ISBN: 9789172919853.

[59] J. Servotte, E. Acha, and L. M. Castro, "Smart frequency control in power transmission systems using a BESS," in *2015 IEEE Innovative Smart Grid Technologies - Asia (ISGT ASIA)*, Nov. 2015, pp. 1–7.

[60] S. M. Alhejaj and F. M. Gonzalez-Longatt, "Investigation on grid-scale BESS providing inertial response support," in *2016 IEEE International Conference on Power System Technology (POWERCON)*, Sep. 2016, pp. 1–6.

[61] L. S. Xavier, W. C. S. Amorim, A. F. Cupertino, V. F. Mendes, W. C. do Boaventura, and H. A. Pereira, "Power converters for battery energy storage systems connected to medium voltage systems: A comprehensive review," *BMC Energy*, vol. 1, no. 1, p. 7, Jul. 16, 2019, ISSN: 2524-4469.

[62] F. Blaabjerg, F. Iov, Z. Chen, and K. Ma, "Power electronics and controls for wind turbine systems," in *2010 IEEE International Energy Conference*, Manama, Bahrain: IEEE, Dec. 2010, pp. 333–344, ISBN: 978-1-4244-9378-4.

[63] M. A. Hannan, I. Hussin, P. J. Ker, *et al.*, "Advanced Control Strategies of VSC Based HVDC Transmission System: Issues and Potential Recommendations," *IEEE Access*, vol. 6, pp. 78 352–78 369, 2018, ISSN: 2169-3536.

[64] L. Lu and N. A. Cutululis, "Virtual synchronous machine control for wind turbines: A review," *Journal of Physics: Conference Series*, vol. 1356, no. 1, p. 012 028, Oct. 1, 2019, ISSN: 1742-6588, 1742-6596.

[65] A. Lunardi, L. F. Normandia Lourenço, E. Munkhchuluun, L. Meegahapola, and A. J. Sguarezi Filho, "Grid-Connected Power Converters: An Overview of Control Strategies for Renewable Energy," *Energies*, vol. 15, no. 11, p. 4151, Jun. 5, 2022, ISSN: 1996-1073.

[66] O. Gomis-Bellmunt, S. D. Tavakoli, V. A. Lacerda, and E. Prieto-Araujo, "Grid-Forming Loads: Can the Loads Be in Charge of Forming the Grid in Modern Power Systems?" *IEEE Transactions on Smart Grid*, vol. 14, no. 2, pp. 1042–1055, Mar. 2023, ISSN: 1949-3061.

[67] J. Girona-Badia, "Grid-forming strategies for Renewable Energy Sources," Ph.D. dissertation, Universitat Politècnica de Catalunya, Barcelona, Spain, 2025.

[68] J. R. Camarillo-Peñaranda, A. C. Cunha, B. W. França, F. d. A. Oliveira, and L. d. O. Senna, "A review on VSC-HVDC control schemes," *Annual Reviews in Control*, vol. 59, p. 100 988, Jan. 1, 2025, ISSN: 1367-5788.

[69] J. Hu, Y. Shan, K. W. Cheng, and S. Islam, "Overview of Power Converter Control in Microgrids—Challenges, Advances, and Future Trends," *IEEE Transactions on Power Electronics*, vol. 37, no. 8, pp. 9907–9922, Aug. 2022, ISSN: 1941-0107.

[70] S. Henninger and J. Jaeger, "Advanced classification of converter control concepts for integration in electrical power systems," *International Journal of Electrical Power & Energy Systems*, vol. 123, p. 106 210, Dec. 2020, ISSN: 01420615.

[71] H. Zhang, W. Xiang, W. Lin, and J. Wen, "Grid Forming Converters in Renewable Energy Sources Dominated Power Grid: Control Strategy, Stability, Application, and Challenges," *Journal of Modern Power Systems and Clean Energy*, vol. 9, no. 6, pp. 1239–1256, Nov. 2021, ISSN: 2196-5420.

[72] R. Rosso, X. Wang, M. Liserre, X. Lu, and S. Engelken, "Grid-forming converters: An overview of control approaches and future trends," in *2020 IEEE Energy Conversion Congress and Exposition (ECCE)*, Oct. 2020, pp. 4292–4299.

[73] IEEE, "IEEE Guide for Control Architecture for High Power Electronics (1 MW and Greater) Used in Electric Power Transmission and Distribution Systems," *IEEE Std 1676-2010*, pp. 1–47, Feb. 2011.

[74] T. Qoria, F. Gruson, F. Colas, X. Guillaud, M.-S. Debry, and T. Prevost, "Tuning of Cascaded Controllers for Robust Grid-Forming Voltage Source Converter," in *2018 Power Systems Computation Conference (PSCC)*, Dublin, Ireland: IEEE, Jun. 2018, pp. 1–7, ISBN: 978-1-910963-10-4.

[75] H. A. Mohammadpour and E. Santi, "Analysis of subsynchronous control interactions in DFIG-based wind farms: ERCOT case study," in *2015 IEEE Energy Conversion Congress and Exposition (ECCE)*, Sep. 2015, pp. 500–505.

[76] M. Beza and M. Bongiorno, "On the Risk for Subsynchronous Control Interaction in Type 4 Based Wind Farms," *IEEE Transactions on Sustainable Energy*, vol. 10, no. 3, pp. 1410–1418, Jul. 2019, ISSN: 1949-3037.

[77] Y. Cheng, L. Fan, J. Rose, *et al.*, "Real-World Subsynchronous Oscillation Events in Power Grids With High Penetrations of Inverter-Based Resources," *IEEE Transactions on Power Systems*, vol. 38, no. 1, pp. 316–330, Jan. 2023, ISSN: 1558-0679.

[78] NERC, "White Paper: Grid Forming Functional Specifications for BPS-Connected Battery Energy Storage Systems," Sep. 2023.

[79] K. Dmitruk, "A Simplified Guide to Control Algorithms for Grid Converters in Renewable Energy Systems," *Energies*, vol. 17, no. 18, p. 4690, Sep. 20, 2024, ISSN: 1996-1073.

[80] L. Harnefors, M. Bongiorno, and S. Lundberg, "Input-Admittance Calculation and Shaping for Controlled Voltage-Source Converters," *IEEE Transactions on Industrial Electronics*, vol. 54, no. 6, pp. 3323–3334, Dec. 2007, ISSN: 1557-9948.

[81] M. Chandorkar, D. Divan, and R. Adapa, "Control of parallel connected inverters in standalone AC supply systems," *IEEE Transactions on Industry Applications*, vol. 29, no. 1, pp. 136–143, Jan. 1993, ISSN: 1939-9367.

[82] A. Tuladhar, H. Jin, T. Unger, and K. Mauch, "Control of parallel inverters in distributed AC power systems with consideration of line impedance effect," *IEEE Transactions on Industry Applications*, vol. 36, no. 1, pp. 131–138, Jan. 2000, ISSN: 1939-9367.

[83] A. Mohd, E. Ortjohann, W. Sinsukthavorn, M. Lingemann, N. Hamsic, and D. Morton, "Isochronous load sharing and control for inverter-based distributed generation," in *2009 International Conference on Clean Electrical Power*, Jun. 2009, pp. 324–329.

[84] J. Guerrero, J. Matas, L. de Vicuna, N. Berbel, and J. Sosa, "Wireless-control strategy for parallel operation of distributed generation inverters," in *Proceedings of the IEEE International Symposium on Industrial Electronics, 2005. ISIE 2005.*, vol. 2, Jun. 2005, 845–850 vol. 2.

[85] J. C. Vasquez, J. M. Guerrero, A. Luna, P. Rodriguez, and R. Teodorescu, "Adaptive Droop Control Applied to Voltage-Source Inverters Operating in Grid-Connected and Islanded Modes," *IEEE Transactions on Industrial Electronics*, vol. 56, no. 10, pp. 4088–4096, Oct. 2009, ISSN: 1557-9948.

[86] W. Yao, M. Chen, J. Matas, J. M. Guerrero, and Z.-M. Qian, "Design and Analysis of the Droop Control Method for Parallel Inverters Considering the Impact of the Complex Impedance on the Power Sharing," *IEEE Transactions on Industrial Electronics*, vol. 58, no. 2, pp. 576–588, Feb. 2011, ISSN: 1557-9948.

[87] Q.-C. Zhong, "Robust Droop Controller for Accurate Proportional Load Sharing Among Inverters Operated in Parallel," *IEEE Transactions on Industrial Electronics*, vol. 60, no. 4, pp. 1281–1290, Apr. 2013, ISSN: 1557-9948.

[88] S. D'Arco, J. A. Suul, and O. B. Fosso, "A Virtual Synchronous Machine implementation for distributed control of power converters in SmartGrids," *Electric Power Systems Research*, vol. 122, pp. 180–197, May 2015, ISSN: 03787796.

[89] M. Yu, A. J. Roscoe, C. D. Booth, *et al.*, "Use of an inertia-less Virtual Synchronous Machine within future power networks with high penetrations of converters," in *2016 Power Systems Computation Conference (PSCC)*, Jun. 2016, pp. 1–7.

[90] O. Mo, S. D'Arco, and J. A. Suul, "Evaluation of Virtual Synchronous Machines With Dynamic or Quasi-Stationary Machine Models," *IEEE Transactions on Industrial Electronics*, vol. 64, no. 7, pp. 5952–5962, Jul. 2017, ISSN: 0278-0046, 1557-9948.

[91] O. Bahwal, "Implementation of Virtual Synchronous Machine to Allow High Penetration of Converter Connected Generation," Chalmers University of Technology, 2018.

[92] L. Zhang, L. Harnefors, and H. Nee, "Power-Synchronization Control of Grid-Connected Voltage-Source Converters," *IEEE Transactions on Power Systems*, vol. 25, no. 2, pp. 809–820, May 2010, ISSN: 1558-0679.

[93] L. Harnefors, M. Hinkkanen, U. Riaz, F. M. M. Rahman, and L. Zhang, "Robust Analytic Design of Power-Synchronization Control," *IEEE Transactions on Industrial Electronics*, vol. 66, no. 8, pp. 5810–5819, Aug. 2019, ISSN: 1557-9948.

[94] H. Wu and X. Wang, "Design-Oriented Transient Stability Analysis of Grid-Connected Converters With Power Synchronization Control," *IEEE Transactions on Industrial Electronics*, vol. 66, no. 8, pp. 6473–6482, Aug. 2019, ISSN: 1557-9948.

[95] Z. Ma and Q.-C. Zhong, "Synchronverter-based Control Strategy for Back-to-back Converters in Wind Power Applications," *IFAC Proceedings Volumes*, vol. 45, no. 21, pp. 349–354, 2012, ISSN: 14746670.

[96] Q. Zhong, P. Nguyen, Z. Ma, and W. Sheng, "Self-Synchronized Synchronverters: Inverters Without a Dedicated Synchronization Unit," *IEEE Transactions on Power Electronics*, vol. 29, no. 2, pp. 617–630, Feb. 2014, ISSN: 1941-0107.

[97] R. Aouini, B. Marinescu, K. B. Kilani, and M. Elleuch, "Synchronverter-Based Emulation and Control of HVDC Transmission," *IEEE Transactions on Power Systems*, vol. 31, no. 1, pp. 278–286, Jan. 2016, ISSN: 1558-0679.

[98] S. Peyghami, P. Davari, H. Mokhtari, P. C. Loh, and F. Blaabjerg, "Synchronverter-Enabled DC Power Sharing Approach for LVDC Microgrids," *IEEE Transactions on Power Electronics*, vol. 32, no. 10, pp. 8089–8099, Oct. 2017, ISSN: 1941-0107.

[99] P. Unruh, M. Nuschke, P. Strauß, and F. Welck, "Overview on Grid-Forming Inverter Control Methods," *Energies*, vol. 13, no. 10, p. 2589, 10 Jan. 2020.

[100] A. Narula, M. Bongiorno, and M. Beza, "Comparison of Grid-Forming Converter Control Strategies," in *2021 IEEE Energy Conversion Congress and Exposition (ECCE)*, Oct. 2021, pp. 361–368.

[101] S. Ansari, A. Chandel, and M. Tariq, "A Comprehensive Review on Power Converters Control and Control Strategies of AC/DC Microgrid," *IEEE Access*, vol. 9, pp. 17 998–18 015, 2021, ISSN: 2169-3536.

[102] S. Ghimire, K. V. Kkuni, S. C. Jakobsen, *et al.*, "Grid-forming control methods for weakly connected offshore WPPs," in *22nd Wind and Solar Integration Workshop (WIW 2023)*, vol. 2023, Sep. 2023, pp. 246–253.

[103] S. D'Arco, J. A. Suul, and O. B. Fosso, "Control system tuning and stability analysis of Virtual Synchronous Machines," in *2013 IEEE Energy Conversion Congress and Exposition*, Sep. 2013, pp. 2664–2671.

[104] E. Rokrok, T. Qoria, A. Bruyere, B. Francois, and X. Guillaud, "Classification and dynamic assessment of droop-based grid-forming control schemes: Application in HVDC systems," *Electric Power Systems Research*, vol. 189, p. 106 765, Dec. 1, 2020, ISSN: 0378-7796.

[105] P. Kundur, *Power System Stability and Control* (The EPRI Power System Engineering Series), N. J. Balu and M. G. Lauby, Eds. New York: McGraw-Hill, 1994, ISBN: 978-0-07-035958-1.

[106] M. G. Ippolito, R. Musca, G. Zizzo, and M. Bongiorno, "Damping Provision by Different Virtual Synchronous Machine Schemes," in *2020 IEEE International Conference on Environment and Electrical Engineering and 2020 IEEE Industrial and Commercial Power Systems Europe (EEEIC / I&CPS Europe)*, Jun. 2020, pp. 1–6.

[107] A. Narula, M. Bongiorno, M. Beza, J. R. Svensson, X. Guillaud, and L. Harnefors, "Impact of steady-state grid-frequency deviations on the performance of grid-forming converter control strategies," in *2020 22nd European Conference on Power Electronics and Applications (EPE'20 ECCE Europe)*, Lyon, France: IEEE, Sep. 2020, P.1–P.10, ISBN: 978-90-75815-36-8.

[108] M. G. Taul, X. Wang, P. Davari, and F. Blaabjerg, "Current Limiting Control With Enhanced Dynamics of Grid-Forming Converters During Fault Conditions," *IEEE Journal of Emerging and Selected Topics in Power Electronics*, vol. 8, no. 2, pp. 1062–1073, Jun. 2020, ISSN: 2168-6777, 2168-6785.

[109] A. Narula, M. Bongiorno, M. Beza, and P. Chen, "Tuning and evaluation of grid-forming converters for grid-support," in *2021 23rd European Conference on Power Electronics and Applications (EPE'21 ECCE Europe)*, Sep. 2021, P.1–P.10.

[110] A. D. Paquette and D. M. Divan, "Virtual Impedance Current Limiting for Inverters in Microgrids With Synchronous Generators," *IEEE Transactions on Industry Applications*, vol. 51, no. 2, pp. 1630–1638, Mar. 2015, ISSN: 1939-9367.

[111] P. Rodriguez, I. Candela, C. Citro, J. Rocabert, and A. Luna, "Control of grid-connected power converters based on a virtual admittance control loop," in *2013 15th European Conference on Power Electronics and Applications (EPE)*, Sep. 2013, pp. 1–10.

[112] C. Verdugo, A. Tarraso, J. I. Candela, J. Rocabert, and P. Rodriguez, "Centralized Synchronous Controller Based on Load Angle Regulation for Photovoltaic Power Plants," *IEEE Journal of Emerging and Selected Topics in Power Electronics*, vol. 9, no. 1, pp. 485–496, Feb. 2021, ISSN: 2168-6785.

[113] J. He and Y. W. Li, "Analysis, Design, and Implementation of Virtual Impedance for Power Electronics Interfaced Distributed Generation," *IEEE Transactions on Industry Applications*, vol. 47, no. 6, pp. 2525–2538, Nov. 2011, ISSN: 0093-9994.

[114] J. Guerrero, L. G. de Vicuna, J. Matas, M. Castilla, and J. Miret, "Output impedance design of parallel-connected UPS inverters with wireless load-sharing control," *IEEE Transactions on Industrial Electronics*, vol. 52, no. 4, pp. 1126–1135, Aug. 2005, ISSN: 1557-9948.

[115] J. Zhang, J. Shu, J. Ning, L. Huang, and H. Wang, "Enhanced proportional power sharing strategy based on adaptive virtual impedance in low-voltage networked microgrid," *IET Generation, Transmission & Distribution*, vol. 12, no. 11, pp. 2566–2576, 2018, ISSN: 1751-8695.

[116] J. He, Y. W. Li, J. M. Guerrero, F. Blaabjerg, and J. C. Vasquez, "An Islanding Microgrid Power Sharing Approach Using Enhanced Virtual Impedance Control Scheme," *IEEE Transactions on Power Electronics*, vol. 28, no. 11, pp. 5272–5282, Nov. 2013, ISSN: 1941-0107.

[117] T. Qoria, F. Gruson, F. Colas, G. Denis, T. Prevost, and X. Guillaud, "Critical Clearing Time Determination and Enhancement of Grid-Forming Converters Embedding Virtual Impedance as Current Limitation Algorithm," *IEEE Journal of Emerging and Selected Topics in Power Electronics*, vol. 8, no. 2, pp. 1050–1061, Jun. 2020, ISSN: 2168-6777, 2168-6785.

[118] B. Fan, T. Liu, F. Zhao, H. Wu, and X. Wang, "A Review of Current-Limiting Control of Grid-Forming Inverters Under Symmetrical Disturbances," *IEEE Open Journal of Power Electronics*, pp. 1–15, 2022, ISSN: 2644-1314.

[119] T. Qoria, S. E. B. Haoua, R. S. M. Aguilar, M. Reinhausen, H. Fakham, and X. Guillaud, "Optimization of Cascaded Control Gains of Grid-Forming Based Energy Conversion System," *Power Systems Computation Conference*, 2024.

[120] A. July, M. Savaghebi, G. Li, M. Saeedifard, and N. A. Cutululis, "Small-Signal Stability Analysis of Inertia-Based Grid-Forming MMC Interfaced with a Grid of Varying Short-Circuit Ratio," in *Proceedings of IEEE ECCE Europe 2025*, Birmingham, UK, 2025.

[121] J. Z. Zhou, H. Ding, S. Fan, Y. Zhang, and A. M. Gole, "Impact of Short-Circuit Ratio and Phase-Locked-Loop Parameters on the Small-Signal Behavior of a VSC-HVDC Converter," *IEEE Transactions on Power Delivery*, vol. 29, no. 5, pp. 2287–2296, Oct. 2014, ISSN: 1937-4208.

[122] B. Wen, D. Boroyevich, R. Burgos, P. Mattavelli, and Z. Shen, "Analysis of D-Q Small-Signal Impedance of Grid-Tied Inverters," *IEEE Transactions on Power Electronics*, vol. 31, no. 1, pp. 675–687, Jan. 2016, ISSN: 1941-0107.

[123] S. Chernet, M. Beza, and M. Bongiorno, "Investigation of subsynchronous control interaction in DFIG-based wind farms connected to a series compensated transmission line," *International Journal of Electrical Power & Energy Systems*, vol. 105, pp. 765–774, Feb. 2019, ISSN: 01420615.

[124] A. J. Agbemuko, J. L. Domínguez-García, O. Gomis-Bellmunt, and L. Harnefors, "Passivity-Based Analysis and Performance Enhancement of a Vector Controlled VSC Connected to a Weak AC Grid," *IEEE Transactions on Power Delivery*, vol. 36, no. 1, pp. 156–167, Feb. 2021, ISSN: 1937-4208.

[125] Q. Hu, L. Fu, F. Ma, G. Wang, C. Liu, and Y. Ma, "Impact of LVRT Control on Transient Synchronizing Stability of PLL-Based Wind Turbine Converter Connected to High Impedance AC Grid," *IEEE Transactions on Power Systems*, vol. 38, no. 6, pp. 5445–5458, Nov. 2023, ISSN: 1558-0679.

[126] European Commission, *COMMISSION REGULATION (EU) 2016/631 - establishing a network code on requirements for grid connection of generators*, Apr. 16, 2016.

[127] Energimarknadsinspektionen, *Energimarknadsinspektionens föreskrifter om fastställande av generellt tillämpliga krav för nätanslutning av generatorer*, Dec. 5, 2018.

[128] IEEE, *P2800/D6.0 (March 2021) - Draft Standard for Interconnection and Interoperability of Inverter-Based Resources Interconnecting with Associated Transmission Systems*, Mar. 2021.

[129] National Energy System Operator, *The Grid Code - Issue 6, Revision 33*, Jun. 11, 2025.

[130] ENTSO-E, N. Modig, R. Eriksson, *et al.*, "FFR Design of Requirements – External document," Feb. 12, 2020, p. 17.

[131] H.-G. Jeong, U.-M. Choi, and K.-B. Lee, "Control strategies for wind power systems to meet grid code requirements," in *IECON 2011 - 37th Annual Conference of the IEEE Industrial Electronics Society*, Nov. 2011, pp. 1250–1255.

[132] M. R. Islam, M. R. I. Sheikh, and Z. Tasneem, "A frequency converter control strategy of DFIG based wind turbine to meet grid code requirements," in *2016 2nd International Conference on Electrical, Computer Telecommunication Engineering (ICECTE)*, Dec. 2016, pp. 1–4.

[133] J. Kim, Y. Liu, B. A. Ross, *et al.*, "Fault Contribution of Grid-Following and Grid-Forming Inverters Considering Generic Inverter Controls and Ride-through Requirements," in *IECON 2024 - 50th Annual Conference of the IEEE Industrial Electronics Society*, Nov. 2024, pp. 1–6.

[134] A. Azizi and A. Hooshyar, "Fault Current Limiting and Grid Code Compliance for Grid-Forming Inverters — Part II: Solution," *IEEE Transactions on Sustainable Energy*, vol. 15, no. 4, pp. 2500–2517, Oct. 2024, ISSN: 1949-3037.

[135] Y. Musi, "Inclusion in Grid Codes of the Requirements for Grid-Forming Inverters as Part of the Generational Mix," in *2024 32nd Southern African Universities Power Engineering Conference (SAUPEC)*, Jan. 2024, pp. 1–6.

[136] P. Partinen, O.-P. Janhunen, A. Harjula, and L. Linnamaa, "Power system stability enhancement with grid forming controls and process towards grid forming grid code," in *23rd Wind & Solar Integration Workshop (WIW 2024)*, vol. 2024, Oct. 2024, pp. 33–38.

[137] C. Zanabria, T. Prevost, A. Guironnet, V. Costan, and C. Cardozo, "Assessing compliance of power park modules with future grid-forming capability requirements," *IET Conference Proceedings*, vol. 2024, no. 16, pp. 448–460, Feb. 2025, ISSN: 2732-4494.

[138] National Grid ESO, *Final Modification Report GC0163: GB Grid Forming (GBGF) - Removal of Virtual Impedance restriction*, May 22, 2024.

[139] European Commission, *COMMISSION REGULATION (EU) 2016/1447 - establishing a network code on requirements for grid connection of high voltage direct current systems and direct current-connected power park modules*, Aug. 26, 2016.

[140] Energimarknadsinspektionen, *Energimarknadsinspektionens föreskrifter om fastställande av generellt tillämpliga krav för nätanslutning av system för högspänd likström och likströmsanslutna kraftparksmoduler*. Mar. 19, 2019.

[141] Fingrid, "Grid Code Specifications for Grid Energy Storage Systems SJV2019," 2019.

[142] Fingrid, "Specific Study Requirements for Grid Energy Storage Systems," Jun. 21, 2023.

[143] Svenska kraftnät, "Svenska Kraftnät's Strategy for 2023," Sundbyberg, Sweden, 2025.

[144] AEMO, "Voluntary Specification for Grid-forming Inverters," May 2023.

[145] UNIFI Consortium, "UNIFI Specifications for Grid-Forming Inverter-Based Resources: Version 2," Mar. 2024.

[146] European Union Agency for the Cooperation of Energy Regulators (ACER), *Recommendation No 03/2023 of the European Union Agency for the Cooperation of Energy Regulators*, Dec. 19, 2023.

[147] European Union Agency for the Cooperation of Energy Regulators (ACER), *Recommendation No 03/2023 of the European Union Agency for the Cooperation of Energy Regulators – Annex 1: Amended RfG Regulation*, Dec. 19, 2023.

[148] European Union Agency for the Cooperation of Energy Regulators (ACER), *Recommendation No 01/2024 of the European Union Agency for the Cooperation of Energy Regulators*, Dec. 19, 2024.

[149] European Union Agency for the Cooperation of Energy Regulators (ACER), *Recommendation No 01/2024 of the European Union Agency for the Cooperation of Energy Regulators – Annex 1: Proposed amended HVDC Regulation*, Dec. 19, 2024.

[150] H. Xin, C. Liu, X. Chen, Y. Wang, E. Prieto-Araujo, and L. Huang, "How Many Grid-Forming Converters Do We Need? A Perspective From Small Signal Stability and Power Grid Strength," *IEEE Transactions on Power Systems*, vol. 40, no. 1, pp. 623–635, Jan. 2025, ISSN: 1558-0679.

[151] ENTSO-E, "Grid forming capability of power park modules," May 3, 2024.

[152] Verband der Elektrotechnik Elektronik Informationstechnik e. V., *VDE FNN Guideline: Grid forming behaviour of HVDC systems and DC-connected PPMs*, 2020.

[153] AEMO, "Voluntary Specification for Grid-forming Inverters: Core Requirements Test Framework," Jan. 2024.

[154] Enstore, "Enstore updated guide for GB Grid Forming Converters – V-005," Jul. 6, 2021.

[155] NERC, "Grid Forming Technology - Bulk Power System Reliability Consideration," Nov. 2021.

[156] H. Deng, Y. Qi, J. Fang, Y. Tang, and V. Debusschere, "A Robust Low-Voltage-Ride-Through Strategy for Grid-Forming Converters Based on Reactive Power Synchronization," *IEEE Transactions on Power Electronics*, vol. 38, no. 1, pp. 346–357, Jan. 2023, ISSN: 1941-0107.

[157] K. G. Saffar, S. Driss, and F. B. Ajaei, "Impacts of Current Limiting on the Transient Stability of the Virtual Synchronous Generator," *IEEE Transactions on Power Electronics*, pp. 1–12, 2022, ISSN: 0885-8993, 1941-0107.

[158] A. Arasteh, A. Jain, O. Göksu, L. Zeni, and N. A. Cutululis, "Fault Ride Through Capability of Grid Forming Wind Turbines: A Comparison of Control Schemes," in *The 9th Renewable Power Generation Conference (RPG Dublin Online 2021)*, vol. 2021, Mar. 2021, pp. 37–41.

[159] A. Arasteh, L. Zeni, and N. A. Cutululis, "Fault ride through capability of grid forming wind turbines: A comparison of three control schemes," *IET Renewable Power Generation*, vol. 16, no. 9, pp. 1866–1881, 2022, ISSN: 1752-1424.

[160] F. Salha, F. Colas, and X. Guillaud, "Virtual resistance principle for the overcurrent protection of PWM voltage source inverter," in *2010 IEEE PES Innovative Smart Grid Technologies Conference Europe (ISGT Europe)*, Oct. 2010, pp. 1–6.

[161] B. Wang, R. Burgos, and B. Wen, "Grid-Forming Inverter Control Strategy with Improved Fault Ride Through Capability," in *2022 IEEE Energy Conversion Congress and Exposition (ECCE)*, Oct. 2022, pp. 1–8.

[162] Z. Jin and X. Wang, "A DQ-Frame Asymmetrical Virtual Impedance Control for Enhancing Transient Stability of Grid-Forming Inverters," *IEEE Transactions on Power Electronics*, vol. 37, no. 4, pp. 4535–4544, Apr. 2022, ISSN: 1941-0107.

[163] J. M. Bloemink and M. R. Iravani, "Control of a Multiple Source Microgrid With Built-in Islanding Detection and Current Limiting," *IEEE Transactions on Power Delivery*, vol. 27, no. 4, pp. 2122–2132, Oct. 2012, ISSN: 1937-4208.

[164] K. Shi, H. Ye, P. Xu, D. Zhao, and L. Jiao, "Low-voltage ride through control strategy of virtual synchronous generator based on the analysis of excitation state," *IET Generation, Transmission & Distribution*, vol. 12, no. 9, pp. 2165–2172, 2018, ISSN: 1751-8695.

[165] J. Chen, F. Prystupczuk, and T. O'Donnell, "Use of voltage limits for current limitations in grid-forming converters," *CSEE Journal of Power and Energy Systems*, vol. 6, no. 2, pp. 259–269, Jun. 2020, ISSN: 2096-0042.

[166] E. Afshari, G. R. Moradi, R. Rahimi, *et al.*, "Control Strategy for Three-Phase Grid-Connected PV Inverters Enabling Current Limitation Under Unbalanced Faults," *IEEE Transactions on Industrial Electronics*, vol. 64, no. 11, pp. 8908–8918, Nov. 2017, ISSN: 1557-9948.

[167] P. Piya, M. Ebrahimi, M. Karimi-Ghartemani, and S. A. Khajehoddin, "Fault Ride-Through Capability of Voltage-Controlled Inverters," *IEEE Transactions on Industrial Electronics*, vol. 65, no. 10, pp. 7933–7943, Oct. 2018, ISSN: 1557-9948.

[168] L. Huang, L. Zhang, H. Xin, Z. Wang, and D. Gan, "Current limiting leads to virtual power angle synchronous instability of droop-controlled converters," in *2016 IEEE Power and Energy Society General Meeting (PESGM)*, Jul. 2016, pp. 1–5.

[169] H. Xin, L. Huang, L. Zhang, Z. Wang, and J. Hu, "Synchronous Instability Mechanism of P-f Droop-Controlled Voltage Source Converter Caused by Current Saturation," *IEEE Transactions on Power Systems*, vol. 31, no. 6, pp. 5206–5207, Nov. 2016, ISSN: 1558-0679.

[170] H. Lin, C. Jia, J. M. Guerrero, and J. C. Vasquez, "Angle Stability Analysis for Voltage-Controlled Converters," *IEEE Transactions on Industrial Electronics*, vol. 64, no. 8, pp. 6265–6275, Aug. 2017, ISSN: 1557-9948.

[171] T. Qoria, F. Gruson, F. Colas, X. Kestelyn, and X. Guillaud, "Current limiting algorithms and transient stability analysis of grid-forming VSCs," *Electric Power Systems Research*, vol. 189, p. 106 726, Dec. 1, 2020, ISSN: 0378-7796.

[172] X. Wang, M. G. Taul, H. Wu, Y. Liao, F. Blaabjerg, and L. Harnefors, "Grid-Synchronization Stability of Converter-Based Resources—An Overview," *IEEE Open Journal of Industry Applications*, vol. 1, pp. 115–134, 2020, ISSN: 2644-1241.

[173] D. Pan, X. Wang, F. Liu, and R. Shi, "Transient Stability of Voltage-Source Converters With Grid-Forming Control: A Design-Oriented Study," *IEEE Journal of Emerging and Selected Topics in Power Electronics*, vol. 8, no. 2, pp. 1019–1033, Jun. 2020, ISSN: 2168-6785.

[174] E. Rokrok, T. Qoria, A. Bruyere, B. Francois, and X. Guillaud, "Transient Stability Assessment and Enhancement of Grid-Forming Converters Embedding Current Reference Saturation as Current Limiting Strategy," *IEEE Transactions on Power Systems*, pp. 1–1, 2021, ISSN: 1558-0679.

[175] P. Imgart, A. Narula, M. Bongiorno, M. Beza, and J. R. Svensson, "A Cascaded Power Controller for Robust Frequency Ride-Through of Grid-Forming Converters," presented at the 2022 IEEE Energy Conversion Congress and Exposition (ECCE), Detroit, MI, USA, 2022.

[176] S. Dadjo Tavakoli, E. Prieto-Araujo, O. Gomis-Bellmunt, and S. Galceran-Arellano, "Fault ride-through control based on voltage prioritization for grid-forming converters," *IET Renewable Power Generation*, vol. 17, no. 6, pp. 1370–1384, 2023, ISSN: 1752-1424.

[177] M. van Wesenbeeck, S. de Haan, P. Varela, and K. Visscher, "Grid tied converter with virtual kinetic storage," in *2009 IEEE Bucharest PowerTech*, Jun. 2009, pp. 1–7.

[178] M. Schweizer, S. Almér, S. Pettersson, A. Merkert, V. Bergemann, and L. Harnefors, "Grid-Forming Vector Current Control," *IEEE Transactions on Power Electronics*, vol. 37, no. 11, pp. 13 091–13 106, Nov. 2022, ISSN: 1941-0107.

[179] Z. Wang, Y. Chen, X. Li, *et al.*, "Impedance-Based Adaptively Reshaping Method for Enhancing Nonlinear Load Sharing and Voltage Quality in Islanded Microgrids With Virtual Synchronous Generator," *IEEE Transactions on Smart Grid*, vol. 13, no. 4, pp. 2568–2578, Jul. 2022, ISSN: 1949-3061.

[180] A. R. Zamani, M. Beza, M. Bongiorno, A. Narula, and J. R. Svensson, "Impact of the Reactive Behavior of Grid-Connected Converters on Resonance Stability," in *2024 IEEE Energy Conversion Congress and Exposition (ECCE)*, Oct. 2024, pp. 4781–4787.

[181] L. Harnefors, X. Wang, A. G. Yepes, and F. Blaabjerg, "Passivity-Based Stability Assessment of Grid-Connected VSCs—An Overview," *IEEE Journal of Emerging and Selected Topics in Power Electronics*, vol. 4, no. 1, pp. 116–125, Mar. 2016, ISSN: 2168-6777, 2168-6785.

[182] M. Beza, M. Bongiorno, and A. Narula, "Passivity characterization of grid-forming converters with fault-ride through capability," in *2021 23rd European Conference on Power Electronics and Applications (EPE'21 ECCE Europe)*, Sep. 2021, pp. 1–10.

[183] A. Narula, P. Imgart, M. Bongiorno, and M. Beza, "Empowering offshore wind with ES-STATCOM for stability margin improvement and provision of grid-forming capabilities," *Electric Power Systems Research*, vol. 234, p. 110 801, Sep. 2024, ISSN: 03787796.

[184] K. Kamalinejad, A. Narula, M. Bongiorno, M. Beza, and J. R. Svensson, "Investigation of Control Parameters' Impact on Damping Property of Grid-Forming Converters," in *2024 IEEE Energy Conversion Congress and Exposition (ECCE)*, Oct. 2024, pp. 686–693.

[185] A. Narula, P. Imgart, M. Bongiorno, P. Mattavelli, M. Beza, and J. R. Svensson, "Power-Response Matrix-Based Modeling of Converter Systems for Small-Signal Analysis," in *2024 IEEE Energy Conversion Congress and Exposition (ECCE)*, Phoenix, AZ, USA: IEEE, Oct. 20, 2024, pp. 4724–4731, ISBN: 9798350376067.

[186] G. R. Mugambi, N. Darii, H. Khazraj, *et al.*, "Methodologies for offshore wind power plant dynamic stability analysis," *Renewable and Sustainable Energy Reviews*, vol. 216, p. 115 635, Jul. 2025, ISSN: 13640321.

[187] D. Yang, H. Wu, X. Wang, and F. Blaabjerg, "Suppression of synchronous resonance for VSGs," *The Journal of Engineering*, vol. 2017, no. 13, pp. 2574–2579, Jan. 2017, ISSN: 2051-3305, 2051-3305.

[188] L. Lu, O. Saborío-Romano, and N. A. Cutululis, "Torsional oscillation damping in wind turbines with virtual synchronous machine-based frequency response," *Wind Energy*, vol. 25, no. 7, pp. 1157–1172, 2022, ISSN: 1099-1824.

[189] M. Li, Y. Wang, W. Hu, *et al.*, "Unified Modeling and Analysis of Dynamic Power Coupling for Grid-Forming Converters," *IEEE Transactions on Power Electronics*, vol. 37, no. 2, pp. 2321–2337, Feb. 2022, ISSN: 1941-0107.

[190] Z. Tang, S. Wang, Y. Cui, X. Cheng, and Y. Zhao, "A Review of Coupling and Interaction Studies of Grid-Forming Converters Based on Transient Stability," in *2024 7th International Conference on Energy, Electrical and Power Engineering (CEEPE)*, Apr. 2024, pp. 259–265.

[191] K. D. Brabandere, B. Bolsens, J. V. den Keybus, *et al.*, "A voltage and frequency droop control method for parallel inverters," in *2004 IEEE 35th Annual Power Electronics Specialists Conference (IEEE Cat. No.04CH37551)*, vol. 4, Jun. 2004, 2501–2507 Vol.4.

[192] L. Ängquist and M. Bongiorno, "Auto-normalizing Phase-Locked Loop for grid-connected converters," in *2009 IEEE Energy Conversion Congress and Exposition*, San Jose, CA: IEEE, Sep. 2009, pp. 2957–2964, ISBN: 978-1-4244-2893-9.

[193] P. Imgart, *FreBaVAT - Frequency-Based Virtual-Admittance Tuning Script for Grid-Forming Converters*, Aug. 27, 2025. DOI: https://doi.org/10.5281/zenodo.16967617. [Online]. Available: https://codeberg.org/pauli_314/FreBaVAT.

[194] J. He, Y. W. Li, and F. Blaabjerg, "An Enhanced Islanding Microgrid Reactive Power, Imbalance Power, and Harmonic Power Sharing Scheme," *IEEE Transactions on Power Electronics*, vol. 30, no. 6, pp. 3389–3401, Jun. 2015, ISSN: 1941-0107.

[195] C. A. Macana and H. R. Pota, "Adaptive synchronous reference frame virtual impedance controller for accurate power sharing in islanded ac-microgrids: A faster alternative to the conventional droop control," in *2017 IEEE Energy Conversion Congress and Exposition (ECCE)*, Oct. 2017, pp. 3728–3735.

[196] R. An, Z. Liu, and J. Liu, "Successive-Approximation-Based Virtual Impedance Tuning Method for Accurate Reactive Power Sharing in Islanded Microgrids," *IEEE Transactions on Power Electronics*, vol. 36, no. 1, pp. 87–102, Jan. 2021, ISSN: 1941-0107.

[197] M. Keddar, M. L. Doumbia, K. Belmokhtar, and M. D. Krachai, "Experimental Validation of an Accurate Reactive Power-Sharing Approach Based on Adaptive Virtual Impedance and Consensus Control," in *2021 12th International Renewable Energy Congress (IREC)*, Oct. 2021, pp. 1–6.

[198] J. Zhang, Y. Jia, Z. Li, X. Ye, C. Yang, and D. Jiang, "Adaptive Virtual Impedance Control Strategy for Multiple Grid-forming Converters in Islanded Microgrid," in *2023 2nd Asia Power and Electrical Technology Conference (APET)*, Dec. 2023, pp. 599–604.

[199] C. Fan, X. Qin, L. Qi, H. Liu, B. Ding, and Z. Meng, "The Function Mechanism of Virtual Impedance in Grid-forming Droop Control and An Adaptive Parameter Tuning Method for Virtual Impedance Based on Network Equivalent Identification," in *2024 IEEE 2nd International Conference on Power Science and Technology (ICPST)*, May 2024, pp. 2171–2176.

[200] A. Bolzoni, G. M. Foglia, L. Frosio, M. F. Iacchetti, and R. Perini, "Impact of Line and Control Parameters on Droop Stability in Inverters for Distributed Generation," *IEEE Transactions on Smart Grid*, vol. 9, no. 6, pp. 6656–6665, Nov. 2018, ISSN: 1949-3061.

[201] A. Rodríguez-Cabero, J. Roldán-Pérez, and M. Prodanovic, "Virtual Impedance Design Considerations for Virtual Synchronous Machines in Weak Grids," *IEEE Journal of Emerging and Selected Topics in Power Electronics*, vol. 8, no. 2, pp. 1477–1489, Jun. 2020, ISSN: 2168-6785.

[202] D. Moutevelis, F. Göthner, J. Roldán-Pérez, and M. Prodanović, "Quasi-Stationary Implementation of Virtual Admittance Controller for Voltage Support from Distributed Generation," in *2022 IEEE PES Innovative Smart Grid Technologies Conference Europe (ISGT-Europe)*, Oct. 2022, pp. 1–5.

[203] X. Zhang, Y. Li, Y. Wen, J. Shen, C. Li, and S. Xiao, "Reactive Power Distribution of Mesh Parallel Distributed Generations Based on Virtual Impedance," in *2022 4th International Conference on Smart Power & Internet Energy Systems (SPIES)*, Dec. 2022, pp. 1254–1259.

[204] Z. Li, L. Liang, R. Yang, and X. Cai, "The Virtual Admittance Control of Sending End Converter for Offshore Wind Farm Integration," in *2023 IEEE 14th International Symposium on Power Electronics for Distributed Generation Systems (PEDG)*, Jun. 2023, pp. 133–136.

[205] O. Oboreh-Snapps, K. J. P. Veeramraju, A. Fernandes, *et al.*, "Small Signal Stability Analysis of Virtual Impedance Control in Islanded Microgrid," in *2023 IEEE Energy Conversion Congress and Exposition (ECCE)*, Oct. 2023, pp. 1005–1011.

[206] W. Zhang, J. Cui, Y. Zhao, and H. Yin, "Parameters Tuning of Flexible Drooped Synchronous Power Controller Based on Small Signal Modeling and Sensitivity Analysis," in *2023 IEEE 18th Conference on Industrial Electronics and Applications (ICIEA)*, Aug. 2023, pp. 886–891.

[207] E. Fedele, N. Campagna, G. Bossi, R. Rizzo, R. Miceli, and A. Damiano, "Stability Analysis of DFIG with Virtual-Admittance-Based Grid-Forming Control under Different Grid Strenghts," in *2024 6th Global Power, Energy and Communication Conference (GPECOM)*, Jun. 2024, pp. 399–404.

[208] J. D. V. Leon, A. Tarraso, J. I. Candela, J. Rocabert, and P. Rodriguez, "Grid-Forming Controller Based on Virtual Admittance for Power Converters Working in Weak Grids," *IEEE Journal of Emerging and Selected Topics in Industrial Electronics*, vol. 4, no. 3, pp. 791–801, Jul. 2023, ISSN: 2687-9743.

[209] L. Guo, S. Zhang, X. Li, Y. W. Li, C. Wang, and Y. Feng, "Stability Analysis and Damping Enhancement Based on Frequency-Dependent Virtual Impedance for DC Microgrids," *IEEE Journal of Emerging and Selected Topics in Power Electronics*, vol. 5, no. 1, pp. 338–350, Mar. 2017, ISSN: 2168-6785.

[210] Y. Zhao, W. Zhang, W. Wang, and Z. Pan, "Grid Forming Control with Inertial and Virtual Admittance Characteristics for Grid-tied Converters," in *2020 39th Chinese Control Conference (CCC)*, Jul. 2020, pp. 6164–6189.

[211] P. Imgart, M. Beza, M. Bongiorno, and J. R. Svensson, "An Overview of Grid-Connection Requirements for Converters and Their Impact on Grid-Forming Control," *EPE'22 ECCE Europe*, 2022.

[212] A. Narula, P. Imgart, M. Bongiorno, M. Beza, J. R. Svensson, and J.-P. Hasler, "Voltage-based Current Limitation Strategy to Preserve Grid-forming Properties Under Severe Grid Disturbances," *IEEE Open Journal of Power Electronics*, pp. 1–13, 2023, ISSN: 2644-1314.

[213] P. Imgart, A. Narula, M. Bongiorno, M. Beza, and J. R. Svensson, "External Inertia Emulation to Facilitate Active-Power Limitation in Grid-Forming Converters," *IEEE Transactions on Industry Applications*, vol. 60, no. 6, pp. 9145–9156, Nov. 2024, ISSN: 1939-9367.

[214] P. Imgart, M. Bongiorno, J. R. Svensson, and M. Beza, "Stability Limits and Improved Robustness of Grid-Forming Converters With External Inertia-Emulation Loop," in *2023 25th European Conference on Power Electronics and Applications (EPE'23 ECCE Europe)*, Aalborg, Denmark: IEEE, Sep. 4, 2023, pp. 1–8, ISBN: 978-90-75815-41-2.

Part II

Papers

PAPER A

An Overview of Grid-Connection Requirements for Converters and Their Impact on Grid-Forming Control

Paul Imgart, Mebtu Beza, Massimo Bongiorno, Jan R. Svensson

Published in 24th European Conference on Power Electronics and Applications, EPE 2022 ECCE Europe.

The layout has been revised.

Abstract

The increasing share of converters in the power system results in the need to revise grid-connection requirements and a shift in converter control strategies towards grid-forming control. This paper analyzes and compares existing standards and future trends in specifications for grid-connected converters and highlights commonalities and differences. The key consequences for converter control performance requirements are presented to facilitate the selection of the most suitable grid-forming control structures.

1 Introduction

The transformation towards a sustainable power system will result in fewer synchronous machines in the power system, and grid-forming converters are suggested as one solution for the associated challenges [2]. As the grid-forming concept is still relatively new, discussions between grid operators, legislators and manufacturers on the design and implementation of grid-forming control are still ongoing today. Technical requirements and standards define the functionality required from grid-forming converters and are accordingly an important part of these discussions.

Since the first proposal of the virtual synchronous machine (VSM) concept, a large variety of grid-forming converter controls has been proposed [3], with some relevant selections shown in Fig. 1 and compared in [4]. Analyzing the capability of different control strategies to fulfill the grid-connection requirements is an important part in selecting the most promising designs for further research and development.

This paper compares and analyzes technical requirements for grid-connected converter systems from a selection of different legal regulations, grid codes and standards with focus on grid-forming control. In addition, possible differences and contradictions among the various documents are investigated. The final goal is to highlight implications of the different requirements on converter control strategy and to facilitate the choice of suitable control structures.

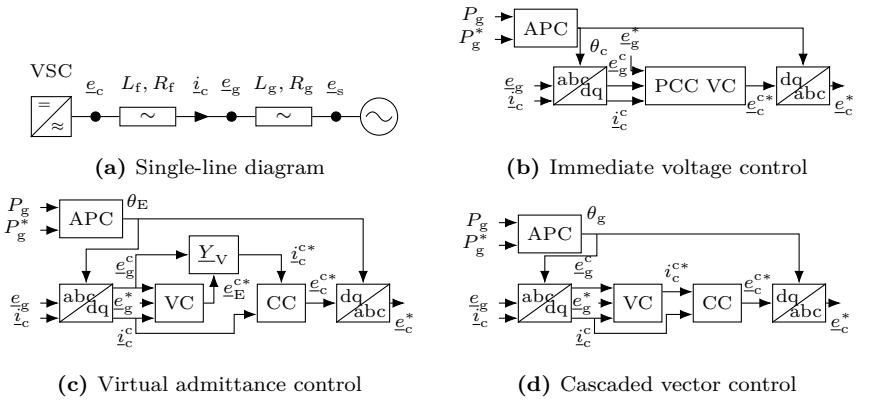

(a) Single-line diagram

(b) Immediate voltage control

(c) Virtual admittance control

(d) Cascaded vector control

Figure 1: Single-line diagram of grid-connected converter system and block-schemes for three different types of grid-forming converter control [4]. Quantities with index E refer to the virtual back EMF. APC: Active power controller; VC: Voltage controller; CC: Current controller; $\underline{Y}_V$: Virtual admittance.

2 Categorization of requirement documents and selection of examples

Documents defining technical requirements for grid-connected converters can be classified according to their author, scope, bindingness and detailedness in the following categories: legal regulations, grid codes, specifications of particular ancilliary services, technical standards and customer requirements. Figure 2 displays how requirements of the different categories are inter-related. Legal regulation is obligatory, but typically less detailed. For connection to a particular grid, additionally the corresponding grid codes have to be followed. The specifications for ancilliary services can be part of the general grid code or provided through additional documents; customers can also provide further requirements. Following technical standards is often voluntary, but can be a requisite for a certain control implementation to be successful.

As illustrated in the figure, the requirements given in different documents are not necessarily the same, but can differ between countries and in some cases even conflict [5]. Moreover standards affect not only the jurisdiction

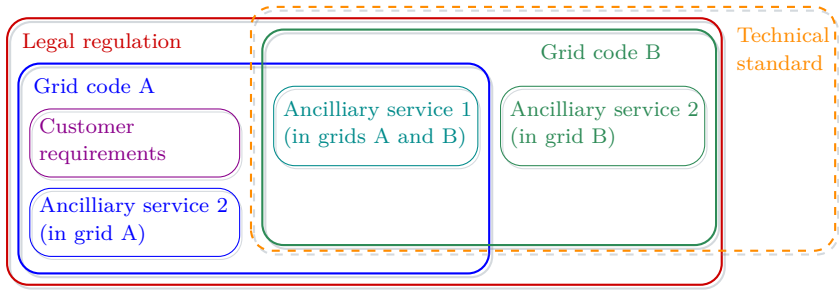

Figure 2: Illustration of different technical requirement document types and their relation. Grid code A and B serve as examples for two independent grid code documents from different system operators, each also specifying the exemplary ancilliary services 1 and 2.

they are valid for, but have an effect on others as well, in particular when concerning development- and testing-intensive equipment such as wind turbines, FACTS and HVDC systems. If one standard explicitly bans a particular implementation, manufacturers are likely to not develop a special solution, but adapt their product to comply with this specification, even if this might result in higher prices and in some cases suboptimal performance for all customers. This is due to the amount of development, testing and tuning needed for these systems, making it uneconomic to maintain a large variety of implementations. While on first glance it might make sense for system operators to tailor requirements to their particular system, a harmonization of requirements could reduce costs, enable share of experience and stimulate innovation by freeing up resources otherwise needed for local adaptations [5]. An exception to this can be certain limits, thresholds, settings or ratings. In conclusion, a harmonization of requirements with option for small local adaptions (as in [6]) is not only in the interest of manufacturers, but even academia and system operators. Consequentially, the regulations shown in Fig. 2 would ideally all coincide or at least be subsets of others. The ENTSO-E network codes for generators [6] and HVDC [7] are recent examples of successful harmonization efforts. However, specifications and requirements for grid-forming converters are still under discussion and development, starting with the definition of grid-forming properties itself. This presents a challenge for all involved parties to find a generally accepted set of required functionalities for grid-forming

converters.

The following paragraph describes the grid codes and standards selected for the overview in this paper. The European Commission's network code with requirements for generators (NC RfG) [6] and HVDC systems and DC connected generation (NC HVDC) [7] are drafted by ENTSO-E and are the underlying legal regulation for grid codes in the European Union. They are concretized in national laws and regulations, e.g. in the case of Sweden [8] for RfG (SE RfG) and [9] for HVDC (SE HVDC), or national standards such as the VDE standard VDE-AR-N 4131 for HVDC in Germany [10]. A relevant technical standard for DC interfaced generation is the draft IEEE P2800 [11]. The UK grid code modification GC0137 (NG GC0137) [12] containing requirements for grid forming capability is an example for an ancilliary service specification. The final investigated document is the ENTSO-E report on the contributions of grid-forming converters [13]. It is not a technical standard but reflects the debate about which features are discussed as a part of grid-forming capabilities. These documents have been chosen due to their relevance to the current and future state of requirements for grid-forming converters and to represent different countries and the categories mentioned above. It should be noted that the used standards in some cases apply to HVDC systems, in some cases to power-electronic interfaced generation and in some cases to either. None of the selected documents is formulated exclusively for FACTS, but often they partly follow HVDC regulations. Different systems such as e.g. wind power parks, grid-connected battery energy storage and HVDC systems will have different purposes and capabilities and comparing the requirements they have to fulfill is consequently meaningful only up to a certain degree. However, as all of these are grid-connected converter systems, they can all be equipped with grid-forming control, which motivates a comparison of the required capabilities.

3 Comparison of requirements

To facilitate the comparison and analysis, the categorization of a selection of the requirements included in the investigated documents is suggested as shown in Fig. 3. This section describes how the requirements belonging to these categories are treated in the selected documents, with Table 1 presenting a summary.

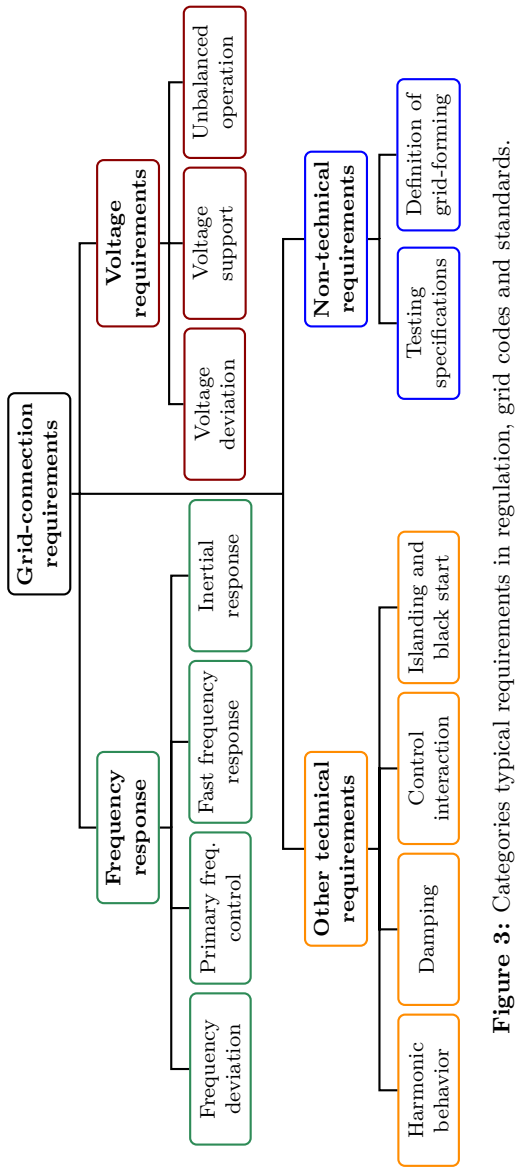

Figure 3: Categories typical requirements in regulation, grid codes and standards.

Table 1: Selection of requirements from the documents. Green: explicitely specified, required by standard or on demand of the TSO; Yellow: unspecific/implicitly specified; Red: not mentioned.

Type of requirement	NC RfG & HVDC	SE RfG & HVDC *	VDE-AR-N 4131	IEEE P2800	NG GC0137	ENTSO-E report
Frequency response						
Frequency deviation	✓	✓	✓	✓	○	○
Primary frequency control	✓	✓	✓	✓	✗	✗
Fast frequency response	✗	✗	✓	✓	✗	✗
Inertial response	✓	✗	✓	✗	✓	✓
Voltage requirements						
Voltage deviation	✓	✓	✓	✓	○	○
Voltage support	✓	✗	✓	✓	○	○
Unbalanced operation	✗	✗	✓	○	✗	✓
Other technical requirements						
Harmonic behavior	✗	✗	✓	✓	○	✓
Damping	✓	✓	✓	○	✓	✓
Control interaction	○	○	✓	○	✓	✓
Islanding and black start capability	✓	✗	✓	✗	✗	○
Non-technical requirements						
Testing specifications	✓	✗	✓	✓	✓	○
Definition of grid-forming capability	✗	✗	✗	○	✓	✓

*: As SE RfG & SE HVDC are national implementations of NC RfG & NC HVDC, respectively, they include the requirements mentioned there. Here is indicated where these documents contain substantial concretizations or additions.

3.1 Frequency response

Frequency deviation. Nearly all of the compared standards contain a range of steady-state frequency deviations from nominal frequency with corresponding minimum operating times, which are summarized in Table 2. The frequency range and times given for NC RfG & HVDC are minimum requirements, which can be further increased by the relevant system operator. Observe that NG GC0137 and the ENTSO-E report do not explicitly indicate low-frequency ride-through, but provide requirements for grid-forming behavior in case of frequency deviations, which implicitly requires operation at lower frequencies. The compared standards provide the requirements in a similar format, but there are significant differences in the required time spans, with the low-inertia systems Great Britain and Ireland placing highest requirements.
Apart from steady-state variations, some standards also define the transient conditions which the converter system has to be able to ride through in the form of maximum phase-angle jump and rate of change of frequency. As detailed in Table 2, NC HVDC, VDE-AR-N 4131 and IEEE P2800 give requirements for maximum rate of change of frequency, where the IEEE norm is considerably stricter than the others. IEEE P2800 even contains the requirement to withstand sub-cycle phase-jumps of 30°. The ability to withstand high frequency gradients can be affected by requirements for high virtual inertia, as the inertia emulation will slow the ability of the converter to track changes in the system frequency.

Primary frequency control. All investigated documents require the capability to control active power in dependency of the deviation of the system frequency from nominal with the exception of NG GC0137 and the ENTSO-E report. In case of NC RfG, the requirements vary with converter rating, with smaller generators only required to act in case of overfrequency. All specifications are based on a deadband around nominal frequency and a proportional gain and take the fluctuating character of renewable resources into consideration, allowing for adjustments based on the availability of primary energy.

Fast frequency reserve. Converters are capable of controlling their active power output significantly faster than required for primary frequency control. This can be used to counter the effects of the decline in synchronous inertia caused by the replacement of synchronous machines with converter interfaced generation [14]. In consequence, requirements for fast frequency reserve (FFR) are contained in VDE-AR-N 4131 in general terms and in IEEE P2800 with

Table 2: Minimum connection time for specific frequency ranges according to selected example requirements. "Gen." denotes requirements for generation, while "HVDC" is for HVDC converter stations.

Frequency range	NC RfG Con. Europe, Nordic & Baltic [6]	NC RfG Great Britain & Ireland [6]	NC HVDC [7]	SE HVDC [9]	VDE AR-N 4131 [10]	IEEE P2800 [11]
0.94 pu – 0.95 pu	$-^{a}$	20 s^{b}	$>$ 20 s^{c}	60 s	60 s^{c}	$-^{a}$
0.95 pu – 0.97 pu	30 min^{c}	90 min	90 min^{c}	100 min	90 min^{c}	5 min^{c}
0.97 pu – 0.98 pu	30 min^{c}	90 min^{c}	90 min^{c}	100 min	90 min^{c}	5 min^{c}
0.98 pu – 1.02 pu	unlimited	unlimited	unlimited	unlimited	unlimited	unlimited
1.02 pu – 1.03 pu	30 min^{d}	90 min	90 min^{c}	100 min	90 min^{c}	5 min^{c}
1.03 pu – 1.04 pu	$-^{a}$	15 min^{b}	15 min^{c}	30 min	15 min^{c}	$-^{b}$
Minimum RoCoF	$-^{e}$	$-^{e}$	2.5 Hz/s	2.5 Hz/s^{f}	2.5 Hz/s	5 Hz/s

^{a}: No connection requirement is given; ^{b}: Great Britain only, no connection requirement given for Ireland.; ^{c}: To be specified by the relevant TSO, but not less than the shown time; ^{d}: In Baltic region, ^{c} applies; ^{e}: To be specified by the relevant TSO; ^{f}: Not explicitly stated, but as national implementation of NC HVDC those requirements apply.

details about performance and possible FFR variants. Even though NC RfG & HVDC do not contain FFR, it has in the meanwhile been defined by ENTSO-E as an auxiliary service in a separate document and is procured as a service e.g. in Sweden [15].

Inertial response. To counteract the effects of the reduction of mechanical inertia synchronously connected to the grid, converters can emulate inertia by modulating the active power output to counteract either changes in the frequency or phase angle of the voltage at the point of common coupling (PCC). NC RfG & HVDC as well as VDE-AR-N 4131 specify that the TSO can require inertial response capability from connected converter system with the relevant control principle and parameters to be agreed upon by TSO and owner of the converter system in that case. In the case of NG GC0137, both frequency-derivative proportional inertial support as well as a response to grid voltage phase jumps are obligatory requirements. Finally, in the ENTSO-E report inertial response is discussed as one of the key capabilities constituting grid-forming control.

Provision of primary frequency control, fast frequency reserve and inertial response requires active power, but none of the investigated documents stipulates the availability of energy storage or prime energy. This means that the control system needs to be able to provide the response, but additional requirements not currently covered by the standards need to be fulfilled for the active participation in this services.

3.2 Voltage requirements

Voltage deviation. This category includes the behavior required from the converter system by some standards during transient disturbances such as faults and voltage dips. These fault ride-through (FRT) requirements are commonly provided as a voltage-time-profile, which represents a minimum requirement, i.e. the converter system must be able to stay connected when subject to a voltage than does not go below the defined curve. This way of defining low-voltage ride-through requirements is common to the European standards, but is not present in IEEE P2800, where instead minimum connection times for different voltage ranges are defined. The FRT requirements from a selection of standards are listed in Table 3, with the shape of the corresponding voltage profile given in Fig. 4. For the summary in Table 3, the IEEE requirements have been rearranged as shown in the dashed profile in Fig. 4.

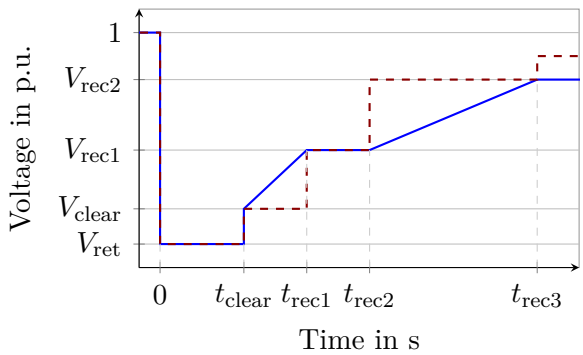

Figure 4: Structure of FRT minimum voltage profile. Solid blue: European standards ([6]–[10]); dashed red: IEEE P2800 minimum connection times.

In some standards FRT is not only a connection requirements, but contains even the obligation of fast fault current injection. NC RfG & HVDC provide the possibility for the TSO to define such requirements. The national implementations SE RfG & HVDC do not concretize this further, while VDE-AR-N 4131 states priority for reactive current and contains specifications for voltage support and unbalanced operation, which can even have an impact on fault current injection. IEEE P2800 contains a very detailed description of different fault modes and expected fault current contributions. None of the mentioned standards provide fault current magnitudes, but place this responsibility on the relevant system operator. In NG GC0137, no minimum connection times are given as they are part of the main grid code, but requirements for grid-forming behavior are mentioned in terms of fast fault current and reactive power injection in case of grid voltage magnitude transients. Emphasis is put on the immediate response, reflecting the voltage source behavior of the grid-forming converter. The same is true, even though less specific, for the analysis in the ENTSO-E report, where fault current contribution is defined as one of the characteristics of grid-forming converters. All fault current requirements take the limited over-current capability of converters into account and allow for appropriate over-current limitation and protection.
Apart from the fault ride-through in response to transient disturbance, the standards also specify connection requirements regarding steady-state voltage

deviations. These are summarized in Table 4.

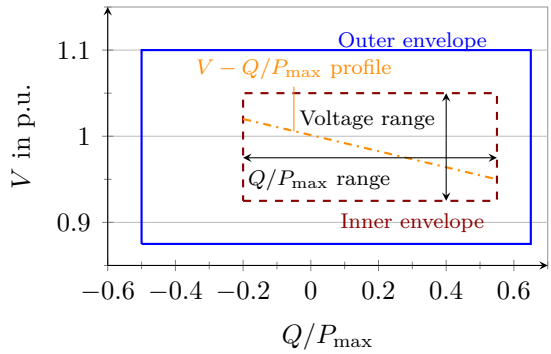

Figure 5: Reactive power capability as defined by NC RfG. The outer envelope is as shown in the standard, the inner and $V - Q$ profile are indicative.

Voltage support. Converter systems are commonly required to contribute to the control of the voltage magnitude at their PCC by exchanging reactive power. For NC RfG & HVDC and their national implementations, this requirement is given in the form illustrated by Fig. 5. The standard defines an outer envelope. The TSO then determines an inner envelope within it, and with a predetermined maximum voltage and reactive power range. Within that envelope, the TSO specifies a profile for the exchange of reactive power in dependence of the voltage. The converter system is required to have the capability of providing the desired reactive power exchange non-withstanding the active power operating point. The reactive power exchange can either be controlled in voltage, reactive power or power factor control mode, which are further specified in NC RfG & HVDC. While SE RfG & HVDC do not add any further requirements regarding voltage support, VDE-AR-N 4131 contains detailed specifications of the control mode and performance requirements as well as inner envelopes for the voltage control profiles. In IEEE P2800, a reactive power requirement is established, which lies within the outer envelope from NC RfG. It also includes detailed control mode and performance requirements for voltage, reactive power and power factor control. NG GC0137 does not add any further specifications regarding voltage support beyond general grid code apply. However, both here and in the ENTSO-E report the capability

Table 3: FRT requirements.

Quantity	NC RfG $< 110\,\text{kV}^a$	NC RfG $\geq 110\,\text{kV}^a$	NC HVDC^a	SE HVDC	VDE AR-N 4131	IEEE P2800^b
V_{ret}	$0.05\,\text{pu} - 0.15\,\text{pu}$	$0\,\text{pu}$	$0\,\text{pu} - 0.3\,\text{pu}$	$0\,\text{pu}$	$0\,\text{pu}$	$0\,\text{pu}$
V_{clear}	V_{ret}	V_{ret}	V_{ret}	V_{ret}	V_{ret}	$0.25\,\text{pu}$
V_{rec1}	V_{clear}	V_{clear}	$0.25\,\text{pu} - 0.85\,\text{pu}$	$0.85\,\text{pu}$	$0.85\,\text{pu}^c$	$0.5\,\text{pu}$
V_{rec2}	$0.85\,\text{pu}$	$0.85\,\text{pu}$	$0.85 - 0.9\,\text{pu}$	$0.85\,\text{pu}$	V_{rec1}	$0.7\,\text{pu}$
t_{clear}	$0.14\,\text{s} - 0.15\,\text{s}^d$	$0.14\,\text{s} - 0.15\,\text{s}^d$	$0.14\,\text{s} - 0.25\,\text{s}$	$0.25\,\text{s}$	$0.15\,\text{s}$	$0.32\,\text{s}$
t_{rec1}	t_{clear}	t_{clear}	$1.5\,\text{s} - 2.5\,\text{s}$	$2\,\text{s}$	$3\,\text{s}$	$1.2\,\text{s}$
t_{rec2}	t_{rec1}	t_{rec1}	t_{rec1}	t_{rec1}	t_{rec1}	$3\,\text{s}$
t_{rec3}	$1.5\,\text{s} - 3.0\,\text{s}$	$1.5\,\text{s} - 3.0\,\text{s}$	$t_{\text{rec1}} - 10\,\text{s}$	$10\,\text{s}$	–	$6\,\text{s}$

^{a}: TSO determines parameters within specified range; ^{b}: Only requirements for voltages $< 0.9\,\text{pu}$ given here. Requirements are shown for plants without auxiliary equipment limiting FRT and rearranged to comply with the form in Fig. 4; ^{c}: $0.894\,\text{pu}$ ($340\,\text{kV}$) if rated voltage is $380\,\text{kV}$; ^{d}: Can be $0.14\,\text{s} - 0.25\,\text{s}$ if required by system protection and secure operation.

Table 4: Minimum connection time for specific voltage ranges according to selected requirements.

Voltage range	NC RfG Con. Europe[a]	NC RfG Nordic[a]	NC RfG Great Britain[a]	NC HVDC Con. Europe[a]	NC HVDC Nordic[a]	NC HVDC Great Britain[a]	VDE AR-N 4131	IEEE P2800[b]
0.85 pu – 0.90 pu	60 min	–[c]	–[c]	unlimited	–[c]	–[c]	unlimited[d]	–[c]
0.90 pu – 1.05 pu	unlimited	unlimited	unlimited	unlimited	unlimited	unlimited	unlimited	unlimited
1.05 pu – 1.10 pu	20 min– 60 min[e]	< 60 min[e]	15 min	60 min[f]	< 60 min[e]	15 min	unlimited	30 min
1.10 pu – 1.20 pu	–[c]	–[c]	–[c]	–[c]	–[c]	–[c]	60 min[g]	1 s

[a]: Applies for a rated voltage of 300 kV to 400 kV, and in case of NC RfG type D power park modules only; [b]: Connection requirements for voltage of 0.9 pu and above are shown here, lower voltages in Table 3; [c]: No connection requirement is given, see Table 3 for FRT; [d]: For rated voltage of 380 kV, this applies for $V > 0.894$ pu (340 kV); [e]: To be specified by the TSO withing the stated range; [f]: To be specified by the TSO as not less than 60 min for 1.05 pu $< V <$ 1.0875 pu, 60 min for 1.0875 pu $< V <$ 1.1 pu; [g]: Requirement of 60 min applies for 1.1 pu<V<1.158 pu.

to create a system voltage is required, i.e. the ability to behave as a voltage source independent of a grid voltage.

Unbalanced operation. Of the studied standards, NC RfG, NC HVDC, SE RfG & SE HVDC do not make any specifications regarding the expected behavior under unbalanced operating conditions apart from FRT during asymmetric faults to be detailed by the TSO. In IEEE P2800, no requirements for unbalanced but otherwise normal operating conditions are given, but negative sequence current injection is required during asymmetric faults. NG GC0137 does not contain requirements of unbalanced operation. In VDE-AR-N 4131 on the other hand, voltage control is required not only for positive, but also for negative and zero sequence, and the ENTSO-E report demands the converter system to act as sink for unbalances, i.e. provide a low-impedance path for negative sequence currents. This indicates a paradigm shift towards more system responsibility, similar to the one described below for harmonic behavior.

3.3 Other technical requirements

Harmonic behavior. Neither NC RfG & HVDC nor SE RfG & HVDC include requirements for the harmonic behavior of the converter system. In VDE-AR-N 4131, maximum values for the total harmonic distortion as well as the magnitude of each of the relevant harmonics in the PCC voltage are specified for DC connected generation, but not for HVDC. In contrast, IEEE P2800 gives requirements for the harmonic distortion of the current, but explicitly does not limit the voltage harmonics. The standard contains a detailed discussion of converter voltage harmonics and liability in the annexes. NG GC0137 does not specify harmonic behavior explicitly, but the required behavior as a voltage source behind a reactance will affect this. In the ENTSO-E report, the ability to act as a sink for harmonics is named as a key capability of a grid-forming converter. This means that the converter should provide an inductive or resistive-inductive path for harmonic current components, improving the quality of the voltage at its PCC. Here, a paradigm shift becomes visible, which already has started to come into effect e.g. in VDE-AR-N 4131: Instead of only being responsible for their own harmonic pollution as previously, converters and grid-forming converters in particular can be expected to be required in the future to increasingly act as sinks for harmonics, actively improving the grid voltage quality.

Damping. This category includes requirements regarding the damping of power oscillations and sub-synchronous resonances. Specifications of control actions involving active power (frequency and inertial response) or reactive power (voltage support) can also contain requirements regarding the damped behavior of the control action, but are not considered here. Contribution to the damping of power oscillations is required in NC RfG & HVDC but not specified further, which is complimented with requirements for damping capability for subsynchronous torsional interaction in NC HVDC. The effective range for the required power system stabilizer is further specified for generation in SE RfG. In VDE-AR-N 4131, HVDC systems are required to contribute to the damping of subsynchronous and power oscillations. While not a formal requirement in IEEE P2800, power oscillation damping and subsynchronous instability are discussed in the annex. The supply of damping power analogous to synchronous machines is a requirement for grid-forming converters in NG GC0137 and the ENTSO-E report.

Control interaction. Adverse control interaction is not a new concern, but before the focus has been on interactions in the sub-synchronous frequency range. However, the increasing amount of converter systems in the grid and the decreasing electrical distance between them has resulted in a much wider frequency range for possible interactions, up to several kHz. This is reflected by the increasing amount of detail in requirements of this category, when compared to earlier versions of the investigated documents. IEEE P2800 does not name control interactions as part of the requirements, but contains an in-detail discussion of control instability in its informative annexes. VDE-AR-N 4131 requires a study about possible interactions of the HVDC system with other grid components. The study's method is not prescribed explicitly, but measurement or simulation of grid and HVDC system input admittance as well as frequency domain and EMT studies are suggested as examples. The ENTSO-E report includes a in-depth discussion of control interactions and the same study methods as in VDE-AR-N 4131 are suggested. Two contradictory viewpoints are discussed; one deeming general specifications able to rule out harmonic interaction in any situation as too conservative and unrealistic, calling for specific case studies instead; the other prescribing a bandwidth limitation with a frequency range in which the converter has to behave as a Thévenin source behind an impedance. The latter perspective is incorporated in NG GC0137, specifying that the grid forming system must

appear passive above a frequency of 5 Hz. Even though none of the studied documents accept adverse interaction between the converter system to be connected and any other component of the grid, NG GC0137 is the only one specifying concrete requirements for how the absence of control interactions should be demonstrated. The discussions of this topic contained in VDE-AR-N 4131, IEEE P2800, NG GC0137 and the ENTSO-E report demonstrate that methods and requirements for ensuring absence of control interactions during high penetration of power electronics in the grid are still under investigation and development.

Islanding and black start capability. According to NC RfG, HVDC and VDE-AR-N 4131, the TSO can request islanding capability and ask for a quotation for black start capability. This capability is not a requirement in IEEE P2800 or NG GC0137, but in the latter grid-forming capability is mentioned as a prerequisite for converters wanting to provide black start capability. The ENTSO-E report does not mention islanding or black start capability explicitly, but places a great emphasis on the ability to create a system voltage as a core capability of grid-forming converters.

3.4 Non-technical requirements

Testing specifications. The provision of testing specification is not only crucial for ensuring compliance of constructed converter systems with the requirements, but also assists researchers and industry in developing and testing prospective design ideas beforehand in simulation and under lab conditions. NC RfG & HVDC describe compliance test in detail regarding the functions to be tested and the responsibilities of the different actors in these tests. However, no concrete testing scenarios are provided. The same applies for VDE-AR-N 4131, but in this case a supplementary document is available that provides a large number of simulation scenarios for the required capabilities [16]. IEEE P2800 contains a verification matrix listing the type of test and the responsible party for each of the requirements. However, no details are given how simulations and tests are to be conducted. In NG GC0137, simulation, testing and online monitoring are specified as compliance requirements, with three simulation scenarios provided to test compliance with specific parts of the grid-forming capability. Testing and benchmarking, as well as simulation studies for some requirements, are discussed in detail in the ENTSO-E report, but due to the general character of the document no concrete scenarios are

suggested.

Definition of grid-forming capability. As discussed in the ENTSO-E report, not all converter systems need to fulfill the same requirements, and grid-forming capability might only be required by a small share of must-run units. For this reason it is instrumental to divide converters in different classes, each coming with a specific set of requirements. The report defines classes 1, 2A, 2B, 2C and 3, where the first four correspond to the type A, B, C and D in NC RfG. Each class or type should fulfill all requirements of the ones below, with further control requirements added subsequently. Common criteria for assigning the class are power and voltage rating of the converter system. In the definition given in the ENTSO-E report, class 3 corresponds to full grid-forming capability on top of the requirements applying for class 2C, which are in essence those specified in NC RfG for type D power park modules or in NC HVDC for HVDC. In this definition, grid-forming means the ability to create system voltage, contribute to fault level, act as a sink for harmonics and unbalances, contribute to inertia, support system survival to enable under-frequency load shedding and prevent adverse control interaction. NG GC0137 likewise defines grid-forming capability as fulfillment of a number of technical requirements, but puts an even stronger emphasis on the voltage-source-behind-a-reactance character of the converter. From the other investigated documents, only IEEE P2800 contains a discussion of the concept grid-forming capability in the annex, while the others do not mention the concept. This is even the case for VDE-AR-N 4131, which contains most of the capabilities typically associated with grid-forming control (e.g. inertial response) as optional requirements.

3.5 Qualitative comparison of the requirements

As visualized in Table 1, the extent and detail of the studied documents vary widely. While the high-level, legally binding documents such as NC RfG & HVDC remain vague in a lot of aspects and rely on underlying standards and agreements for concretion, low-level norms such as VDE-AR-N 4131 and IEEE P2800 contain an extensive description of requirements with great detail. Additionally there are specifications for specific ancilliary services such as NG GC0137, which contain detailed requirements for the service they concern, but otherwise rely on the underlying grid code. Finally, the ENTSO-E report is a report reviewing and discussing challenges, practices and research and

has therefore a different character than the normative documents. It serves as an indication for trends emerging in the standards and shows very clearly in which areas development in the requirements is discussed the most.

3.6 Demand for grid-forming capabilities in existing and future standards

Table 1 shows that none of the obligatory requirements currently in effect mention grid-forming converter control or contain a definition of it. IEEE P2800 discusses grid-forming control in its informative appendices, and only NG GC0137 and the ENTSO-E report define the concept.

When discussing grid-forming converter control as an emerging concept, it is important to be aware of how the meaning of this term has shifted. In 2012, grid-forming control defined a control strategy solely determining the grid voltage in magnitude and frequency, like it is the case in micro- and island grids [17]. Converters with these properties have been in operation for more than 20 years [18]. In the current discussion however, the term grid-forming is commonly not longer used for converters serving as a slack bus, but instead for converters participating in voltage and frequency control by acting as a voltage source behind an impedance [2], [12], [13].

Even though none of specifications currently in effect requires grid-forming converter control, VDE-AR-N 4131 contains a number of optional requirements that are part of the definition of grid-forming capabilities in the ENTSO-E report and typically associated with grid-forming converters, such as inertial response, acting as a sink for harmonics and islanding capability, albeit without utilizing the label grid-forming. To a lesser extent, this also applies to IEEE P2800. With the introduction of NG GC0137, grid-forming capability has become an ancilliary service in Great Britain. Even though standards do not yet require full grid-forming capability, step by step more of the capabilities associated with grid-forming control are becoming part of them as optional or mandatory requirements.

3.7 Impact of requirements on grid-forming control topologies

It is important to underline that the compared standards in general are technology agnostic, i.e. not prescribing how the requirements have to be imple-

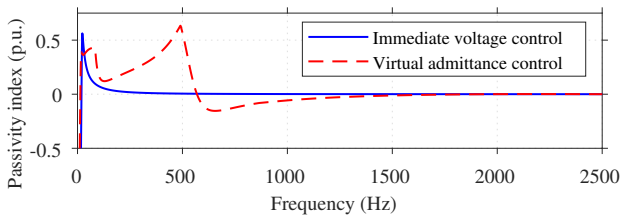

Figure 6: Passivity index over *dq*-frequency for immediate voltage control (blue) and virtual admittance control (dashed red) [19].

mented in hard- and software, but instead posing performance requirements to be fulfilled. This allows for the development of different solutions and drives a competition of ideas leading towards the most efficient implementation. However, there can still be consequences for which control strategies are suitable, as not all implementations might be able to comply with the given performance requirements. One notable exception from this is NG GC0137, which explicitly excludes the usage of a virtual impedance with reference to the high bandwidths required.

Even though not explicitly ruled out, some control topologies might not be able to fulfill specific performance requirements. One example for this is non-passive behavior caused by a current controller, as demonstrated by [19] and shown in Fig. 6. In consequence this means that the grid-forming control schemes shown in Fig. 1 (b) and (c) cannot fulfill the passivity requirements formulated in NG GC0137, and that the topology from (a) cannot rely on a current controller for FRT if this requirement is to be met. This illustrates how the grid code requirements currently in place or under discussion can be very challenging to fulfill with existing grid-forming converter control topologies.

4 Conclusions

This paper has compared and analyzed current technical requirements for grid-connected converters and future trends. It has shown qualitative differences between different standards and discussed the need for harmonization. Furthermore, the impacts of specific requirements on the control topology of converters were demonstrated. Grid-forming control is not a requirement in

any of the existing standards, but has been recently included as an ancilliary service in the UK grid code and specific capabilities associated with grid-forming control are appearing as optional requirements in other standards currently in effect as well. This demonstrates the importance of further development of grid-forming converter control as well as the need for harmonized specifications in line with both capabilities of existing control structures and the grid operator's needs.

References

[1] P. Imgart, M. Beza, M. Bongiorno, and J. R. Svensson, "An Overview of Grid-Connection Requirements for Converters and Their Impact on Grid-Forming Control," *EPE'22 ECCE Europe*, 2022.

[2] J. Matevosyan, B. Badrzadeh, T. Prevost, *et al.*, "Grid-Forming Inverters: Are They the Key for High Renewable Penetration?" *IEEE Power and Energy Magazine*, vol. 17, no. 6, pp. 89–98, Nov. 2019, ISSN: 1558-4216.

[3] R. Rosso, X. Wang, M. Liserre, X. Lu, and S. Engelken, "Grid-Forming Converters: Control Approaches, Grid-Synchronization, and Future Trends — A Review," *IEEE Open Journal of Industry Applications*, vol. 2, pp. 93–109, 2021, ISSN: 2644-1241.

[4] A. Narula, M. Bongiorno, and M. Beza, "Comparison of Grid-Forming Converter Control Strategies," in *2021 IEEE Energy Conversion Congress and Exposition (ECCE)*, Oct. 2021, pp. 361–368.

[5] M. Alt, Ö. Göksu, R. Teodorescu, P. Rodriguez, B.-B. Jensen, and L. Helle, "Overview of Recent Grid Codes for Wind Power Integration," presented at the 12th International Conference on Optimization of Electrical and Electronic Equipment, 2010, p. 9.

[6] European Commission, *COMMISSION REGULATION (EU) 2016/631 - establishing a network code on requirements for grid connection of generators*, Apr. 16, 2016.

[7] European Commission, *COMMISSION REGULATION (EU) 2016/1447 - establishing a network code on requirements for grid connection of high voltage direct current systems and direct current-connected power park modules*, Aug. 26, 2016.

[8] Energimarknadsinspektionen, *Energimarknadsinspektionens föreskrifter om fastställande av generellt tillämpliga krav för nätanslutning av generatorer*, Dec. 5, 2018.

[9] Energimarknadsinspektionen, *Energimarknadsinspektionens föreskrifter om fastställande av generellt tillämpliga krav för nätanslutning av system för högspänd likström och likströmsanslutna kraftparksmoduler.* Mar. 19, 2019.

[10] Verband der Elektrotechnik Elektronik Informationstechnik e. V., *Technical requirements for grid connection of high voltage direct current systems and direct current-connected power park modules (VDE-AR-N 4131 TAR HVDC)*, Mar. 2019.

[11] IEEE, *P2800/D6.0 (March 2021) - Draft Standard for Interconnection and Interoperability of Inverter-Based Resources Interconnecting with Associated Transmission Systems*, Mar. 2021.

[12] National Grid ESO, *Final Modification Report GC0137: Minimum Specification Required for Provision of GB Grid Forming (GBGF) Capability*, Nov. 11, 2021.

[13] ENTSO-E, "High Penetration of Power Electronic Interfaced Power Sources and the Potential Contribution of Grid Forming Converters," 2020.

[14] ENTSO-E, E. Ørum, L. Haarla, *et al.*, "Future system inertia 2," 2018.

[15] ENTSO-E, N. Modig, R. Eriksson, *et al.*, "FFR Design of Requirements – External document," Feb. 12, 2020, p. 17.

[16] Verband der Elektrotechnik Elektronik Informationstechnik e. V., *VDE FNN Guideline: Grid forming behaviour of HVDC systems and DC-connected PPMs*, 2020.

[17] J. Rocabert, A. Luna, F. Blaabjerg, and P. Rodríguez, "Control of Power Converters in AC Microgrids," *IEEE Transactions on Power Electronics*, vol. 27, no. 11, pp. 4734–4749, Nov. 2012, ISSN: 0885-8993.

[18] Hitachy Energy, "It's time to connect," 2021.

[19] M. Beza and M. Bongiorno, "Impact of converter control strategy on low- and high-frequency resonance interactions in power-electronic dominated systems," *International Journal of Electrical Power & Energy Systems*, vol. 120, p. 105 978, Sep. 2020, ISSN: 01420615.

PAPER B

Voltage-based Current Limitation Strategy to Preserve Grid-forming Properties Under Severe Grid Disturbances

Anant Narula, **Paul Imgart**, Massimo Bongiorno, Mebtu Beza, Jan R. Svensson, Jean-Philippe Hasler

Published in IEEE Open Journal of Power Electronics, vol. 4, pp. 176–188, Feb. 2023.

The layout has been revised.

Abstract

Grid-forming (GFM) converters are a promising solution to enable large scale integration of renewable energy sources into the power system. However, due to the intrinsic voltage-source behaviour of GFM converters, current limitation during large grid disturbances is challenging. This paper presents a novel limitation strategy that preserves the GFM properties of the converter and at the same time effectively limits the converter current to the desired value. Through the limitation of the converter's internal voltage, stable operation even during faults and in case of large frequency disturbances in the grid is achieved. Experimental results show the effectiveness of the proposed current limitation strategy in case of various grid disturbances.

1 Introduction

In the 2015 Paris Agreement on climate change, 189 signature states have agreed to limit global temperature rise to below 2 °C by the end of the century, and to aim for 1.5 °C [2]. A crucial part of these efforts is the decarbonization of the electrical power systems worldwide by using renewable power sources, which are commonly interfaced to the grid by power-electronic converters. Trends such as higher utilization and flexibility demands on power system assets accompanied by stronger interconnections between different systems, as well as the proliferation of drive systems and consumer electronics, further increase the share of power electronics in the grid [3]. This development has raised concerns about the stability and feasibility of converter dominated grids [4]. Grid-forming (GFM) converters emulate the voltage-source behaviour of synchronous machines [3]–[8], and are widely discussed as a solution to the challenges associated with increased penetration of converter-based resources [3], [4], [9]. A common element of most GFM converter designs is that the active power transfer is used for synchronization to the grid, replacing the phase locked-loop (PLL) typically used in the more conventional grid-following control [10].

As power-electronic converters have limited overcurrent capability, the ability to limit the current not only during normal operation but also during grid disturbances is a necessity for all converter control schemes. In contrast to grid-following control, GFM-based converters are controlled to emulate a voltage source behind an impedance; as a consequence, the current exchanged between the converter and the grid is indirectly controlled and thereby its limitation is challenging [11]. Current limitation is typically reached during large grid disturbances, such as faults or large frequency excursions, during which the grid is most vulnerable and in need of support. For this reason, the converter should retain as much of the GFM behavior as possible even during current limitation. This implies that, if at all necessary, the converter dynamic properties should be changed for the shortest time possible, typically up to a few cycles at fundamental frequency; then the converter should return into linear control mode [12], [13].

Various current-limitation strategies have been investigated and reported in the literature in the recent years; these can be summarized into four main categories [11]:

- *Immediate current limitation*: This method is commonly applied in cascaded voltage and current vector controllers [14]–[16] and in virtual admittance control [17]–[19], since both control schemes contain an explicit current reference and a current controller (CC). The approach requires a CC that is active at least during current limitation, so that the controller's current reference can be limited. As described more in detail in the following section, stability problems can occur under severe grid disturbances [20] if this method is used.
  A variation of this scheme is applied in power synchronization control [21], [22], where the CC is only activated when the current limiter saturates. Thus, the synchronization task switches from the active-power loop (APL) to a PLL, and the converter behaves as a current source instead of a voltage source during limitation.

- *Indirect current limitation by virtual impedance*: GFM converters behave as a voltage source behind an impedance, and a (virtual) increase of the impedance reduces the current exchanged with the grid. The virtual impedance based limitation approach [23]–[26] can be realized with or without a current control loop [11]. The method's main challenge is that the selection of virtual impedance parameters requires system knowledge

and assumptions regarding the worst case. System conditions differing from those assumptions can result in overcurrent or low utilization of the converter fault current contribution capability [11]. Moreover, an adaptive virtual impedance can result in system instability [27].

- *Indirect current limitation by voltage limitation*: A different approach to limit the current in a GFM converter is to vary the converter's virtual-back electromotive force (EMF) voltage instead of the impedance, which can be implemented in different ways. Some require knowledge of the grid voltage angle [28], [29], which in practice can result in mode-switching into PLL-based synchronization. In [30], only the magnitude of the voltage reference is limited. A power reference limiter is used to prevent overcurrent due to excessive load angles, but the issue of instability due to frequency disturbances remains unsolved.

- *Indirect current limitation by power limiter*: Here, the input to the active- and reactive-power control loops is limited to prevent overcurrent [18], [31], [32]. These methods rely on fault detection, which is challenging for disturbances where the voltage magnitude remains unaffected. Furthermore, for controllers with slow outer control loops, overcurrent can not be prevented reliably during transients [11].

In addition to the challenges described above, it is important to highlight that the majority of the studies available in the literature focus on current limitation and transient stability for GFM converters in case of voltage dips [18], [33]–[40]; on the other hand, large frequency disturbances can also be a significant source of instability, especially when high-inertia support is demanded from the converter [41]. The referred methods for current limitation do not address the impact of limitation on robustness against frequency disturbances.

This paper presents a novel current limitation strategy for GFM converters that ensures accurate current limitation during symmetric and asymmetric faults as well as during frequency disturbances and phase jumps; through adequate limitation of the reference active power and magnitude of the virtual-back EMF reference, the proposed strategy does not require any system knowledge and retains the converter's GFM properties even during current limitation.

The paper is structured as follows: Section II is a theoretical study of the GFM converter transient stability problem. In Section III and IV, the

basic converter control and the proposed limitation strategy are presented, respectively. Section V contains the experimental verification of the proposed strategy, and the conclusions are put forward in Section VI.

2 GFM Converter Angle Stability Problem

The GFM converter angle stability problem is analyzed by using the system in Fig. 1. It consists of a GFM converter with a virtual-back EMF $\underline{V}_{\mathrm{EMF}}$ and a virtual impedance R_{v}, L_{v}. The virtual impedance includes the converter filter impedance and the virtual part R_{v1}, L_{v1}. The R-L filter connects the converter terminals at the point of common coupling (PCC) to the grid, which is represented by the Thévenin equivalent $\underline{V}_{\mathrm{s}}$ and $\underline{Z}_{\mathrm{g}}$. Neglecting the system losses, the steady state per-unit converter current in the synchronous reference frame aligned with the converter's virtual-back EMF voltage is

$$\underline{I}_{\mathrm{c}} = \frac{\underline{V}_{\mathrm{EMF}} - \underline{V}_{\mathrm{s}}}{\mathrm{j}X} = \frac{V_{\mathrm{s}} \sin\delta + \mathrm{j}(V_{\mathrm{s}} \cos\delta - V_{\mathrm{EMF}})}{X}, \tag{B.1}$$

where $\delta = \angle\underline{V}_{\mathrm{EMF}} - \angle\underline{V}_{\mathrm{s}}$, and X is the total reactance between the two sources. The active-power transfer from the converter to the grid is defined as

$$P = \mathfrak{Re}\{\underline{V}_{\mathrm{EMF}}\ \mathrm{conj}\{\underline{I}_{\mathrm{c}}\}\} = \frac{V_{\mathrm{s}} V_{\mathrm{EMF}}}{X} \sin\delta, \tag{B.2}$$

and shown in blue in Fig. 2 for an example system.

The current exchanged with the grid needs to be limited to prevent damage to the converter hardware due to overcurrent. Following the immediate current limitation approach introduced in the previous section, a CC is used and its reference is limited with a current-magnitude limiter [11] (also addressed as circular-current limiter [18]). Applying this to limit the current reference $\underline{I}^*$ to the maximum allowed converter current $I_{\max}$ yields

$$\underline{I}^*_{\mathrm{lim}} = \underline{I}^* \frac{I_{\max}}{I^*} \qquad \forall\ I^* > I_{\max} \tag{B.3}$$

as the limited converter current reference. This current limitation is equivalent to a variation of the phasor $\underline{V}_{\mathrm{EMF}}$, defined as $\underline{V}'_{\mathrm{EMF}}$ in the phasor diagram in Fig. 3. The figure shows that the current limitation results in a reduction of the load angle δ when compared with the angle of the unlimited output of

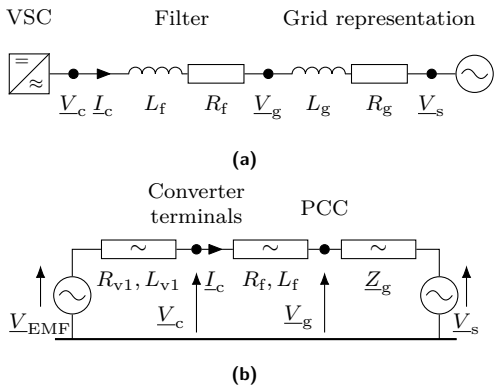

Figure 1: (a): Single-line diagram of the investigated system. (b): Equivalent circuit representation of a GFM converter control approach with virtual-back EMF and virtual impedance.

the APL, denoted as δ_{APL}. Even though the load angle is manipulated by the current limitation, the APL's output angle δ_{APL} still has an impact on the exchanged active power by determining the angle of the current references $\underline{I}^*$ and consequently $\underline{I}^*_{\mathrm{lim}}$. Using (B.1)-(B.3), the relation between the current-limited active power P_{lim} and the APL output angle δ_{APL} can be determined by

$$\begin{aligned} P_{\mathrm{lim}} &= \mathfrak{Re}\{\underline{V}_{\mathrm{s}}\ \mathrm{conj}\{\underline{I}^*_{\mathrm{lim}}\}\} \\ &= \frac{V_{\mathrm{s}} V_{\mathrm{EMF}} I_{\mathrm{max}} \sin\delta_{\mathrm{APL}}}{\sqrt{V_{\mathrm{s}}^2 + V_{\mathrm{EMF}}^2 - 2V_{\mathrm{s}}V_{\mathrm{EMF}}\cos\delta_{\mathrm{APL}}}}, \qquad I^* > I_{\mathrm{max}} \end{aligned} \tag{B.4}$$

Figure 2 illustrates the current-limited P-δ_{APL} relationship following from (B.4) in red. The current reaches its limit at operating point B, and in contrary to the unlimited case presented in blue increasing δ_{APL} further results in a decreasing power transfer.

Based on this analysis, the two main sources for GFM converter angle instability [41] can be studied: firstly, an active power reference that during a fault or in post-fault steady-state is too large for the grid conditions (i.e. grid voltage magnitude and grid strength), and secondly the inability of the APL to follow the grid voltage angle in case of a frequency disturbance or phase-angle jump. The former is studied widely in the literature [18], [33],

[35]–[38], [40], while the latter is rarely regarded in existing publications [41]. Both instability mechanisms are summarized in this section.

2.1 Voltage-Dip Induced Converter Angle Instability

The first of the two angle instability mechanisms is caused by a voltage dip at the PCC. Equations (B.2) and (B.4) demonstrate that the active-power transfer between converter and grid is proportional to the product of V_s and V_EMF. Consequently, a voltage dip will result in a reduced active power transfer capability, no matter how the converter back EMF magnitude is controlled in response to the voltage dip (compare case 2 and 3 in Fig. 2). As described in [27], instability can under this conditions occur due to violated equal-area criterion, which mainly affects GFM converters providing inertial support, or due to lack of a stable post-fault operating point. This type of instability has been studied widely in literature and several solutions have been proposed [38]. The most popular solutions are scaling of the power references proportional to the voltage magnitude [18], control-mode switching (e.g. deactivation of inertia [42]), inclusion of additional control terms [43] and moving to a grid-following control mode [22]. Of these approaches, voltage-proportional power reference scaling has the advantage of retaining as much of the GFM capabilities as possible, while at the same time aiding in current-limitation. In contrast to approaches modifying the control structure, it does not require any fault detection [38].

2.2 Frequency-Disturbance Induced Converter Angle Instability

The second angle instability mechanism is caused by severe frequency disturbances or phase angle jumps in the grid, resulting in the inability of the APL to follow the grid voltage angle and moving the operating point to the unstable part in Fig. 2. This phenomenon is discussed more in-depth in [41]. As the APL in a GFM converter does not only provide power reference tracking but also synchronization, a power control error is required to follow a change in the grid frequency by letting the APL adapt its internal frequency. For instance, a decline in grid frequency causes the load angle δ to increase until the additional decelerating power $P_\mathrm{d} = -2H\frac{\mathrm{d}\omega}{\mathrm{d}t}$ is reached. During current limitation the decelerating power might not be large enough to keep the con-

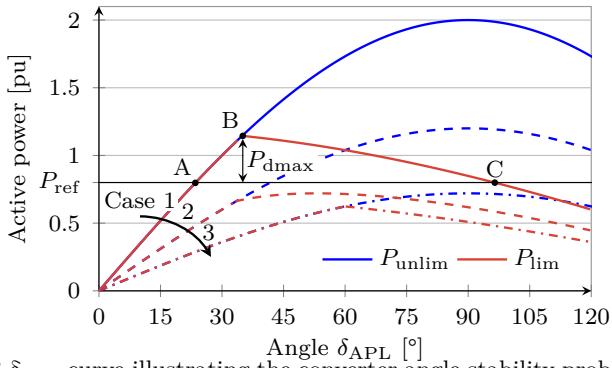

Figure 2: P-δ_{APL} curve illustrating the converter angle stability problem for a current limit of 1.2 pu. A: pre-disturbance operating point; B: current limit reached; C: transient stability limit; P_{dmax}: maximum decelerating power; all outlined for case 1: $V_{\text{EMF}} = V_{\text{s}} = 1$ pu. Case 2: $V_{\text{EMF}} = 1$ pu & $V_{\text{s}} = 0.6$pu; case 3: $V_{\text{EMF}} = V_{\text{s}} = 0.6$ pu.

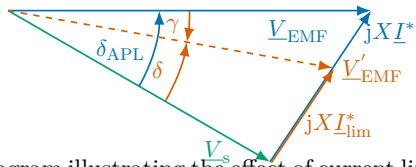

Figure 3: Phasor diagram illustrating the effect of current limitation on the virtual-back EMF. Unlimited in blue, limited in red.

verter's internal frequency synchronized with the grid frequency, which would lead to the load angle continuing to increase. If the unstable equilibrium point C is passed synchronism is lost, equivalent to synchronous machine first swing instability.

Limitation of the outer loop references as introduced in the previous instability mechanism cannot prevent loss of synchronism in this case. This is because the active power exceeding the current-limited maximum is not caused by a change in reference, but by the inability of the slow APL to reject the grid disturbance. This slowness is desired to provide inertia to the grid, but causes instability when the converter current limits are reached. Not only the GFM control structure used for illustration in this section, but all GFM converters with non-zero inertia that rely on the APL for synchronization and provision of inertia are vulnerable to this type of instability. As the APL

angle output is manipulated to guarantee current limitation, the synchronization signal is lost. The risk for this type of instability is increased by large inertia, high rate of change of frequency (RoCoF) and operating points close to the maximum power transfer, due to more decelerating power being needed or less current reserve being available for it, respectively.

While these instability mechanisms are studied here for a GFM converter with circular-current limitation, the same principles apply for GFM converters relying on a virtual impedance for current limitation. This can be understood from (B.2), showing that an increase in the reactance between the virtual-back EMF and the grid voltage will reduce the active-power transfer for any given load angle, which results in similar dynamics for both instability types.

3 Basic GFM Converter Control

The GFM control adopted in this work is based on the virtual admittance-based approach from [19], with the improvements to the APL described in [41]. The controller implementation is illustrated in Fig. 4 and its main blocks are described in the following.

3.1 Active Power Loop (APL)

For the investigated GFM control, the APL provides both active-power reference tracking and grid synchronization. The implemented APL is depicted in Fig. 5 and consists of a PI regulator for accurate reference tracking and an active-damping term R_a to improve the controller's dynamic performance. Neglecting the system's losses, the maximum transmittable active power is given by:

$$P_{\max} = \frac{V_{\mathrm{EMF}} V_{\mathrm{g}}}{X_{\mathrm{v}}},$$

where X_{v} is sum of the converter's virtual reactance X_{v1} and filter reactance X_{f}. Using the controller active damping R_{a} and the proportional and integral gains K_{p} and K_{i}, the closed-loop transfer function for the APL can be written as

$$G_{\mathrm{PC}}(s) = \frac{K_{\mathrm{p}} s + K_{\mathrm{i}}}{P_{\max}^{-1} s^2 + (K_{\mathrm{p}} + R_{\mathrm{a}}) s + K_{\mathrm{i}}}, \tag{B.5}$$

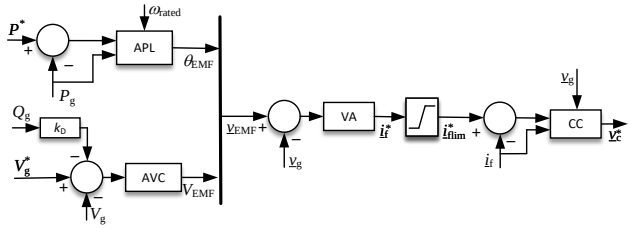

Figure 4: Block diagram of investigated GFM control structure.

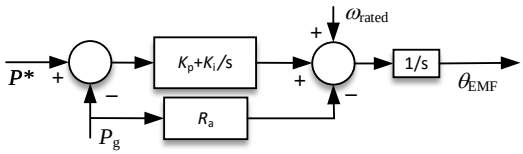

Figure 5: Block diagram of implemented active power loop (APL).

assuming that the CC is sufficiently fast to be treated as ideal. The APL control parameters are tuned using loop-shaping approach as described in [41] to yield

$$G_{\mathrm{PC}}(s) = \frac{\alpha_{\mathrm{PC}}}{s + \alpha_{\mathrm{PC}}} \tag{B.6}$$

with

$$K_{\mathrm{p}} = \frac{\alpha_{\mathrm{PC}}}{P_{\max}}, \quad K_{\mathrm{i}} = \frac{\alpha_{\mathrm{PC}}^2}{P_{\max}}, \quad \text{and} \quad R_{\mathrm{a}} = K_{\mathrm{p}},$$

where α_{PC} denotes the desired APL closed-loop bandwidth.

3.2 AC Voltage Controller (AVC)

The magnitude of the virtual-back EMF is determined by the AC voltage controller (AVC), which controls the voltage at the PCC. To allow operation in strong grids and alongside other converters, an integral controller with a reactive droop is used. Denoting with V_{N} the nominal grid voltage and with k_{D} the droop constant, the control law for the AVC is defined by [19]:

$$V_{\mathrm{EMF}} = V_{\mathrm{N}} + \frac{K_{\mathrm{iv}}}{s}(V_{\mathrm{g}}^* - V_{\mathrm{g}} - k_{\mathrm{D}} Q_{\mathrm{g}}), \tag{B.7}$$

where, for a desired closed-loop bandwidth α_{VC}, $K_{\mathrm{iv}} = \alpha_{\mathrm{VC}} \frac{X_{\mathrm{v}}+X_{\mathrm{g}}}{X_{\mathrm{g}}}$. The value of the grid reactance, X_{g}, used for calculating the integral gain of the AVC is typically set for the strongest grid strength provided by the system operator, to ensure an acceptable performance even with varying grid strengths.

3.3 Virtual Admittance (VA)

The virtual-back EMF voltage vector determined by the outer loops is translated into a current reference input for the CC by a virtual admittance (VA)[1]. The VA generates the reference currents by providing filtering and damping action (through L_{v} and R_{v}, respectively) on the difference between the virtual-back EMF and the grid voltage. It also reduces the impact of variations in grid strength on the converter dynamic performance by reducing the share of the grid impedance in the total impedance [44]. As proposed in [17], the virtual reactance is chosen in the range of a typical synchronous machine transient reactance. Due to this relatively large virtual reactance, changes in the virtual-back EMF result in a DC current component. The virtual resistance is chosen to provide a small time constant for the decay of this current offset. The current reference output of the VA block is:

$$\underline{i}_{\mathrm{f}}^{*} = \frac{\underline{v}_{\mathrm{EMF}} - \underline{v}_{\mathrm{g}}}{sL_{\mathrm{v}} + \mathrm{j}\omega_{\mathrm{N}} L_{\mathrm{v}} + R_{\mathrm{v}}}. \tag{B.8}$$

3.4 Current Controller (CC)

The current references generated by the VA are limited to the maximum converter current as in (B.3) and sent to the CC to calculate the reference voltages for the converter's modulation stage. The implemented CC has a classical structure and is based on a PI regulator with cross-coupling cancellation and voltage feedforward that is low-pass filtered with a closed-loop bandwidth of α_{FF} as:

$$\underline{v}_{\mathrm{c}}^{*} = \frac{\alpha_{\mathrm{FF}}}{s+\alpha_{\mathrm{FF}}} \underline{v}_{\mathrm{g}} + \mathrm{j}\omega_{\mathrm{N}} L_{\mathrm{f}} \underline{i}_{\mathrm{f}} + (K_{\mathrm{pc}} + \frac{K_{\mathrm{ic}}}{s})(\underline{i}_{\mathrm{f}}^{*} - \underline{i}_{\mathrm{f}}). \tag{B.9}$$

The controller gains are tuned to the selected controller bandwidth α_{CC} as [45]

$$K_{\mathrm{pc}} = \alpha_{\mathrm{CC}} L_{\mathrm{f}}, \quad K_{\mathrm{ic}} = \alpha_{\mathrm{CC}} R_{\mathrm{f}}. \tag{B.10}$$

[1] The VA corresponds to the inverse of the virtual impedance shown in Fig. 1.

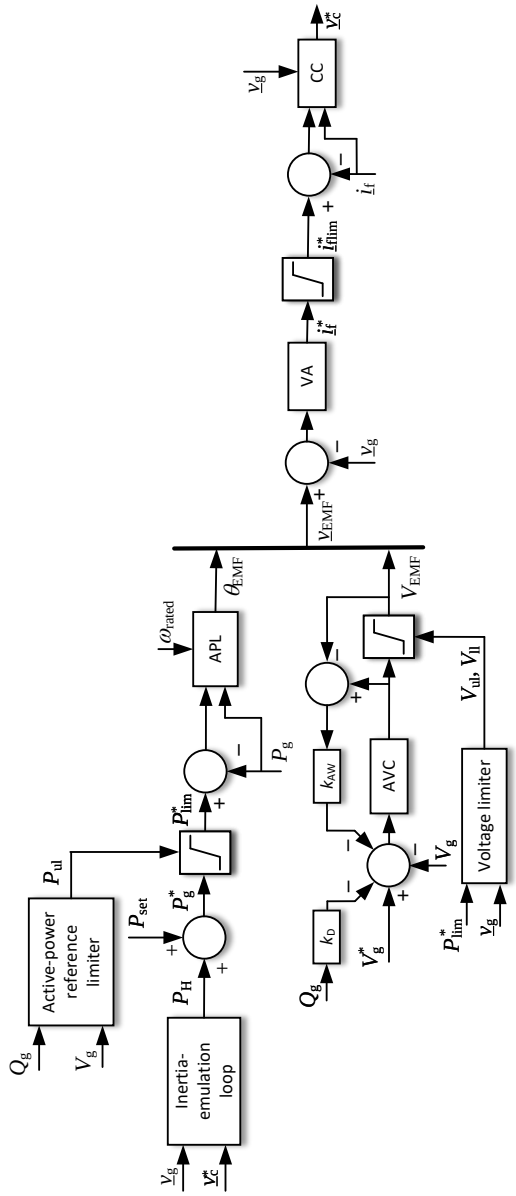

Figure 6: Block diagram of proposed control structure for GFM converters.

4 Proposed Methodology to Limit Converter Current

From Section 2, it is understood that limitation of the current reference for the CC (henceforth referred to as hard-current limiter) might in GFM converters result in a loss of synchronization with the AC grid. Furthermore, the use of the hard-current limiter introduces non-linearities in the control system and modifies the dynamic properties of the converter (by hiding the impact of the voltage controller and the virtual admittance) while activated, which is not desirable as discussed earlier [12], [13]. This section presents a novel strategy that allows to keep the converter current within its permissible value without relying on the hard-current limiter and alteration of the GFM properties.

In a grid-following converter, the use of a hard-current limiter is effective because such converters are modeled as a current source. Following the same philosophy for GFM converters, which are modeled as a voltage source instead, current limitation can be achieved by dynamically limiting the generated virtual-back EMF, $\underline{v}_{\mathrm{EMF}}$, so that the resulting current reference is within the limits. This is realized through the GFM control structure depicted in Fig. 6. It is of importance to consider that, unlike the magnitude, limiting the phase of the voltage vector $\underline{v}_{\mathrm{EMF}}$ is challenging. This is because in the absence of a PLL in GFM converters, there is no direct information about the load angle; and hence, the active-power flow from the converter dictates the phase of the emulated voltage source. Therefore, one obvious solution is to include a PLL in the design of the APL to calculate the converter's load angle. However, this can have a negative impact on the stability of the converter in weak grids, and restrict the converter's GFM properties [46]. Another alternative to limit the resulting phase of the converter at all times without the aforementioned restrictions is to limit the active-power reference. However, as discussed in Section 2.2.2, this solution is not effective in GFM converter systems emulating inertia, owing to their slow APL. To overcome this issue, the cascaded active-power controller described in the following section is used. The calculation of the limits for the active power and voltage magnitude references is described in the subsequent sections.

4.1 Cascaded Active-Power Controller

The cascaded active-power controller consists of an inertia-emulation loop (IEL) in cascade with a fast APL, as first reported in [41]. The IEL is illustrated in Fig. 7 and is based on the structure of a PLL. It is used to calculate the inertial power, P_{H}, to be injected (or absorbed) by the converter in case of frequency disturbances. As from the figure and denoting with θ_{g} the angle of the PCC voltage $\underline{v}_{\mathrm{g}}$, the inertial power output from the IEL is given by

$$P_{\mathrm{H}} = -\frac{V_{\mathrm{g}} V_{\mathrm{c}}}{X_{\mathrm{f}}} \sin(\theta_{\mathrm{g}} - \theta_{\mathrm{IEL}}), \tag{B.11}$$

where $\theta_{\mathrm{g}} = \theta_{\mathrm{IEL}}$ in steady state. In the case of a frequency variation, the IEL angle will track the grid angle with a speed of response determined by the desired amount of emulated inertia H. For this, the IEL's proportional ($K_{\mathrm{p,IEL}}$) and integral ($K_{\mathrm{i,IEL}}$) gains are selected as [41]

$$K_{\mathrm{p,IEL}} = \zeta \sqrt{\frac{2\omega_{\mathrm{N}} X_{\mathrm{f}}}{H V_{\mathrm{cr}} V_{\mathrm{gr}}}},\ K_{\mathrm{i,IEL}} = \frac{\omega_{\mathrm{N}}}{2H}, \tag{B.12}$$

where ζ denotes the damping ratio of the second-order response, while V_{cr} and V_{gr} represent the rated converter and PCC voltage, respectively. Note that in the implementation of the IEL, the magnitude of the reference voltage vector $\underline{v}_{\mathrm{c}}^{*}$ output from the CC is used instead of its measured signal V_{c}. The inertial power P_{H} is then added onto the active power set-point of the converter, P_{set}, to form the reference power $P_{\mathrm{g}}^{\star}$ for the APL, which can be effectively limited. The PI-based APL then tracks the power reference, $P_{\mathrm{lim}}^{\star}$, and synchronizes the converter with the grid. Providing the inertia through the active-power reference allows a higher closed-loop bandwidth for the APL, thus making synchronization and reference tracking fast. Decoupling the synchronization task of the APL from the inertia provision gives the flexibility to limit and achieve a fast control over the active-power injection from the converter, and ultimately the resulting phase of the virtual back-EMF. The magnitude of the virtual back-EMF, V_{EMF}, can then be limited based on the available PCC voltage and estimated power flow as described in Section 4.4.3. In this way it is possible to limit the generated current reference vector without triggering the hard-current limiter.

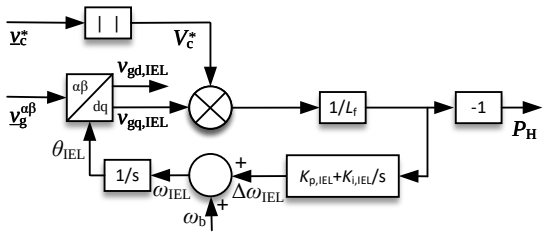

Figure 7: Block diagram of inertia emulation loop (IEL).

4.2 Calculation of Active-Power Limits

As stated earlier, the phase of the virtual-back EMF is a resultant of the active-power flow from the converter. Therefore, setting the limits for the active-power reference would limit the resulting phase of the virtual-back EMF. During limitation, prioritizing active or reactive-power injection from the converter depends upon the grid-code requirements. Here, reactive-power injection is prioritized [2]; accordingly, the upper limit for the active-power reference, P_{ul}, is calculated as

$$P_{\mathrm{ul}} = \sqrt{S_{\mathrm{avail}}^2 - Q_{\mathrm{g}}^2}, \tag{B.13}$$

where S_{avail} denotes the available apparent power of the converter, and Q_{g} is the reactive power injected from the converter (or, eventually, the reactive power demanded by the grid codes). At any time instant, depending upon the PCC-voltage magnitude, V_{g}, the available apparent power of the converter to keep the current within its rated value is calculated as $S_{\mathrm{avail}} = \frac{S_{\mathrm{N}} V_{\mathrm{g}}}{V_{\mathrm{N}}}$, where S_{N} and V_{N} denote the rated power and voltage of the converter, respectively. If $Q_{\mathrm{g}} \geq S_{\mathrm{avail}}$ (this condition prevails during a voltage dip for instance, when the converter current momentarily rises above its rated value), the upper limit for the active-power reference is set to zero.

4.3 Calculation of Voltage-Magnitude Limits

The limits for the magnitude of virtual-back EMF can be calculated by using the estimated power flow. Considering the sign convention for the current

[2] Prioritization of active and reactive power can be modified depending upon the system requirements.

in Fig. 1, a decrease in the PCC voltage will result in a positive reactive-power injection into the grid. Hence, the upper limit for the magnitude of the virtual-back EMF, V_{ul}, is calculated as

$$V_{\mathrm{ul}} = \left| \underline{v}_{\mathrm{g}} + \frac{P^{\star}_{\mathrm{lim}} - jQ_{\mathrm{avail}}}{\mathrm{conj}(\underline{v}_{\mathrm{g}})} (R_{\mathrm{v}} + jX_{\mathrm{v}}) \right|; \quad \text{with } Q_{\mathrm{avail}} = \sqrt{S^2_{\mathrm{avail}} - P^{\star 2}_{\mathrm{lim}}}. \tag{B.14}$$

Similarly, if a voltage swell at the PCC is to be considered, the lower limit for the virtual-back EMF, V_{ll}, can be calculated accordingly, i.e.,

$$V_{\mathrm{ll}} = \left| \underline{v}_{\mathrm{g}} + \frac{P^{\star}_{\mathrm{lim}} + jQ_{\mathrm{avail}}}{\mathrm{conj}(\underline{v}_{\mathrm{g}})} (R_{\mathrm{v}} + jX_{\mathrm{v}}) \right|. \tag{B.15}$$

It is worth mentioning here that during limitation, $P^{\star}_{\mathrm{lim}}$ will be equal to P_{ul} as defined in (B.13). Thus, reactive-power injection is prioritized here. Furthermore, as $P_{\mathrm{g}} = P^{\star}_{\mathrm{lim}}$ during limitation, the angle of the voltage phasors $\underline{V}_{\mathrm{ul}}$ and $\underline{V}_{\mathrm{ll}}$ will be equal to zero in the controller's dq frame.

In order to prevent the accumulation of the voltage error during limitation, an anti-windup loop with the gain k_{AW} is implemented in the AVC as shown in Fig. 6.

5 Experimental Validation of Proposed Current-Limitation Strategy

In order to validate the effectiveness of the proposed current-limitation strategy, experimental verification is made and discussed for various grid scenarios in this section. A photo of the laboratory setup is depicted in Fig. 8 and it resembles the system shown in Fig. 1. The grid is emulated using a REGATRON's four quadrant programmable AC power source. Furthermore, the GFM converter system used here comprises of a 2-level VSC supplied by an ideal DC voltage source. It is controlled using dSPACE dS1006, and is connected at the PCC through a phase reactor of resistance R_{f} and inductance L_{f}. Various system and control parameters used for the grid-interfaced converter system are shown in Table I. The closed-loop bandwidths of the APL and AVC are chosen to comply with the recommendations for GFM control action defined in [47].

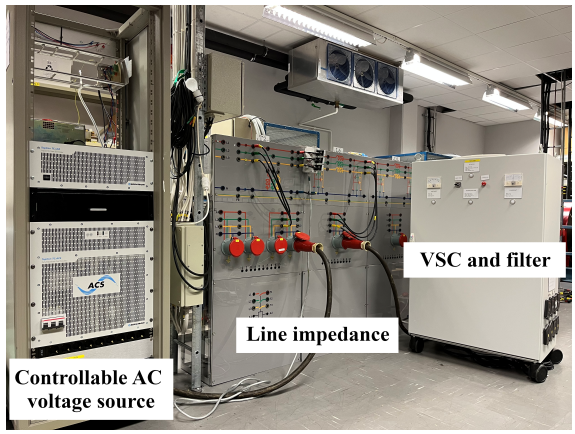

Figure 8: Photo of laboratory setup.

5.1 Dynamic Performance in Case of a RoCoF Event

In order to investigate the dynamic performance of the GFM converter system during a RoCoF event, the frequency, f_s, of the voltage source behind grid impedance is varied from 50.0 Hz to 48.0 Hz at a rate of -2.0 Hz/s between 0.5 s and 1.5 s. The active power set-point of the converter is selected as 0.8 pu in this case. The blue curves in Fig. 9 show the dynamic response of the converter system emulating an inertia of 5.0 s using the proposed control structure and current-limitation strategy. For comparison, the dynamic performance of a converter system emulating the same amount of inertia within the APL and deploying circular-current limitation (henceforth referred as *Integrated GFM*

Table 1: System and control parameters

System parameters		Control parameters	
S_N	1 kVA	L_{v1}	0.35 pu
V_N	100 V	R_{v1}	0.235 pu
ω_N	314.16 rad/s	α_{PC}	2π 5 rad/s
L_f	0.15 pu	ζ	0.707
R_f	0.015 pu	α_{CC}	2π 500 rad/s
SCR	3	α_{VC}	2π 1 rad/s

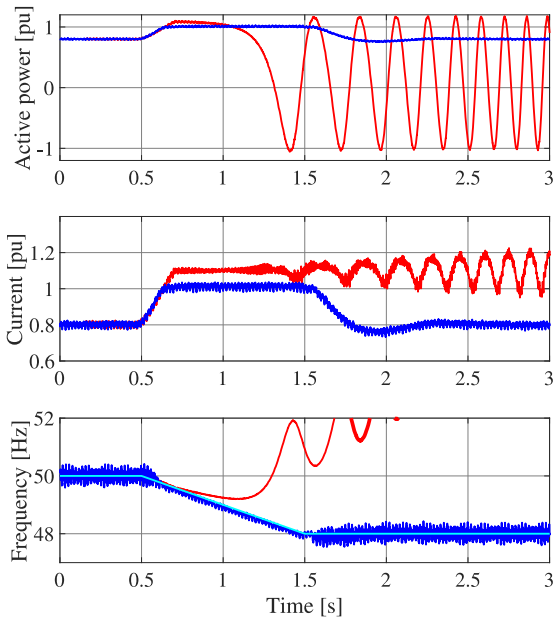

Figure 9: Dynamic response of GFM converter to a frequency disturbance with proposed control structure (blue curves), and Integrated GFM control (red curves). Top: measured active power; middle: measured converter-current magnitude; bottom: measured PCC frequency (light-blue curve depicts the frequency disturbance imposed by the controllable AC power source).

control[3]) is shown with red curves in Fig. 9, where the upper-limit for the hard-current limiter is set to 1.1 pu.

It can be seen from the figure that by using the proposed control structure and current-limitation strategy, it is possible to limit the converter current close to its rated value without triggering the hard-current limiter. Additionally, the internal frequency of the converter closely follows the declining grid frequency (light-blue curve), i.e., the converter keeps its synchronism with the grid. Furthermore, the active-power flow from the converter is limited close

[3]The integrated GFM control used here for comparison corresponds to the structure displayed in Fig. 4, but provides inertia through the APL by proper selection of a lower APL bandwidth resulting in the desired inertia.

to 1.0 pu which otherwise would have reached 1.2 pu without limitation (corresponding to set-point power of 0.8 pu and inertial power of 0.4 pu). On the other hand, due to the presence of inertia within the APL in the second case, the converter loses it synchronism when the maximum-current limit of the converter is reached.

5.2 Dynamic Performance in Case of a Balanced Three-Phase Voltage Dip

In order to investigate the dynamic performance of the converter system during a balanced three-phase voltage dip, starting at 0.5 s, the magnitude of the source voltage, V_s, is reduced by 50% for a duration of 1.0 s. The set point for the active power is zero and inertia provision from the converter is minimized by deactivating the IEL for this case. Figure 10 shows the dynamic response of the GFM converter system against a balanced three-phase voltage dip.

It can be seen from the figure that following the voltage dip, the converter current is immediately limited close to its rated value without triggering the hard-current limiter, thus, without changing the converter's dynamics. Additionally, maximum reactive power (red curve) is injected from the converter instantaneously to support the system. It can also be observed that after the fault clearance, the active and reactive powers as well as the converter current immediately return to their initial operating points.

5.3 Dynamic Performance in Case of a Balanced Three-Phase Voltage Dip Accompanied by a RoCoF Event

In order to investigate the dynamic performance of the converter during a balanced three-phase voltage dip accompanied by a RoCoF event, V_s is reduced as in the previous case. At the same time, f_s is varied from 50.0 Hz to 48.0 Hz at a rate of -2.0 Hz/s. Such a severe event, comprising of a combination of large voltage and frequency disturbance, might happen in extreme system conditions like the system event reported in [48] or during the 2021 European system split between France and Spain [49], and is here used to test the capabilities and robustness of the suggested converter control. Figure 11 shows the dynamic response of the GFM converter system emulating an inertia of 5.0 s for this case.

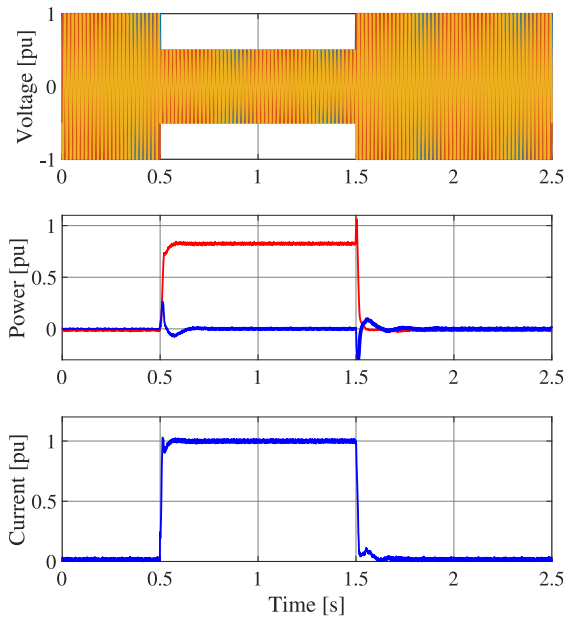

Figure 10: Dynamic response of GFM converter to a balanced three-phase voltage dip. Top: three-phase source voltage; middle: measured active (blue curve) and reactive power (red curve); bottom: measured converter-current magnitude.

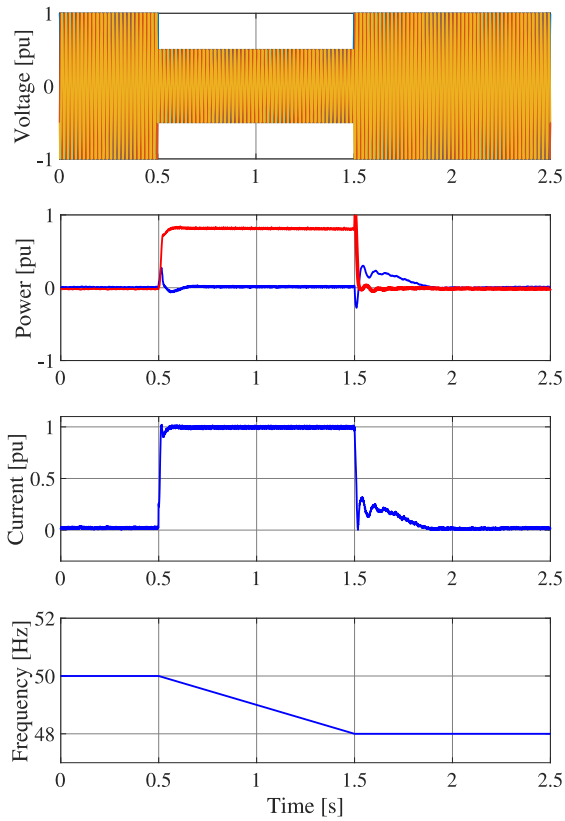

Figure 11: Dynamic response of GFM converter to a balanced three-phase voltage dip accompanied by a frequency disturbance. Top: three-phase source voltage; top-middle: measured active (blue curve) and reactive power (red curve); bottom-middle: measured converter-current magnitude; bottom: frequency disturbance imposed by the controllable AC power source.

It can be observed from the figure that following the specified event, the converter current is immediately limited close to its rated value without triggering the hard-current limiter. Additionally, the converter injects maximum reactive power (red curve) instantaneously to support the system. Since the converter current reaches its rated value, there is no room for the active-power injection, and hence the active-power flow from the converter stays at zero. This results from the choice of prioritizing reactive power injection over active power made in (B.13). Since it's a matter of choice only, it is possible to reduce the reactive power injection if an inertial support is desired from the converter during limitation. It can also be observed that after the fault is cleared, the reactive power immediately returns to its initial operating point. Furthermore, the inertial response of the converter becomes evident from a decrease in the inertial power of the converter from the moment the frequency transient ends.

6 Controller Modifications for Unbalanced Grid Conditions

According to the latest reports from the European Network of Transmission System Operators for Electricity (ENTSO-e), the GFM converters should act as a sink for unbalances in the grid voltage [3]. This means that in case of unbalanced grid conditions (for example, during unbalanced faults), the converter must offer an inductive behavior towards the grid. As an example, the recent VDE-AR-N 4120 Technical Connection Rules establishes requirements for the negative-sequence current injection from the grid-connected converter systems [50]. In particular, for an unbalanced voltage dip the converter should absorb a negative-sequence current proportional to the negative-sequence grid voltage, following the relation

$$I_{\mathrm{f}}^{-} = k_{\mathrm{n}} V_{\mathrm{g}}^{-},\ 2 \leq k_{\mathrm{n}} \leq 6 \tag{B.16}$$

where the gain k_{n} specifies the relation between the magnitude of the negative-sequence component in the grid voltage, V_{g}^{-}, and the corresponding negative-sequence converter current I_{f}^{-}. During current limitation, prioritizing positive- or negative-sequence current depends upon the system requirements. This implies that we should be able to effectively control and limit both the positive-

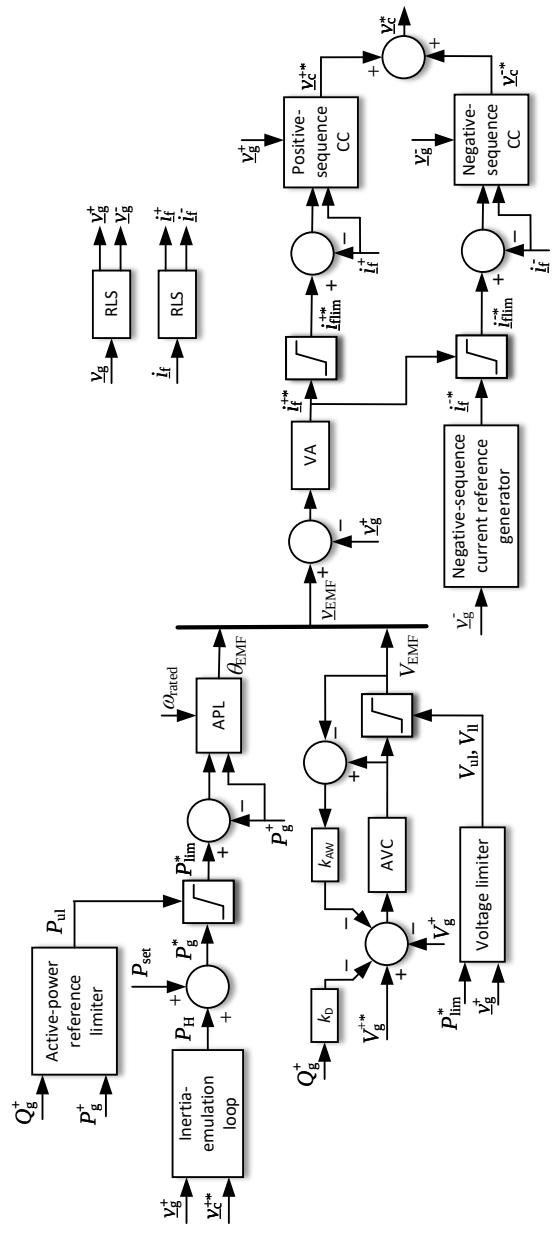

Figure 12: Block diagram of proposed control structure for GFM converters with adaptations for unbalanced grid conditions.

and negative-sequence currents individually. Figure 12 shows the modifications made to the controller for this purpose, where a negative-sequence CC has been added to the original control structure. It generates a negative-sequence reference voltage for the converter, $\underline{v}_{\mathrm{c}}^{-\star}$, which is added to the positive-sequence reference voltage, $\underline{v}_{\mathrm{c}}^{+\star}$, generated by the original control structure.

During unbalanced grid conditions, the magnitude of the voltage and current vectors, as well as the instantaneous active and reactive powers will present oscillations at twice the fundamental frequency. This will lead to double-frequency oscillations in both the internal frequency of the converter and magnitude of the virtual-back EMF. To prevent this, positive-sequence components of the measured voltages and currents are used as inputs in the APL and AVC, while the negative-sequence components for the negative-sequence CC. In this paper, Recursive Least Square (RLS) algorithm based method is used to separate the voltage and current vectors into their respective sequence components [51]. To adapt to the changes in the grid frequency, the internal frequency of the converter is used as an input to the RLS-based sequence separator.

In accordance with the relation between negative-sequence voltage and current provided in (B.16), the converter should exhibit negative-sequence reactance, $X_{\mathrm{n}} = k_{\mathrm{n}}^{-1}$. Therefore, the reference for the negative-sequence CC, $\underline{i}_{\mathrm{f}}^{-\star}$, is calculated as

$$\underline{i}_{\mathrm{f}}^{-\star} = \frac{\underline{v}_{\mathrm{g}}^{-}}{jX_{\mathrm{n}}}, \tag{B.17}$$

where $\underline{v}_{\mathrm{g}}^{-}$ represents the negative-sequence component of the PCC-voltage vector. The factor, k_{n}, is selected here equal to 2. Circular limitation is used here for the negative-sequence current in order to keep the total converter current within its rated value, I_{N}. Giving positive-sequence current priority for active and reactive-power support, the upper and lower limits for the magnitude of the negative-sequence current reference, denoted by $I_{\mathrm{f,ul}}^{-}$ and $I_{\mathrm{f,ll}}^{-}$, respectively, are calculated as

$$\begin{aligned} I_{\mathrm{f,ul}}^{-} &= I_{\mathrm{N}} - I_{\mathrm{f}}^{+\star}, \\ I_{\mathrm{f,ll}}^{-} &= -I_{\mathrm{f,ul}}^{-}. \end{aligned} \tag{B.18}$$

$I_{\mathrm{f}}^{+\star}$ denotes the magnitude of the positive-sequence current reference and is

calculated as $I_{\mathrm{f}}^{+\star} = \sqrt{(i_{\mathrm{f,d}}^{+\star})^2 + (i_{\mathrm{f,q}}^{+\star})^2}$. During limitation, the magnitude of the negative-sequence current reference, $I_{\mathrm{f}}^{-\star}$, is saturated at its upper or lower limit according to (B.18). On the other hand, its phase angle, i.e., $\angle \underline{i}_{\mathrm{f}}^{-\star}$ is kept unchanged and is determined using (B.17).

6.1 Experimental Validation Under Unbalanced Grid Conditions

The following test cases validate the effectiveness of the proposed limitation strategy during unbalanced grid conditions. The set point for the active-power flow from the converter is zero for the case studies presented here.

Dynamic Performance in Case of a Small Unbalance

In order to investigate the dynamic performance of the converter during a small unbalance, the magnitude of the source voltage in phase B and C is reduced by 30% for a duration of 1.0 s. Figure 13 shows the dynamic response of converter system for this case.

It can be observed from the figure that following the specified disturbance, the converter injects reactive power (red curve) to boost the positive-sequence voltage at the PCC. Since $k_{\mathrm{n}} = 2$, the converter exhibits a negative-sequence reactance of 0.5 pu (calculated by dividing the measured negative-sequence voltage with resulting negative-sequence current during unbalance), hence allowing the negative-sequence current to flow. Furthermore, the positive sign of negative-sequence reactance confirms the inductive behavior of the converter to counter unbalance in the PCC voltage.

Dynamic Performance in Case of a Severe Unbalance

In order to investigate the dynamic performance of the converter against a severe unbalance, the magnitude of the source voltage in phase B and C is reduced by 80% for a duration of 1.0 s. Figure 14 shows the dynamic response of converter system for this case. It can be observed from the figure that giving positive-sequence current priority over the negative sequence results in an injection of maximum reactive power (red curve) from the converter. Since the converter current reaches its rated value, there is no room left for the negative-sequence current to flow, i.e, $\underline{i}_{\mathrm{f}}^{-\star}$ is automatically set to zero from

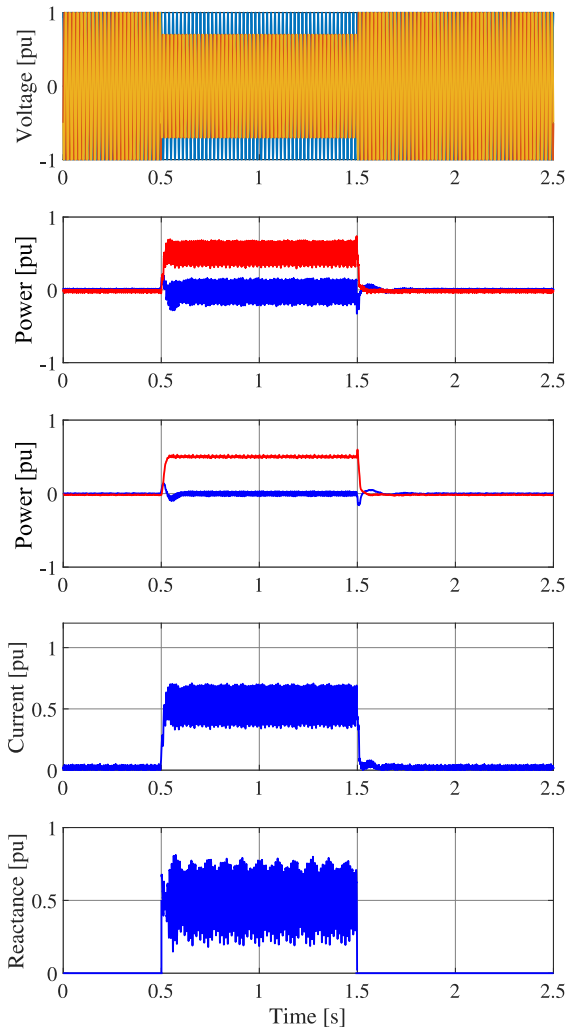

Figure 13: Dynamic response of GFM converter to a shallow unbalanced voltage dip. From top to bottom: three-phase source voltage, measured active (blue curve) and reactive power (red curve), measured positive-sequence active (blue curve) and reactive (red curve) power, measured converter-current magnitude, measured negative-sequence reactance of the converter.

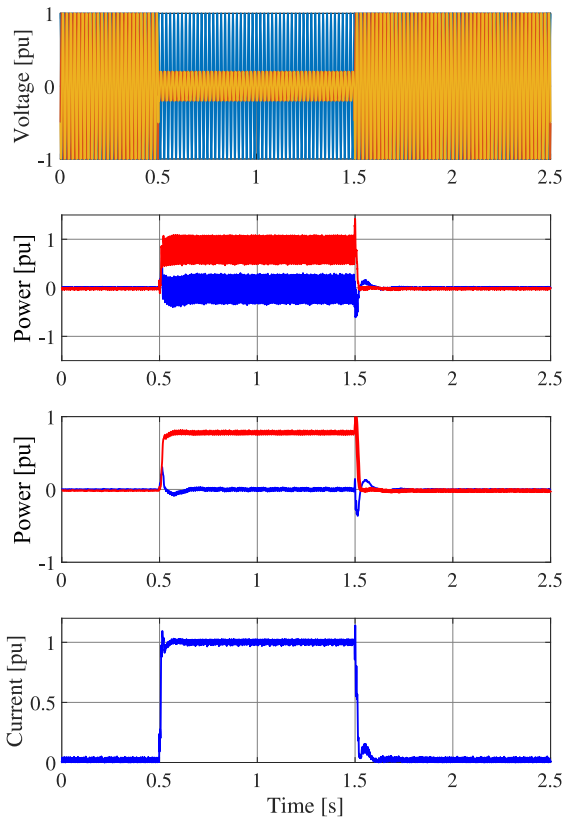

Figure 14: Dynamic response of GFM converter to a severe unbalanced voltage dip. From top to bottom: three-phase source voltage, measured active (blue curve) and reactive power (red curve), measured positive-sequence active (blue curve) and reactive (red curve) power, measured converter-current magnitude.

(B.18). Consequently, the measured converter current is composed of positive-sequence component only unlike the current in Fig. 13, where the 100.0 Hz oscillation due to negative-sequence component is evident.

7 Conclusions

In this paper, a novel current limitation strategy for grid-forming converters has been presented. The existing current limitation strategies for GFM converters have been discussed, together with causes for instability in case of large disturbances. In order to guarantee converter's stability and at the same time preserve its GFM behaviour also during current limitation, a novel limitation strategy has been presented. In the proposed strategy, current limitation is achieved by dynamically limiting the virtual-back EMF vector. Experimental results show the ability to effectively limit the current output of the converter to the desired value for several system events, without the need to activate the reference-current limiter at the input of the CC. Furthermore, modifications to cope with unbalanced grid conditions and fulfil the related grid codes have been presented.

References

[1] A. Narula, P. Imgart, M. Bongiorno, M. Beza, J. R. Svensson, and J.-P. Hasler, "Voltage-based Current Limitation Strategy to Preserve Grid-forming Properties Under Severe Grid Disturbances," *IEEE Open Journal of Power Electronics*, pp. 1–13, 2023, ISSN: 2644-1314.

[2] United Nations Framework Convention on Climate Change, "Adoption of the Paris Agreement - 21st Conference of the Parties," Paris, 2015.

[3] ENTSO-E, "High Penetration of Power Electronic Interfaced Power Sources and the Potential Contribution of Grid Forming Converters," 2020.

[4] J. Matevosyan, B. Badrzadeh, T. Prevost, *et al.*, "Grid-Forming Inverters: Are They the Key for High Renewable Penetration?" *IEEE Power and Energy Magazine*, vol. 17, no. 6, pp. 89–98, Nov. 2019, ISSN: 1558-4216.

[5] J. Rocabert, A. Luna, F. Blaabjerg, and P. Rodríguez, "Control of Power Converters in AC Microgrids," *IEEE Transactions on Power Electronics*, vol. 27, no. 11, pp. 4734–4749, Nov. 2012, ISSN: 0885-8993.

[6] S. D'Arco and J. A. Suul, "Virtual synchronous machines — Classification of implementations and analysis of equivalence to droop controllers for microgrids," in *2013 IEEE Grenoble Conference*, Jun. 2013, pp. 1–7.

[7] H.-P. Beck and R. Hesse, "Virtual synchronous machine," in *2007 9th International Conference on Electrical Power Quality and Utilisation*, Barcelona, Spain: IEEE, Oct. 2007, pp. 1–6, ISBN: 978-84-690-9441-9.

[8] Q. Zhong and G. Weiss, "Synchronverters: Inverters That Mimic Synchronous Generators," *IEEE Transactions on Industrial Electronics*, vol. 58, no. 4, pp. 1259–1267, Apr. 2011, ISSN: 1557-9948.

[9] A. Tayyebi, F. Dörfler, F. Kupzog, Z. Miletic, and W. Hribernik, "Grid-Forming Converters – Inevitability, Control Strategies and Challenges in Future Grids Application," *CIRED Workshop*, no. 0236, p. 5, 2018.

[10] R. Rosso, X. Wang, M. Liserre, X. Lu, and S. Engelken, "Grid-Forming Converters: Control Approaches, Grid-Synchronization, and Future Trends — A Review," *IEEE Open Journal of Industry Applications*, vol. 2, pp. 93–109, 2021, ISSN: 2644-1241.

[11] B. Fan, T. Liu, F. Zhao, H. Wu, and X. Wang, "A Review of Current-Limiting Control of Grid-Forming Inverters Under Symmetrical Disturbances," *IEEE Open Journal of Power Electronics*, pp. 1–15, 2022, ISSN: 2644-1314.

[12] Enstore, "Enstore updated guide for GB Grid Forming Converters – V-005," Jul. 6, 2021.

[13] NERC, "Grid Forming Technology - Bulk Power System Reliability Consideration," Nov. 2021.

[14] S. D'Arco, J. A. Suul, and O. B. Fosso, "Control system tuning and stability analysis of Virtual Synchronous Machines," in *2013 IEEE Energy Conversion Congress and Exposition*, Sep. 2013, pp. 2664–2671.

[15] T. Qoria, F. Gruson, F. Colas, X. Guillaud, M.-S. Debry, and T. Prevost, "Tuning of Cascaded Controllers for Robust Grid-Forming Voltage Source Converter," in *2018 Power Systems Computation Conference (PSCC)*, Dublin, Ireland: IEEE, Jun. 2018, pp. 1–7, ISBN: 978-1-910963-10-4.

[16] H. Deng, Y. Qi, J. Fang, Y. Tang, and V. Debusschere, "A Robust Low-Voltage-Ride-Through Strategy for Grid-Forming Converters Based on Reactive Power Synchronization," *IEEE Transactions on Power Electronics*, vol. 38, no. 1, pp. 346–357, Jan. 2023, ISSN: 1941-0107.

[17] P. Rodriguez, I. Candela, C. Citro, J. Rocabert, and A. Luna, "Control of grid-connected power converters based on a virtual admittance control loop," in *2013 15th European Conference on Power Electronics and Applications (EPE)*, Sep. 2013, pp. 1–10.

[18] M. G. Taul, X. Wang, P. Davari, and F. Blaabjerg, "Current Limiting Control With Enhanced Dynamics of Grid-Forming Converters During Fault Conditions," *IEEE Journal of Emerging and Selected Topics in Power Electronics*, vol. 8, no. 2, pp. 1062–1073, Jun. 2020, ISSN: 2168-6777, 2168-6785.

[19] A. Narula, M. Bongiorno, M. Beza, and P. Chen, "Tuning and evaluation of grid-forming converters for grid-support," in *2021 23rd European Conference on Power Electronics and Applications (EPE'21 ECCE Europe)*, Sep. 2021, P.1–P.10.

[20] K. G. Saffar, S. Driss, and F. B. Ajaei, "Impacts of Current Limiting on the Transient Stability of the Virtual Synchronous Generator," *IEEE Transactions on Power Electronics*, pp. 1–12, 2022, ISSN: 0885-8993, 1941-0107.

[21] L. Zhang, L. Harnefors, and H. Nee, "Power-Synchronization Control of Grid-Connected Voltage-Source Converters," *IEEE Transactions on Power Systems*, vol. 25, no. 2, pp. 809–820, May 2010, ISSN: 1558-0679.

[22] L. Harnefors, M. Hinkkanen, U. Riaz, F. M. M. Rahman, and L. Zhang, "Robust Analytic Design of Power-Synchronization Control," *IEEE Transactions on Industrial Electronics*, vol. 66, no. 8, pp. 5810–5819, Aug. 2019, ISSN: 1557-9948.

[23] F. Salha, F. Colas, and X. Guillaud, "Virtual resistance principle for the overcurrent protection of PWM voltage source inverter," in *2010 IEEE PES Innovative Smart Grid Technologies Conference Europe (ISGT Europe)*, Oct. 2010, pp. 1–6.

[24] J. He and Y. W. Li, "Analysis, Design, and Implementation of Virtual Impedance for Power Electronics Interfaced Distributed Generation," *IEEE Transactions on Industry Applications*, vol. 47, no. 6, pp. 2525–2538, Nov. 2011, ISSN: 0093-9994.

[25] A. D. Paquette and D. M. Divan, "Virtual Impedance Current Limiting for Inverters in Microgrids With Synchronous Generators," *IEEE Transactions on Industry Applications*, vol. 51, no. 2, pp. 1630–1638, Mar. 2015, ISSN: 1939-9367.

[26] B. Wang, R. Burgos, and B. Wen, "Grid-Forming Inverter Control Strategy with Improved Fault Ride Through Capability," in *2022 IEEE Energy Conversion Congress and Exposition (ECCE)*, Oct. 2022, pp. 1–8.

[27] Z. Jin and X. Wang, "A DQ-Frame Asymmetrical Virtual Impedance Control for Enhancing Transient Stability of Grid-Forming Inverters," *IEEE Transactions on Power Electronics*, vol. 37, no. 4, pp. 4535–4544, Apr. 2022, ISSN: 1941-0107.

[28] J. M. Bloemink and M. R. Iravani, "Control of a Multiple Source Microgrid With Built-in Islanding Detection and Current Limiting," *IEEE Transactions on Power Delivery*, vol. 27, no. 4, pp. 2122–2132, Oct. 2012, ISSN: 1937-4208.

[29] K. Shi, H. Ye, P. Xu, D. Zhao, and L. Jiao, "Low-voltage ride through control strategy of virtual synchronous generator based on the analysis of excitation state," *IET Generation, Transmission & Distribution*, vol. 12, no. 9, pp. 2165–2172, 2018, ISSN: 1751-8695.

[30] J. Chen, F. Prystupczuk, and T. O'Donnell, "Use of voltage limits for current limitations in grid-forming converters," *CSEE Journal of Power and Energy Systems*, vol. 6, no. 2, pp. 259–269, Jun. 2020, ISSN: 2096-0042.

[31] E. Afshari, G. R. Moradi, R. Rahimi, *et al.*, "Control Strategy for Three-Phase Grid-Connected PV Inverters Enabling Current Limitation Under Unbalanced Faults," *IEEE Transactions on Industrial Electronics*, vol. 64, no. 11, pp. 8908–8918, Nov. 2017, ISSN: 1557-9948.

[32] P. Piya, M. Ebrahimi, M. Karimi-Ghartemani, and S. A. Khajehoddin, "Fault Ride-Through Capability of Voltage-Controlled Inverters," *IEEE Transactions on Industrial Electronics*, vol. 65, no. 10, pp. 7933–7943, Oct. 2018, ISSN: 1557-9948.

[33] L. Huang, L. Zhang, H. Xin, Z. Wang, and D. Gan, "Current limiting leads to virtual power angle synchronous instability of droop-controlled converters," in *2016 IEEE Power and Energy Society General Meeting (PESGM)*, Jul. 2016, pp. 1–5.

[34] H. Xin, L. Huang, L. Zhang, Z. Wang, and J. Hu, "Synchronous Instability Mechanism of P-f Droop-Controlled Voltage Source Converter Caused by Current Saturation," *IEEE Transactions on Power Systems*, vol. 31, no. 6, pp. 5206–5207, Nov. 2016, ISSN: 1558-0679.

[35] H. Lin, C. Jia, J. M. Guerrero, and J. C. Vasquez, "Angle Stability Analysis for Voltage-Controlled Converters," *IEEE Transactions on Industrial Electronics*, vol. 64, no. 8, pp. 6265–6275, Aug. 2017, ISSN: 1557-9948.

[36] T. Qoria, F. Gruson, F. Colas, G. Denis, T. Prevost, and X. Guillaud, "Critical Clearing Time Determination and Enhancement of Grid-Forming Converters Embedding Virtual Impedance as Current Limitation Algorithm," *IEEE Journal of Emerging and Selected Topics in Power Electronics*, vol. 8, no. 2, pp. 1050–1061, Jun. 2020, ISSN: 2168-6777, 2168-6785.

[37] T. Qoria, F. Gruson, F. Colas, X. Kestelyn, and X. Guillaud, "Current limiting algorithms and transient stability analysis of grid-forming VSCs," *Electric Power Systems Research*, vol. 189, p. 106 726, Dec. 1, 2020, ISSN: 0378-7796.

[38] X. Wang, M. G. Taul, H. Wu, Y. Liao, F. Blaabjerg, and L. Harnefors, "Grid-Synchronization Stability of Converter-Based Resources—An Overview," *IEEE Open Journal of Industry Applications*, vol. 1, pp. 115–134, 2020, ISSN: 2644-1241.

[39] D. Pan, X. Wang, F. Liu, and R. Shi, "Transient Stability of Voltage-Source Converters With Grid-Forming Control: A Design-Oriented Study," *IEEE Journal of Emerging and Selected Topics in Power Electronics*, vol. 8, no. 2, pp. 1019–1033, Jun. 2020, ISSN: 2168-6785.

[40] E. Rokrok, T. Qoria, A. Bruyere, B. Francois, and X. Guillaud, "Transient Stability Assessment and Enhancement of Grid-Forming Converters Embedding Current Reference Saturation as Current Limiting Strategy," *IEEE Transactions on Power Systems*, pp. 1–1, 2021, ISSN: 1558-0679.

[41] P. Imgart, A. Narula, M. Bongiorno, M. Beza, and J. R. Svensson, "A Cascaded Power Controller for Robust Frequency Ride-Through of Grid-Forming Converters," presented at the 2022 IEEE Energy Conversion Congress and Exposition (ECCE), Detroit, MI, USA, 2022.

[42] J. Alipoor, Y. Miura, and T. Ise, "Power System Stabilization Using Virtual Synchronous Generator With Alternating Moment of Inertia," *IEEE Journal of Emerging and Selected Topics in Power Electronics*, vol. 3, no. 2, pp. 451–458, Jun. 2015, ISSN: 2168-6785.

[43] H. Wu and X. Wang, "A Mode-Adaptive Power-Angle Control Method for Transient Stability Enhancement of Virtual Synchronous Generators," *IEEE Journal of Emerging and Selected Topics in Power Electronics*, vol. 8, no. 2, pp. 1034–1049, Jun. 2020, ISSN: 2168-6785.

[44] A. Narula, M. Bongiorno, and M. Beza, "Comparison of Grid-Forming Converter Control Strategies," in *2021 IEEE Energy Conversion Congress and Exposition (ECCE)*, Oct. 2021, pp. 361–368.

[45] L. Harnefors, *Control of Variable-Speed Drives*. Västerås: Applied Signal Processing and Control, Department of Electronics, Mälardalen University, 2002.

[46] R. Rosso, M. Andresen, S. Engelken, and M. Liserre, "Analysis of the Interaction Among Power Converters Through Their Synchronization Mechanism," *IEEE Transactions on Power Electronics*, vol. 34, no. 12, pp. 12 321–12 332, Dec. 2019, ISSN: 1941-0107.

[47] National Grid ESO, *Final Modification Report GC0137: Minimum Specification Required for Provision of GB Grid Forming (GBGF) Capability*, Nov. 11, 2021.

[48] Australian Energy Market Operator, "Trip of multiple generators and lines in Central Queensland and associated under-frequency load shedding on 25 May 2021," Oct. 2021.

[49] ENTSO-E, "Continental Europe Synchronous Area Separation on 24 July 2021 - Technical report," Nov. 12, 2021.

[50] Verband der Elektrotechnik Elektronik Informationstechnik e. V., *Technical Connection Rules for High-Voltage (VDE-AR-N 4120)*, Nov. 2018.

[51] M. Beza and M. Bongiorno, "Application of Recursive Least Squares Algorithm With Variable Forgetting Factor for Frequency Component Estimation in a Generic Input Signal," *IEEE Transactions on Industry Applications*, vol. 50, no. 2, pp. 1168–1176, Mar. 2014, ISSN: 1939-9367.

PAPER C

A Cascaded Power Controller for Robust Frequency Ride-Through of Grid-Forming Converters

Paul Imgart, Anant Narula, Massimo Bongiorno, Mebtu Beza, Jan R. Svensson

Published in 2022 IEEE Energy Conversion Congress and Exposition (ECCE).

The layout has been revised.

Abstract

The aim of this paper is to present a grid-forming (GFM) control strategy with a novel active-power loop (APL) structure facilitating limitation of active power while providing maximum available inertial support. This is achieved by decoupling the synchronization duties of the APL from the inertial support. The latter is provided by calculating an active-power reference through a dedicated inertia-emulation loop (IEL), which is connected in cascade with the APL. The effectiveness of the proposed method is demonstrated through time-domain simulations including frequency transients of varying size and unbalanced operating conditions.

1 Introduction

World-wide transformation efforts towards the future renewable-based power system result in the replacement of synchronous with converter-interfaced generation. Thanks to their voltage source behaviour and ability to easily provide a number of ancilliary services such as inertial support, grid-forming (GFM) converters are the preferred solution for the challenges associated with this development [2]. One of the main challenges for GFM converters is to be able to limit the converter current and at the same time maintain a stable operation and GFM properties [3]. In this regard there is a lot of focus in existing studies dealing with converter angle stability and related design improvements on current limitation during voltage dips [4]–[8]. However, as this paper will show, grid frequency disturbance is a relevant source of angular instability; this kind of disturbance is particularly challenging when large inertial support is required and grid synchronization is provided by the active-power loop (APL).

Even though the focus of existing work has been on instability caused by voltage fluctuations, there exist some publications suggesting solutions for frequency-disturbance induced instability. From the existing literature, mainly three strategies have been identified. The first is control-mode switching (CMS), as suggested in [9], where a complex modified droop control manipulates the active and reactive power references based on the converter

currents to prevent loss of synchronism due to current saturation. A different approach involving CMS is presented in [10], selecting different frequency response strategies based on frequency deviation and the typically noise-sensitive estimate of the rate of change of frequency (RoCoF). The second strategy is to adapt the inertia, which in [11] is based on a grid impedance estimation to ensure a selected stability margin for the GFM converter. The third strategy is to switch the synchronization duty during current limitation to a backup synchronization unit, typically a phase-locked loop (PLL) [12], [13]. CMS as well as parameter adaptation change the converter's properties abruptly. Some implementations require typically unknown system parameters to properly estimate the converter's actual capabilities and otherwise limit too conservatively or have the risk of not staying within the limits [14]. The use of a backup PLL during current saturation can result in the removal of the converter's GFM capabilities, which is undesirable as they are typically needed the most during grid disturbances. Furthermore, the suggested solutions to the GFM converter stability problem are closely integrated with the rest of the suggested control system, making them highly specific.

The aim of this paper is to propose a solution to the GFM stability problem by decoupling the synchronization task of the APL from the provision of inertia. To address the issue properly, first it is investigated what the root causes of angular instability in GFM converters are and why controllers which provide inertial support are prone to instability when subjected to large grid frequency disturbances. It is shown that existing solutions available in the literature, typically based on variation of the active-power reference [4]–[8], are not effective for this kind of event. Based on this analysis, a new solution consisting of an inertia-emulation loop (IEL) in cascade with a fast active-power controller is presented. The IEL is based on the structure of a PLL and is used to generate an active-power reference emulating the desired amount of inertia, whereas the APL provides synchronization with the grid. Next, the tuning procedure for APL and IEL is established, demonstrating how the IEL parameters relate to the desired inertia constant and damping ratio of the inertial response. This is followed by results of time-domain simulations, presented to demonstrate that the desired behavior is achieved. Thanks to the proposed control strategy, it is possible to keep the grid-forming properties and the converter current limits without the need for control-mode switching or parameter adaptation.

2 Grid-forming converter stability problem

The common property of the majority of the GFM control structures suggested in the literature is that the converter should be modelled as a voltage source behind an impedance [15], [16]. This behavior can be achieved using different grid-synchronization methods, e.g. using a dedicated synchronization unit like a PLL. However, GFM converters typically synchronize by relying on the active-power transfer, which can even provide increased robustness in weak grids and islanding operation [17]. In this work, the virtual admittance-based approach from [18] is implemented with the structure displayed in Fig. 1. A detailed description of the control system follows in the next section, as the results of this study are not specific for this control structure.

Angle instability in GFM converters mainly occurs due to two reasons: firstly, the power reference being too large for the grid conditions such as grid strength and voltage, e.g. during a fault [4]–[8]; secondly, the power controller being unable to follow the grid voltage angle in case of an angle jump or frequency disturbance. The latter is the focus of this paper.

For the system depicted in Fig. 1 (bottom figure), neglecting the system losses the steady state per-unit converter current is

$$\underline{I}_{\mathrm{c}} = \frac{\underline{V}_{\mathrm{EMF}} - \underline{V}_{\mathrm{s}}}{\mathrm{j}X} = \frac{V_{\mathrm{s}} \sin\delta + \mathrm{j}(V_{\mathrm{s}} \cos\delta - V_{\mathrm{EMF}})}{X}, \tag{C.1}$$

where the dq-frame is aligned with the converter back EMF, δ denotes the phase displacement between $\underline{V}_{\mathrm{EMF}}$ and $\underline{V}_{\mathrm{s}}$, and X is the sum of reactances between them[1]. The active-power transfer from the converter to the grid is defined with $*$ symbolizing the complex conjugate as

$$P = \mathfrak{Re}\{\underline{V}_{\mathrm{EMF}} \underline{I}_{\mathrm{c}}^{*}\} = \frac{V_{\mathrm{s}} V_{\mathrm{EMF}}}{X} \sin\delta, \tag{C.2}$$

and shown in blue in Fig. 2 for an example system.

Denoting with $I_{\max}$ the maximum allowed converter current and using circular current limitation [7] on the current reference I_{ref}, the limited converter current reference is

$$\underline{I}_{\mathrm{ref,lim}} = \underline{I}_{\mathrm{ref}} \frac{I_{\max}}{I_{\mathrm{ref}}} \qquad \forall\ I_{\mathrm{ref}} > I_{\max}. \tag{C.3}$$

[1] The virtual admittance $\underline{Y}_{\mathrm{v}} = \underline{Z}_{\mathrm{v}}^{-1}$ in Fig. 1 is the inverse of the series of the virtual impedance $\underline{Z}_{\mathrm{v1}}$ and the physical filter impedance $\underline{Z}_{\mathrm{f}}$.

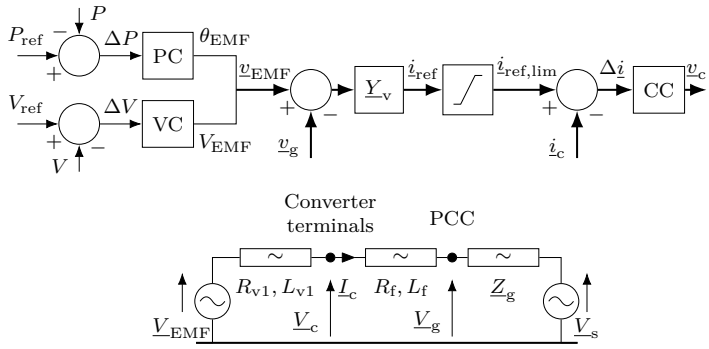

Figure 1: Block scheme (top) and equivalent circuit (bottom) representation of the virtual admittance-based GFM control approach.

Note that the activation of the current limiter is equivalent to a variation of the phasor $\underline{V}_{\mathrm{EMF}}$, defined as $\underline{V}'_{\mathrm{EMF}}$ in Fig. 3. From the figure, current limitation results in a reduction of the load angle δ when compared with the unlimited case, denoted as δ_{APL}. Even despite this reduction, the angle δ_{APL} still has an impact on the exchanged active power, as it determines the angle of the current reference $\underline{I}_{\mathrm{ref}}$. Using (C.1)-(C.3), the relation between δ_{APL} and the current-limited active power P_{limited} is given as

$$\begin{aligned} P_{\mathrm{limited}} &= \mathfrak{Re}\{\underline{V}_{\mathrm{s}}\underline{I}^{*}_{\mathrm{ref,lim}}\} \\ &= V_{\mathrm{s}}V_{\mathrm{EMF}}\sin\delta_{\mathrm{APL}}\frac{I_{\mathrm{max}}}{\sqrt{V_{\mathrm{s}}^2+V_{\mathrm{EMF}}^2-2V_{\mathrm{s}}V_{\mathrm{EMF}}\cos\delta_{\mathrm{APL}}}}, \\ &\qquad \forall\ I_{\mathrm{ref}} > I_{\mathrm{max}}. \end{aligned} \tag{C.4}$$

Figure 2 illustrates the current-limited P-δ_{APL} relationship following from (C.4) in red. After the current saturates at B, the power transfer decreases for increasing δ_{APL}.

The type of instability highlighted in this section occurs due to the inability of the APL to follow the grid voltage angle in case of a severe frequency disturbance or phase angle jump. To follow a change in the grid frequency, a power control error is required, causing the APL to adapt its internal frequency. As an example, a frequency decline would cause the angle to increase until the additional decelerating power $P_{\mathrm{d}} = -2H\frac{\mathrm{d}\omega}{\mathrm{d}t}$ is achieved. When the current is

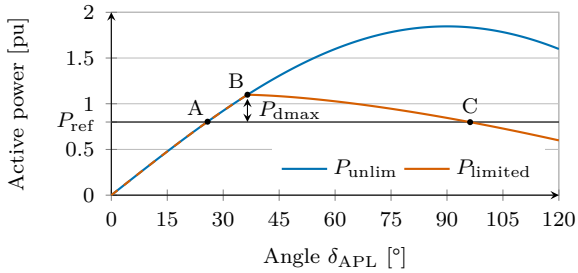

Figure 2: P-δ_{APL} curve illustrating the converter angle stability problem for a current limit of 1.1 pu with $V_{\mathrm{g}} = 1$ pu. A: Pre-disturbance operating point; B: Current limit reached; C: transient stability limit; P_{dmax}: maximum decelerating power.

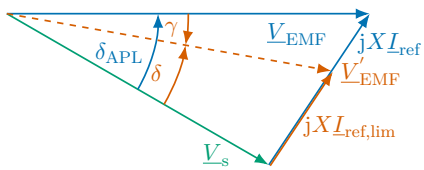

Figure 3: Phasor diagram illustrating the effect of current limitation on the virtual back EMF. Unlimited in blue, limited in red.

limited, the needed decelerating power might not be reached and the angle continues to increase. Synchronism is lost if the unstable equilibrium point C is passed, equivalent to synchronous machine first swing instability.

The simulation shown in Fig. 4 illustrates this instability mechanism caused by a frequency decrease. During unsaturated operation, γ defined in Fig. 3 is zero. During limitation, the required deceleration power P_{d} cannot be reached and the APL angle δ_{APL} increases steadily. As a consequence, γ is decreasing at an accelerating rate, which demonstrates the loss of the synchronization signal. In this case, loss of synchronism cannot be prevented by limiting the active-power reference, because the additional power is not caused by a change in reference, but by the slow APL's inability to reject the grid disturbance. GFM converters are prone to this type of instability when they rely on the active power transfer for synchronization. Due to this, the APL output is not a load angle, but a ramp-formed phase angle. When the APL angle output is

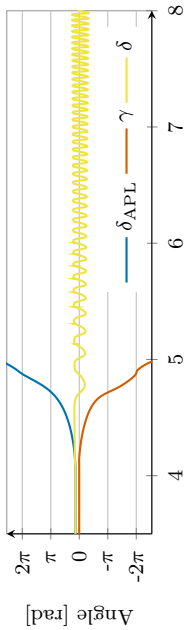

Figure 4: δ_{APL}, γ and δ for converter instability due to frequency disturbance at 4 s.

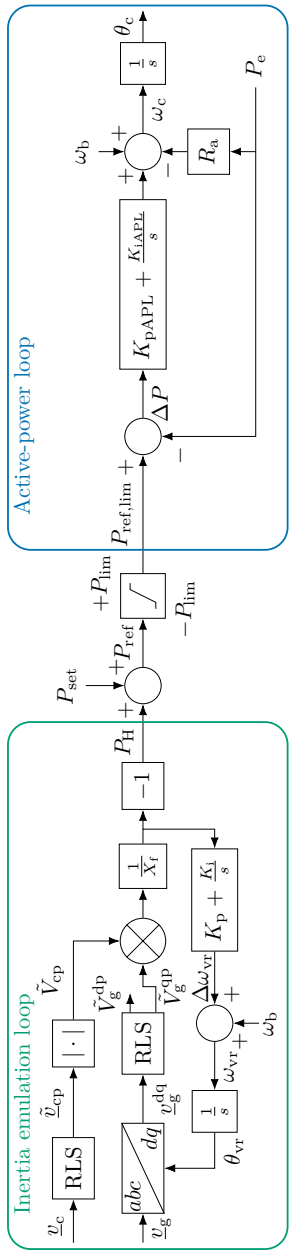

Figure 5: Proposed cascaded structure for the active-power controller of GFM converters.

manipulated to guarantee current limitation, the synchronization signal is lost. Large inertia, high RoCoF and operating points close to the maximum power transfer will increase the risk for this kind of instability, as the necessary decelerating power increases or the available current for decelerating power decreases, respectively.

3 Proposed solution

The GFM design incorporating both synchronization and inertial response in the APL is the approach typically encountered in the literature [17], and will here be referred to as *integrated GFM*. To overcome the described risk for instability present in these approaches, the cascaded structure for the converter's active-power controller displayed in Fig. 5 is proposed here. The PI-based APL tracks the active-power reference and synchronizes with the grid, and generates the angle for the converter virtual back EMF. To avoid the previously described problem, the bandwidth of the APL has to be relatively high, so that its inertial contribution is negligible.

The inertia response P_{H} is instead calculated by the IEL and added onto the APL's power reference P_{set}. This is similar to the approach proposed in [19], where a PLL is used to provide an inertial response from a grid-following converter. The advantage of the proposed approach over other methods to provide RoCoF-proportional inertial response is that the frequency derivative is implicitly determined within the PLL. This replaces the noise-sensitive derivation step and means that the RoCoF estimate is immediately available, reducing delays in the converter's inertial response [19]. By generating the inertial response explicitly as a part of the power reference, it can be effectively limited, preventing the previously demonstrated instability. For this, the admissible converter power $S_{\mathrm{lim}} = \frac{V_{\mathrm{g}} S_{\mathrm{N}}}{V_{\mathrm{N}}}$ is estimated with the rated converter power S_{N} and rated voltage V_{N}. It is used together with the reactive power injected by the converter, Q, to calculate the active-power limit, $P_{\mathrm{lim}} = (S_{\mathrm{lim}}^2 - Q^2)^{1/2}$, which is then applied to the active-power reference P_{ref}.

In contrast to the proposed solution, the inertial response from an actual or virtual synchronous machine is not achieved by varying the power reference, but is a natural reaction to a frequency transient while mechanical torque or power reference, respectively, are held constant. Due to that it is nontrivial in these control designs to limit the active power without compromising the

loop's synchronization task. Separating the inertia from the APL as in the proposed cascaded controller gives on the other hand the possibility to prevent the current from exceeding its rated value by limiting the inertial power, which in turn avoids the triggering of the current limiter in Fig. 1. Generating the inertial response through the APL power setpoint comes furthermore with the advantage that the presented IEL can be used with any sufficiently fast APL, and can be even employed in grid-following converters to provide inertial response. Even though it is based on a PLL structure, the IEL does only provide inertia emulation, while the APL is exclusively responsible for active-power reference tracking and in a GFM for synchronization with the grid.

The other parts of the controller shown in Fig. 1 are tuned according to the method presented in [18]. While the active-power controller generates the virtual back EMF angle, its magnitude is determined by the voltage controller, here consisting of a simple integrator. The virtual admittance (VA) is used for calculation of the reference current input to the current controller. Thanks to its resistive-inductive nature, the VA provides reference-current filtering (through X_v) and damping (through R_v); furthermore, it helps in preserving the converter's dynamic performance under varying grid strengths by reducing the impact of the grid impedance on the total impedance variation [20][2]. The current references generated by the VA are limited with a circular current limitation and finally fed to the vector-current controller.

3.1 Active-power loop tuning

The APL employed in this paper is based on a PI-regulator. The adopted controller is tuned using a loop shaping approach with active damping. The active-power transfer from the converter to the grid neglecting resistances is given by the two port equation (C.2), which can be applied here due to the relatively slow speed of APLs, allowing to use quasi-steady state equations. To tune the controller properly, the equation is formulated with regard to the measurable PCC voltage instead of the Thévenin source, with $\delta = \theta_\mathrm{EMF} - \theta_\mathrm{g}$. Linearizing this equation for small angle differences, and formulating the transfer function for a change in the converter angle with a constant grid

[2]The virtual reactance is selected in the range of typical SM output reactance [21], while the virtual resistance is chosen to provide a small time constant for the dc-current offset originated from the large virtual reactance.

voltage phase angle gives the plant model for the controller design as

$$G_\theta(s) = \frac{\Delta P}{\Delta \theta_{\mathrm{EMF}}} = \frac{V_{\mathrm{EMF}} V_{\mathrm{g}}}{X_{\mathrm{V}}} = P_{\mathrm{vmax}}. \tag{C.5}$$

The linearized system model corresponds to a PI-controller controlling an integrator, which will result in a zero in the closed-loop transfer function and a pronounced overshoot in the step response. To remove this overshoot, the active damping term displayed in Fig. 5 is introduced. This is similar to the approach typically used for vector current controllers (e.g. as suggested in [22]) and results in the transfer function from the output of the PI-regulator to the injected active power

$$G_\omega(s) = \frac{\Delta P}{\Delta \omega_{\mathrm{c}}} = \frac{1}{R_{\mathrm{a}}} \frac{R_{\mathrm{a}} P_{\mathrm{vmax}}}{s + R_{\mathrm{a}} P_{\mathrm{vmax}}}, \tag{C.6}$$

which corresponds to a first-order system with the bandwidth $\alpha_\omega = R_{\mathrm{a}} P_{\mathrm{vmax}}$. As suggested in [22], this bandwidth is selected to match the desired control-loop bandwidth α_{PC}, resulting in

$$R_{\mathrm{a}} = \alpha_{\mathrm{PC}} / P_{\mathrm{vmax}}. \tag{C.7}$$

The closed-loop transfer function from the reference to the actual active power then becomes

$$G_{\mathrm{PC}}(s) = \frac{K_{\mathrm{pAPL}} s + K_{\mathrm{iAPL}}}{s^2 P_{\mathrm{vmax}}^{-1} + (K_{\mathrm{pAPL}} + R_{\mathrm{a}}) s + K_{\mathrm{iAPL}}}. \tag{C.8}$$

A proper selection of the loop's gains reduces the system order to one:

$$G_{\mathrm{PC}}(s) = \frac{\alpha_{\mathrm{PC}} s + \alpha_{\mathrm{PC}}^2}{s^2 + 2\alpha_{\mathrm{PC}} s + \alpha_{\mathrm{PC}}^2} = \frac{\alpha_{\mathrm{PC}}}{s + \alpha_{\mathrm{PC}}}, \quad \text{with} \tag{C.9}$$

$$K_{\mathrm{pAPL}} = R_{\mathrm{a}} = \frac{\alpha_{\mathrm{PC}}}{P_{\mathrm{vmax}}} \quad \text{and} \quad K_{\mathrm{iAPL}} = \frac{\alpha_{\mathrm{PC}}^2}{P_{\mathrm{vmax}}} = \alpha_{\mathrm{PC}} R_{\mathrm{a}}.$$

To keep in line with the proposed solution and limit the amount of inertia in the active-power loop, α_{PC} should be selected as high as feasible. As reported in [23], there exist grid code requirements limiting the APL bandwidth to 5 Hz, which corresponds to an inertia constant of approximately 0.32 s.

3.2 Inertia-emulation loop tuning

The IEL is tuned to behave equivalent in terms of inertial power contribution to a synchronous machine (SM). The IEL's output is the pure inertial response P_{H}, which is equivalent to a lossless synchronous condenser (SC), where the mechanical power $P_{\mathrm{m}} = 0$. The fundamental idea is that both SC and IEL track the phase angle of the grid voltage with a given speed, which corresponds to their inertia.

The relation between a change in rotor speed of the SM and an active-power imbalance is given by the swing equation:

$$2H\frac{\mathrm{d}\omega_{\mathrm{r}}}{\mathrm{d}t} = P_{\mathrm{m}} - P_{\mathrm{e}} - K_{\mathrm{d}}(\omega_{\mathrm{r}} - \omega_{\mathrm{s}}). \tag{C.10}$$

Here, H denotes the inertia constant in seconds, ω_{r} is the angular rotor frequency, ω_{g} the angular frequency of the grid voltage, P_{e} the electrical power injected to the grid and K_{d} the damping coefficient of the machine, with all quantities but H in pu. For a SM operating in a stable steady-state operating point, electrical and mechanical power must be equal. During a grid disturbance, the power imbalance in such a machine will be its inertial response $P_{\mathrm{H}} = P_{\mathrm{m}} - P_{\mathrm{e}}$. Laplace-transforming and rearranging yields

$$\omega_{\mathrm{r}} s = \frac{-P_{\mathrm{H}}}{2H} - \frac{K_{\mathrm{d}}}{2H}(\omega_{\mathrm{r}} - \omega_{\mathrm{s}}). \tag{C.11}$$

As the mechanical time constants are much higher than the electrical, the SM's electrical power P_{e} can be expressed in quasi-steady state as in (C.2), neglecting the resistances. Assuming a dq-coordinate frame that is aligned with the machine's back EMF results in

$$P_{\mathrm{e}} = \frac{V_{\mathrm{EMF}} V_{\mathrm{s}}}{X}\sin(\theta_{\mathrm{r}} - \theta_{\mathrm{s}}) = -\frac{V_{\mathrm{EMF}}}{X} V_{\mathrm{s}}^{\mathrm{q}}, \tag{C.12}$$

where $V_{\mathrm{s}}^{\mathrm{q}}$ denotes the source voltage q-component, and X the sum of reactances between the back EMF and source voltage. In the SC case with $P_{\mathrm{m}} = 0$, back EMF and grid voltage are aligned with each other in steady state and $V_{\mathrm{s}}^{\mathrm{q}}$ is zero. A change in the grid voltage phase angle would result in a misalignment of the voltages and an active power $P_{\mathrm{H}} = P_{\mathrm{e}}$.

For small angle differences, this can be linearized as

$$P_{\mathrm{H}} = \frac{V_{\mathrm{EMF}} V_{\mathrm{s}}}{X}(\theta_{\mathrm{r}} - \theta_{\mathrm{s}}) = \frac{V_{\mathrm{EMF}} V_{\mathrm{s}}}{Xs}(\omega_{\mathrm{r}} - \omega_{\mathrm{g}}), \tag{C.13}$$

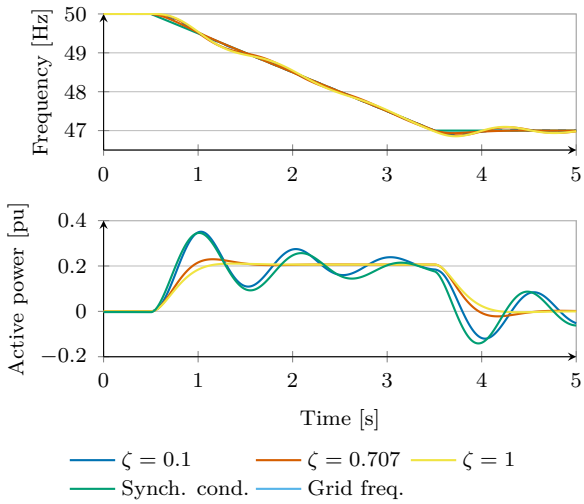

Figure 6: Comparison with synchronous condenser and impact of the damping ratio on rise time and overshoot.

using the angular frequency and phase angle relationships

$$\theta_{\mathrm{r}} s = \omega_{\mathrm{r}} \qquad \text{and} \qquad \theta_{\mathrm{s}} s = \omega_{\mathrm{s}}. \tag{C.14}$$

In most cases the additional power and consequently angle difference due to inertial response is small, and the linearization creates only negligible deviations. Using the previous equation to rearrange (C.11) with the SM maximum transferable active power $P_{\mathrm{smax}} = \frac{V_{\mathrm{EMF}} V_{\mathrm{s}}}{X}$ results in

$$\omega_{\mathrm{r}} s = -\left(\frac{K_{\mathrm{d}}}{2HP_{\mathrm{smax}}} s + \frac{1}{2H}\right) P_{\mathrm{H}}. \tag{C.15}$$

Equivalent behaviour can be established for the IEL. If the emulated inertial-power reference P_{H} is chosen as the input to the IEL's PI-regulator, the derivative of the loop's internal frequency is determined as

$$\omega_{\mathrm{vr}} s = -(K_{\mathrm{p}} s + K_{\mathrm{i}}) P_{\mathrm{H}}, \tag{C.16}$$

where ω_{vr} is the loop's frequency estimate and K_{p} and K_{i} the proportional

and integral gain, respectively. P_{H} is given by

$$P_{\mathrm{H}} = -\frac{V_{\mathrm{c}}}{X_{\mathrm{f}}} V_{\mathrm{g}}^{\mathrm{q}}, \tag{C.17}$$

with the PCC voltage q-component $V_{\mathrm{g}}^{\mathrm{q}}$ in the coordinate system aligned with the IEL angle θ_{vr}, and the filter reactance X_{f}. This equation is the two-port equation formulated with the converter terminal and PCC voltage. The virtual back EMF is replaced with the converter terminal voltage because the virtual resistance can take values that are too high to be neglected, making the use of the simplified two-port equation inaccurate. The Thévenin source voltage $\underline{V}_{\mathrm{s}}$ is replaced with the PCC voltage because the latter can be directly measured. The tracking behaviour of SM and IEL given in (C.11) and (C.16), respectively, can be related to each other to establish equivalent behavior with the following tuning:

$$K_{\mathrm{i}} = \frac{\omega_{\mathrm{b}}}{2H}, \quad K_{\mathrm{p}} = \frac{\omega_{\mathrm{b}} K_{\mathrm{d}}}{2H P_{\mathrm{max}}}, \quad \text{with} \quad P_{\mathrm{max}} = \frac{V_{\mathrm{c}} V_{\mathrm{g}}}{X_{\mathrm{f}}}. \tag{C.18}$$

This formulation assumes all quantities in the IEL are in pu with the exception of virtual angular frequency ω_{vr} and virtual rotor angle θ_{vr}, which is why the base angular frequency ω_{b} appears in both expressions. Thus, the integral gain of the IEL directly relates to the inertia constant of the SM behavior to be reproduced, while the proportional gain represents the damping. To receive an accurate replication of the desired inertial response it is advisable to substract the inertia constant remaining in the APL from the inertia constant used for the IEL so that the cumulative effect is as required.

3.3 Selection of damping

As mentioned above, the proportional gain relates to the damping of the inertial response from the IEL. The relation in (C.18) determines K_{p} if a specific SM damping coefficient is to be reproduced. In a SM, damping is linked to physical properties such as friction and typically associated with losses. In consequence, SMs are usually poorly dampened. In the IEL, the damping does not imply any losses, which means it becomes an additional degree of freedom. Increased damping comes however with the downside of a slower response.

In the previous section was established that inertial response relates to tracking changes in the grid voltage angle with a specific speed. This tracking

speed is determined by the IEL closed loop transfer function, given as

$$G_{\mathrm{IEL}}(s) = \frac{\Delta\theta_{\mathrm{vr}}}{\Delta\theta_{\mathrm{g}}} = \frac{P_{\max}(K_{\mathrm{p}}s + K_{\mathrm{i}})}{s^2 + P_{\max}K_{\mathrm{p}}s + P_{\max}K_{\mathrm{i}}}, \tag{C.19}$$

employing the small angle linearization

$$\Delta\theta_{\mathrm{g}} = \frac{1}{V_{\mathrm{g}}}\Delta V_{\mathrm{g}}^{\mathrm{q}}. \tag{C.20}$$

This is a damped second order response with a zero,

$$G_{\mathrm{IEL}}(s) = \frac{2\zeta\omega_{\mathrm{n}}s + \omega_{\mathrm{n}}^2}{s^2 + 2\zeta\omega_{\mathrm{n}}s + \omega_{\mathrm{n}}^2}, \quad \text{where} \tag{C.21}$$

$$\omega_{\mathrm{n}} = \sqrt{\frac{\omega_{\mathrm{b}}P_{\max}}{2H}}, \quad \text{and} \quad \zeta = \sqrt{\frac{\omega_{\mathrm{b}}}{2HP_{\max}}}K_{\mathrm{d}}$$

using (C.18), which allows to determine the proportional gain based on the damping ratio as

$$K_{\mathrm{p}} = \zeta\sqrt{\frac{2\omega_{\mathrm{b}}}{HP_{\max}}}. \tag{C.22}$$

The effect of different damping ratios is shown in the results from time-domain simulations in Fig. 6. For this study case, the frequency of the voltage source is reduced with 1 Hz/s from 50 Hz to 47 Hz, while the steady-state active-power reference is set to $P_{\mathrm{set}} = 0\,\mathrm{pu}$. The inertia constant is selected as $H = 4.68\,\mathrm{s}$, which together with the inertial contribution from the APL results in a total inertia constant of 5 s, meaning that the frequency disturbance should result in an inertial response of 0.2 pu. The figure demonstrates that the proposed controller is able to reproduce the behavior of a synchronous machine with good accuracy. The chosen approach to combine a fast APL with a change in the power reference causes a minor delay when compared to the physics based response of the SM. It can also be seen that the low damping of the SM causes a challenging behavior. As the IEL damping can be freely adapted without any losses, a response without overshoot ($\zeta = 1$) can be selected. To reduce the rise time, a damping ratio of $\zeta = 0.707$ is suggested as a compromise between speed and damping of the inertial response.

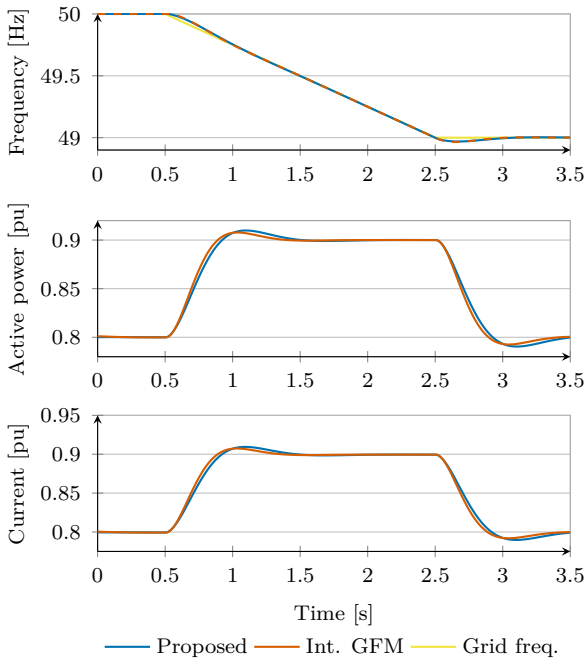

Figure 7: Dynamic response of GFM converter to the smaller simulated frequency disturbance (0.5 Hz/s), not causing current saturation.

3.4 Sequence separation and harmonic filtering

Unbalanced conditions or operation under distorted grid voltages impact the IEL and result in an unsteady inertial-power reference. To avoid this, a sequence separation is applied to the PCC and converter terminal voltages as shown in Fig. 5. For this paper, the recursive least square (RLS) based method from [24] is implemented in *dq*-coordinates. The transfer functions resulting from transforming the state-space model presented in [24] into *dq*-coordinates

Table 1: System and control parameters

System parameters		Control parameters	
S_N	1 kVA	L_v1	0.35 pu
V_N	100 V	R_v1	0.235 pu
ω_b	314.16 rad/s	α_pc	2π 5 rad/s
L_f	0.15 pu	H	4.68 s
R_f	0.015 pu	ζ	0.707
SCR	3	ξ	0.9 pu

is

$$G_\mathrm{RLSp}(s) = \frac{\tilde{v}_\mathrm{p}^\mathrm{dq}}{v^\mathrm{dq}} = \frac{(\omega\xi - \mathrm{j}\omega\frac{\xi^2}{2})s + \omega^2\xi^2 + 2\mathrm{j}\omega^2\xi}{s^2 + (2\omega\xi + 2\mathrm{j}\omega)s + \omega^2\xi^2 + 2\mathrm{j}\omega^2\xi} \tag{C.23}$$

$$G_\mathrm{RLSn}(s) = \frac{\tilde{v}_\mathrm{n}^\mathrm{dq}}{v^\mathrm{dq}} = \frac{(\omega\xi + \mathrm{j}\omega\frac{\xi^2}{2})s}{s^2 + (2\omega\xi + 2\mathrm{j}\omega)s + \omega^2\xi^2 + 2\mathrm{j}\omega^2\xi}, \tag{C.24}$$

where $\tilde{v}_\mathrm{p}^\mathrm{dq}$ and $\tilde{v}_\mathrm{n}^\mathrm{dq}$ are the voltage dq-vector positive and negative sequence estimates, ω is the grid frequency[3] and ξ is the estimator's relative bandwidth. The RLS-algorithm provides not only sequence separation, but also effective harmonic filtering [24].

4 Simulation results

The effectiveness of the proposed solution is validated by time-domain simulations of an average model of the grid-connected converter system shown in Fig. 1. The first case study compares the cascaded controller suggested here with an *integrated GFM* design for two frequency disturbances with different RoCoF, demonstrating both equivalence for operation below the active-power limit as well as the effectiveness of the suggested solution for ensuring robust operation in current saturation. In the next part, the effect of the RLS sequence separation is demonstrated, both in terms of added delay as well as the ability for unbalanced operation. Finally, operation under distorted grid voltage conditions is shown. The system and controller parameters used in

[3] Here a fixed grid frequency is assumed and $\omega = \omega_\mathrm{b}$, but as shown in [24] a frequency adaptation can be used as well.

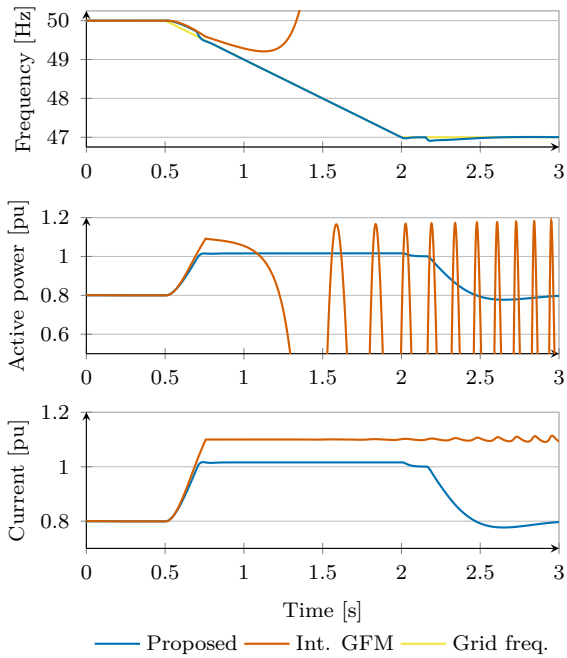

Figure 8: Dynamic response of GFM converter to the larger simulated frequency disturbance (2 Hz/s), causing current saturation.

the simulations are given in Table 1. The over-current limit of the converter is set to 1.1 pu, S_{N} is 1.0 pu and a circular current limiter is used to limit the current reference.

4.1 Comparison with integrated GFM

The proposed cascaded power controller is compared to the integrated GFM control [7], which is tuned to the same inertia constant, by simulating two disturbances. In both cases the PCC-voltage is controlled by the converter to 1.0 pu, with an active-power reference of $P_{\mathrm{set}} = 0.8$ pu. The first study case is a frequency reduction of the infinite voltage source, ω_{s}, from 50.0 Hz to 49.0 Hz at a rate of 0.5 Hz/s, while in the second case the frequency is varied with 2.0 Hz/s to a minimum of 47.0 Hz. As shown in Fig. 7, in case of the

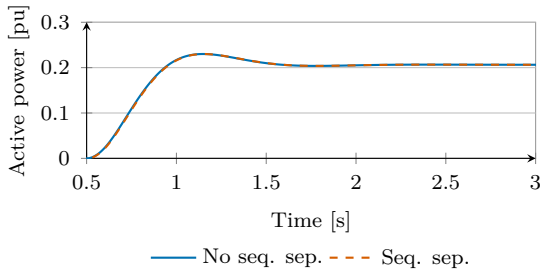

Figure 9: Delay introduced to the inertial response due to the inclusion of the RLS sequence estimation.

smaller frequency disturbance the inertial power response from the two control structures is practically equal, demonstrating that an equivalent response can be achieved with the proposed design. The internal converter frequencies ω_c shown in the top plot are following the declining grid frequency closely. The active-power response exhibits a small delay for the cascaded controller, as in this case the inertial response is coming not from within the APL, but as a change in the power reference.

For the larger frequency disturbance shown in Fig. 8, synchronization is lost when the virtual inertia is provided directly in the APL and consequently the current limiter is saturated (integrated GFM control, red curves). The converter control with the proposed cascaded structure (blue curves) on the other hand is able to limit the current close to its rated value and keep synchronism with the grid. The active power exceeds the limit imposed on P_{ref} (1 pu), because despite of its high bandwidth the APL still contributes some inertia. Still, the converter current can be effectively limited to close to 1 pu without saturating the circular current limitation. It can also be noted that the inertial response continues for approximately 200 ms after the frequency transient has finished. This is due to the fact that the unlimited inertial response reference from the IEL is 0.4 pu, but the response is limited at 0.2 pu. The unlimited inertial response reference starts to decrease from the moment the transient ends, e.g. as in Fig. 7, but due to the limitation this becomes not visible before it has reduced to less than 0.2 pu. This effect could be minimized by including an anti-windup, which increases the IEL bandwidth based on the saturation of the power reference limiter.

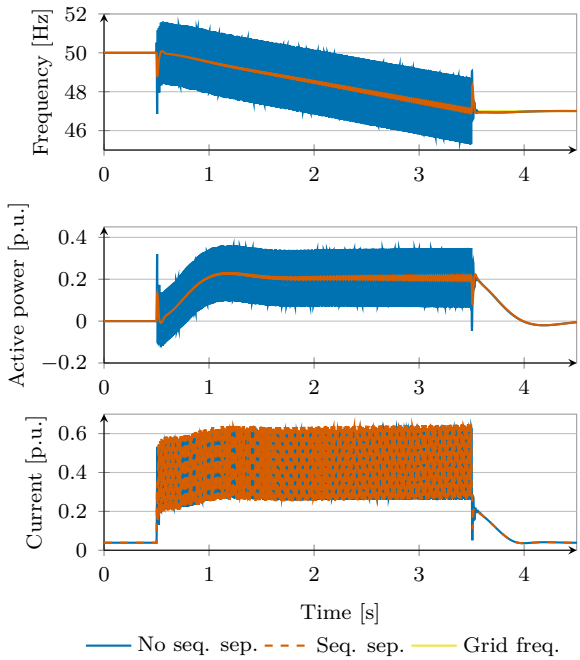

Figure 10: IEL performance without and with sequence separation during an unbalanced voltage dip.

It has even been verified through simulations that there is no notable difference between the cascaded controller's and an integrated GFM's reaction to a grid voltage phase angle jump, apart from the cascaded controller's ability to prevent instability.

4.2 Unbalanced operation and harmonic filtering

The addition of the RLS-based sequence separation causes a small delay to the generated inertial response signal. As demonstrated in Fig. 9, this delay is only minimal. A more detailed analysis shows that the delay is around 5 ms and has therefore a neglectable impact on the inertial timescale. To demonstrate the necessity of sequence separation, additionally to the frequency transient a single-phase voltage dip is applied and the results are presented in Fig. 10.

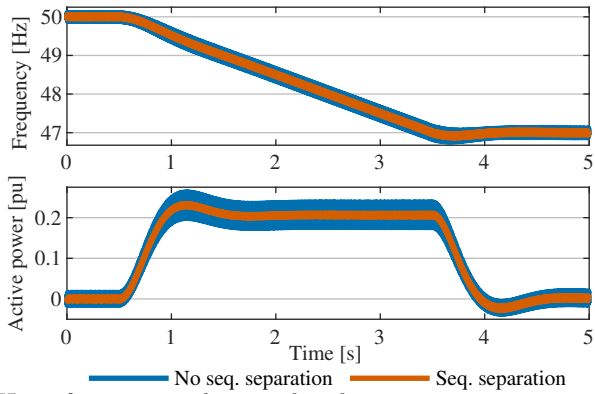

Figure 11: IEL performance without and with sequence separation under the presence of voltage harmonics.

Without the sequence separation (blue curve), the negative sequence causes a 100 Hz-oscillation in the dq-voltage vector, which is transferred into the voltage q-component and consequently inertial-power reference. The red curve shows the results including the sequence separation, and in this case the inertial-power reference is free from harmonic components. The only exception are transient oscillations at the beginning and end of the fault, which are caused by the time needed for the RLS to correctly estimate the sequence components. In Fig. 11, a 5^{th} and 7^{th} harmonic of 0.05 pu magnitude each are added to the source voltage. Even though the RLS is not tuned explicitely to remove these harmonic components, it can be seen that the majority of harmonic content is removed by the RLS and APL, both of which have a low-pass characteristic. This shows that a sequence separation is necessary, that the suggested method has a neglegible impact on the speed of the inertial response and that it effectively rejects oscillations due to unbalanced conditions and harmonic components. It has been verified with simulations that the RLS does not impact the robustness of the proposed approach negatively.

5 Conclusions

This paper demonstrates that grid frequency disturbances can cause instability in inertia-providing GFM converters, and that the existing strategies to

manipulate the power reference during current saturation are ineffective in this case. To solve the problem of loss of synchronism due to a slow active-power loop exposed to current limitation, a cascaded power controller consisting of an IEL and a fast active-power controller is proposed. This approach effectively decouples the control elements responsible for provision of inertia and synchronization to the grid, resulting in a robust behavior even during frequency transients. The structure of the IEL is presented along with simulation results verifying that the proposed approach maintains a stable operation even during major disturbances. Future work on the proposed controller is necessary to investigate the stability limits of the proposed approach and improvements to its large disturbance robustness, as well as lab verification of the presented results.

References

[1] P. Imgart, A. Narula, M. Bongiorno, M. Beza, and J. R. Svensson, "A Cascaded Power Controller for Robust Frequency Ride-Through of Grid-Forming Converters," presented at the 2022 IEEE Energy Conversion Congress and Exposition (ECCE), Detroit, MI, USA, 2022.

[2] J. Matevosyan, B. Badrzadeh, T. Prevost, *et al.*, "Grid-Forming Inverters: Are They the Key for High Renewable Penetration?" *IEEE Power and Energy Magazine*, vol. 17, no. 6, pp. 89–98, Nov. 2019, ISSN: 1558-4216.

[3] L. Huang, L. Zhang, H. Xin, Z. Wang, and D. Gan, "Current limiting leads to virtual power angle synchronous instability of droop-controlled converters," in *2016 IEEE Power and Energy Society General Meeting (PESGM)*, Jul. 2016, pp. 1–5.

[4] H. Lin, C. Jia, J. M. Guerrero, and J. C. Vasquez, "Angle Stability Analysis for Voltage-Controlled Converters," *IEEE Transactions on Industrial Electronics*, vol. 64, no. 8, pp. 6265–6275, Aug. 2017, ISSN: 1557-9948.

[5] T. Qoria, F. Gruson, F. Colas, G. Denis, T. Prevost, and X. Guillaud, "Critical Clearing Time Determination and Enhancement of Grid-Forming Converters Embedding Virtual Impedance as Current Limitation Algorithm," *IEEE Journal of Emerging and Selected Topics in*

Power Electronics, vol. 8, no. 2, pp. 1050–1061, Jun. 2020, ISSN: 2168-6777, 2168-6785.

[6] X. Wang, M. G. Taul, H. Wu, Y. Liao, F. Blaabjerg, and L. Harnefors, "Grid-Synchronization Stability of Converter-Based Resources—An Overview," *IEEE Open Journal of Industry Applications*, vol. 1, pp. 115–134, 2020, ISSN: 2644-1241.

[7] M. G. Taul, X. Wang, P. Davari, and F. Blaabjerg, "Current Limiting Control With Enhanced Dynamics of Grid-Forming Converters During Fault Conditions," *IEEE Journal of Emerging and Selected Topics in Power Electronics*, vol. 8, no. 2, pp. 1062–1073, Jun. 2020, ISSN: 2168-6777, 2168-6785.

[8] E. Rokrok, T. Qoria, A. Bruyere, B. Francois, and X. Guillaud, "Transient Stability Assessment and Enhancement of Grid-Forming Converters Embedding Current Reference Saturation as Current Limiting Strategy," *IEEE Transactions on Power Systems*, pp. 1–1, 2021, ISSN: 1558-0679.

[9] Y. Geng, L. Zhu, X. Song, K. Wang, and X. Li, "A Modified Droop Control for Grid-Connected Inverters With Improved Stability in the Fluctuation of Grid Frequency and Voltage Magnitude," *IEEE Access*, vol. 7, pp. 75 658–75 669, 2019, ISSN: 2169-3536.

[10] L. Xiong, X. Liu, D. Zhang, and Y. Liu, "Rapid Power Compensation-Based Frequency Response Strategy for Low-Inertia Power Systems," *IEEE Journal of Emerging and Selected Topics in Power Electronics*, vol. 9, no. 4, pp. 4500–4513, Aug. 2021, ISSN: 2168-6785.

[11] L. Huang, C. Yang, M. Song, *et al.*, "An Adaptive Inertia Control to Improve Stability of Virtual Synchronous Machines Under Various Power Grid Strength," in *2019 IEEE Power Energy Society General Meeting (PESGM)*, Aug. 2019, pp. 1–5.

[12] Z.-l. Li, J. Hu, and K. W. Chan, "A New Current Limiting and Overload Protection Strategy for Droop-Controlled Voltage-Source Converters in Islanded AC Microgrids Under Grid Faulted Conditions," in *2020 IEEE Energy Conversion Congress and Exposition (ECCE)*, Oct. 2020, pp. 3888–3893.

[13] L. Zhang, L. Harnefors, and H. Nee, "Power-Synchronization Control of Grid-Connected Voltage-Source Converters," *IEEE Transactions on Power Systems*, vol. 25, no. 2, pp. 809–820, May 2010, ISSN: 1558-0679.

[14] A. Gkountaras, S. Dieckerhoff, and T. Sezi, "Evaluation of current limiting methods for grid forming inverters in medium voltage microgrids," in *2015 IEEE Energy Conversion Congress and Exposition (ECCE)*, Sep. 2015, pp. 1223–1230.

[15] J. Rocabert, A. Luna, F. Blaabjerg, and P. Rodríguez, "Control of Power Converters in AC Microgrids," *IEEE Transactions on Power Electronics*, vol. 27, no. 11, pp. 4734–4749, Nov. 2012, ISSN: 0885-8993.

[16] ENTSO-E, "High Penetration of Power Electronic Interfaced Power Sources and the Potential Contribution of Grid Forming Converters," 2020.

[17] R. Rosso, X. Wang, M. Liserre, X. Lu, and S. Engelken, "Grid-Forming Converters: Control Approaches, Grid-Synchronization, and Future Trends — A Review," *IEEE Open Journal of Industry Applications*, vol. 2, pp. 93–109, 2021, ISSN: 2644-1241.

[18] A. Narula, M. Bongiorno, M. Beza, and P. Chen, "Tuning and evaluation of grid-forming converters for grid-support," in *2021 23rd European Conference on Power Electronics and Applications (EPE'21 ECCE Europe)*, Sep. 2021, P.1–P.10.

[19] M. van Wesenbeeck, S. de Haan, P. Varela, and K. Visscher, "Grid tied converter with virtual kinetic storage," in *2009 IEEE Bucharest PowerTech*, Jun. 2009, pp. 1–7.

[20] A. Narula, M. Bongiorno, and M. Beza, "Comparison of Grid-Forming Converter Control Strategies," in *2021 IEEE Energy Conversion Congress and Exposition (ECCE)*, Oct. 2021, pp. 361–368.

[21] P. Rodriguez, I. Candela, C. Citro, J. Rocabert, and A. Luna, "Control of grid-connected power converters based on a virtual admittance control loop," in *2013 15th European Conference on Power Electronics and Applications (EPE)*, Sep. 2013, pp. 1–10.

[22] L. Harnefors, *Control of Variable-Speed Drives*. Västerås: Applied Signal Processing and Control, Department of Electronics, Mälardalen University, 2002.

[23] P. Imgart, M. Beza, M. Bongiorno, and J. R. Svensson, "An Overview of Grid-Connection Requirements for Converters and Their Impact on Grid-Forming Control," *EPE'22 ECCE Europe*, 2022.

[24] M. Beza and M. Bongiorno, "Application of Recursive Least Squares Algorithm With Variable Forgetting Factor for Frequency Component Estimation in a Generic Input Signal," *IEEE Transactions on Industry Applications*, vol. 50, no. 2, pp. 1168–1176, Mar. 2014, ISSN: 1939-9367.

PAPER D

External Inertia Emulation to Facilitate Active-Power Limitation in Grid-Forming Converters

Paul Imgart, Anant Narula, Massimo Bongiorno, Mebtu Beza, Jan R. Svensson

Published in IEEE Transactions on Industry Applications, vol. 60, pp. 9145-9156, Nov. 2024.

The layout has been revised.

Abstract

The aim of this paper is to present a grid-forming (GFM) control strategy with a novel active-power loop (APL) structure facilitating limitation of active power while providing maximum available inertial support. This is achieved by decoupling the synchronization duties of the APL from the inertial support. The latter is provided by calculating the active-power reference through a dedicated inertia-emulation loop (IEL), which is connected in cascade with the APL. The effectiveness of the proposed method is demonstrated through laboratory experiments including frequency transients of varying size and unbalanced operating conditions.

1 Introduction

World-wide transformation efforts towards the future renewable-based power system result in the replacement of synchronous with converter-interfaced generation. The preferred solution for the challenges associated with this development are grid-forming (GFM) converters, which typically rely on their active-power loop (APL) for grid synchronization [2]. This allows the converter to act as a voltage source and enables to easily provide a number of ancilliary services such as inertial support and fault current contribution [3]. One of the main challenges for GFM converters is the necessity to limit the converter current and at the same time maintain stable operation and the required GFM properties [4]. Due to this, as reviewed recently in [5] a large number of publications is available on the topic of current limitation in GFM converters. The vast number of current-limitation strategies for GFM converters can be sorted into three main categories [5]: strategies employing a type of current-reference limiter such as [6]–[10], strategies relying on a virtual impedance for current limitation as for example [11], [12], and finally strategies employing a limitation of the virtual back electro-motive force (EMF) such as [13]. The referenced articles as well as the majority of existing studies dealing with the stability of current-limited GFM converters [7], [14], [15] focus on current limitation during voltage dips. However, as this article will show, grid-frequency disturbances are a relevant cause of current saturation

that can lead to angular instability. This kind of disturbance is particularly challenging when the APL provides not only grid synchronization, but also inertial support.

From the few available publications dealing with frequency-disturbance induced instability, mainly three types of current limitation strategies have been identified. The first is control-mode switching (CMS), as suggested e.g. in [16], where a complex modified droop control manipulates the active and reactive power references based on the converter currents to prevent loss of synchronism due to current saturation. A different approach involving CMS is presented in [17], selecting different frequency-response strategies based on frequency deviation and an estimate of the rate of change of frequency (RoCoF). A third example is given in [18], where a re-synchronization aid function is employed to limit frequency variation while the converter is in current control mode. The second type of strategy is to adapt the inertia, which in [19] is based on grid impedance estimation, to ensure a chosen stability margin for the GFM converter. The third strategy is to switch the synchronization duty during current limitation to a backup synchronization unit, typically a phase-locked loop (PLL) [20]–[22].

CMS as well as parameter adaptation change the converter's properties abruptly, which is typically not desirable. Furthermore, some implementations require knowledge of system parameters such as the grid impedance, which is typically unknown. Inaccurate estimation of these parameters results in either too conservative or excessive limits, making it challenging to fully utilize the converter's actual capabilities without risk of overcurrent [23]. Furthermore, these solutions are typically tailor-made for a specific GFM controller, resulting in a challenging adaptation for usage with other control strategies. The use of a backup PLL during current saturation changes the controller's characteristics and, depending on the implementation, can result in the loss of some of the converter's GFM capabilities [24], which is undesirable as they are typically needed the most during grid disturbances.

The aim of this article is to propose a solution to the GFM stability problem by decoupling the synchronization task of the APL from the provision of inertia. To address the issue properly, the root causes of angular instability in GFM converters are investigated. Here, the focus lies on the sources of instability for inertia-providing controllers in case of large grid-frequency disturbances. It is shown that existing solutions available in the literature,

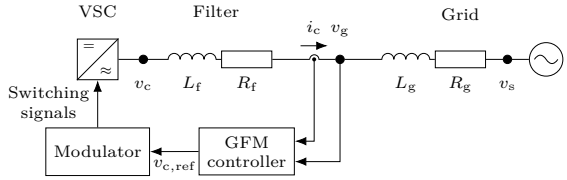

Figure 1: Circuit diagram and control system of a grid-connected converter.

typically based on variation of the active-power reference [6], [7], [11], [14], [15], are not effective for this kind of event because the inertial effect appears in the APL after the reference variation. Based on this analysis, a new solution originally presented in [25] is investigated, consisting of an inertia-emulation loop (IEL) in cascade with a fast APL. The IEL is based on the structure of a PLL and is used to generate an active-power reference emulating the desired amount of inertia, whereas the APL provides synchronization with the grid. Decoupling the synchronization loop from the inertia provision enables to dynamically limit the converter's load angle through the limitation of the active-power reference. As a consequence, the current output of the converter can always be controlled within the converter's ratings without the need for a current-reference limiter, thus preventing instability due to grid-frequency disturbances [26], [27]. Next, the tuning procedure for APL and IEL is established, demonstrating how the IEL parameters relate to the desired inertia constant and damping ratio of the inertial response. This is followed by experimental validation, demonstrating that the desired behavior is achieved. Thanks to the proposed control strategy, it is possible to preserve the GFM properties and limit the converter current without the need for control-mode switching or parameter adaptation.

2 Grid-Forming Converter Stability Problem

The common property of the majority of the GFM control structures suggested in the literature is that the converter should be modelled as a voltage source behind an impedance [3], [28]. This behavior can be achieved using different grid-synchronization methods, e.g. using a dedicated synchronization unit like a PLL. Figure 1 shows a typical grid-connected converter with its controller and the control input and output signals. GFM converters typically syn-

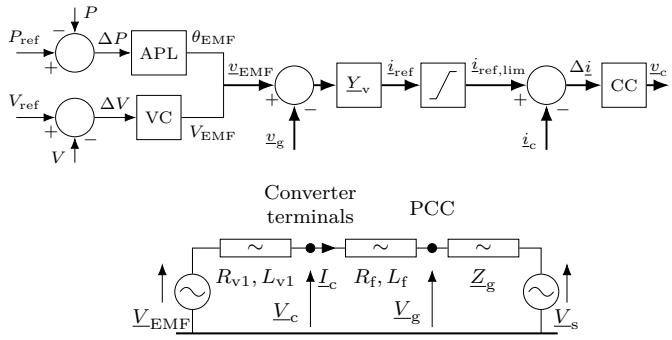

Figure 2: Block scheme (top) and equivalent circuit (bottom) representation of the virtual admittance-based GFM control approach.

chronize by relying on the active-power transfer, which can provide increased robustness in weak grids and islanding operation [29]. In this work, the virtual admittance-based approach from [30] is implemented with the structure displayed in Fig. 2. A detailed description of the control system follows in the next section, as the results of this study are not specific for this control structure.

Angle instability in GFM converters mainly occurs due to two reasons: firstly, the power reference being too large for the grid conditions such as grid strength and voltage, e.g. during a fault [6], [7], [11], [14], [15]; secondly, the power controller being unable to follow the grid voltage angle in case of an angle jump or frequency disturbance. The latter is the focus of this paper.

For the system depicted in Fig. 2 (bottom figure), neglecting the system losses the steady state per-unit converter current is

$$\underline{I}_\mathrm{c} = \frac{\underline{V}_\mathrm{EMF} - \underline{V}_\mathrm{s}}{\mathrm{j}X} = \frac{V_\mathrm{s}\sin\delta + \mathrm{j}(V_\mathrm{s}\cos\delta - V_\mathrm{EMF})}{X}, \tag{D.1}$$

where the *dq*-frame is aligned with the converter back EMF, δ denotes the phase displacement between $\underline{V}_\mathrm{EMF}$ and $\underline{V}_\mathrm{s}$, and X is the sum of reactances between them[1]. The active-power transfer from the converter to the grid is

[1]The virtual admittance $\underline{Y}_\mathrm{v} = \underline{Z}_\mathrm{v}^{-1}$ in Fig. 2 is the inverse of the series of the virtual impedance $\underline{Z}_\mathrm{v1}$ and the physical filter impedance $\underline{Z}_\mathrm{f}$.

defined with $*$ symbolizing the complex conjugate as

$$P = \mathfrak{Re}\{\underline{V}_{\mathrm{EMF}}\underline{I}_{\mathrm{c}}^{*}\} = \frac{V_{\mathrm{s}}V_{\mathrm{EMF}}}{X}\sin\delta, \tag{D.2}$$

and shown in blue in Fig. 3 for an example system.

Denoting with $I_{\max}$ the maximum allowed converter current and using circular current limitation [6] on the current reference I_{ref}, the limited converter-current reference is

$$\underline{I}_{\mathrm{ref,lim}} = \underline{I}_{\mathrm{ref}}\frac{I_{\max}}{I_{\mathrm{ref}}} \qquad \forall\ I_{\mathrm{ref}} > I_{\max}. \tag{D.3}$$

Note that the activation of the current limiter is equivalent to a variation of the phasor $\underline{V}_{\mathrm{EMF}}$, defined as $\underline{V}'_{\mathrm{EMF}}$ in Fig. 4. From the figure, current limitation results in a reduction of the load angle δ when compared with the unlimited case, denoted as δ_{APL}. Even despite this reduction, the angle δ_{APL} still has an impact on the exchanged active power, as it determines the angle of the current reference $\underline{I}_{\mathrm{ref}}$. Using (D.1)-(D.3), the relation between δ_{APL} and the current-limited active power P_{lim} is given as

$$\begin{aligned} P_{\mathrm{lim}} &= \mathfrak{Re}\{\underline{V}_{\mathrm{s}}\underline{I}_{\mathrm{ref,lim}}^{*}\} \\ &= V_{\mathrm{s}}V_{\mathrm{EMF}}\sin\delta_{\mathrm{APL}}\frac{I_{\max}}{\sqrt{V_{\mathrm{s}}^2 + V_{\mathrm{EMF}}^2 - 2V_{\mathrm{s}}V_{\mathrm{EMF}}\cos\delta_{\mathrm{APL}}}}, \\ &\qquad \forall\ I_{\mathrm{ref}} > I_{\max}. \end{aligned} \tag{D.4}$$

Figure 3 illustrates the current-limited P-δ_{APL} relationship following from (D.4) in red. After the current saturates at B, the power transfer decreases for increasing δ_{APL}.

The type of instability highlighted in this section is caused by an inability of inertia-providing APLs to follow the grid voltage angle in case of severe frequency disturbances or phase angle jumps. To follow a change in the grid frequency, the APL needs to adapt its internal frequency, which requires a power control error. As an example, a frequency decline would cause the load angle δ to increase until the additional decelerating power $P_{\mathrm{d}} = -2H\frac{\mathrm{d}\omega_{\mathrm{g}}}{\mathrm{d}t}$ is achieved, where H is the APL's inertia constant in s and ω_{g} is the grid-voltage angular frequency in rad/s. This decelerating power will appear as a steady-state error in the active power for a constant RoCoF. When the current is limited, the needed decelerating power might not be reached, resulting in an

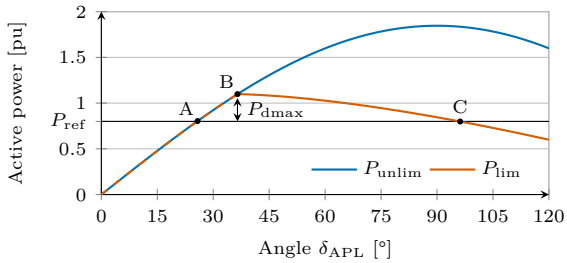

Figure 3: P-δ_{APL} curve illustrating the converter angle stability problem for a current limit of 1.1 pu with $V_{\mathrm{g}} = 1$ pu. A: Pre-disturbance operating point; B: Current limit reached; C: transient stability limit; P_{dmax}: maximum decelerating power.

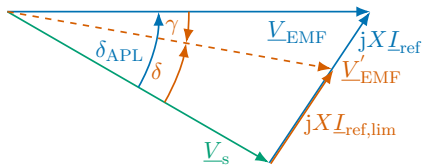

Figure 4: Phasor diagram illustrating the effect of current limitation on the virtual back EMF. Unlimited in blue, limited in red.

continuously increasing load angle. This can cause the loss of synchronism if the unstable equilibrium point C is passed, equivalent to first swing instability in a synchronous machine (SM). It should be noted that the decelerating power only depends on the APL's control parameters and the grid disturbance, not on the active power reference. It is therefore impossible to affect this power control error by limiting the reference, and even during operation with an active-power reference of zero the decelerating power can cause the converter's current limiter to saturate for large inertia constants and frequency disturbances.

The simulation shown in Fig. 5 illustrates this instability mechanism caused by a frequency decrease. During unsaturated operation, the angle γ defined in Fig. 4 is zero. During limitation, the required deceleration power P_{d} cannot be reached and the APL angle δ_{APL} increases steadily. As a consequence, γ is decreasing at an accelerating rate, which demonstrates the loss of the

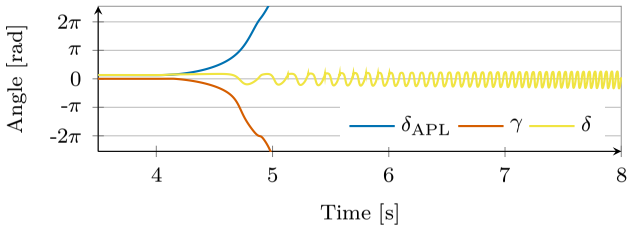

Figure 5: δ_{APL}, γ and δ for converter instability due to frequency disturbance at 4 s.

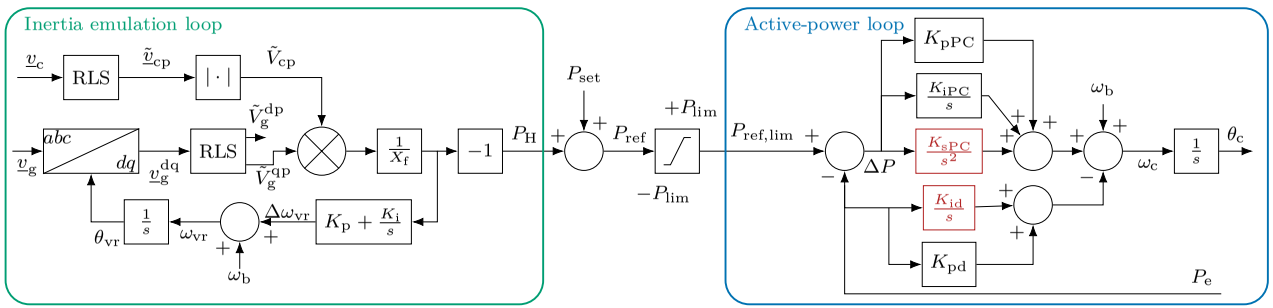

Figure 6: Proposed cascaded structure for the active-power controller of GFM converters with the optional additions for a second-order APL shown in red.

synchronization signal. In this case, loss of synchronism cannot be prevented by limiting the active-power reference, because the additional power is not caused by a change in reference, but by the APL's inability to reject the grid disturbance. GFM converters are prone to this type of instability when they rely on the active-power transfer for synchronization. Due to this, the APL output is not a load angle, but a ramp-formed phase angle. When the APL angle output is manipulated to guarantee current limitation, the synchronization signal is lost. Large inertia, high RoCoF and operating points close to the maximum power transfer will increase the risk for this kind of instability, as the necessary decelerating power increases or the available current for decelerating power decreases, respectively.

3 Proposed Solution

The GFM design incorporating both synchronization and inertial response in the APL is the approach typically encountered in the literature for GFM converters providing an inertial response [29], and will here be referred to as *integrated GFM*. To overcome the described risk for instability present in these approaches, the cascaded structure for the converter's active-power controller displayed in Fig. 6 is proposed here. The PI-based APL tracks the active-power reference and synchronizes with the grid by generating the angle for the converter virtual back EMF. As the duty of the APL is to provide sychronization only, a relatively high loop bandwidth can be selected to ensure good dynamic performance regarding both disturbance rejection (e.g. in the case of phase jumps) and reference tracking.

The inertia response P_{H} is instead calculated by the IEL and added onto the APL's power reference P_{set}. This is similar to the approaches proposed in [31], [32], where a PLL is used to provide an inertial response from a grid-following converter. The advantage of the proposed approach over other methods to provide RoCoF-proportional inertial response is that the frequency derivative is implicitly determined within the IEL. This replaces the noise-sensitive derivation step and means that the RoCoF estimate is immediately available, reducing delays in the converter's inertial response [31]. By generating the inertial response explicitly as a part of the power reference, it can be effectively limited, preventing the previously described instability. In the integrated GFM, a large frequency disturbance would cause the current limiter

to saturate. In the proposed solution, the active-power reference is adequately limited instead, which prevents saturation of the current and the consequential instability. For this, the admissible converter power $S_{\mathrm{lim}} = \frac{V_{\mathrm{g}} S_{\mathrm{N}}}{V_{\mathrm{N}}}$ is estimated with the rated converter power S_{N} and rated voltage ${V_{\mathrm{N}}}^2$. It is used together with the reactive power injected by the converter, Q, to calculate the active-power limit, $P_{\mathrm{lim}} = (S_{\mathrm{lim}}^2 - Q^2)^{1/2}$, which is then applied to the active-power reference P_{ref} [26].

In contrast to the proposed solution, the inertial response from an actual or virtual SM is not achieved by varying the power reference, but is a natural reaction to a frequency transient while mechanical torque or power reference, respectively, are held constant. Due to that it is nontrivial in these control designs to limit the active power without compromising the loop's synchronization task. Separating the inertia from the APL as in the proposed cascaded controller gives on the other hand the possibility to prevent the current from exceeding its rated value by limiting the inertial power, which in turn avoids the triggering of the current limiter in Fig. 2. Generating the inertial response through the APL power reference comes with the additional advantage that the presented IEL can be used with any sufficiently fast APL, and consequently can even be employed in grid-following converters to provide inertial response. Despite of being based on a PLL structure, the IEL does only provide inertia emulation, while the APL is exclusively responsible for active-power reference tracking and, in a GFM, for synchronization with the grid. To enable operation under unbalanced and distorted grid voltage conditions, a sequence separation and harmonic filtering method based on a recursive least square algorithm (RLS) is used on the inputs of the IEL.

The other parts of the controller shown in Fig. 2 are tuned according to the method presented in [26]. While the active-power controller generates the virtual back EMF angle, its magnitude is determined by the voltage controller (VC), here consisting of a simple integrator with a droop. The voltage-based limiter presented in [26] is used to ensure current limitation by reducing the back-EMF magnitude when necessary. The virtual admittance (VA) is used to calculate current references from the limited back EMF voltage and the PCC voltage. Thanks to its resistive-inductive nature, the VA provides reference-

[2] This applies if the converter-power reference should be limited so that 1 pu current is not exceeded. If it is admissible for the converter to temporary inject larger current, e.g. thanks to a temporary overcurrent capability, $S_{\mathrm{lim}} = V_{\mathrm{N}} I_{\mathrm{max}}$ instead, with I_{max} being the temporary current limit.

current filtering (through X_{v}) and damping (through R_{v}); furthermore, it helps in preserving the converter's dynamic performance under varying grid strengths by reducing the impact of the grid impedance on the total impedance variation [33][3]. To ensure proper protection of the converter hardware, a circular current limitation as described in (D.3) is applied to the current references. Note that this current limiter has a protection function only; the controller is designed such that the limiter at maximum saturates for a few samples during the beginning of severe disturbances and relies on the limiters in the outer loop to keep the current within its limit. The limited current references are then fed to a vector-current controller to generate a converter-voltage reference.

3.1 Active-Power Loop Tuning

The APL employed in this paper is based on a PI-regulator, as described in [30], to guarantee proper tracking of the active-power reference even when the grid frequency varies from the rated frequency [35]. The controller's PI-regulator is tuned using a loop-shaping approach with active damping. Following the tuning approach in [25], the controller parameters are selected as

$$K_{\mathrm{pd}} = 2\frac{\alpha_{\mathrm{PC}}}{P_{\mathrm{vmax}}},\ K_{\mathrm{pPC}} = \frac{\alpha_{\mathrm{PC}}}{P_{\mathrm{vmax}}},\ K_{\mathrm{iPC}} = \alpha_{\mathrm{PC}} K_{\mathrm{pd}}, \tag{D.5}$$

where K_{pd} is the active damping term[4], K_{pPC} is the controller's proportional and K_{iPC} the integral gain. α_{PC} is the APL's desired closed-loop control bandwidth, and

$$P_{\mathrm{vmax}} = \frac{V_{\mathrm{EMF}} V_{\mathrm{g}}}{X_{\mathrm{V}}} \tag{D.6}$$

is the converter's power transfer limit as determined by small-signal stability. As demonstrated in [25], this controller is suitable for the desired separation of inertial support from the APL and provides perfect power-reference tracking for constant grid-frequencies.

An ongoing grid-frequency disturbance will however result in a steady-state error in the active power, similar to an inertial response. This can be shown

[3]The virtual reactance is selected in the range of typical SM output reactance [34], while the virtual resistance is chosen to provide a small time constant for the dc-current offset originated from the large virtual reactance.

[4]Note that here the active damping has been changed in comparison to [25] to provide additional active damping in case of active-power reference steps.

by examining the transfer function from a change the grid voltage angle θ_g to the change in the active power ΔP,

$$G_\mathrm{g}(s) = \frac{\Delta P}{\Delta\theta_\mathrm{g}} = \frac{-s^2}{P_\mathrm{vmax}^{-1}s^2 + (K_\mathrm{pPC} + K_\mathrm{pd})s + K_\mathrm{iPC}}. \tag{D.7}$$

A constant RoCoF can be expressed by $\Delta\theta_\mathrm{g} = \frac{k\omega_\mathrm{b}}{s^3}$, where k is the RoCoF in pu and ω_b is the base angular frequency in rad/s. The steady-state error is then given by applying the final value theorem:

$$\lim_{t\to\infty} \Delta P = \lim_{s\to 0} sG_\mathrm{g}(s)\frac{k\omega_\mathrm{b}}{s^3} = -\frac{k\omega_\mathrm{b}}{K_\mathrm{iPC}}. \tag{D.8}$$

If desired, inertial contribution from the APL under the presence of a constant RoCoF can be removed by adding a second-order integrator. In this case, an integrative gain has to be included in the active-damping term to achieve the desired control behavior. This corresponds to the APL shown in Fig. 6 including the blocks in red. The tuning of this second-order APL follows the same loop-shaping approach and is shown below.

The active-power transfer from the converter to the grid neglecting resistances is given by the two port equation (D.2), which can be applied here due to the relatively slow speed of APLs, allowing to use quasi-steady state equations. To tune the controller properly, the equation is formulated with regard to the measurable PCC voltage instead of the Thévenin source, with $\delta = \theta_\mathrm{EMF} - \theta_\mathrm{g}$. Linearizing this equation for small angle differences, and formulating the transfer function for a change in the converter angle with a constant grid voltage phase angle gives the plant model for the controller design as

$$G_\theta(s) = \frac{\Delta P}{\Delta\theta_\mathrm{EMF}} = \frac{V_\mathrm{EMF}V_\mathrm{g}}{X_\mathrm{V}} = P_\mathrm{vmax}. \tag{D.9}$$

The closed-loop transfer function for a step in the power reference including the controller and plant model contains a first- and second-order zero, which results in a pronounced overshoot in the step response. To remove this overshoot, the active damping terms K_pd and K_id/s are introduced as displayed in Fig. 6. This is similar to the approach typically used for vector current controllers (e.g. as suggested in [36]), but in this case an integrative term is included in the active damping as well to cancel the second-order zero. This

results in the transfer function from the output of the PI-regulator to the injected active power

$$G_\omega(s) = \frac{\Delta P}{\Delta \omega_\mathrm{c}} = \frac{1}{K_\mathrm{id}} \frac{P_\mathrm{vmax} K_\mathrm{id} s}{s^2 + P_\mathrm{vmax} K_\mathrm{pd} s + P_\mathrm{vmax} K_\mathrm{id}}, \tag{D.10}$$

which corresponds to a second-order system with natural frequency $\omega_0 = \sqrt{P_\mathrm{vmax} K_\mathrm{id}}$ and the damping ratio $\zeta_\mathrm{D} = P_\mathrm{vmax} K_\mathrm{pd} (2\omega_0)^{-1}$. Good results have been achieved by selecting the natural frequency to match half of the desired control-loop bandwidth α_PC, and choosing a damping ratio of 2, which results in

$$\begin{aligned} K_\mathrm{id} &= \frac{\omega_0^2}{P_\mathrm{vmax}} = \frac{\alpha_\mathrm{PC}^2}{4 P_\mathrm{vmax}} \qquad \text{and} \\ K_\mathrm{pd} &= \frac{2\omega_0 \zeta_\mathrm{D}}{P_\mathrm{vmax}} = \frac{2\alpha_\mathrm{PC}}{P_\mathrm{vmax}}. \end{aligned} \tag{D.11}$$

The closed-loop transfer function from the reference to the actual active power is

$$G_\mathrm{PC}(s) = \frac{\Delta P}{\Delta P_\mathrm{ref}} = \frac{P_\mathrm{vmax} F_\mathrm{PC}}{s + P_\mathrm{vmax}(F_\mathrm{PC} + F_\mathrm{D})}, \tag{D.12}$$

with

$$\begin{aligned} F_\mathrm{PC} &= K_\mathrm{pPC} + \frac{K_\mathrm{iPC}}{s} + \frac{K_\mathrm{sPC}}{s^2} \qquad \text{and} \\ F_\mathrm{D} &= K_\mathrm{pd} + \frac{K_\mathrm{id}}{s} \end{aligned} \tag{D.13}$$

A proper selection of the controller gains by comparing coefficient reduces the system order to one:

$$G_\mathrm{PC}(s) = \frac{P_\mathrm{vmax} F_\mathrm{PC}}{s + P_\mathrm{vmax}(F_\mathrm{PC} + F_\mathrm{D})} = \frac{\alpha_\mathrm{PC}}{s + \alpha_\mathrm{PC}}, \tag{D.14}$$

with

$$\frac{s}{\alpha_\mathrm{PC}} = \frac{s + P_\mathrm{vmax} F_\mathrm{D}}{P_\mathrm{max} F_\mathrm{PC}} \tag{D.15}$$

resulting in

$$F_\mathrm{D} = F_\mathrm{PC} \frac{s}{\alpha_\mathrm{PC}} - \frac{s}{P_\mathrm{vmax}} \tag{D.16}$$

and finally in

$$K_{\mathrm{pd}} + \frac{K_{\mathrm{id}}}{s} = K_{\mathrm{pPC}} \frac{s}{\alpha_{\mathrm{PC}}} + \frac{K_{\mathrm{iPC}}}{\alpha_{\mathrm{PC}}} + \frac{K_{\mathrm{sPC}}}{\alpha_{\mathrm{PC}} s} - \frac{s}{P_{\mathrm{vmax}}}. \tag{D.17}$$

This yields the controller gains

$$\begin{aligned} K_{\mathrm{pPC}} &= \frac{\alpha_{\mathrm{PC}}}{P_{\mathrm{vmax}}} \\ K_{\mathrm{iPC}} &= \alpha_{\mathrm{PC}} K_{\mathrm{pd}} = \frac{2\alpha_{\mathrm{PC}}^2}{P_{\mathrm{vmax}}} \\ K_{\mathrm{sPC}} &= \alpha_{\mathrm{PC}} K_{\mathrm{id}} = \frac{\alpha_{\mathrm{PC}}^3}{4P_{\mathrm{vmax}}} \end{aligned} \tag{D.18}$$

As mentioned before, the addition of a second-order integrator in the APL is optional with the aim to reduce the amount of inertial response from the APL. If a first-order controller is preferred, setting the parameters K_{sPC} and K_{id} in (D.11) and (D.18) to 0 results in the same parameter values as (D.5).

Since in the proposed controller the IEL provides the inertial response and the APL is only responsible for power reference tracking and synchronization, the bandwidth α_{PC} can be selected as desired. Advantages of a fast APL include better rejection of grid-frequency disturbances and consequently more robust synchronization as well as better power reference tracking. In this publication, an APL loop bandwith of 5 Hz is chosen, which is in the frequency range typical used in PLLs used for synchronization in grid-following converters while still respecting the upper limit for control-loop bandwidths for GFM control from the grid codes reported in [37].

3.2 Inertia-Emulation Loop Tuning

The IEL is tuned to behave equivalent in terms of inertial power contribution to a SM. The IEL's output is the pure inertial response P_{H}, which is equivalent to a lossless synchronous condenser (SC), where the mechanical power $P_{\mathrm{m}} = 0$. The fundamental idea is that both SC and IEL track the phase angle of the grid voltage with a given speed, which corresponds to their inertia.

The relation between a change in rotor speed of the SM and an active-power imbalance is given by the swing equation:

$$2H \frac{\mathrm{d}\omega_{\mathrm{r}}}{\mathrm{d}t} = P_{\mathrm{m}} - P_{\mathrm{e}} - K_{\mathrm{d}}(\omega_{\mathrm{r}} - \omega_{\mathrm{s}}). \tag{D.19}$$

Here, H denotes the inertia constant in seconds, ω_r is the angular rotor frequency, ω_g the angular frequency of the grid voltage, P_e the electrical power injected to the grid and K_d the damping coefficient of the machine, with all quantities but H in pu. For a SM operating in a stable steady-state operating point, electrical and mechanical power must be equal. During a grid disturbance, the power imbalance in such a machine will be its inertial response $P_\mathrm{H} = P_\mathrm{m} - P_\mathrm{e}$. Laplace-transforming and rearranging yields

$$\omega_\mathrm{r} s = \frac{-P_\mathrm{H}}{2H} - \frac{K_\mathrm{d}}{2H}(\omega_\mathrm{r} - \omega_\mathrm{s}). \tag{D.20}$$

As the mechanical time constants are much higher than the electrical, the SM's electrical power P_e can be expressed in quasi-steady state as in (D.2), neglecting the resistances. Assuming a dq-coordinate frame that is aligned with the machine's back EMF results in

$$P_\mathrm{e} = \frac{V_\mathrm{EMF} V_\mathrm{s}}{X} \sin(\theta_\mathrm{r} - \theta_\mathrm{s}) = -\frac{V_\mathrm{EMF}}{X} V_\mathrm{s}^\mathrm{q}, \tag{D.21}$$

where V_s^q denotes the source voltage q-component, and X the sum of reactances between the back EMF and source voltage. In the SC case with $P_\mathrm{m} = 0$, back EMF and grid voltage are aligned with each other in steady state and V_s^q is zero. A change in the grid voltage phase angle would result in a misalignment of the voltages and an active power $P_\mathrm{H} = P_\mathrm{e}$.

For small angle differences, this can be linearized as

$$P_\mathrm{H} = \frac{V_\mathrm{EMF} V_\mathrm{s}}{X}(\theta_\mathrm{r} - \theta_\mathrm{s}) = \frac{V_\mathrm{EMF} V_\mathrm{s}}{Xs}(\omega_\mathrm{r} - \omega_\mathrm{g}), \tag{D.22}$$

using the angular frequency and phase angle relationships

$$\theta_\mathrm{r} s = \omega_\mathrm{r} \qquad \text{and} \qquad \theta_\mathrm{s} s = \omega_\mathrm{s}. \tag{D.23}$$

In most cases, the additional power and consequently angle difference due to inertial response is small, and the linearization creates only negligible deviations. Using the previous equation to rearrange (D.20) with the SM maximum transferable active power $P_\mathrm{smax} = \frac{V_\mathrm{EMF} V_\mathrm{s}}{X}$ results in

$$\omega_\mathrm{r} s = -(\frac{K_\mathrm{d}}{2H P_\mathrm{smax}} s + \frac{1}{2H}) P_\mathrm{H}. \tag{D.24}$$

Equivalent behaviour can be established for the IEL. If the emulated inertial-power reference P_{H} is chosen as the input to the IEL's PI-regulator, the derivative of the loop's internal frequency is determined as

$$\omega_{\mathrm{vr}} s = -(K_{\mathrm{p}} s + K_{\mathrm{i}}) P_{\mathrm{H}}, \tag{D.25}$$

where ω_{vr} is the loop's frequency estimate and K_{p} and K_{i} the proportional and integral gain, respectively. P_{H} is given by

$$P_{\mathrm{H}} = -\frac{V_{\mathrm{c}}}{X_{\mathrm{f}}} V_{\mathrm{g}}^{\mathrm{q}}, \tag{D.26}$$

with the PCC voltage q-component $V_{\mathrm{g}}^{\mathrm{q}}$ in the coordinate system aligned with the IEL angle θ_{vr}, and the filter reactance X_{f}[5]. This equation is the two-port equation formulated with the converter terminal and PCC voltage. The virtual back EMF is replaced with the converter terminal voltage because the virtual resistance can take values that are too high to be neglected, making the use of the simplified two-port equation inaccurate. The Thévenin source voltage $\underline{V}_{\mathrm{s}}$ is replaced with the PCC voltage because the latter can be directly measured. The tracking behaviour of SM and IEL given in (D.24) and (D.25), respectively, can be related to each other to establish equivalent behavior with the following tuning:

$$K_{\mathrm{i}} = \frac{\omega_{\mathrm{b}}}{2H}, \quad K_{\mathrm{p}} = \frac{\omega_{\mathrm{b}} K_{\mathrm{d}}}{2H P_{\max}}, \quad \text{with} \quad P_{\max} = \frac{V_{\mathrm{c}} V_{\mathrm{g}}}{X_{\mathrm{f}}}. \tag{D.27}$$

This formulation assumes all quantities in the IEL are in pu with the exception of virtual angular frequency ω_{vr} and virtual rotor angle θ_{vr}, which is why the base angular frequency ω_{b} appears in both expressions. Thus, the integral gain of the IEL directly relates to the inertia constant of the SM behavior to be reproduced, while the proportional gain represents the damping. It should be noted that that the inertial effect from the IEL and the APL are cumulative. This is due to the reason that the IEL's inertial effect is added to the active-power reference fed to the APL, while the APL's inertial effect manifests as a power control error, i.e. in addition to the loop's power reference. To achieve the desired total inertial effect, the APL's inertia constant should be

[5] Instead of V_{c} and X_{f}, V_{EMF} and X_{v} could be chosen instead. Here, the converter voltage and filter reactance are chosen to avoid the power coupling dynamics introduced by R_{v} and to couple the emulated inertia closer to the grid voltage.

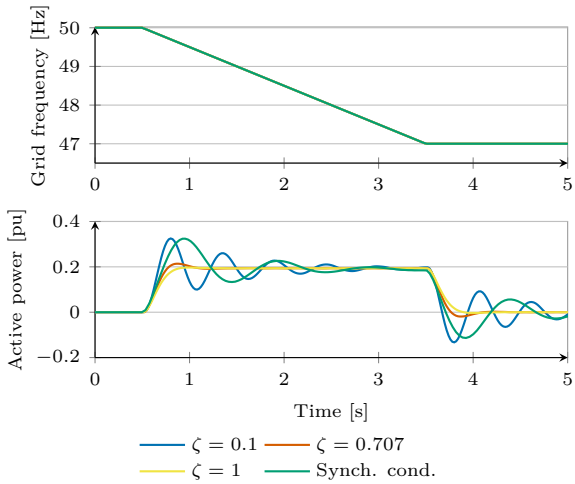

Figure 7: Comparison with synchronous condenser and impact of the damping ratio on rise time and overshoot.

subtracted from the total inertia constant to determine the inertia constant used for tuning the IEL. The first-order APL's inertial effect is, based on (D.8), (D.18), and (D.24), given as $H_{\mathrm{PC}} = \omega_{\mathrm{b}} P_{\mathrm{vmax}}/(4\alpha_{\mathrm{PC}}^2)$. In case a second-order APL is used, the IEL is tuned with the total inertia constant. In either case, the cumulative inertial effect will be equivalent to a SM with the same inertia constant.

To enable the controller to leave active-power saturation after extreme grid-frequency disturbances more quickly, the auxiliary PI-controller suggested in [38] is implemented in the IEL.

3.3 Selection of Damping

As mentioned above, the proportional gain relates to the damping of the inertial response from the IEL. The relation in (D.27) determines K_{p} if a specific SM damping coefficient is to be reproduced. In a SM, damping is linked to physical properties such as friction and typically associated with losses. In consequence, SMs are usually poorly dampened. In the IEL, the damping does not imply any losses, which means it becomes an additional

degree of freedom. Increased damping comes however with the downside of a slower response.

In the previous section was established that inertial response relates to tracking changes in the grid voltage angle with a specific speed. This tracking speed is determined by the IEL closed loop transfer function, given as

$$G_{\mathrm{IEL}}(s) = \frac{\Delta\theta_{\mathrm{vr}}}{\Delta\theta_{\mathrm{g}}} = \frac{P_{\max}(K_{\mathrm{p}}s + K_{\mathrm{i}})}{s^2 + P_{\max}K_{\mathrm{p}}s + P_{\max}K_{\mathrm{i}}}, \tag{D.28}$$

employing the small angle linearization

$$\Delta\theta_{\mathrm{g}} = \frac{1}{V_{\mathrm{g}}}\Delta V_{\mathrm{g}}^{\mathrm{q}}. \tag{D.29}$$

This is a damped second order response with a zero,

$$G_{\mathrm{IEL}}(s) = \frac{2\zeta\omega_{\mathrm{n}}s + \omega_{\mathrm{n}}^2}{s^2 + 2\zeta\omega_{\mathrm{n}}s + \omega_{\mathrm{n}}^2}, \quad \text{where} \tag{D.30}$$
$$\omega_{\mathrm{n}} = \sqrt{\frac{\omega_{\mathrm{b}}P_{\max}}{2H}}, \quad \text{and} \quad \zeta = \sqrt{\frac{\omega_{\mathrm{b}}}{2HP_{\max}}}K_{\mathrm{d}}$$

using (D.27), which allows to determine the proportional gain based on the damping ratio as

$$K_{\mathrm{p}} = \zeta\sqrt{\frac{2\omega_{\mathrm{b}}}{HP_{\max}}}. \tag{D.31}$$

The effect of different damping ratios is shown in the results from time-domain simulations in Fig. 7. For this study case, the frequency of the voltage source is reduced with 1 Hz/s from 50 Hz to 47 Hz, while the steady-state active-power reference is set to $P_{\mathrm{set}} = 0$ pu. The inertia constant is selected as $H = 4.68$ s, which together with the inertial contribution from the first-order APL employed in this simulation results in a total inertia constant of 5 s, meaning that the frequency disturbance should result in an inertial response of 0.2 pu. The figure demonstrates that the proposed controller is able to reproduce the behavior of a SM with good accuracy. The proposed approach combines a fast APL with a change in the power reference, while the response from the SM is purely based on its mechanical behavior. From the figure, it can be appreciated that the proposed solution has a smaller rise time when tuned to the same damping ratio as the SM. This can be understood from

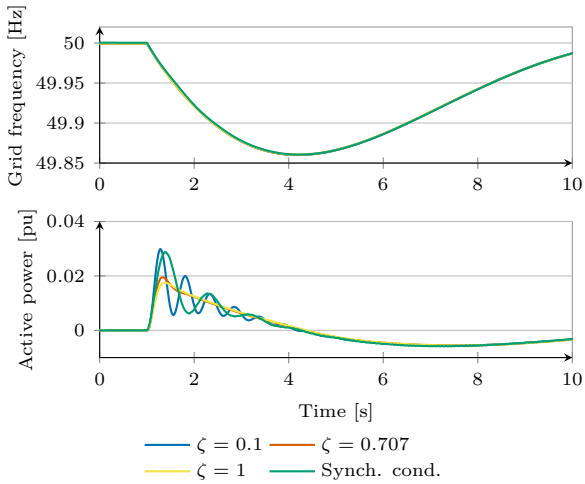

Figure 8: Comparison of the inertial contribution from a synchronous condenser and an IEL with varying damping ratio during a frequency disturbance caused by a load step.

(D.24), (D.25) and (D.27): As the filter reactance X_f used for the parameter selection in the IEL is smaller than a typical SM's transient reactance, the IEL's inertia is coupled more closely to the grid voltage and thereby reacts faster to frequency changes. It can also be seen that the low damping of the SM causes a challenging behavior. As the IEL damping can be freely adapted without any losses, a response without overshoot ($\zeta = 1$) can be selected. As an additional degree of freedom in the controller tuning, the damping ratio of the inertial response can be selected according to the needs and specifications of the converter system and the connecting grid. To achieve a compromise between speed and damping of the inertial response, a damping ratio of $\zeta = 0.707$ is suggested and chosen in this paper.

To study the impact of the damping of the inertial response under a more realistic grid frequency disturbance, a load step is simulated. The grid model employed is based on the lumped-mass representation of the Nordic synchronous area detailed in [39]. The lumped-mass model has a PID-governor and hydro-turbine model, which are tuned using the parameters given in [39].

The system model's ratings have been chosen in relation the size of the converter used for the experimental validation in Section 4, and are given in Table 2 in the appendix. The simulation results for a load step of 0.02 pu are shown in Fig. 8. As can be seen from the figure, the proposed controller can reproduce SM behaviour even for this disturbance type. Furthermore, the results show that increased damping does not have a notable effect on the frequency nadir.

3.4 Sequence Separation and Harmonic Filtering

Unbalanced conditions or operation under distorted grid voltages impact the IEL and result in an unsteady inertial-power reference. To avoid this, a sequence separation algorithm is applied to the PCC and converter-terminal voltages, as shown in Fig. 6. The RLS based method from [40] in its implementation in *dq*-coordinates as described in [26] is used here. As mentioned in [40], the method can be used to not only separate positive and negative sequences, but can in distorted grids also be used to simultaneously estimate selected harmonic components. The harmonics present in the grid voltage will lead to oscillations in $v_{\mathrm{g,q}}$ in the IEL's reference frame, and are therefore added to the power reference by the IEL. Due to this, it can be advisable to use the RLS for harmonic estimation, in particular to the IEL's input signals, which allows to keep the active-power reference as free from harmonic content as possible. Due to the low-pass filtering characteristic of the RLS, the RLS provides some harmonic filtering even for the harmonics not explicitly included in the separation [40].

In this paper, for both the APL's and the IEL's RLS estimator the same relative bandwidth of $\xi = \omega_{\mathrm{RLS}}/\omega b = 0.9$ is selected to provide a good compromise between estimation time and estimation accuracy. In this paper, the IEL's estimator is tuned to provide sequence separation as well as harmonic estimation for 5th and 7th harmonic. The delay added by the RLS estimator has been shown to be neglegible [25].

4 Experimental Validation

In this section the results of laboratory validation of the proposed controller are presented and discussed, verifying the effectiveness of the proposed solu-

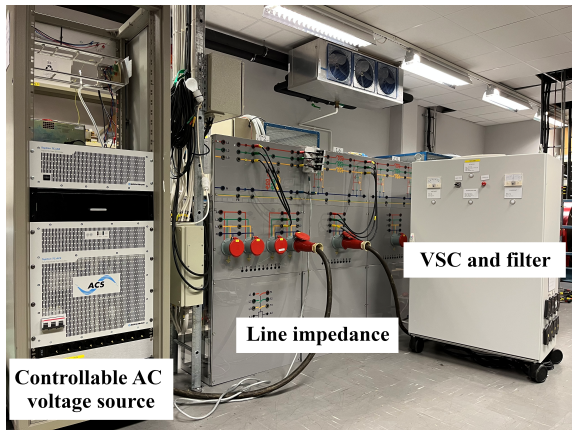

Figure 9: Photo of the laboratory setup used for validation.

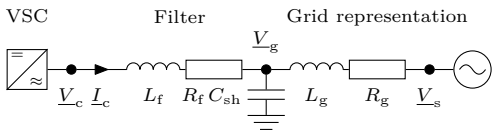

Figure 10: Single-line diagram of the laboratory setup.

tion in dealing with the challenges described in Section 2. The experiments are conducted using the setup depicted in Fig. 9, which is illustrated in the single-line diagram in Fig. 10. In the laboratory setup, a REGATRON four-quadrant controllable AC power source is utilized to emulate the Thévenin voltage of the power grid, and inductors are used to adapt the grid strength according to $X_g = 1/\mathrm{SCR}$. The GFM converter system is realized using a 2-level voltage source converter supplied by an ideal DC voltage source. The converter system is connected to the grid at the PCC through a filter reactor with inductance L_f and resistance R_f. A dSPACE DS1006 processor board is used to control the GFM converter. The setup's system and control parameters are given in Table 1.

To validate the converter's response to a frequency disturbance, a linear frequency variation (frequency ramp) is considered, in accordance with [41]–[43]. A frequency ramp is the harshest condition for the synchronization

system, as it leads to a constant phase variation (which depends on the ramp's slope). Furthermore, the use of a frequency ramp allows to directly verify that the inertia contribution corresponds to the desired inertia constant.

4.1 Comparison of Active-Power Loops

A step in the active-power reference is used to compare the performance of the first-order APL used in [25] and the second-order APL described in the previous section. At $t = 1\,\mathrm{s}$, the active-power reference is stepped from 0 to 0.5 pu. The IEL is deactivated during steps in the active-power reference to appreciate the dynamic performance of the APL. The results from this test are shown in Fig. 11. From the figure can be seen that the second-order APL's response in yellow is following the first-order APL's response in red. This shows that both APL designs provide equivalent reference tracking performance if the same closed-loop bandwidth is chosen due to the loop-shaping approach used to tune the controller parameters.

As explained, the reason to add a second-order integrator to the APL is to completely remove the APL's inertial response for constant RoCoFs. This effect is illustrated in Fig. 12, where the response of a first- and second-order APL to a frequency ramp of 5 Hz/s is shown. In both cases, the IEL is deactivated to emphasize the difference between the two APLs. As can be seen from the figure, the first-order APL provides an undesired inertial response during the RoCoF. In the second-order APL, the second-order integrator compensates for the constant RoCoF, removing the inertial contribution after a short

Table 1: System and control parameters.

System parameters		Control parameters	
S_N	1 kVA	L_v1	0.343 pu
V_N	100 V	R_v1	0.2343 pu
ω_b	314.16 rad/s	α_PC	2π 5 rad/s
L_f	0.157 pu	ζ_P	2
R_f	0.0157 pu	α_CC	2π 500 rad/s
SCR	3.18	α_VC	2π 1 rad/s
C_sh	0.0942 pu	H	5 s
		ζ	0.707

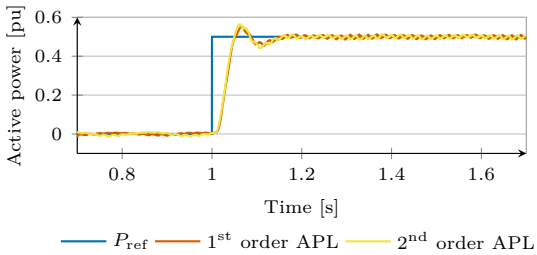

Figure 11: Step response of the first- and second-order APL. Displayed is the positive-sequence active power.

time. Even though the inertial contribution from the first-order APL may appear small in relation to the RoCoF, this power exceeds the active-power reference. In applications with limited energy storage such as a STATCOM, it is necessary to reduce the APL's inertia as much as possible to allow for tight control of the active-power exchange. Furthermore, as this inertial contribution is added onto the limited active-power reference, the injected power can exceed the limit if the reference saturates during a grid-frequency disturbance, to a lesser extent than but not unlike the integrated GFM.

4.2 Comparison with Integrated GFM

The proposed solution is here compared to an *integrated GFM* controller; as described in Section 3, the latter consists of the first-order APL tuned to provide the same inertia and damping as the combined IEL and APL in the proposed solution. To compare the performance of the proposed solution to this controller, two experiments are conducted. In both cases the PCC-voltage is controlled by the converter to 1.0 pu, with an active-power reference of $P_{\text{set}} = 0.8\,\text{pu}$. The first study case is a frequency reduction of the infinite voltage source, ω_{s}, from 50.0 Hz to 49.25 Hz at a rate of 0.5 Hz/s, while in the second case the frequency is varied with 2.0 Hz/s to a minimum of 47 Hz. In both cases, the disturbance has a duration of 1.5 s and begins at $t = 1\,\text{s}$.

The results for the smaller RoCoF are shown in Fig. 13. From the figure it can be seen that the proposed GFM controller, plotted in red, is able to recreate the inertial response of the internal GFM controller in blue, with the only exception being a slightly larger overshoot at the beginning and end of

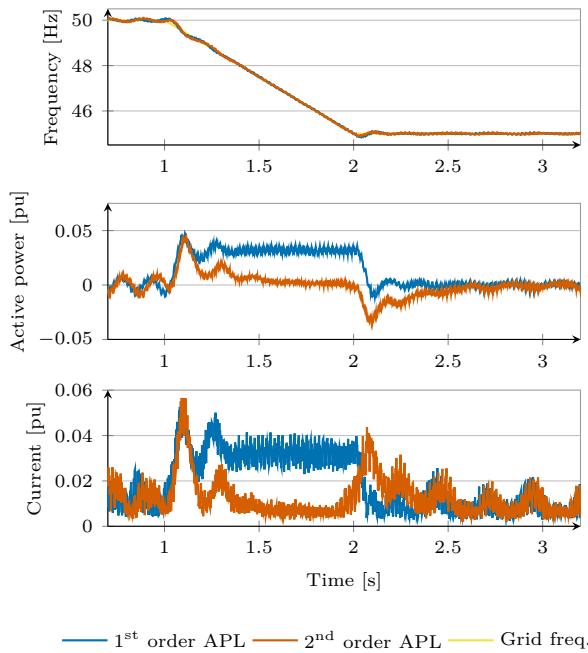

Figure 12: Dynamic response of first- and second-order APL to a grid-frequency disturbance of 5 Hz/s during $t = 0\,\mathrm{s}$ to 1 s. Top: Grid and internal converter frequency ($f_\mathrm{c} = \omega_\mathrm{c}/(2\pi)$). Middle: Positive sequence active power. Bottom: Converter-current magnitude I_c.

the response. As the integrated GFM controller's provides inertia through a slow APL, the internal converter frequency ω_c is filtered in this case. Since the proposed controller's APL has a higher bandwidth, which comes with the advantages of improved synchronization and robustness as well as faster reference tracking, the converter frequency shows a higher harmonic content in this case. This increased harmonic content, however, does not result in more oscillations in the active power or current exchanged with the grid, as can be seen from the two lower plots showing active power and current. This experiment shows that the proposed control structure is able to recreate the inertial response of an integrated GFM or other VSM implementations.

Figure 14 contains the results for the larger frequency disturbance. In this

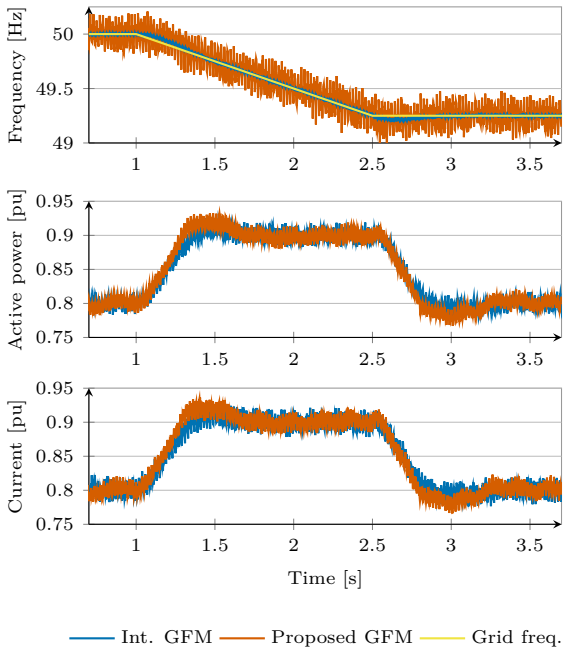

Figure 13: Dynamic response of integrated GFM and proposed solution to a grid-frequency disturbance of 0.5 Hz/s during $t = 0\,\text{s}$ to $1.5\,\text{s}$. Top: Grid and internal converter frequency. Middle: Positive sequence active power. Bottom: Converter-current magnitude I_c.

case the integrated GFM controller (blue) demonstrates the instability described in Section 2: The current limiter prevents the power exchange to reach the necessary acceleration power, and the converter in consequence loses synchronism. The proposed GFM control structure shown in red is on the other hand able to limit the active-power exchange to 1 pu and maintains stable operation. It is important to stress that in the proposed solution, current limitation is purely achieved by the manipulation of the reference active-power signal and that the reference-current limiter (see Fig. 2) is never triggered. In contrast to the simulations presented in [25], the active power of the proposed solution does not exceed 1 pu and does immediately end when the RoCoF subsides. This is the result of the inclusion of the auxiliary PI controller described

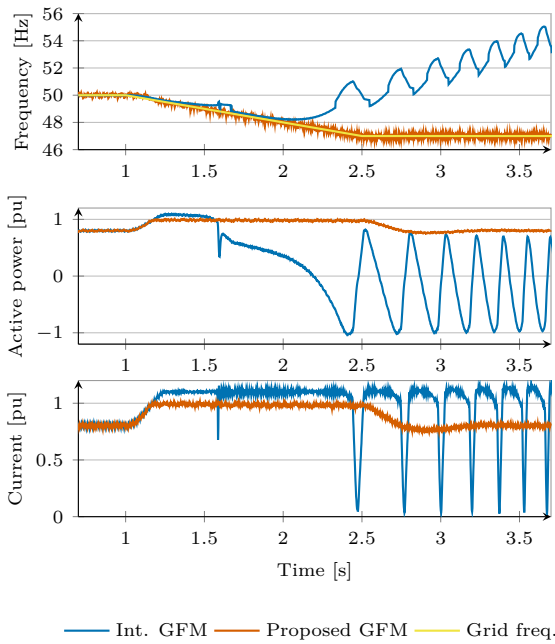

Figure 14: Dynamic response of integrated GFM and proposed solution to a grid-frequency disturbance of 2 Hz/s during $t = 0$ s to 1.5 s. Top: Grid and internal converter frequency. Middle: Positive sequence active power. Bottom: Converter-current magnitude I_c.

in [38].

4.3 Operation Under the Presence of Grid-Voltage Unbalance

The capability of the proposed solution to withstand unbalanced grid condition is tested in an experiment involving a single-phase voltage dip of 0.5 pu, together with a frequency disturbance of 1 Hz/s. This test also demonstrates the importance of sequence separation in the IEL. The results of the experiment are illustrated in Fig. 15, with the blue curves showing the results of deactivated sequence separation in the IEL, and the red curves the results of

an active RLS providing sequence separation for the IEL. In both cases, the sequence separation for APL and current controller remains active.

As can be seen from the figure, without sequence separation the active power from the GFM is highly distorted. Without the sequence separation, the negative sequence causes a 100 Hz-oscillation in the dq-voltage vector, which is transferred into the voltage q-component and consequently to the inertial-power reference. The plot shows that there is even a notable amount of harmonic distortion before and after the disturbance, which is due to the unavoidable presence of unbalance and low-order harmonics in the laboratory setup. The addition of the RLS-based sequence separation in the IEL reduces the oscillations in the full active power drastically, and even removes most of the oscillations present in the positive-sequence active power. The small transient oscillations at the beginning and end of the fault are caused by the time needed for the RLS to correctly estimate the sequence components.

4.4 Operation Under the Presence of Grid-Voltage Harmonics

The IEL can not only cause oscillations in the active-power reference and active power exchanged with the grid when there are unbalances in the grid voltage, but also due to the presence of harmonics. This effect is demonstrated in the experiment shown in Fig. 16, where a 5th and 7th harmonic of 0.05 pu magnitude each are added to the grid voltage. As in the previous study, a grid-frequency disturbance of 1 Hz/s is applied for 1.5 s. Similar to the unbalanced case, the figure shows that the controller without filtering in the IEL (blue) causes more harmonic content in the active power. It can also be seen that this controller is not capable of providing the desired inertial response - this is due to the oscillation in the power reference exceeding the active-power limit. This saturation causes the active-power flow which is subjected to the filtering effect of the APL to have a reduced mean. The red curve, illustrating the controller with activated RLS estimator, shows reduced harmonic content in the power flows and the desired inertial response. If other harmonics are present in the intended application, they can similarly be removed by including them in the RLS estimation algorithm.

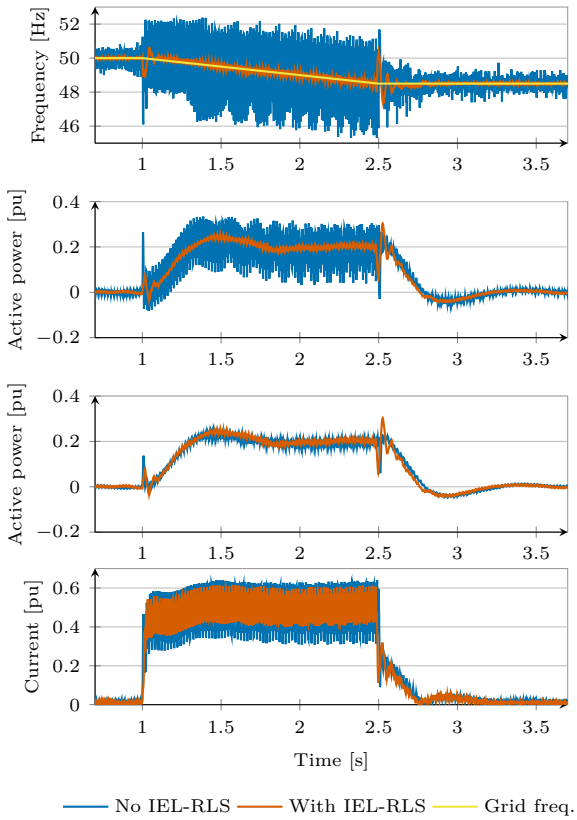

Figure 15: Dynamic response of the proposed solution to a simultaneous single-phase voltage dip of 0.5 pu and grid-frequency disturbance of 1 Hz/s during $t = 0\,\mathrm{s}$ to $1.5\,\mathrm{s}$. From top to bottom: Grid and internal converter frequency, active power, positive-sequence active power, converter-current magnitude I_c.

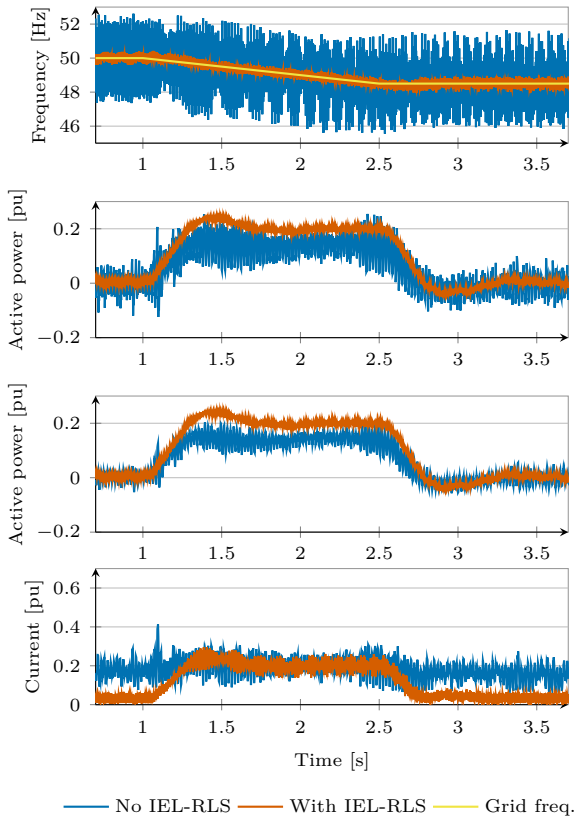

Figure 16: Dynamic response of the proposed solution to a grid-frequency disturbance of 1 Hz/s during $t = 0\,\mathrm{s}$ to $1.5\,\mathrm{s}$ under the presence of 5th- and 7th harmonic with a magnitude of 0.05 pu each. From top to bottom: Grid and internal converter frequency, active power, positive sequence active power, converter-current magnitude I_c.

5 Conclusions

This paper has demonstrated that grid-frequency disturbances can be the cause of instability in inertia-providing GFM converters, and that the existing strategies to manipulate the power reference during current saturation are ineffective in this case. To solve the problem of loss of synchronism due to a slow active-power loop exposed to current limitation, a cascaded power controller consisting of an IEL in cascade with a fast APL has been proposed. A second-order integrator can be added to the APL to completely remove the APL's inertia. The experimental validation has confirmed that this approach effectively decouples the control elements responsible for provision of inertia and synchronization to the grid, resulting in a stable operation even during major disturbances. The proposed controller has been shown to be robust against unbalanced and distorted grid voltage conditions and to allow for effective active-power limitation while at the same time providing inertial support.

Appendix

Table 2: Lumped-mass model parameters for load step simulation

System parameters	
S_{G}	10 kVA
V_{N}	100 V
H_{sys}	5 s

References

[1] P. Imgart, A. Narula, M. Bongiorno, M. Beza, and J. R. Svensson, "External Inertia Emulation to Facilitate Active-Power Limitation in Grid-Forming Converters," *IEEE Transactions on Industry Applications*, vol. 60, no. 6, pp. 9145–9156, Nov. 2024, ISSN: 1939-9367.

[2] J. Matevosyan, B. Badrzadeh, T. Prevost, *et al.*, "Grid-Forming Inverters: Are They the Key for High Renewable Penetration?" *IEEE Power and Energy Magazine*, vol. 17, no. 6, pp. 89–98, Nov. 2019, ISSN: 1558-4216.

[3] ENTSO-E, "High Penetration of Power Electronic Interfaced Power Sources and the Potential Contribution of Grid Forming Converters," 2020.

[4] L. Huang, L. Zhang, H. Xin, Z. Wang, and D. Gan, "Current limiting leads to virtual power angle synchronous instability of droop-controlled converters," in *2016 IEEE Power and Energy Society General Meeting (PESGM)*, Jul. 2016, pp. 1–5.

[5] B. Fan, T. Liu, F. Zhao, H. Wu, and X. Wang, "A Review of Current-Limiting Control of Grid-Forming Inverters Under Symmetrical Disturbances," *IEEE Open Journal of Power Electronics*, pp. 1–15, 2022, ISSN: 2644-1314.

[6] M. G. Taul, X. Wang, P. Davari, and F. Blaabjerg, "Current Limiting Control With Enhanced Dynamics of Grid-Forming Converters During Fault Conditions," *IEEE Journal of Emerging and Selected Topics in Power Electronics*, vol. 8, no. 2, pp. 1062–1073, Jun. 2020, ISSN: 2168-6777, 2168-6785.

[7] E. Rokrok, T. Qoria, A. Bruyere, B. Francois, and X. Guillaud, "Transient Stability Assessment and Enhancement of Grid-Forming Converters Embedding Current Reference Saturation as Current Limiting Strategy," *IEEE Transactions on Power Systems*, pp. 1–1, 2021, ISSN: 1558-0679.

[8] R. Rosso, S. Engelken, and M. Liserre, "On The Implementation of an FRT Strategy for Grid-Forming Converters Under Symmetrical and Asymmetrical Grid Faults," *IEEE Transactions on Industry Applications*, vol. 57, no. 5, pp. 4385–4397, Sep. 2021, ISSN: 1939-9367.

[9] B. Wang, R. Burgos, and B. Wen, "Grid-Forming Inverter Control Strategy with Improved Fault Ride Through Capability," in *2022 IEEE Energy Conversion Congress and Exposition (ECCE)*, Oct. 2022, pp. 1–8.

[10] Y. Liu, H. Geng, M. Huang, and X. Zha, "Dynamic Current Limiting of Grid-forming Converters for Transient Synchronization Stability Enhancement," *IEEE Transactions on Industry Applications*, pp. 1–11, 2023, ISSN: 0093-9994, 1939-9367.

[11] T. Qoria, F. Gruson, F. Colas, G. Denis, T. Prevost, and X. Guillaud, "Critical Clearing Time Determination and Enhancement of Grid-Forming Converters Embedding Virtual Impedance as Current Limitation Algorithm," *IEEE Journal of Emerging and Selected Topics in Power Electronics*, vol. 8, no. 2, pp. 1050–1061, Jun. 2020, ISSN: 2168-6777, 2168-6785.

[12] Z. Yang, G. Zhao, and H. Yu, "Current limiting control method with adaptive virtual impedance for grid-forming STATCOM," *Energy Reports*, vol. 9, pp. 453–460, Apr. 2023, ISSN: 23524847.

[13] J. Erdocia, A. Urtasun, and L. Marroyo, "Dual Voltage–Current Control to Provide Grid-Forming Inverters With Current Limiting Capability," *IEEE Journal of Emerging and Selected Topics in Power Electronics*, vol. 10, no. 4, pp. 3950–3962, Aug. 2022, ISSN: 2168-6777, 2168-6785.

[14] H. Lin, C. Jia, J. M. Guerrero, and J. C. Vasquez, "Angle Stability Analysis for Voltage-Controlled Converters," *IEEE Transactions on Industrial Electronics*, vol. 64, no. 8, pp. 6265–6275, Aug. 2017, ISSN: 1557-9948.

[15] X. Wang, M. G. Taul, H. Wu, Y. Liao, F. Blaabjerg, and L. Harnefors, "Grid-Synchronization Stability of Converter-Based Resources—An Overview," *IEEE Open Journal of Industry Applications*, vol. 1, pp. 115–134, 2020, ISSN: 2644-1241.

[16] Y. Geng, L. Zhu, X. Song, K. Wang, and X. Li, "A Modified Droop Control for Grid-Connected Inverters With Improved Stability in the Fluctuation of Grid Frequency and Voltage Magnitude," *IEEE Access*, vol. 7, pp. 75 658–75 669, 2019, ISSN: 2169-3536.

[17] L. Xiong, X. Liu, D. Zhang, and Y. Liu, "Rapid Power Compensation-Based Frequency Response Strategy for Low-Inertia Power Systems," *IEEE Journal of Emerging and Selected Topics in Power Electronics*, vol. 9, no. 4, pp. 4500–4513, Aug. 2021, ISSN: 2168-6785.

[18] T. Qoria, X. Wang, and R. Kadri, "Grid-forming control VSC-based including current limitation and re-synchronization functions to deal with symmetrical and asymmetrical faults," *Electric Power Systems Research*, vol. 223, p. 109 647, Oct. 2023, ISSN: 03787796.

[19] L. Huang, C. Yang, M. Song, *et al.*, "An Adaptive Inertia Control to Improve Stability of Virtual Synchronous Machines Under Various Power Grid Strength," in *2019 IEEE Power Energy Society General Meeting (PESGM)*, Aug. 2019, pp. 1–5.

[20] Z.-l. Li, J. Hu, and K. W. Chan, "A New Current Limiting and Overload Protection Strategy for Droop-Controlled Voltage-Source Converters in Islanded AC Microgrids Under Grid Faulted Conditions," in *2020 IEEE Energy Conversion Congress and Exposition (ECCE)*, Oct. 2020, pp. 3888–3893.

[21] L. Zhang, L. Harnefors, and H. Nee, "Power-Synchronization Control of Grid-Connected Voltage-Source Converters," *IEEE Transactions on Power Systems*, vol. 25, no. 2, pp. 809–820, May 2010, ISSN: 1558-0679.

[22] J. Chen, F. Prystupczuk, and T. O'Donnell, "Use of voltage limits for current limitations in grid-forming converters," *CSEE Journal of Power and Energy Systems*, vol. 6, no. 2, pp. 259–269, Jun. 2020, ISSN: 2096-0042.

[23] A. Gkountaras, S. Dieckerhoff, and T. Sezi, "Evaluation of current limiting methods for grid forming inverters in medium voltage microgrids," in *2015 IEEE Energy Conversion Congress and Exposition (ECCE)*, Sep. 2015, pp. 1223–1230.

[24] L. Huang, C. Wu, D. Zhou, and F. Blaabjerg, "A Power-Angle-Based Adaptive Overcurrent Protection Scheme for Grid-Forming Inverter Under Large Grid Disturbances," *IEEE Transactions on Industrial Electronics*, vol. 70, no. 6, pp. 5927–5936, Jun. 2023, ISSN: 1557-9948.

[25] P. Imgart, A. Narula, M. Bongiorno, M. Beza, and J. R. Svensson, "A Cascaded Power Controller for Robust Frequency Ride-Through of Grid-Forming Converters," presented at the 2022 IEEE Energy Conversion Congress and Exposition (ECCE), Detroit, MI, USA, 2022.

[26] A. Narula, P. Imgart, M. Bongiorno, M. Beza, J. R. Svensson, and J.-P. Hasler, "Voltage-based Current Limitation Strategy to Preserve Grid-forming Properties Under Severe Grid Disturbances," *IEEE Open Journal of Power Electronics*, pp. 1–13, 2023, ISSN: 2644-1314.

[27] M. Bongiorno, J. Svensson, and J.-P. Hasler, "A Control System Configured for, and a Method for, Emulating a Virtual Synchronous Machine of a Grid-Forming Voltage Source Converter," pat. WO/2024/074214, Apr. 11, 2024.

[28] J. Rocabert, A. Luna, F. Blaabjerg, and P. Rodríguez, "Control of Power Converters in AC Microgrids," *IEEE Transactions on Power Electronics*, vol. 27, no. 11, pp. 4734–4749, Nov. 2012, ISSN: 0885-8993.

[29] R. Rosso, X. Wang, M. Liserre, X. Lu, and S. Engelken, "Grid-Forming Converters: Control Approaches, Grid-Synchronization, and Future Trends — A Review," *IEEE Open Journal of Industry Applications*, vol. 2, pp. 93–109, 2021, ISSN: 2644-1241.

[30] A. Narula, M. Bongiorno, M. Beza, and P. Chen, "Tuning and evaluation of grid-forming converters for grid-support," in *2021 23rd European Conference on Power Electronics and Applications (EPE'21 ECCE Europe)*, Sep. 2021, P.1–P.10.

[31] M. van Wesenbeeck, S. de Haan, P. Varela, and K. Visscher, "Grid tied converter with virtual kinetic storage," in *2009 IEEE Bucharest PowerTech*, Jun. 2009, pp. 1–7.

[32] M. Schweizer, S. Almér, S. Pettersson, A. Merkert, V. Bergemann, and L. Harnefors, "Grid-Forming Vector Current Control," *IEEE Transactions on Power Electronics*, vol. 37, no. 11, pp. 13 091–13 106, Nov. 2022, ISSN: 1941-0107.

[33] A. Narula, M. Bongiorno, and M. Beza, "Comparison of Grid-Forming Converter Control Strategies," in *2021 IEEE Energy Conversion Congress and Exposition (ECCE)*, Oct. 2021, pp. 361–368.

[34] P. Rodriguez, I. Candela, C. Citro, J. Rocabert, and A. Luna, "Control of grid-connected power converters based on a virtual admittance control loop," in *2013 15th European Conference on Power Electronics and Applications (EPE)*, Sep. 2013, pp. 1–10.

[35] A. Narula, M. Bongiorno, M. Beza, J. R. Svensson, X. Guillaud, and L. Harnefors, "Impact of steady-state grid-frequency deviations on the performance of grid-forming converter control strategies," in *2020 22nd European Conference on Power Electronics and Applications (EPE'20 ECCE Europe)*, Lyon, France: IEEE, Sep. 2020, P.1–P.10, ISBN: 978-90-75815-36-8.

[36] L. Harnefors, *Control of Variable-Speed Drives*. Västerås: Applied Signal Processing and Control, Department of Electronics, Mälardalen University, 2002.

[37] P. Imgart, M. Beza, M. Bongiorno, and J. R. Svensson, "An Overview of Grid-Connection Requirements for Converters and Their Impact on Grid-Forming Control," *EPE'22 ECCE Europe*, 2022.

[38] P. Imgart, M. Bongiorno, J. R. Svensson, and M. Beza, "Stability Limits and Improved Robustness of Grid-Forming Converters With External Inertia-Emulation Loop," in *2023 25th European Conference on Power Electronics and Applications (EPE'23 ECCE Europe)*, Aalborg, Denmark: IEEE, Sep. 4, 2023, pp. 1–8, ISBN: 978-90-75815-41-2.

[39] ENTSO-E, E. Ørum, L. Haarla, *et al.*, "Future system inertia 2," 2018.

[40] M. Beza and M. Bongiorno, "Application of Recursive Least Squares Algorithm With Variable Forgetting Factor for Frequency Component Estimation in a Generic Input Signal," *IEEE Transactions on Industry Applications*, vol. 50, no. 2, pp. 1168–1176, Mar. 2014, ISSN: 1939-9367.

[41] Verband der Elektrotechnik Elektronik Informationstechnik e. V., *VDE FNN Guideline: Grid forming behaviour of HVDC systems and DC-connected PPMs*, 2020.

[42] Verband der Elektrotechnik Elektronik Informationstechnik e. V., *Technical requirements for grid connection of high voltage direct current systems and direct current-connected power park modules (VDE-AR-N 4131 TAR HVDC)*, Mar. 2019.

[43] National Grid ESO, *Final Modification Report GC0137: Minimum Specification Required for Provision of GB Grid Forming (GBGF) Capability*, Nov. 11, 2021.

PAPER E

Stability Limits and Improved Robustness of Grid-Forming Converters With External Inertia-Emulation Loop

Paul Imgart, Massimo Bongiorno, Jan R. Svensson, Mebtu Beza

Published in 25th European Conference on Power Electronics and Applications (EPE'23 ECCE Europe).

The layout has been revised.

Abstract

An external inertia emulation loop (IEL) prevents instability in grid-forming converters during frequency disturbances. This paper investigates IEL stability limits and compares three alternatives to improve IEL performance under power limitation. Simulations confirm the IEL's robustness and the effectiveness of the proposed solution in avoiding undesired active-power injection at the disturbance end.

1 Introduction

The world-wide transformation towards sustainable power grids is leading to an increased share of grid-connected power electronics, which challenges the grid stability. Grid-forming (GFM) converter control is the preferred solution discussed for these challenges, since the converter behaves as a slowly changing voltage source. This behaviour allows the converter to enhance grid stability for example by providing inertial response or short-circuit current [2], [3]. However, this behavior can also give rise to control instability during grid disturbances and in particular when the converter current is to be limited [4]. To deal with these instabilities and preserve the GFM behaviour in all operating conditions, a cascaded power controller (CPC) has been proposed in [5] and [6]. This controller consists of a fast active-power loop (APL) for reference tracking and synchronization, and an inertia-emulation loop (IEL), which generates the desired inertial response as part of the APL's reference. As shown in [5], [6], the CPC significantly increases the robustness of the converter system against grid frequency disturbances.

While the effectiveness of the CPC in providing grid support and at the same time maintaining synchronous operation of the converter even in case of extreme grid disturbances has been established, the stability limits of this control strategy have not been investigated yet. The tests conducted in [6] have shown that the CPC is robust even for a high rate of change of frequency (ROCOF), but it is important to understand at which ROCOF the CPC loses the ability to track the grid voltage angle for a given inertia constant. This can be relevant in particular for operation in weak grids, where the local ROCOF can deviate notably from the system ROCOF experienced at the center

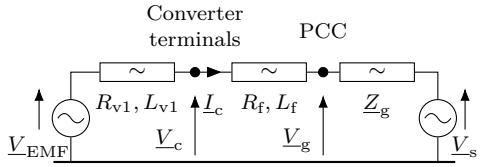

Figure 1: Investigated system setup.

of inertia, putting high stress on the GFM converter [7]. Furthermore, it is important to consider that GFM converters in future grids can be required to operate with inertia constants much higher than typical for synchronous machines, up to several tens of seconds, which can reduce the stability margin of the CPC. An example for an application with a high inertia constant could be a large offshore wind farm combined with an GFM controlled energy-storage equipped static compensator (ES-STATCOM) to provide inertial support and other ancillary services [8].

The aim of this paper is to understand possible stability limits for the IEL in terms of maximum ROCOF and emulated inertia, and to provide suitable modifications to the original IEL controller. After a theoretical investigation of the IEL robustness, three alternatives to improve the IEL are presented and compared through time-domain simulations.

2 IEL Stability Limits

The theoretical stability limits of the IEL are analyzed using the system depicted in Fig. 1, and the converter control presented in [6] and shown in Fig. 2. The controller is a virtual admittance-based GFM converter controller, with a CPC consisting of a fast APL and an IEL, an AC voltage controller, a virtual admittance (VA) and a current controller. In this controller, a voltage-based current limitation is employed, based on the limitation of the active power reference and virtual back EMF magnitude to prevent current-limiter induced instability as described in [6]. The IEL enables effective limitation of the APL's power reference by providing the desired inertial response as part of the reference; its structure is presented in Fig. 3. The proportional gain $K_{p,IEL}$ and the integral gain $K_{i,IEL}$ of the IEL are tuned following the procedure from

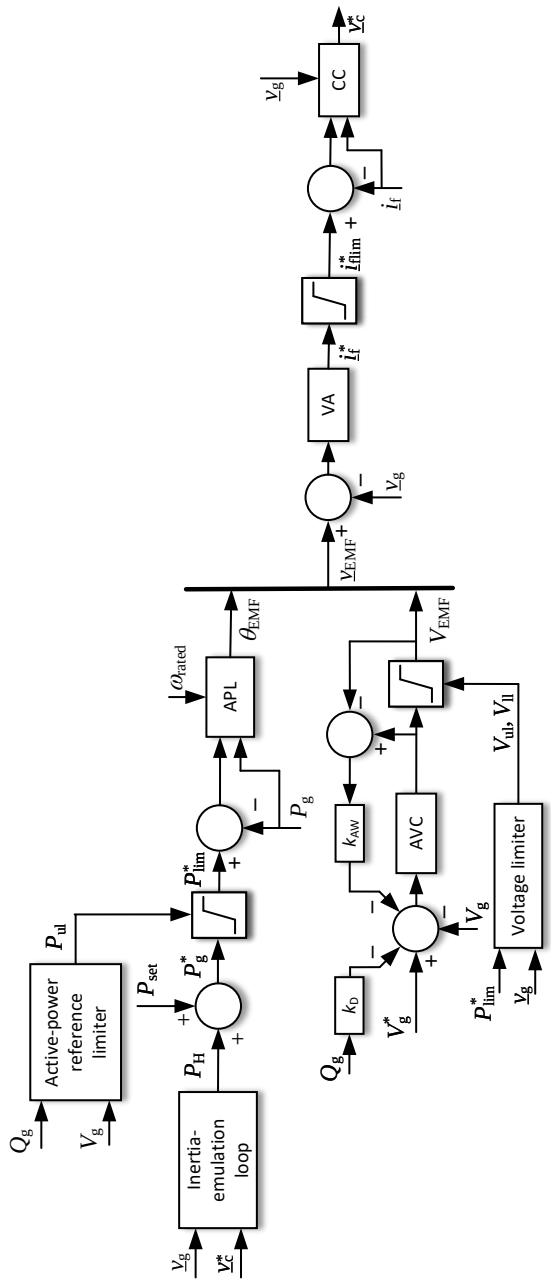

Figure 2: Block diagram of the investigated GFM converter control with CPC [6].

[5] and depend on the desired inertia constant and damping:

$$K_{\mathrm{p,IEL}} = \zeta\sqrt{\frac{2\omega_{\mathrm{b}}L_{\mathrm{f}}}{H}} \quad \text{and} \quad K_{\mathrm{i,IEL}} = \frac{\omega_{\mathrm{b}}}{2H}, \tag{E.1}$$

where ζ is the damping ratio of the inertial response, ω_{b} is the nominal angular frequency of the grid voltage, L_{f} is the converter filter inductance in pu and H is the inertia constant emulated by the IEL.

In a weak grid, the IEL indirectly influences the grid voltage by changing the active power reference. This interaction will alter the ROCOF experienced at the grid connection point by the converter. To reduce unnecessary complexity and investigate the worst case, an infinitely strong grid is assumed here.

As can be seen from the IEL block diagram in Fig. 3, the inertial power P_{H} is determined by

$$P_{\mathrm{H}} = -\frac{v_{\mathrm{gq,IEL}}V_{\mathrm{c}}^{*}}{L_{\mathrm{f}}}, \tag{E.2}$$

where V_{c}^{*} is the magnitude of the converter voltage reference in pu and $v_{\mathrm{gq,IEL}}$ is the q-component of the grid voltage in pu in the IEL reference frame. The latter is given as

$$v_{\mathrm{gq,IEL}} = V_{\mathrm{g}}\sin(\delta_{\mathrm{IEL}}), \tag{E.3}$$

where V_{g} is the grid voltage magnitude and $\delta_{\mathrm{IEL}} = \theta_{\mathrm{g}} - \theta_{\mathrm{IEL}}$ is the angle difference between the grid voltage vector phase angle θ_{g} and the internal IEL angle θ_{IEL}. Consequently, the IEL tracks the grid angle with a bandwidth determined by L_{f} and the parameters of the PI-controller. In steady-state, δ_{IEL} (and consequently P_{H}) is zero; in case of phase-angle jumps or grid frequency excursions however, the result is a non-zero angle difference δ_{IEL}, causing an inertial response. This inertial response is proportional to the size of the phase-angle jump or the ROCOF, respectively, and thereby mimics the mechanical inertia of a synchronous machine. To achieve this, the presence of an angle difference as a reaction to a ROCOF is intentional. The IEL is a second-order controller, and a constant ROCOF results in a constant angle difference.

Depending on the ROCOF, selected inertia, and active power set-point P_{set}, the sum of P_{set} and inertial response P_{H} can exceed the active power capacity of the converter. In this case the active power reference needs to

be limited. This is also the case in presence of voltage disturbances, such as voltage dips, when reactive power might need to be prioritized. Under active power reference limitation, δ_{IEL} exceeds the value that is required to provide the actual available inertial response given by $P_{\mathrm{lim}} - P_{\mathrm{set}}$. This results in an active power injection that continues even after the frequency disturbance subsides. A large angle difference δ_{IEL} can also lead to IEL instability. Both problems are investigated in detail in continuation.

2.1 IEL Instability

To determine at which ROCOF an IEL with a given tuning loses the ability to track the grid voltage angle, an analysis of the controller in Fig. 3 that takes the non-linearity into account is neccessary. The internal IEL frequency ω_{IEL} and the angle separation δ_{IEL} are determined by

$$\omega_{\mathrm{IEL}} = \frac{1}{L_{\mathrm{f}}}\Bigg(K_{\mathrm{p,IEL}} V_{\mathrm{c}} v_{\mathrm{gq,IEL}} + K_{\mathrm{i,IEL}} \int V_{\mathrm{c}} v_{\mathrm{gq,IEL}}\,\mathrm{d}t\Bigg) + \omega_{\mathrm{b}} \tag{E.4}$$

$$\delta_{\mathrm{IEL}} = \int (\omega_{\mathrm{g}} - \omega_{\mathrm{IEL}})\,\mathrm{d}t + \theta_{\mathrm{g0}}, \tag{E.5}$$

where ω_{g} is the grid frequency. With the aim to identify the critical ROCOF that causes IEL instability, the voltage magnitudes V_{c} and V_{g} are assumed to be constant. Under these conditions, differentiating (E.4) by time results in

$$\dot{\omega}_{\mathrm{IEL}} = \frac{1}{L_{\mathrm{f}}}\left(K_{\mathrm{p,IEL}} V_{\mathrm{c}} \dot{v}_{\mathrm{g,q}} + K_{\mathrm{i,IEL}} V_{\mathrm{c}} v_{\mathrm{gq,IEL}}\right). \tag{E.6}$$

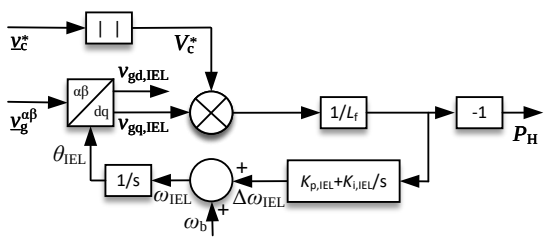

Figure 3: Block diagram of the IEL [6].

If the ROCOF is constant, δ_{IEL} will approach a constant value. For this analysis, the dynamics of the inertial response are disregarded and this final value is considered, which results in $\dot{v}_{\mathrm{g,q}} = 0$. Substituting this in (E.6) yields

$$\dot{\omega}_{\mathrm{IEL}} = \frac{V_{\mathrm{c}} V_{\mathrm{g}}}{L_{\mathrm{f}}} K_{\mathrm{i,IEL}} \sin \delta_{\mathrm{IEL}}. \tag{E.7}$$

A constant angle difference requires ω_{IEL} to be equal to ω_{g}. In the constant-ROCOF case that is considered here, this results also in $\dot{\omega}_{\mathrm{IEL}} = \dot{\omega}_{\mathrm{g}}$. However, as can be seen from (E.7), the maximum ROCOF that the IEL can follow is reached for a δ_{IEL} of $\pm 90°$, when $\sin \delta_{\mathrm{IEL}} = 1$. This is the critical ROCOF and a larger ROCOF will result in the inability of the IEL to track the grid voltage angle, i.e. instability. From (E.7), the critical ROCOF is given as

$$\dot{\omega}_{\mathrm{g,crit}} = \pm \frac{V_{\mathrm{c}} V_{\mathrm{g}}}{L_{\mathrm{f}}} K_{\mathrm{i,IEL}} = \pm \frac{V_{\mathrm{c}} V_{\mathrm{g}} \omega_{\mathrm{b}}}{2 H L_{\mathrm{f}}}, \tag{E.8}$$

where in the second expression the integral gain has been substituted according to (E.1).

To illustrate this, the IEL differential equation is numerically solved with the parameters in Table 1 to estimate the angle separation between the grid voltage and the internal IEL angle. For this isolated simulation of the IEL, the magnitude of the grid and converter voltage are assumed to 1 pu and the inertial power reference P_{H} is limited between 0 and 1 pu. The results for a stable (ROCOF $= -3$ Hz/s) and an unstable (ROCOF $= -3.75$ Hz/s) case are shown in Fig. 4. In the stable case, the absolute value of the angle separation remains below 90° during the complete disturbance, whereas in the unstable case, the stability limit is exceeded approximately 0.75 s after the disturbance begins. As can be seen from the figure, the IEL does not lose stability at the instant the ROCOF starts, but after the disturbance has persisted for some time, during which the angle separation to grow until it surpasses the stability limit. It is important to stress that the frequency has already decreased to approximately 47 Hz at this point.

Table 1: IEL parameters.

Parameter	Value
H	50 s
ζ	0.707
L_{f}	0.15 pu

The non-negligible duration before instability occurs motivates further study of the relation between the inertia constant, the ROCOF, and the ROCOF duration causing IEL instability. For this purpose, a parameter study has been conducted based on the same numerical model. The IEL's response is simulated for a selection of inertia constants and over a wide range of ROCOFs.

The results shown in Fig. 5 are used to investigate the stability margin as a function of inertia constant and ROCOF. In the top plot, the duration of constant ROCOF it takes δ_{IEL} to surpass the stability limit of 90° is depicted, denoted as time to instability. At the bottom, instead the grid frequency at the instant when the stability limit is crossed is shown. From these results it can be concluded that the IEL is stable for all realistic ROCOF values. In conventional power plants with synchronous generators, the inertia constant is typically in the range of 2 s to 10 s [9], and in this range, IEL instability does not occur for a ROCOF and grid frequency close to the operating limits defined in current grid codes [10]. Even with the expectation that the decrease in inertia caused by an increasing share of converter-interfaced generation results in larger frequency deviations and ROCOFs in future power systems [11], risk for instability might only occur if exceptionally high inertia provision is required from the converter.

This could be the case in situations where a single GFM converter provides inertial response for a number of other units, such as an ES-STATCOM for a wind farm. In this situation, the required inertia constant – a relative value depending on the unit's rated power – can be notably higher than in today's conventional power plants. As indicated by [3], it can be expected that in future converter-dominated power grids only a minority of converters will have GFM capabilities, which increases the probability that unusually high inertia constants are required.

Nevertheless, Fig. 5 shows that even for an emulated inertia of 50 s, a high constant ROCOF of ±5 Hz/s can be sustained for 0.5 s before the IEL loses stability. Although it is of vital importance to guarantee stable converter operation in all feasible operating conditions, based on these considerations the main motivation for the modifications suggested in this paper lies not in the risk of IEL instability, but in the consequences of operation under power reference saturation described below.

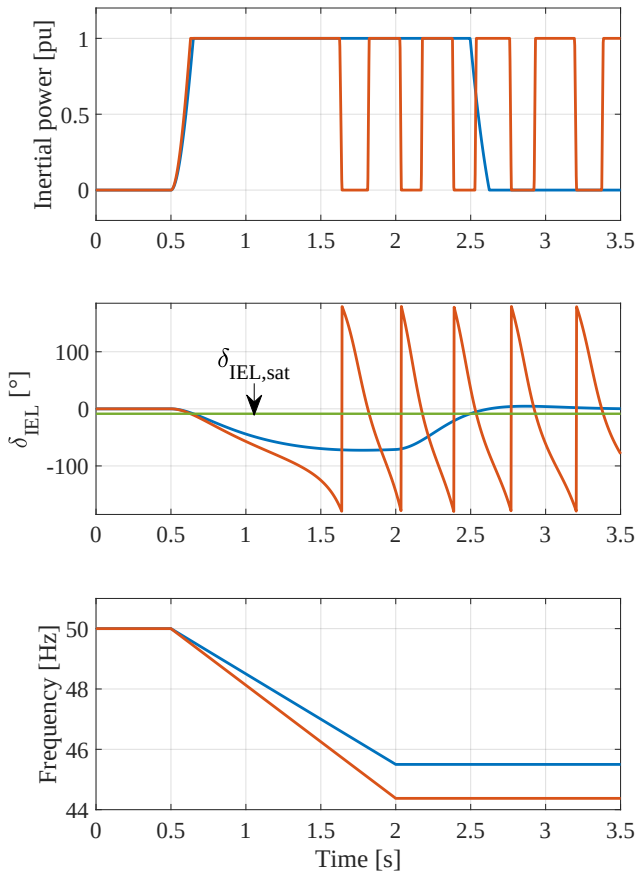

Figure 4: Top: Limited inertial power reference for a stable (blue) and an unstable case (red). Middle: Angle separation between grid voltage angle and internal IEL angle. Bottom: Grid frequency.

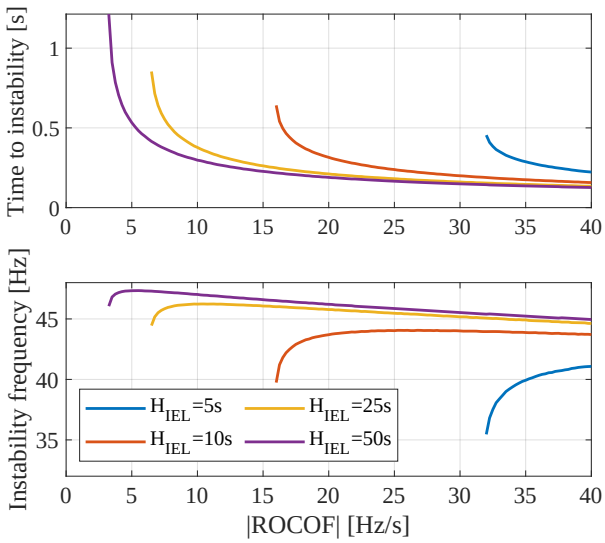

Figure 5: Top: Estimated critical ROCOF and time to occurence of IEL instability, depending on the inertia constant. Bottom: Estimated critical ROCOF and frequency at occurence of IEL instability.

2.2 IEL under power limitation

As can be seen from the stable case presented in Fig. 4, the inertial power continues to be injected for approximately 500 ms even after the ROCOF subsides. The reason for this is shown in the second plot in the same figure, where the estimated δ_{IEL} is shown. Due to the large ROCOF, the angle difference is much larger than what is needed to achieve the maximum possible inertial power of $P_{\mathrm{H}} = 1\,\mathrm{pu}$, indicated as $\delta_{\mathrm{IEL,sat}}$ in the figure.

The consequence of this extended supply is an excessive inertial support, which can unnecessarily increase the energy storage requirements of the converter system. This effect can also have a negative impact on grid frequency restoration dynamics, since P_{H} does not follow the frequency derivative during this time. Finally, the saturation of the angle difference results in the IEL losing its damping ability during the ROCOF. Thus, the excessive angle difference causes the IEL to lose control over P_{H} while $|\delta_{\mathrm{IEL}}| > \delta_{\mathrm{IEL,sat}}$, which is undesirable.

3 IEL Modifications for Improved Performance

To improve the IEL behaviour in the areas described in the previous section, three modifications of the IEL are suggested in this section. They are shown in Fig. 6a – 6c with the changes to the basic controller from Fig. 3 highlighted in red.

3.1 Angle-Based IEL

From (E.7) follows that the sine-function introduces a non-linearity into the IEL, which limits the maximum ROCOF. Replacing $\sin\delta_{\mathrm{IEL}}$ with an estimation of δ_{IEL} itself would address this problem. δ_{IEL} is estimated by using the atan2-function, since it correctly estimates the sign of δ_{IEL} and is insensitive to changes in the grid voltage magnitude. Using atan2 without further adaptations increases the linear control range up to an angle difference of $\pm 180°$, where the estimated angle will switch its sign.

The derivations in [5] resulting in the presented tuning of the IEL assume $v_{\mathrm{gq,IEL}}$, not δ_{IEL} as the IEL input. However, $\delta_{\mathrm{IEL,sat}}$ can be considered small for values of L_{f} that are typical for grid-connected converter system. Thus, replacing the IEL input as described here will not have a significant impact

on the inertial response.

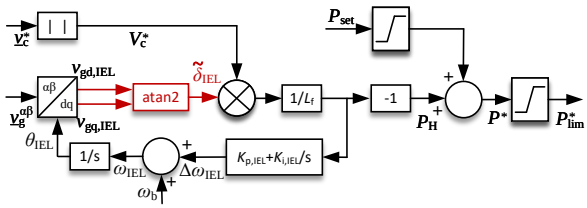

(a) Angle-based IEL adaptation.

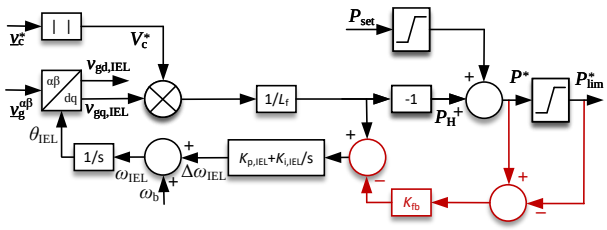

(b) Saturation feedback IEL adaptation.

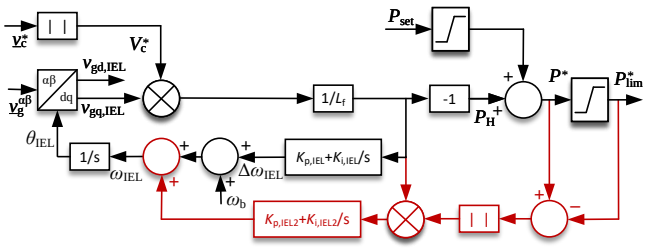

(c) IEL adaptation with auxiliary PI-controller.

Figure 6: IEL modification suggestions.

3.2 Saturation Feedback

The two problems described in the previous section are both caused by δ_{IEL} exceeding $\delta_{\mathrm{IEL,sat}}$ (or $P_{\mathrm{H}} + P_{\mathrm{set}}$ exceeding P_{lim}, which is equivalent). Because of this, a feedback of the difference between the unlimited and the limited active power references $P^* - P^*_{\mathrm{lim}}$ can be used to mitigate these problems.

Table 2: System and control parameters for the simulations.

System parameters		Control parameters	
S_N	1 kVA	L_v1	0.35 pu
V_N	100 V	R_v1	0.235 pu
ω_N	314.16 rad/s	α_APL	2π 15 rad/s
R_f	0.015 pu	α_CC	2π 500 rad/s
SCR	10	α_VC	2π 1 rad/s

Ideally, the angle difference should saturate as little as possible, which is why the usage of a gain K_fb in the feedback path is advised. An excessive gain on the other hand has a negative impact on dynamic behaviour and stability. The best choice for this gain is system dependent, but for the simulated setup a gain of $K_\mathrm{fb} = 100$ has been proven a good choice and is used here.

3.3 Auxiliary PI-Controller

The third modification suggestion is based on the idea to use a second, parallel PI-controller with larger gains to speed up the tracking capability of the IEL during saturation. The higher bandwidth of the auxiliary PI-controller allows the angle estimate to stay close to $\delta_\mathrm{IEL,sat}$ to prevent both instability and the negative effects of operation under power limitation. To ensure that the auxiliary PI-controller is only active during saturation, its input is scaled with the absolute value of the difference between unlimited and limited active power reference $|P^* - P^*_\mathrm{lim}|$. Using this difference as a scaling factor instead of adding it to the input signal ensures smooth insertion and removal of the second PI. It should be noted that the integrators of both PI controllers are always active, even when not in limitation. To achieve its goal to keep δ_IEL as close to $\delta_\mathrm{IEL,sat}$ as possible during limitation, the auxiliary PI should have a significantly higher bandwidth than the original IEL. For the cases in this paper, the gains were tuned as for an IEL with an inertia $H = 0.05\,\mathrm{s}$.

The insertion of the second PI is equivalent to adapting the inertia constant of the IEL to exactly the value that, with the given active power headroom and ROCOF, can be provided. However, this adaptation does first occur when limitation is reached, meaning that the initial inertial response is not affected. An advantage of this solution is that the damping provided by the IEL can be

adapted through the tuning of the second PI. This allows to provide additional damping during saturation without slowing down the initial inertial response, which would be the case if the damping ratio of the IEL is increased instead. For this reason, a higher damping ratio was chosen for the auxiliary PI-control ($\xi = 1$).

4 Simulation Results

The performance of the proposed modifications is investigated using time-domain simulations of the complete system shown in Figs. 1 to 2. For these simulations, the parameters from Tables 1 and 2 are used. $\alpha_{\mathrm{APL}}, \alpha_{\mathrm{CC}}$ and α_{VC} are the closed-loop bandwidth used to tune the APL, current controller and voltage controller, respectively. According to (E.8), for the simulated inertia constant of $H = 50\,\mathrm{s}$ the critical ROCOF causing instability is $\pm 3.33\,\mathrm{Hz/s}$. To replicate the instability and the consequences of saturated operation from Section II, the same cases are simulated: First, a ROCOF of $-3.75\,\mathrm{Hz/s}$ that causes instability in the unmodified IEL; and second, a ROCOF of $-3\,\mathrm{Hz/s}$ where even the unmodified IEL remains stable.

The simulation results for the higher ROCOF are shown in Fig. 7. The blue curves represented the base model, using the unmodified IEL illustrated in Fig. 3. The ROCOF starts at $t = 0.5\,\mathrm{s}$, and from the middle plot the angle difference passes 90° less than 800 ms later. At this point, the IEL loses track of the grid voltage angle and becomes unstable. It can be seen that all three proposed adaptations are able to maintain stable operation even during this higher ROCOF.

Figure 8 shows the simulation results for the lower ROCOF. Here, even the base model maintains stable operation. However, it can be seen that due to the saturation of the inertial power, the full inertial support continues for approximately 500 ms after the ROCOF has ended. This is due to the fact that the angle difference widely exceeds the angle that is needed for the maximum inertial support, $\delta_{\mathrm{IEL,sat}} = -8.6°$ (marked in green in the second plot), and that the decrease in the angle difference is not reflected in a decrease of inertial response as long as $|\delta_{\mathrm{IEL}}| > \delta_{\mathrm{IEL,sat}}|$.

The results for the angle-based IEL described in Section III.A are given in red. They show that the angle difference remains below 70° for the higher ROCOF, and around 50° for the lower. This difference to the base model

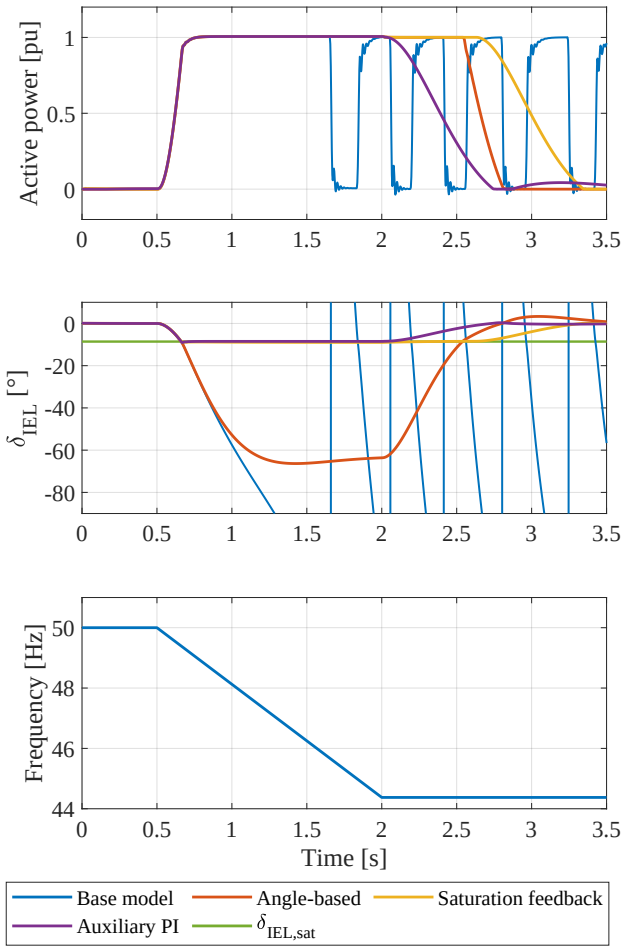

Figure 7: Simulated active power (top), angle difference (middle) and frequency (bottom) for a ROCOF of $-3.75\,\mathrm{Hz/s}$, causing instability in the base model.

can be explained by the elimination of the nonlinearity, resulting in a smaller angle difference for the same ROCOF. Nevertheless, the angle difference is in both cases more than five times higher than $\delta_{\mathrm{IEL,sat}}$. In consequence, even in this case the inertial support continues unreduced for about 500 ms after the frequency disturbance ends.

In contrast to this, the addition of a saturation feedback to the IEL as introduced in Section III.B allows to keep the angle very close to $\delta_{\mathrm{IEL,sat}}$. In the high ROCOF case, the maximum angle difference for this case is $-8.97°$, only $0.37°$ larger than $\delta_{\mathrm{IEL,sat}}$. Although the inertial power reference barely saturates, the simulation results show that the injection of excessive power due to operation under saturation is even worse than in the two cases discussed previously. This can be explained by the fact that the feedback increases the impact of the proportional part of the IEL's PI controller, and reduces the integral part's. This means that, with this adaptation, the integrator state differs more from the actual grid frequency as in the previously discussed solutions. As the ROCOF ends, the additional input into the PI from the saturation feedback subsides, which results in additional time required for the IEL to eliminate the angle difference. A study of different gains has shown that the post-disturbance performance of this approach cannot be improved significantly by varying K_{fb}.

The final modification suggestion is the introduction of an auxiliary PI-controller as described in Section III.C. The results of this case are shown as purple curves. The angle difference remains even closer to $\delta_{\mathrm{IEL,sat}}$ than for the saturation feedback, but in this case, the inertial response starts to reduce as soon as the ROCOF is removed. This means that the IEL maintains control throughout the whole disturbance, because the state of the auxiliary integrator is kept active, even as P_{H} drops below its limit. In consequence, not only the angle difference is kept close to its saturation limit, but the IEL's estimate of the grid frequency is kept accurate throughout the disturbance.

The energy injected to the grid during the frequency disturbance is the same for all simulated cases, but the amount injected after the end of the disturbance varies significantly. Since the ROCOF has ended at this point, additional inertial support can be considered superfluous, and the goal is to reduce the unnecessary inertial support. Figure 9 shows the energy that is injected after the disturbance has ended for all four controller variants, where an energy of 1 s corresponds to the injection of 1 pu power for the duration

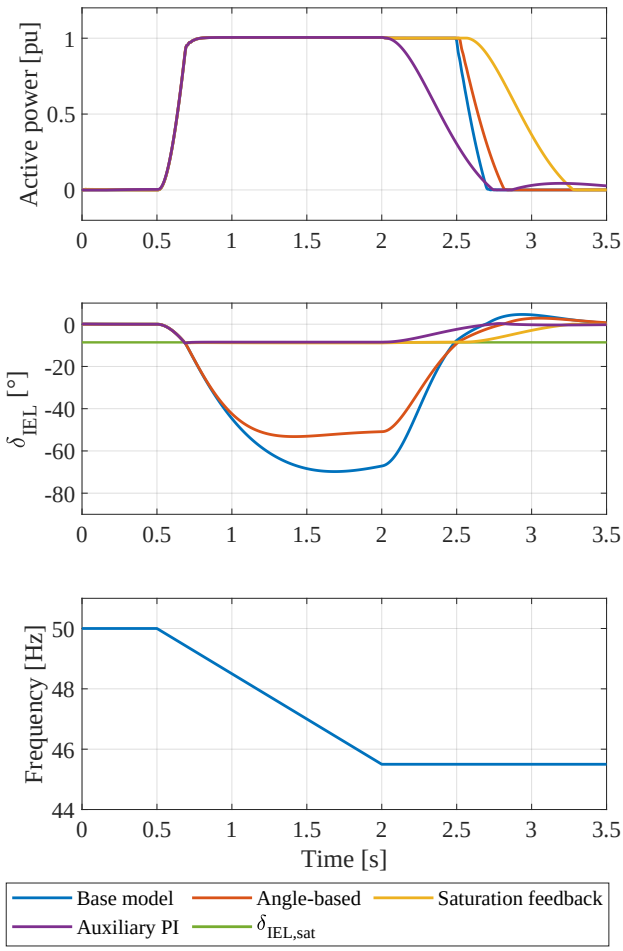

Figure 8: Simulated active power (top), angle difference (middle) and frequency (bottom) for a ROCOF of $-3\,\mathrm{Hz/s}$, a stable case in the base model.

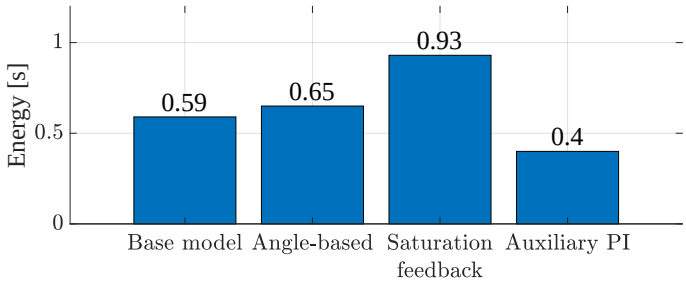

Figure 9: Energy injected after disturbance end.

of 1 s. The data confirm that the auxiliary PI results in the least additional energy injected, achieving a reduction of 33 % from the base model.

The active power plots in Figs. 7 and 8 show that the inertial power at the beginning of the disturbance increases much faster than it decreases in the end. This is the case even for the best modification, the auxiliary PI-controller. This effect is caused due to the de-facto limitation introduced by the second PI: At the beginning of the disturbance, the ROCOF causes the grid voltage and the internal IEL angle to separate. Without addition of the second PI controller, this would result in the same angle difference as shown for the base model. Consequently, the angle follows the shape of a step response ending in a final value of approximately 70°. But as soon as $\delta_{\mathrm{IEL,sat}}$ is reached, the second PI with a much higher bandwidth is introduced, which in effect limits the angle difference to this value. This means that the step response is terminated here, and only the first part of the rise is visible. The end of the disturbance, on the other hand, is an uncut step response from δ_{IEL} down to zero. As this step is much smaller than the (unlimited) one at the beginning of the disturbance would be, the same rise time results in a flatter response.

The impact of the second PI is in this aspect of the response limited to maintaining the angle difference close to $\delta_{\mathrm{IEL,sat}}$. This becomes obvious when comparing to the base case. At the end of the disturbance the angle difference in the base case reduces with the same steepness as at the beginning. Nevertheless, this reduction is not visible in the inertial response before the angle difference reaches $\delta_{\mathrm{IEL,sat}}$ again due to the saturation. Because the rise time of the control loop is the same in both cases, the inertial response from both

the base case and the auxiliary PI-control reaches zero again at approximately the same time, circa 650 ms after the disturbance ends. Even so, the IEL with an auxiliary PI starts reduction immediately, which reduces the amount of unnecessary energy injection and reflects an improved control performance.

5 Conclusions

This paper has shown that the original IEL design from [4] is very robust and is prone to instability only under extreme operating conditions far beyond the limits of today's power grids. The analysis has also revealed that for large ROCOFs, the saturation of the inertial support and IEL angle difference causes the inertial power to not follow the ROCOF while in saturation, even when stability is maintained. This operation under power limitation results in an undesirable power injection after the disturbance ends.

This motivated the proposal, investigation and comparison of three solutions to improve the robustness and controllability of the IEL. The simulation results show that of these suggestions, only the addition of an auxiliary PI-controller is able to mitigate both problems. This adaptation is equivalent to immediate dynamic scaling of the IEL's inertia constant based on ROCOF and headroom when the active power limit is hit, and is able to improve the IEL robustness notably without having an impact on the initial inertial response. The auxiliary PI also makes it possible to dynamically change the IEL damping during limitation. Based on these observations, it is advisable to include the auxiliary PI-controller in the IEL.

References

[1] P. Imgart, M. Bongiorno, J. R. Svensson, and M. Beza, "Stability Limits and Improved Robustness of Grid-Forming Converters With External Inertia-Emulation Loop," in *2023 25th European Conference on Power Electronics and Applications (EPE'23 ECCE Europe)*, Aalborg, Denmark: IEEE, Sep. 4, 2023, pp. 1–8, ISBN: 978-90-75815-41-2.

[2] J. Matevosyan, B. Badrzadeh, T. Prevost, *et al.*, "Grid-Forming Inverters: Are They the Key for High Renewable Penetration?" *IEEE Power and Energy Magazine*, vol. 17, no. 6, pp. 89–98, Nov. 2019, ISSN: 1558-4216.

[3] ENTSO-E, "High Penetration of Power Electronic Interfaced Power Sources and the Potential Contribution of Grid Forming Converters," 2020.

[4] B. Fan, T. Liu, F. Zhao, H. Wu, and X. Wang, "A Review of Current-Limiting Control of Grid-Forming Inverters Under Symmetrical Disturbances," *IEEE Open Journal of Power Electronics*, pp. 1–15, 2022, ISSN: 2644-1314.

[5] P. Imgart, A. Narula, M. Bongiorno, M. Beza, and J. R. Svensson, "A Cascaded Power Controller for Robust Frequency Ride-Through of Grid-Forming Converters," presented at the 2022 IEEE Energy Conversion Congress and Exposition (ECCE), Detroit, MI, USA, 2022.

[6] A. Narula, P. Imgart, M. Bongiorno, M. Beza, J. R. Svensson, and J.-P. Hasler, "Voltage-based Current Limitation Strategy to Preserve Grid-forming Properties Under Severe Grid Disturbances," *IEEE Open Journal of Power Electronics*, pp. 1–13, 2023, ISSN: 2644-1314.

[7] M. D. Librandi, T. Wuerl, D. Stenzel, *et al.*, "Local Frequency Transients in the Future European Synchronous Transmission Grid," in *NEIS 2021; Conference on Sustainable Energy Supply and Energy Storage Systems*, Sep. 2021, pp. 1–7.

[8] S. K. Chaudhary, R. Teodorescu, J. R. Svensson, Ł. H. Kocewiak, P. Johnson, and B. Berggren, "Islanded Operation of Offshore Wind Power Plant using IBESS," in *2021 IEEE Power & Energy Society General Meeting (PESGM)*, Jul. 2021, pp. 1–5.

[9] P. Kundur, *Power System Stability and Control* (The EPRI Power System Engineering Series), N. J. Balu and M. G. Lauby, Eds. New York: McGraw-Hill, 1994, ISBN: 978-0-07-035958-1.

[10] P. Imgart, M. Beza, M. Bongiorno, and J. R. Svensson, "An Overview of Grid-Connection Requirements for Converters and Their Impact on Grid-Forming Control," *EPE'22 ECCE Europe*, 2022.

[11] ENTSO-E, E. Ørum, L. Haarla, *et al.*, "Future system inertia 2," 2018.

PAPER F

Decoupled PQ Grid-Forming Control with Tunable Converter Frequency Behaviour

Paul Imgart, Anant Narula, Massimo Bongiorno, Mebtu Beza, Jan R. Svensson, Jean-Phillipe Hasler, Paolo Mattavelli

Submitted to IEEE Transactions for consideration.

The layout has been revised.

1 Introduction

Global efforts to limit climate change through the reduction of greenhouse gas emissions result in an increase of electricity generation from renewable sources [1]. Together with other factors such as increased utilization and flexibility of power grid assets as well as changing consumer technologies, the share of power electronics in electric power grids is rising [2]. Associated with this increase are concerns and challenges regarding the stability of converter-dominated power grids. Examples for these challenges are the decrease of mechanical inertia, reduced short-circuit current and risk for adverse control interaction [3].

A proposed solution to the challenges is the usage of grid-forming (GFM) converters, which are controlled as a slowly varying voltage source behind an impedance [3], [4]. A common feature in the large variety of GFM converter control designs available from the literature is that the active power control determines the angle and reactive power determines the magnitude of the voltage source [5]–[7]. The assumption behind is a mainly inductive impedance between the controlled voltage and the grid connection, similar to a synchronous machine. Among the most popular GFM control designs are the power-synchronization control (PSC) [8] and the virtual admittance-based GFM control (VA-GFM) [9].

Notwithstanding their contribution to the improvement of the aforementioned challenges for power system stability, GFM-controllers also face challenges, such as:

- Coupling between active and reactive power [10], [11];
- Non-trivial limitation of converter current [12];
- Poor damping of DC-current offsets [13];
- Poor characterization and tunability of the converter input admittance in the subsynchronous and supersynchronous frequency ranges [13], [14].

As a response to these challenges, this paper introduces a decoupled GFM converter controller. Several solutions for GFM controllers aiming for decoupling between active and reactive power loops are avaiable in the literature [15]–[21]. Some of these are only able to decouple active and reactive power for the fundamental frequency, which can lead to unexpected behaviour at

other frequencies [15]–[19]. Other solutions add significant complexity to the controller, increasing the risk to introduce unwanted dynamics [20], [21]. The controller proposed in this paper eliminates the power coupling in the frequency range where the power controllers are active and allows to freely tune the damping provided by the converter.

The paper is organized as follows: In Section 2, two existing GFM control strategies are compared and the need for decoupling and frequency characterization is highlighted. This is followed by a presentation of the proposed decoupled GFM controller in Section 3 and the controller's frequency characteristics in Section 4. Finally, the results from the experimental validation are discussed in Section 5 and the conclusions are given in Section 6.

2 GFM Control Structure and Need for Power Decoupling and Frequency Characterization

This section introduces two widely used GFM control strategies: PSC and VA-GFM. Additionally, some of the common challenges associated with GFM controllers are examined, using the two control strategies under consideration as examples. Finally, the need for proper frequency characterization of GFM converter systems is motivated.

Figure 1 depicts the single-line diagram of the network under investigation. The network consists of a voltage-source converter (VSC) system connected to an electrical AC grid through an R-L filter, characterized by a resistance R_f and an inductance L_f. The AC grid is represented using its Thévenin equivalent, with R_g and L_g denoting the grid resistance and inductance, respectively. A constant DC-link voltage for the VSC system is assumed. The converter current vector is represented by $\underline{i}_\mathrm{f}$ while the voltage vectors at the point of common coupling (PCC), the converter terminal, and the Thévenin equivalent voltage source are denoted by $\underline{v}_\mathrm{g}$, $\underline{v}_\mathrm{c}$, and $\underline{v}_\mathrm{s}$ respectively.

2.1 Review of Existing GFM Control Strategies and Their Challenges

As shown in Fig. 2, both the PSC and the VA-GFM controllers share a similar general structure. Specifically, the outer-control loops, namely the active-power loop (APL) and the reactive-power loop (RPL), calculate the reference

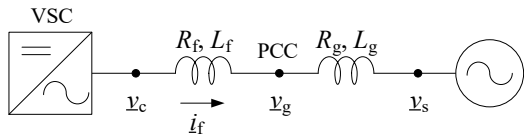

Figure 1: Single-line circuit diagram of the investigated network.

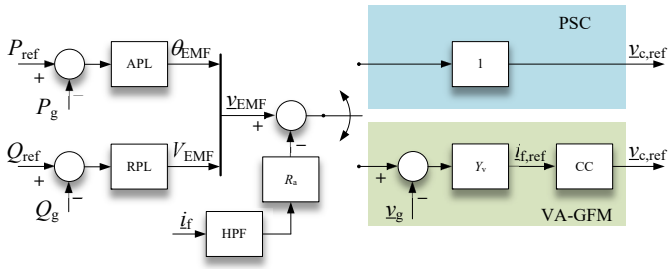

Figure 2: Generalized structure of GFM control strategies under consideration.

values for the virtual-voltage source $\underline{v}_{\mathrm{EMF}}$. The APL regulates the active-power flow at the PCC, P_{g}, and calculates the angle of the virtual voltage source, θ_{EMF}, while the RPL[1] determines the magnitude of the virtual-voltage source, V_{EMF}, to regulate the reactive-power flow at the PCC, Q_{g}. In both GFM controllers, the APL is responsible for tracking the reference active power, P_{ref}, as well as for the grid synchronization of the converter system. Different configurations for the APL can be used, ranging from a simple proportional controller [8], [22] or a proportional-integral (PI) controller [23], to a controller that emulates the electromechanical dynamics of a synchronous machine [6].

The main structural difference between the PSC and the VA-GFM lies in the design of the inner control loops. The PSC uses an embedded current controller to enable fault-ride-through operation of the converter system [8], [22]. Since the current controller operates only during over-current conditions and is transparent during normal operation, it is represented as a static gain block with unity gain in Fig. 2. Accordingly, the converter voltage-vector reference for the modulation stage, $\underline{v}_{\mathrm{c,ref}}$, is directly calculated by the outer loops. In contrast, the VA-GFM employs a current controller (CC) that tracks the refer-

[1] Depending on the specific application, an AC-voltage controller may also be used.

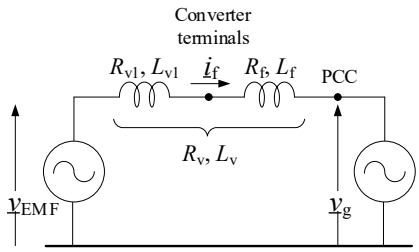

Figure 3: Equivalent circuit to determine power to grid from the voltages $\underline{v}_{\mathrm{EMF}}$ and $\underline{v}_{\mathrm{g}}$ together with impedance $\underline{Z}_{\mathrm{v}}$.

ence current vector, $\underline{i}_{\mathrm{f,ref}}$, which is calculated using the virtual admittance $\underline{Y}_{\mathrm{v}}$. The converter voltage-vector reference is thus determined by the CC. Figure 3 illustrates an equivalent circuit of the GFM controllers. The parameters R_{v} and L_{v} correspond to the equivalent resistance and inductance, respectively, between the emulated voltage source and the PCC. These parameters are here referred to as virtual resistance and virtual inductance. It can be observed from the figure that the equivalent impedance consists of two components: a fixed part, determined by the physical converter filter resistance and inductance, and a tunable virtual component, represented by R_{v1} and L_{v1}. In the case of PSC, the emulated voltage source behaviour is directly imposed at the converter terminals, meaning the tunable virtual component is zero, i.e., $R_{\mathrm{v1}} = L_{\mathrm{v1}} = 0$.

As demonstrated in [22], the PSC utilizes a high-pass filtered converter current with gain R_{a} (referred to as active resistance, AR, in [22]) to provide damping at the synchronous-frequency resonance (SFR), where the resonance frequency of the output power of the converter closely aligns with the fundamental frequency. It is important to note that the SFR in the output power of a GFM-VSC system results from a DC component (corresponding to 0 Hz resonance) in the AC output converter current due to frequency shift. The SFR results from the plant dynamics of the APL, which can be understood through the small-signal model describing the power-angle relationship in a GFM-VSC system[2]. For the PSC without AR and assuming constant V_{EMF},

[2]Here, this relationship is described at the PCC to be consistent with derivations further below, assuming a stiff PCC voltage. An equivalent expression can be given with respect to the internal grid voltage by substituting V_{g0} with V_{s0} and adding $R_{\mathrm{g}}, L_{\mathrm{g}}, X_{\mathrm{g}}$ to $R_{\mathrm{v}}, L_{\mathrm{v}}, X_{\mathrm{v}}$, respectively.

the power-angle relationship at the PCC is

$$H_{\mathrm{P}\delta}(s) = \frac{\Delta P_{\mathrm{g}}}{\Delta\delta} = \frac{as^2 + bs + c}{(R_{\mathrm{v}} + sL_{\mathrm{v}})^2 + X_{\mathrm{v}}^2}, \tag{F.1}$$

with

$$a = \frac{V_{\mathrm{EMF0}} L_{\mathrm{v}}^2}{R_{\mathrm{v}}^2 + X_{\mathrm{v}}^2}(-V_{\mathrm{EMF0}} X_{\mathrm{v}} + V_{\mathrm{g0}} R_{\mathrm{v}} \sin\delta_0 + V_{\mathrm{g0}} X_{\mathrm{v}} \cos\delta_0),$$

$$b = 2\frac{V_{\mathrm{EMF0}} R_{\mathrm{v}} L_{\mathrm{v}}}{R_{\mathrm{v}}^2 + X_{\mathrm{v}}^2}(-V_{\mathrm{EMF0}} X_{\mathrm{v}} + V_{\mathrm{g0}} R_{\mathrm{v}} \sin\delta_0 + V_{\mathrm{g0}} X_{\mathrm{v}} \cos\delta_0),$$

$$c = V_{\mathrm{EMF0}} V_{\mathrm{g0}} R_{\mathrm{v}} \sin\delta_0 + V_{\mathrm{EMF0}} V_{\mathrm{g0}} X_{\mathrm{v}} \cos\delta_0.$$

Here, the load angle δ represents the difference between the voltage angles of the virtual voltage source and PCC voltage. The subscript '0' is used to indicate steady-state values.

From (F.1), it can be observed that $H_{\mathrm{P}\delta}(s)$ has two conjugate poles given by

$$s_{1,2} = -\frac{R_{\mathrm{v}}}{L_{\mathrm{v}}} \pm \mathrm{j}\omega_{\mathrm{N}}, \tag{F.2}$$

as has been highlighted in [8]. The imaginary part of (F.2) represents the natural frequency of the conjugate poles, which corresponds to the fundamental angular frequency, ω_{N}. As shown in the Bode plot of $H_{\mathrm{P}\delta}(s)$ in Fig. 4, this results in an amplification at the fundamental frequency, leading to the SFR phenomenon in the output active power of the VSC-GFM system. The virtual resistance, which includes only the resistance of the series filter in case of PSC, plays a crucial role in damping the SFR. However, due to the relatively small value of R_{f}, the natural damping of the SFR remains insufficient in the PSC. The AR proposed in e.g. [22] dynamically increases the equivalent resistance between the virtual back EMF and the grid voltage, thereby enhancing SFR damping, as observed in Fig. 4. Since this resistance is incorporated in the control loop, it does not cause additional losses. Furthermore, the high-pass fillter (HPF) prevents the influence of the AR in steady state. However, as shown in [22], the AR limits the attainable closed-loop bandwidth of the

PSC. As a consequence, tuning of R_a becomes a trade-off between desired damping and bandwidth limitation, which furthermore is altered by operating conditions. These restrictions can result in reduced damping of the SFR, as can be observed in the experimental results using the recommended control parameters in [22].

Due to the similarity in the plant dynamics, the VA-GFM encounters the same fundamental challenge of the SFR phenomenon. However, the introduction of the virtual admittance (VA) enables an increase in damping (via the virtual resistance) without additional losses or the drawbacks associated with the AR used in the PSC. Figure 5 shows the Bode plot of $H_{\mathrm{P}\delta}(s)$ for the VA-GFM with three different values of virtual resistance, R_v. It can be observed that increasing the virtual resistance reduces the resonant peak around the fundamental frequency, thereby improving SFR damping. While increasing the virtual resistance further can effectively mitigate the SFR, it introduces greater coupling between active- and reactive-power controllers. This can be understood by considering the following quasi-steady-state equations governing power flow between two voltage sources.

Assuming a stiff grid connection, the power flow at the PCC in the investigated network (Fig. 1 and 3) is given by

$$\underline{S}_\mathrm{g} = \underline{V}_\mathrm{g}\underline{I}_\mathrm{f}^* = \frac{\underline{V}_\mathrm{g}\underline{V}_\mathrm{EMF}^* - V_\mathrm{g}^2}{R_\mathrm{v} - \mathrm{j}X_\mathrm{v}}, \tag{F.3}$$

which results in

$$P_\mathrm{g} = \frac{R_\mathrm{v}(V_\mathrm{g}V_\mathrm{EMF}\cos\delta - V_\mathrm{g}^2) + X_\mathrm{v}V_\mathrm{g}V_\mathrm{EMF}\sin\delta}{R_\mathrm{v}^2 + X_\mathrm{v}^2}, \tag{F.4}$$

$$Q_\mathrm{g} = \frac{-R_\mathrm{v}V_\mathrm{g}V_\mathrm{EMF}\sin\delta + X_\mathrm{v}(V_\mathrm{g}V_\mathrm{EMF}\cos\delta - V_\mathrm{g}^2)}{R_\mathrm{v}^2 + X_\mathrm{v}^2}, \tag{F.5}$$

where $\underline{V}_\mathrm{g} = V_\mathrm{g}$ and $\underline{V}_\mathrm{EMF} = V_\mathrm{EMF}\,\mathrm{e}^{\mathrm{j}\delta}$ are the phasors describing the two voltage sources, and $R_\mathrm{v} = R_\mathrm{v1} + R_\mathrm{f}$ and $X_\mathrm{v} = X_\mathrm{v1} + X_\mathrm{f}$ represent the (partially virtual) resistance and reactance, respectively, between these two sources. Assuming a negligible resistance, the equations for active- and reactive-power flow become

$$P_\mathrm{g} = \frac{V_\mathrm{g}V_\mathrm{EMF}\sin\delta}{X_\mathrm{v}}, \tag{F.6}$$

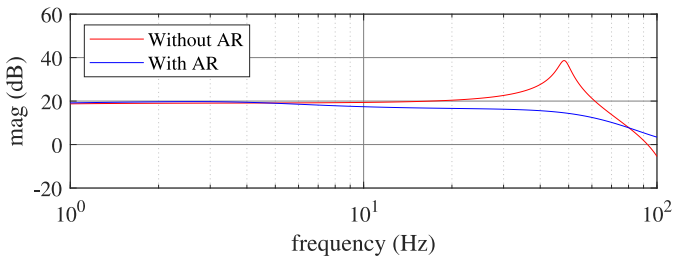

Figure 4: Bode plot of $H_{\mathrm{P}\delta}(s)$ for PSC.

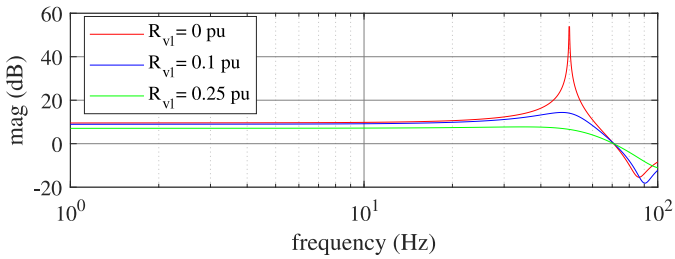

Figure 5: Bode plot of $H_{\mathrm{P}\delta}(s)$ for VA-GFM.

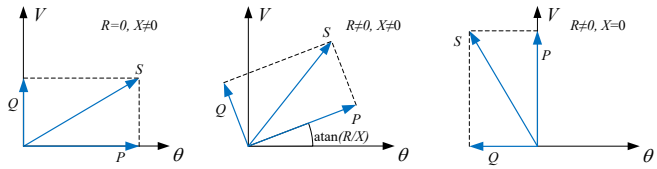

Figure 6: Impact of impedance angle on relation between voltage's amplitude and angle and active and reactive power.

and

$$Q_{\mathrm{g}} = \frac{V_{\mathrm{g}} V_{\mathrm{EMF}} \cos\delta - V_{\mathrm{g}}^2}{X_{\mathrm{v}}}. \tag{F.7}$$

The linearized form of (F.6) and (F.7) clearly reveals the dependence of active power on voltage angle and reactive power on voltage magnitude, which forms the fundamental basis of GFM control. However, as the R/X-ratio increases, this simplification becomes increasingly inaccurate. For a predominantly resistive impedance, the previously stated relation is reversed, resulting in the active power being determined mainly by voltage magnitude, and reactive power by voltage angle. These relations are illustrated in Fig. 6 [15]. Consequently, an impedance with non-negligible inductive and resistive components causes both controlled parameters—voltage angle and magnitude—to influence both power components, leading to power coupling. This phenomenon is undesirable, as it degrades controller performance, which is typically designed based on the assumption of a purely reactive system model. The assumption of a decoupled system as given by (F.6) and (F.7) is a valid simplification for transmission systems, where losses are negligible. However, an increased (virtual) resistance would introduce power coupling, thus limiting feasible choices of R_{v} to small values.

2.2 Frequency Characterization

While the standardization and requirements for GFM converters are still evolving, there are growing indications that converter behaviour in the frequency domain is becoming an increasingly important criterion for assessing compliance with grid codes and system requirements [24]. In [3], a range of requirements for GFM converters are outlined. Apart from behaving as

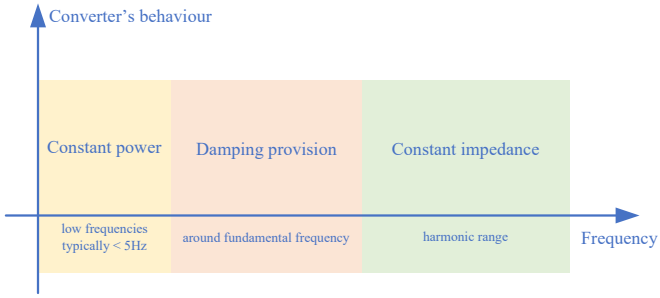

Figure 7: Desired GFM control behaviour at different frequencies.

a slow-varying voltage source, GFM converters are also required to act as a sink for harmonics and prevent adverse control interactions. These properties can only be verified through an analysis of the converter's behaviour in the frequency domain. In [25], GFM behaviour is defined as acting as a voltage source behind an impedance, with the control bandwidth being limited to a specified frequency. Examples of methods used to characterize and analyze converter behaviour in the frequency domain include transfer function Bode plots, impedance-based stability analysis [26], passivity studies [27], network-frequency perturbation plots [28], and power-response matrix-based modeling [29].

The desired behaviour of GFM converters varies across the frequency spectrum and can be illustrated as shown in Fig. 7. At low frequencies, governed by the bandwidth of outer-control loops (typically up to 5 Hz), the GFM converter should exhibit constant-power behaviour, meaning it should track its power setpoints. This range is generally where the converter exhibits active behaviour [30]. For higher frequencies up to the fundamental, the converter is required to provide damping, for example to prevent adverse control interactions and the risk for Subsynchronous resonances. In the harmonic range, beyond this, the converter should behave as a constant impedance, thereby acting as a sink for harmonics [3].

As discussed in the previous section, the investigated GFM controllers give rise to SFR in the converter's power output, leading to the introduction of a DC component in the converter current during changes in the operating point. This poses a risk to the operation of equipment such as transformers and

must be effectively damped. The GFM controllers under investigation require specific control solutions to ensure the stability and damping of SFR. In the case of the PSC, this is achieved through the use of an AR, which must be tuned while considering factors such as the desired controller bandwidth and expected grid strength. However, this typically results in underdamped SFR. Additionally, the HPF used for the AR further complicates the converter's behavior across the frequency spectrum, restricting the independent tuning of the converter's response in different frequency ranges. In contrast, the VA-GFM allows for the inclusion of a virtual resistance that is active across all frequencies. However, the damping effect provided by this resistance is limited due to the power coupling it introduces, which negatively impacts controller's performance.

Thanks to the ability to independently select the parameters of the VA, the Decoupled VA-GFM control proposed in this paper effectively dampens SFR without the need for additional damping contorllers. Furthermore, as demonstrated in Section 4, the proposed controller enables independent tuning of the converter's response across different frequency ranges, as identified in Fig. 7, by adjusting separate control parameters. Specifically, in the low-frequency region—up to a few Hz in the *dq*-frame, which is primarily influenced by the outer control loops—the converter exhibits constant power behavior. Beyond this frequency range, the converter essentially behaves as a constant voltage source behind an impedance, thereby satisfying the grid-connection requirements for GFM converters.

3 Decoupled VA-GFM Control

Figure 9 shows the block diagram of the proposed decoupled VA-GFM control. The controller is based on the VA-GFM in Fig. 2, with the main difference that the complex output signal $\underline{\kappa}$ formed by the output of the APL and RPL is passed through a phase-compensation block that compensates for the power coupling introduced by the virtual admittance $\underline{Y}_{\mathrm{v}}$. This allows the selection of arbitrary values for virtual resistance and inductance, while maintaining near-perfect decoupling between the active- and reactive-power loops in their active frequency range. Note that the APL and RPL have exactly the same structure, allowing for control symmetry if the corresponding parameters are selected equal, which will aid system analysis through single-input single-

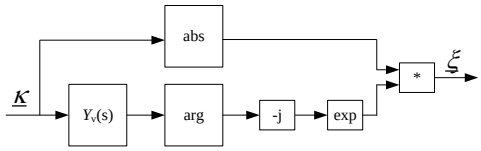

Figure 8: Implemented VA phase compensation.

output representation. The output of the complex-power controller and the VA phase compensation is the voltage $\underline{v}_{\mathrm{EMF}}$ in the stationary $\alpha\beta$-plane.

3.1 VA Phase Compensation

A key element of the proposed controller is the VA phase compensation applied to the output of the APL and RPL. This technique effectively decouples active and reactive power, making them independent of the selection of the parameters of the VA. The decoupling is achieved by dynamically rotating the complex signal $\underline{\kappa}$ by the frequency-dependent virtual-impedance angle, $\varphi_{\mathrm{Y}}(s)$ as shown in Fig. 8. Consequently, the resulting power flow appears as if governed by a purely resistive network, where voltage magnitude controls active power and voltage-phase angle controls reactive power (see Fig. 6). Conceptually, the VA phase compensation proposed here is similar to the method proposed in [15], as it rotates the complex-apparent power vector to remove the coupling introduced by an admittance with both resistive and inductive elements. However, it is important to note that the dynamic implementation proposed here applies not only to the fundamental frequency, but also to the whole constant-power frequency range as indicated in Fig. 7, where the power controllers are active, as will be demonstrated in the next section.

The decoupling mechanism can be illustrated using two generic voltages $\underline{v}_1 = V_1\,\mathrm{e}^{\mathrm{j}\theta_1}$ and $\underline{v}_2 = V_2\,\mathrm{e}^{\mathrm{j}0^\circ}$, which are connected by a generic admittance $\underline{Y} = \frac{1}{R+\mathrm{j}X} = Y\,\mathrm{e}^{\mathrm{j}\varphi_{\mathrm{Y}}}$. This allows to express the complex-apparent power at $\underline{v}_2$ as

$$\underline{S} = \underline{v}_2\underline{i}^* = V_2 Y(V_1\,\mathrm{e}^{-\mathrm{j}(\theta_1+\varphi_{\mathrm{Y}})} - V_2\,\mathrm{e}^{-\mathrm{j}\varphi_{\mathrm{Y}}}). \tag{F.8}$$

Rotating this power vector by φ_{Y} results in

$$\underline{S}_{\mathrm{shift}} = V_2 Y(V_1\,\mathrm{e}^{-\mathrm{j}\theta_1} - V_2), \tag{F.9}$$

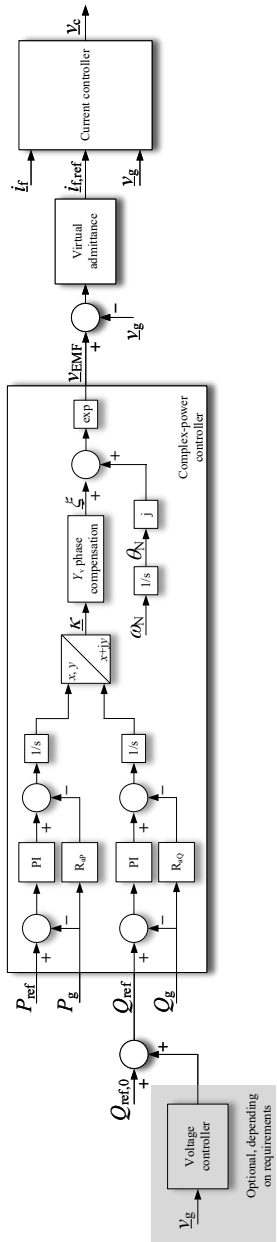

Figure 9: Block diagram of proposed decoupled GFM control, including detailed description of apparent-power controller.

which is the power flow over the purely resistive admittance $Y = (R^2 + X^2)^{-1/2}$. In consequence, this rotation of the complex power vector cancels the coupling effect of the complex admittance $\underline{Y}$.

As illustrated in Fig. 6 and visible by linearizing (F.9), reactive power is determined by the negative voltage phase angle for the resulting purely resistive case. To maintain the same sign for both components, the proposed VA phase compensation multiplies the angle of the (unshifted) complex-power vector with -1, which corresponds to mirroring the vector on the V-axis of the resistive case in Fig. 6.

As result of the phase compensation, active power depends on voltage magnitude, while reactive power depends on voltage angle of the converter's (virtual) internal voltage. By achieving this decoupling, the VA phase compensation enables for arbitrary selection of the virtual resistance and inductance, without the previously mentioned negative side-effects. Furthermore, this enables to tune the virtual resistance to effectively dampen the SFR discussed in the previous section, without the need for additional damping controllers.

Based on the discussion above, it is important to note that the use of the phase-compensation scheme chosen based on the dynamic model of the VA is to present a resistive network to the outputs of the power controllers in the constant-power frequency range as indicated in the equivalent circuit representation in Fig. 10 in the next section. Beyond this frequency range and especially in the constant impedance region, the output voltage $\underline{v}_{\mathrm{EMF}}$ will be such that its magnitude is dictated by the RPC and its phase by the ACP loop as in a classical GFM control structure.

The VA phase compensation can be altered easily so that the VA appears as a purely inductive network for the output of the power controllers, as in the classical approach. However, this removes the possibility to present the controller behaviour as a real-valued transfer function as presented below in (F.20). Regardless, in both schemes the decoupled power controller minimizes the coupling, which is introduced by high values of virtual resistance, in the frequency range of interest without affecting the basic GFM characteristics of the converter in both schemes.

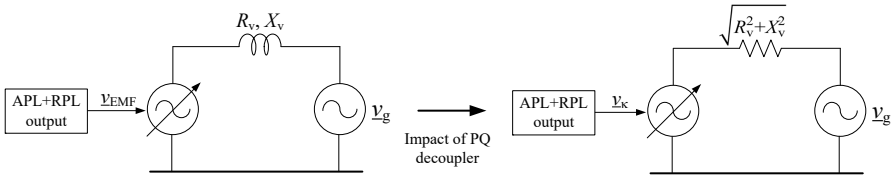

Figure 10: Impact of the VA phase compensation. Left: conventional VA-GFM as in Fig. 2; right: Decoupled VA-GFM

.

3.2 Derivation of Decoupled VA-GFM Control Parameters

Tuning of Complex-Power Controller

The complex-power controller provides both complex power-reference tracking as well as grid-voltage synchronization. The complex-power controller proposed here has identical structure for active and reactive power, respectively, consisting of a PI controller and an active damping term (see Fig. 9). The tuning of the controller is detailed below and is similar to the loop shaping approach described in [31].

To achieve the desired power decoupling without limitations for the selection of R_v and L_v, the VA phase compensation is applied. Following the explanation provided in the previous section, phase compensation should be applied to the input signals to the complex-power controller, P_{ref} and P_g, as well as Q_{ref} and Q_g. This would result in both controllers sharing the control of active and reactive power, in proportion to the ratio between R_v and L_v (i.e., corresponding to the VA angle φ_{Y_v}). This is the case since the VA phase compensation rotates the complex-power vector to take the coupling effect of the VA into account. To enable independent choice of parameters for the APC and RPC and keep the dynamics separate (e.g. to provide inertial support by slowing down the APC only), the phase compensation is instead applied at the controller outputs, as shown in Fig. 9.

The impact of the VA phase compensation and the complex VA is shown in Fig. 10. For the voltage $\underline{v}_{\underline{\kappa}} = e^{\underline{\kappa}}$ obtained from the output $\underline{\kappa} = \gamma + j\varepsilon$ of the complex-power controller, the VA appears as purely resistive thanks to

the provided phase compensation[3]. This means that under the assumption of an ideal current controller, the plant model for the complex-power controller can be formulated by substituting $\underline{v}_\kappa$ for $\underline{v}_1$ and $\underline{v}_\mathrm{g} = V_\mathrm{g}$ for $\underline{v}_2$ in (F.9):

$$\underline{S}_\mathrm{g} = P_\mathrm{g} + jQ_\mathrm{g} = V_\mathrm{g} Y_\mathrm{v} (V_\kappa \, \mathrm{e}^{-\mathrm{j}\varepsilon} - V_\mathrm{g}) \tag{F.10}$$

with $Y_\mathrm{v} = \sqrt{R_\mathrm{v}^2 + X_\mathrm{v}^2}^{-1}$. Assuming $V_\mathrm{g0} = 1$ pu and, for simplicity of the derivation, $P_\mathrm{ref} = Q_\mathrm{ref} = 0$ pu, the initial for the output of the complex-power controller $\underline{\kappa}_0 = 0$ yielding $\underline{v}_{\kappa 0} = 1$ pu, the linearized active and reactive powers can be expressed as

$$\Delta P_\mathrm{g} = Y_\mathrm{v} \Delta\gamma \tag{F.11}$$

$$\Delta Q_\mathrm{g} = Y_\mathrm{v} \Delta\varepsilon, \tag{F.12}$$

With the control law of the complex-power controller given as

$$\gamma = \frac{1}{s}\left[(K_\mathrm{pP} + \frac{K_\mathrm{iP}}{s})(P_\mathrm{ref} - P_\mathrm{g}) - R_\mathrm{aP} P_\mathrm{g}\right] \tag{F.13}$$

$$\varepsilon = \frac{1}{s}\left[(K_\mathrm{pQ} + \frac{K_\mathrm{iQ}}{s})(Q_\mathrm{ref} - Q_\mathrm{g}) - R_\mathrm{aQ} Q_\mathrm{g}\right], \tag{F.14}$$

the closed-loop transfer function from the active-power reference to the active power can be expressed as

$$G_{\mathrm{P_{ref}} \to \mathrm{P_g}} = \frac{\Delta P_\mathrm{g}}{\Delta P_\mathrm{ref}} = \frac{Y_\mathrm{v}(K_\mathrm{pP} s + K_\mathrm{iP})}{s^2 + (R_\mathrm{aP} + K_\mathrm{pP}) s + K_\mathrm{iP}}. \tag{F.15}$$

A similar expression can be derived for $G_{\mathrm{Q_{ref}} \to \mathrm{Q_g}}$. This transfer function can be loop-shaped to a second-order low-pass filter (LPF) by selecting the following control parameters:

$$K_\mathrm{p,P} = \alpha_\mathrm{P} Y_\mathrm{v}^{-1}, \tag{F.16}$$

$$K_\mathrm{i,P} = \alpha_\mathrm{P}^2 Y_\mathrm{v}^{-1}, \tag{F.17}$$

$$R_\mathrm{a,P} = \alpha_\mathrm{P} Y_\mathrm{v}^{-1} (2\zeta_\mathrm{P} - 1), \tag{F.18}$$

where α_P is the desired loop bandwidth and ζ_P the desired damping ratio. If $\zeta_\mathrm{P} = 1$,

$$R_\mathrm{a,P} = K_\mathrm{p,P} \tag{F.19}$$

[3] In this derivation, the term $\mathrm{e}^{\mathrm{j}\theta_\mathrm{N}}$ is neglected as it simply provides a ramp signal for the transformation to the $\alpha\beta$ plane.

and the closed-loop transfer function becomes a first-order LPF.
The parameters for the RPL are tuned equivalently, and are determined by the selection of the desired loop bandwidth α_{Q} and damping ratio ζ_{Q}. In the case that the loop bandwidths and damping ratios for the APL and RPL are selected to be the same, both transfer functions can be expressed through a single, real-valued transfer function for the complex-apparent power:

$$G_{\mathrm{S_{ref}}\to\mathrm{S_g}} = \frac{\Delta \underline{S}_{\mathrm{g}}}{\Delta \underline{S}_{\mathrm{ref}}} = \frac{\alpha\,(s+\alpha)}{s^2 + 2\zeta\alpha + \alpha^2}. \tag{F.20}$$

α_{P}-selection for inertia provision

As shown in [32], the APL in the proposed design can be tuned to provide an inertial response equivalent to that of a synchronous machine (SM) or a virtual synchronous machine, i.e. a GFM converter implementing the SM's mechanical equation as its active-power control law. The closed-loop transfer function from grid-voltage angle θ_{g} to active power is given as

$$G_{\theta_{\mathrm{g}}\to\mathrm{P}} = \frac{X_{\mathrm{v}} Y_{\mathrm{v}}^2 s^2}{s^2 + \alpha_{\mathrm{P}}\zeta_{\mathrm{P}} s + \alpha_{\mathrm{P}}^2}. \tag{F.21}$$

Based on this, the inertial response can be estimated as

$$G_{\dot{\omega}_{\mathrm{g}}\to\mathrm{P}} = \frac{G_{\theta_{\mathrm{g}}\to\mathrm{P}}}{s^2} = \frac{X_{\mathrm{v}} Y_{\mathrm{v}}^2}{s^2 + \alpha_{\mathrm{P}}\zeta_{\mathrm{P}} s + \alpha_{\mathrm{P}}^2} = P_{\mathrm{H}} \tag{F.22}$$

The inertial response relates to the provided inertia-time constant as $H = P_{\mathrm{H}}\frac{\omega_{\mathrm{N}}}{2}$, yielding to

$$\alpha_{\mathrm{P}} = \sqrt{\frac{X_{\mathrm{v}} Y_{\mathrm{v}}^2}{H}\frac{\omega_{\mathrm{N}}}{2}}. \tag{F.23}$$

4 Frequency Analysis

As argued in Section 2, the frequency domain analysis of the converter's behaviour is an indispensable tool to ensure compliance with grid code requirements and demonstrate some of the GFM properties, e.g. absence of adverse control interactions. Taking into account that the time constant of the VA is selected to be much smaller than that of the outer APL and RPL, a first analysis is made using the steady-state representation of the VA. This is followed

by an analysis including the dynamics introduced by the virtual inductance, to highlight differences and the impacts of control parameters. The system and control parameters used for this analysis are shown in Table 1, with deviating values mentioned in the text.

4.1 Analysis with Steady-State VA Representation

The steady-state representation of the VA results from letting $sL_\mathrm{v} = 0$, yielding $\underline{Y}_\mathrm{v}^\mathrm{ss} = (R_\mathrm{v} + \mathrm{j}X_\mathrm{v})^{-1}$. The transfer function from power reference to grid power using this simplification is given in (F.20). The Bode diagram of this function is displayed in Fig. 11 and shows the expected LPF-behaviour as well as the absence of any cross-coupling between active and reactive power.

Using the steady-state representation of the VA and neglecting the dynamics of the current controller, the converter's input admittance is for zero power setpoints given as

$$\begin{bmatrix}\Delta i_\mathrm{f}^\mathrm{d}\\ \Delta i_\mathrm{f}^\mathrm{q}\end{bmatrix} = -\underbrace{\begin{bmatrix}\frac{R_\mathrm{v}}{R_\mathrm{v}^2+X_\mathrm{v}^2}\frac{s^2}{(s+\alpha_\mathrm{P})^2} & \frac{X_\mathrm{v}}{R_\mathrm{v}^2+X_\mathrm{v}^2}\frac{s^2}{(s+\alpha_\mathrm{P})^2}\\ -\frac{X_\mathrm{v}}{R_\mathrm{v}^2+X_\mathrm{v}^2}\frac{s^2}{(s+\alpha_\mathrm{Q})^2} & \frac{R_\mathrm{v}}{R_\mathrm{v}^2+X_\mathrm{v}^2}\frac{s^2}{(s+\alpha_\mathrm{Q})^2}\end{bmatrix}}_{\mathbf{Y}_{\mathrm{c,ss}}(s)}\begin{bmatrix}\Delta v_\mathrm{g}^\mathrm{d}\\ \Delta v_\mathrm{g}^\mathrm{q}\end{bmatrix}. \tag{F.24}$$

This expression can be further simplified for the case that the same bandwidth is selected for both power control loops, $\alpha_\mathrm{P} = \alpha_\mathrm{Q} = \alpha$. In this case, $\mathbf{Y}_{\mathrm{c,ss}}$ becomes Hermitian and can be written as a complex expression instead:

$$\Delta \underline{i}_\mathrm{f}^{(\mathrm{dq})} = -\frac{R_\mathrm{v} - \mathrm{j}X_\mathrm{v}}{R_\mathrm{v}^2 + X_\mathrm{v}^2}\frac{s^2}{(s+\alpha)^2}\Delta \underline{v}_\mathrm{g}^{(\mathrm{dq})}. \tag{F.25}$$

Table 1: System and control parameters for the frequency analysis.

System parameters		Control parameters	
S_N	100 MVA	L_v1	0.35 pu
V_N	400 kV	R_v1	0.485 pu
ω_b	314.16 rad/s	$\alpha_\mathrm{P} = \alpha_\mathrm{Q}$	2π 5 rad/s
L_f	0.15 pu	$\zeta_\mathrm{P} = \zeta_\mathrm{Q}$	1
R_f	0.015 pu	α_CC	2π 200 rad/s
SCR	3 pu		

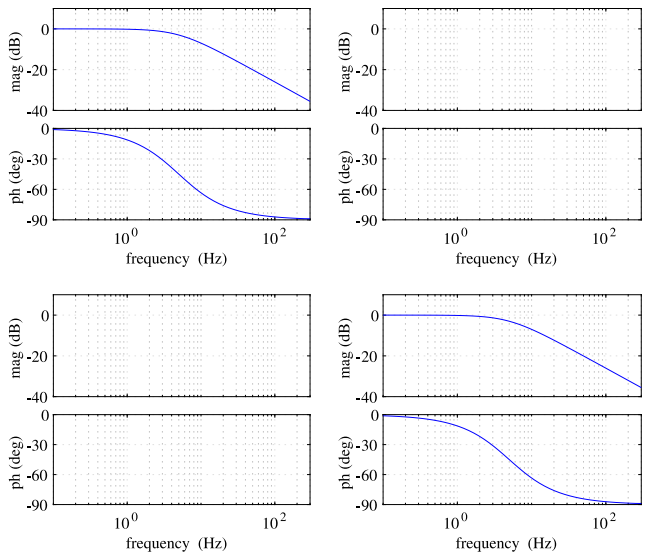

Figure 11: Closed-loop response of decoupled GFM controller. Virtual reactor dynamics neglected. Top left: P_{ref} to P_{g}; Top right: Q_{ref} to P_{g}; Bottom left: P_{ref} to Q_{g}; Bottom right: Q_{ref} to Q_{g}.

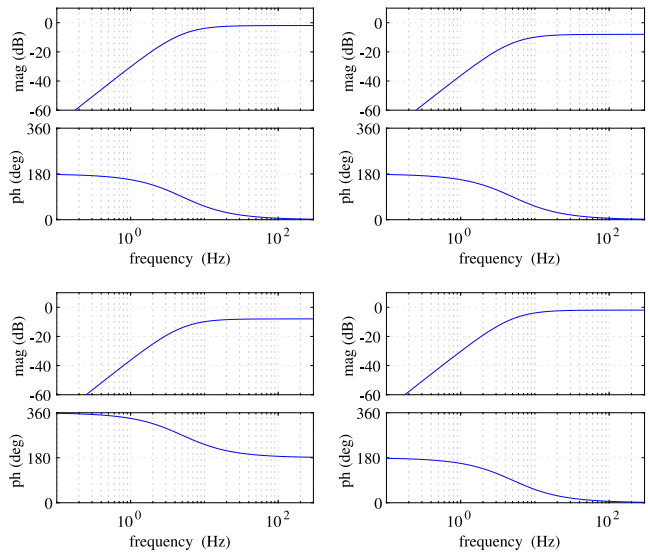

Figure 12: Input admittance of decoupled GFM controller. Virtual reactor dynamics neglected. Top left: Y_{dd}; Top right: Y_{qd}; Bottom left: Y_{dq} Bottom right: Y_{qq}.

Figure 12 contains the Bode diagram for the input admittance, representing the expected HPF-behaviour. This behaviour is expected, as the converter system exhibits constant power behaviour, i.e. a very low admittance, at low frequencies, while approximating a constant admittance for higher frequencies[4].

4.2 Analysis with Dynamic VA Representation

For a complete analysis it is necessary to take the dynamics of the VA into account. In Fig. 13, the Bode diagram of the closed-loop transfer function including the frequency dynamics is shown for different values of the APL bandwidth α_{P}. The impact of the VA frequency dynamics can be seen when comparing the blue curves to Fig. 11. Even with those dynamics, the LPF-behaviour of the response is preserved. As a main difference, it can be observed

[4] As the steady-state representation is chosen here, the admittance's frequency dependency is not represented in these figures.

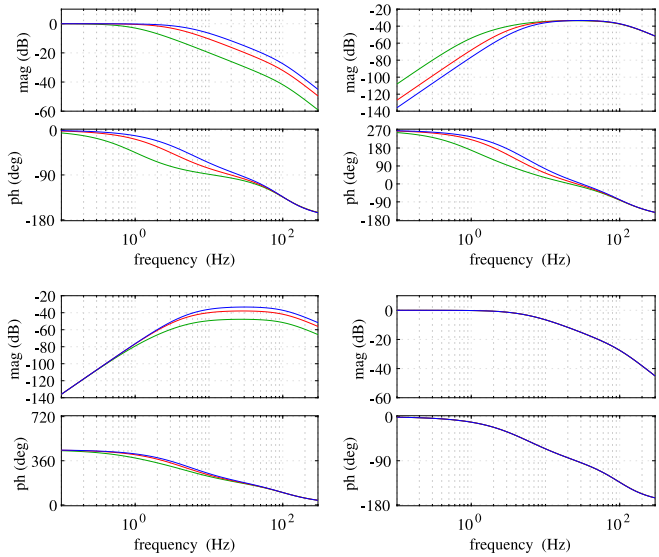

Figure 13: Closed-loop response of decoupled GFM controller for different values of α_{P}. Top left: P_{ref} to P_{g}; Top right: Q_{ref} to P_{g}; Bottom left: P_{ref} to Q_{g}; Bottom right: Q_{ref} to Q_{g}. Green curves: $\alpha_{\mathrm{P}} = 1 \cdot 2 \cdot \pi$ rad/s; Red curves: $\alpha_{\mathrm{P}} = 3 \cdot 2 \cdot \pi$; Blue curves: $\alpha_{\mathrm{P}} = 5 \cdot 2 \cdot \pi$.

that the cross-coupling between Q_{ref} and P_{g} as well as between P_{ref} and Q_{g}, respectively, is non-zero but remains very small. Comparing the curves representing different bandwidths in Fig. 11 shows that reducing α_{P} leads to a faster decay of the gain as expected, resulting in narrower frequency range with constant-power behaviour. It can also be seen that the change of the APL's bandwidth α_{P} does not have an impact on the reactive-power response Q_{ref} to Q. Manipulating the RPL's α_{Q} gives equivalent results[5], and in particular no impact on the active-power response.

In Fig. 14, the impact of the damping ratio on the frequency response of the APL and RPL can be studied. A reduction of the damping ratio ζ from 1 (blue) over 0.7 (red) to 0.5 (green) results in an amplification at frequencies around α_{P} and α_{Q}.

The same effects can be seen in Fig. 15, showing the converter's input

[5]The corresponding figure is not shown here due to space constraints

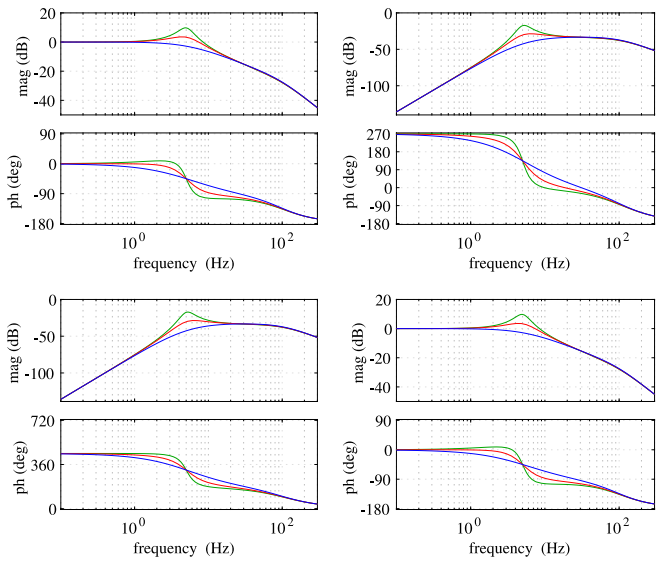

Figure 14: Closed-loop response of decoupled GFM controller for different values of damping ζ in the power-control loops; $\zeta_P = \zeta_Q = \zeta$. Green curves: $\zeta = 0.5$; Red curves: $\zeta = 0.7$; Blue curves: $\zeta = 1$.

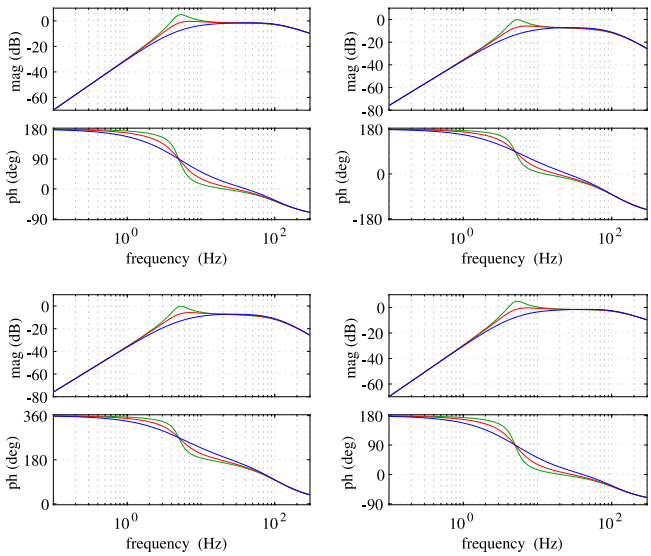

Figure 15: Input admittance of decoupled GFM controller for different values of damping ζ in the power-control loops; $\zeta_{\mathrm{P}} = \zeta_{\mathrm{Q}} = \zeta$. Top left: Y_{dd}; Top right: Y_{qd}; Bottom left: Y_{dq} Bottom right: Y_{qq}. Green curves: $\zeta = 0.5$; Red curves: $\zeta = 0.7$; Blue curves: $\zeta = 1$.

admittance for changing damping ratios ζ under consideration of the VA frequency dynamics. As a main difference compared to the case depicted Fig. 12, the frequency dynamics become visible as a decaying magnitude in the high frequency range, caused by the growing impact of the term sL_{v}. The amplification caused by low damping ratios in the power controllers is also replicated in the input admittance, which makes it clear that this parameter has a large impact on the provision of damping in the sub-harmonic range. This is particularly relevant if the converter system is required to dampen power system oscillations, which often appear have a similar frequency.

As expected from the analysis in Section 2, changing the virtual resistance, R_{v}, mainly has an impact on the damping in the subsynchronous-frequency range and particularly at the SFR, which lies at 50 Hz. This is visible in Fig. 16, which shows the input admittance for different values of R_{v}.

The inertial response provided by the APL can be examined with help of the frequency response from grid voltage frequency derivative $\mathrm{d}f/\mathrm{d}t$ to

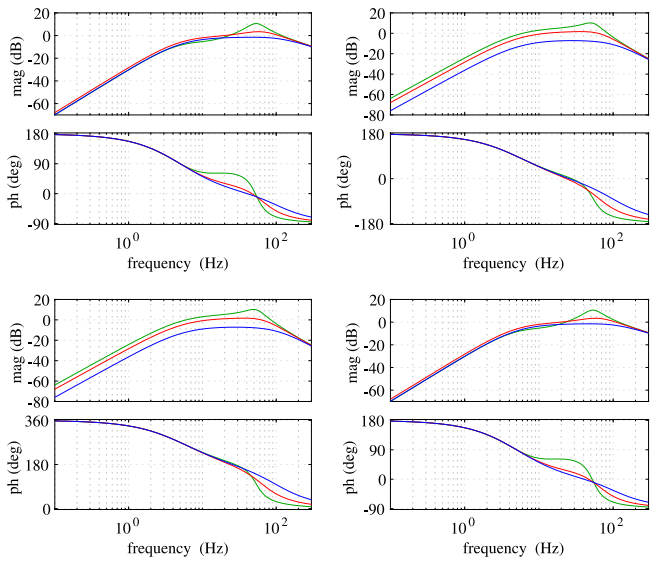

Figure 16: Input admittance of decoupled GFM controller for different values of the virtual resistance R_v. Green curves: $R_v = 0.25$ pu; Red curves: $R_v = 0.5$ pu; Blue curves: $R_v = 1$ pu.

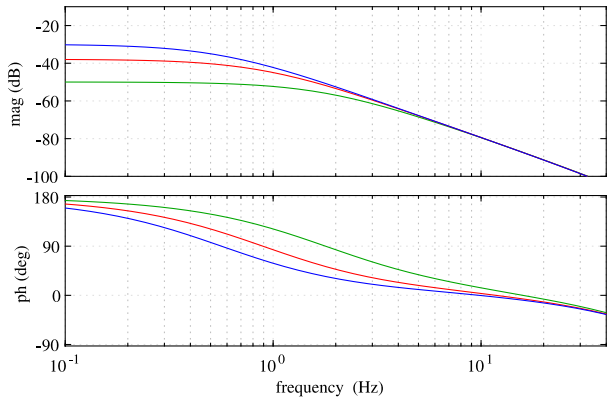

Figure 17: Frequency response of decoupled GFM controller from grid frequency derivative to P_{g} for different values of inertia-time constant H. Green curves: $H = 0.5$ s; Red curves: $H = 2$ s; Blue curves: $H = 5$ s.

active power P_{g}, shown in Fig. 17. As can be seen from the figure, a higher inertia constant, corresponding to a lower α_{P}, results in a higher gain, which corresponds to a larger inertial response.

To summarize, the frequency analysis of the proposed decoupled controller shows that the proposed design addresses both the problem of SFR as well as power coupling, as demonstrated by the presented frequency responses. It has furthermore shown how different control parameters can be used to influence the controller response in different frequency ranges. These findings are summarized in Fig. 18, which shows the *dd*-element of the converter's input admittance as a comparison to the desired converter behaviour shown in Fig. 7. For comparison, the response of a pure admittance, without controller, is also shown in black. From the figure, it can be seen that the main difference to the pure admittance appears for frequencies around and below the APL's and RPL's bandwidth, as the converter shows a constant power behaviour in this range. As can be seen from the dashed green curve, the main way to impact the controller's response at frequencies around the power controller's loop bandwidth (apart from tuning the controller's parameters to a different bandwidth) is the damping ratio ζ. At higher frequencies (here up to about 100 Hz) and in particular around the fundamental, the virtual resistance R_{v} becomes the dominant factor. This parameter also plays the main role in the

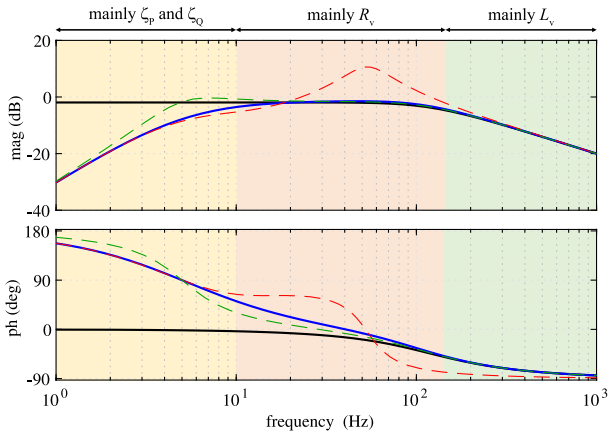

Figure 18: Comparison of Y_{dd} of virtual admittance and decoupled GFM controller. Virtual reactance is 0.5pu. Solid black curves: virtual admittance response, with $R_{\mathrm{v}} = 1$ pu; Solid blue curves: GFM controller response, with $R_{\mathrm{v}} = 1$ pu and $\zeta_{\mathrm{P}} = \zeta_{\mathrm{Q}} = 1$. Dashed green curves: GFM controller response, with $R_{\mathrm{v}} = 1$ pu and $\zeta = 0.7$; Dashed red curves: GFM controller response, with $R_{\mathrm{v}} = 0.25$ pu and $\zeta = 1$.

damping of the SFR. For frequencies above this, the main impact on the input admittance gradually shifts from R_{v} to the virtual inductance L_{v}, until the bandwidth limitation of the CC deteriorates the representation of the VA.

5 Experimental Validation

To validate the claimed performance of the controller, an experimental validation has been carried out in the laboratory. A photo of the laboratory setup is shown in Fig. 19, with a single-line diagram in Fig. 20. The grid voltage is emulated using a four quadrant programmable AC power source by REGATRON, and the grid impedance is realized with the help of physical reactors. The GFM converter system comprises of a 2-level VSC supplied by an ideal DC voltage source. The VSC is controlled using dSPACE dS1006, and is connected at the PCC through a phase reactor with the inductance L_{f} and resistance R_{f}. The system and control parameters used for the experimental validation are given in Table 2. The APL and RPL bandwidths are chosen to

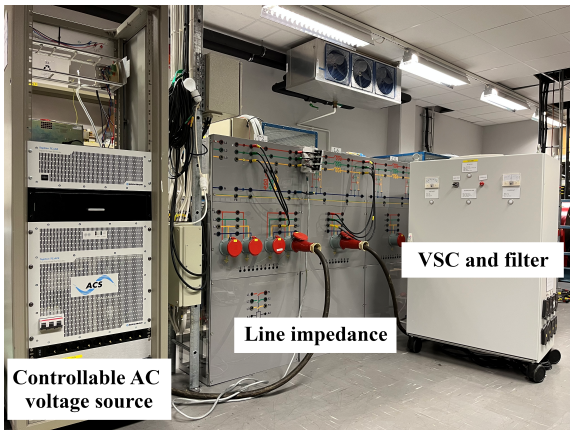

Figure 19: Photo of the laboratory setup used for validation.

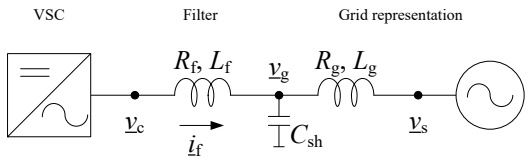

Figure 20: Single-line diagram of the laboratory setup.

comply with the recommendations for GFM control action defined in [24].

At first, the performance of the Decoupled VA-GFM is investigated. In Fig. 21, the reaction to steps in the active- and reactive-power reference is shown for a relatively weak grid with a short-circuit ratio (SCR) of 3.3 (blue), and for a stronger grid with a SCR of 6.6 (red). Both curves show that the controller works as intended and follows the steps in the reference at 1 s, 2 s, 3 s and 4 s for P_{ref}, as well as 0.5 s, 1.5 s, 2.5 s and 3.5 s for Q_{ref}, respectively. It can be observerd that the converter's performance is independent of the grid strength. The curves also demonstrate that the VA phase compensation is able to achieve the intended decoupling effect, and the impact of the steps in P_{ref} is caused by the variation in grid voltage.

In the results shown in Fig. 22 the impact of the virtual resistance R_{v} on the SFR can be studied. A step in the active power reference is conducted with a R_{v} of 0.25 pu (green) and 1 pu (blue). It can be seen that for the lower

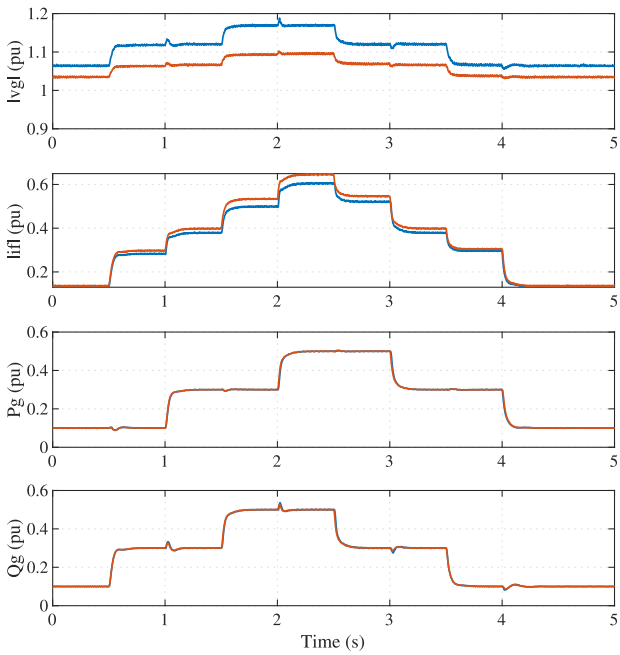

Figure 21: Results of a step in the power references of the proposed controller with a variation in the grid strength. Blue curves: SCR = 3.3; Red curves: SCR = 6.6.

resistance there is a visible oscillation close to the synchronous frequency, which becomes significantly more damped for the higher resistance value. A poorly damped, low amplitude 50-Hz-oscillation in (primarily reactive) power can be observed even before the power reference step, due to the dynamics of the REGATRON grid simulator. It can be seen that the virtual resistance not only dampens the transient DC-component caused by the power-reference step, but also the interaction with the grid emulator. The figure also shows that the coupling between active and reactive power does not increase for increasing values of R_v, as would to be expected for a classical GFM.

In Fig. 23, the impact of the damping ratio ζ on the reaction to a step in the power reference is shown. For the green curves, with $\zeta_\mathrm{P} = \zeta_\mathrm{Q} = 0.5$, the reference step results in a large and poorly-damped overshoot. As to be expected from the frequency analysis in the previous section and Fig. 14 in particular, the frequency of this oscillation is close to 5 Hz, the bandwidth of the APL. Increasing the damping ratios to 0.7 (red) or 1 (blue) dampens the oscillation significantly. Between these higher values there is a trade-off between speed (lower damping is faster) and acceptable overshoot (lower damping is unable to prevent overshoot completely), that can be tailored to use-case specific requirements.

6 Conclusion

In this paper a novel control strategy for VA-GFM for effective decoupling between the active- and reactive-power responses has been presented. The pro-

Table 2: System and control parameters for the laboratory setup.

System parameters		Control parameters	
S_N	1 kVA	L_v1	0.343 pu
V_N	100 V	R_v1	0.9843 pu
ω_b	314.16 rad/s	$\alpha_\mathrm{P} = \alpha_\mathrm{Q}$	2π 5 rad/s
L_f	0.157 pu	$\zeta_\mathrm{P} = \zeta_\mathrm{Q}$	1
R_f	0.0157 pu	α_CC	2π 200 rad/s
SCR	3.18		
C_sh	0.0942 pu		

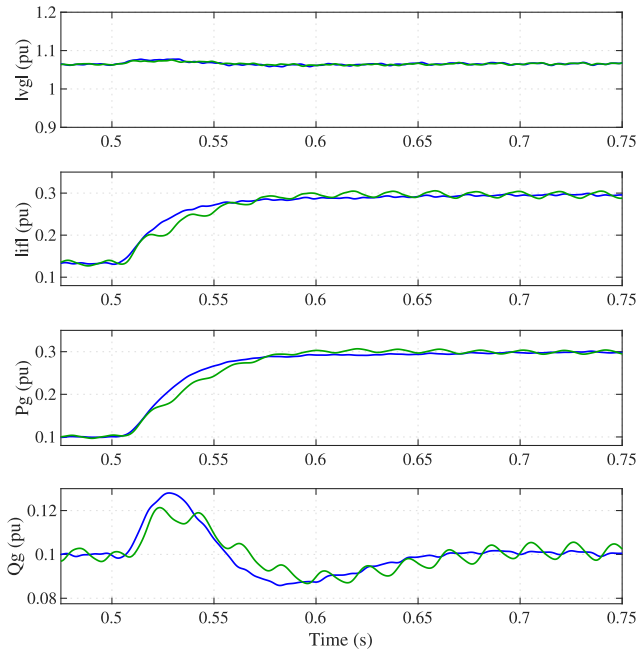

Figure 22: Experimental results of a step in the power references of the proposed controller with a variation in the virtual resistance. Green curves: $R_\mathrm{v} = 0.25\,\mathrm{pu}$; Blue curves: $R_\mathrm{v} = 1\,\mathrm{pu}$.

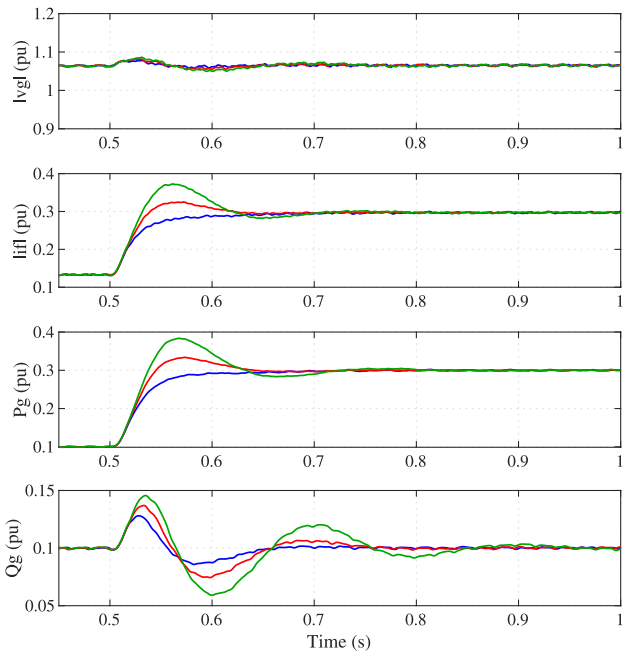

Figure 23: Experimental results of a step in the power references of the proposed controller with a variation in the APL's damping ratio. Green curves: $\zeta_P = \zeta_Q = 0.5$; Red curves: $\zeta_P = \zeta_Q = 0.7$; Blue curves: $\zeta_P = \zeta_Q = 1$.

posed Decoupled VA-GFM controller is based on a complex-power outer control loop and employs a VA-compensation algorithm to achieve near-perfect decoupling between active and reactive power for any selection of the VA parameters. As a consequence, the virtual resistance in the VA can be selected arbitrary, depending on the system needs for damping in the subsynchronous-frequency range and at SFR.

This paper also presents a detailed frequency analysis of the proposed controller. This analysis confirms the decoupling and demonstrates that the different degrees of freedom in the controller can be used to influence the behaviour in different frequency ranges independently from each other. Furthermore, it is shown that for equal selection of the APL and RPL bandwidths, both the closed-loop transfer function and the converter's input admittance can be expressed as a single-dimensional transfer-function, thus allowing for single-input/single-output representation of the Decoupled VA-GFM.

References

[1] International Energy Agency, "Net Zero by 2050 - A Roadmap for the Global Energy Sector," Paris, France, Oct. 2021.

[2] B. K. Bose, "Global Energy Scenario and Impact of Power Electronics in 21st Century," *IEEE Transactions on Industrial Electronics*, vol. 60, no. 7, pp. 2638–2651, Jul. 2013, ISSN: 1557-9948.

[3] ENTSO-E, "High Penetration of Power Electronic Interfaced Power Sources and the Potential Contribution of Grid Forming Converters," 2020.

[4] J. Matevosyan, B. Badrzadeh, T. Prevost, *et al.*, "Grid-Forming Inverters: Are They the Key for High Renewable Penetration?" *IEEE Power and Energy Magazine*, vol. 17, no. 6, pp. 89–98, Nov. 2019, ISSN: 1558-4216.

[5] R. Rosso, X. Wang, M. Liserre, X. Lu, and S. Engelken, "Grid-Forming Converters: Control Approaches, Grid-Synchronization, and Future Trends — A Review," *IEEE Open Journal of Industry Applications*, vol. 2, pp. 93–109, 2021, ISSN: 2644-1241.

[6] S. D'Arco and J. A. Suul, "Virtual synchronous machines — Classification of implementations and analysis of equivalence to droop controllers for microgrids," in *2013 IEEE Grenoble Conference*, Jun. 2013, pp. 1–7.

[7] M. Tozak, S. Taskin, I. Sengor, and B. P. Hayes, "Modeling and Control of Grid Forming Converters: A Systematic Review," *IEEE Access*, vol. 12, pp. 107 818–107 843, 2024, ISSN: 2169-3536.

[8] L. Zhang, L. Harnefors, and H. Nee, "Power-Synchronization Control of Grid-Connected Voltage-Source Converters," *IEEE Transactions on Power Systems*, vol. 25, no. 2, pp. 809–820, May 2010, ISSN: 1558-0679.

[9] P. Rodriguez, I. Candela, C. Citro, J. Rocabert, and A. Luna, "Control of grid-connected power converters based on a virtual admittance control loop," in *2013 15th European Conference on Power Electronics and Applications (EPE)*, Sep. 2013, pp. 1–10.

[10] M. Li, Y. Wang, W. Hu, *et al.*, "Unified Modeling and Analysis of Dynamic Power Coupling for Grid-Forming Converters," *IEEE Transactions on Power Electronics*, vol. 37, no. 2, pp. 2321–2337, Feb. 2022, ISSN: 1941-0107.

[11] Z. Tang, S. Wang, Y. Cui, X. Cheng, and Y. Zhao, "A Review of Coupling and Interaction Studies of Grid-Forming Converters Based on Transient Stability," in *2024 7th International Conference on Energy, Electrical and Power Engineering (CEEPE)*, Apr. 2024, pp. 259–265.

[12] B. Fan, T. Liu, F. Zhao, H. Wu, and X. Wang, "A Review of Current-Limiting Control of Grid-Forming Inverters Under Symmetrical Disturbances," *IEEE Open Journal of Power Electronics*, pp. 1–15, 2022, ISSN: 2644-1314.

[13] F. Zhao, X. Wang, and T. Zhu, "Low-Frequency Passivity-Based Analysis and Damping of Power-Synchronization Controlled Grid-Forming Inverter," *IEEE Journal of Emerging and Selected Topics in Power Electronics*, vol. 11, no. 2, pp. 1542–1554, Apr. 2023, ISSN: 2168-6785.

[14] K. Kamalinejad, A. Narula, M. Bongiorno, M. Beza, and J. R. Svensson, "Investigation of Control Parameters' Impact on Damping Property of Grid-Forming Converters," in *2024 IEEE Energy Conversion Congress and Exposition (ECCE)*, Oct. 2024, pp. 686–693.

[15] K. De Brabandere, B. Bolsens, J. Van den Keybus, A. Woyte, J. Driesen, and R. Belmans, "A Voltage and Frequency Droop Control Method for Parallel Inverters," *IEEE Transactions on Power Electronics*, vol. 22, no. 4, pp. 1107–1115, Jul. 2007, ISSN: 1941-0107.

[16] T. Wu, Z. Liu, J. Liu, S. Wang, and Z. You, "A Unified Virtual Power Decoupling Method for Droop-Controlled Parallel Inverters in Microgrids," *IEEE Transactions on Power Electronics*, vol. 31, no. 8, pp. 5587–5603, Aug. 2016, ISSN: 1941-0107.

[17] B. Li and L. Zhou, "Power Decoupling Method Based on the Diagonal Compensating Matrix for VSG-Controlled Parallel Inverters in the Microgrid," *Energies*, vol. 10, no. 12, p. 2159, 12 Dec. 2017, ISSN: 1996-1073.

[18] C. R. Shah, M. Molinas, R. Nilsen, and M. Amin, "Impedance Reshaping of GFM Converters with Selective Resistive Behaviour for Small-signal Stability Enhancement," in *2024 IEEE Applied Power Electronics Conference and Exposition (APEC)*, Feb. 2024, pp. 1619–1626.

[19] P. Wang, M. Chen, J. Wang, G. Zhu, and F. Jiang, "An Active Power Feedforward Compensation-Based Power Decoupling Method for Droop Control Converters," *IEEE Transactions on Power Electronics*, vol. 40, no. 5, pp. 6726–6739, May 2025, ISSN: 1941-0107.

[20] P. Zhang, H. Zhao, H. Cai, J. Shi, and X. He, "Power decoupling strategy based on 'virtual negative resistor' for inverters in low-voltage microgrids," *IET Power Electronics*, vol. 9, no. 5, pp. 1037–1044, 2016, ISSN: 1755-4543.

[21] Y. Tao, Y. Jie, L. Chenguang, *et al.*, "Power Decoupling Control of Grid-Forming Converter Based on Voltage and Angle Compensation," in *2023 6th International Conference on Electrical Engineering and Green Energy (CEEGE)*, Jun. 2023, pp. 95–100.

[22] L. Harnefors, M. Hinkkanen, U. Riaz, F. M. M. Rahman, and L. Zhang, "Robust Analytic Design of Power-Synchronization Control," *IEEE Transactions on Industrial Electronics*, vol. 66, no. 8, pp. 5810–5819, Aug. 2019, ISSN: 1557-9948.

[23] M. G. Taul, X. Wang, P. Davari, and F. Blaabjerg, "Current Limiting Control With Enhanced Dynamics of Grid-Forming Converters During Fault Conditions," *IEEE Journal of Emerging and Selected Topics in Power Electronics*, vol. 8, no. 2, pp. 1062–1073, Jun. 2020, ISSN: 2168-6777, 2168-6785.

[24] P. Imgart, M. Beza, M. Bongiorno, and J. R. Svensson, "An Overview of Grid-Connection Requirements for Converters and Their Impact on Grid-Forming Control," *EPE'22 ECCE Europe*, 2022.

[25] National Energy System Operator, *The Grid Code*, Nov. 7, 2024.

[26] L. Harnefors, M. Bongiorno, and S. Lundberg, "Input-Admittance Calculation and Shaping for Controlled Voltage-Source Converters," *IEEE Transactions on Industrial Electronics*, vol. 54, no. 6, pp. 3323–3334, Dec. 2007, ISSN: 1557-9948.

[27] L. Harnefors, X. Wang, A. G. Yepes, and F. Blaabjerg, "Passivity-Based Stability Assessment of Grid-Connected VSCs—An Overview," *IEEE Journal of Emerging and Selected Topics in Power Electronics*, vol. 4, no. 1, pp. 116–125, Mar. 2016, ISSN: 2168-6777, 2168-6785.

[28] M. Yu, A. J. Roscoe, A. Dyśko, *et al.*, "Instantaneous penetration level limits of non-synchronous devices in the British power system," *IET Renewable Power Generation*, vol. 11, no. 8, pp. 1211–1217, 2017, ISSN: 1752-1424.

[29] A. Narula, P. Imgart, M. Bongiorno, P. Mattavelli, M. Beza, and J. R. Svensson, "Power-Response Matrix-Based Modeling of Converter Systems for Small-Signal Analysis," in *2024 IEEE Energy Conversion Congress and Exposition (ECCE)*, Phoenix, AZ, USA: IEEE, Oct. 20, 2024, pp. 4724–4731, ISBN: 9798350376067.

[30] A. Narula, M. Bongiorno, and M. Beza, "Comparison of Grid-Forming Converter Control Strategies," in *2021 IEEE Energy Conversion Congress and Exposition (ECCE)*, Oct. 2021, pp. 361–368.

[31] P. Imgart, A. Narula, M. Bongiorno, M. Beza, and J. R. Svensson, "A Cascaded Power Controller for Robust Frequency Ride-Through of Grid-Forming Converters," presented at the 2022 IEEE Energy Conversion Congress and Exposition (ECCE), Detroit, MI, USA, 2022.

[32] P. Imgart, A. Narula, M. Bongiorno, M. Beza, and J. R. Svensson, "External Inertia Emulation to Facilitate Active-Power Limitation in Grid-Forming Converters," *IEEE Transactions on Industry Applications*, vol. 60, no. 6, pp. 9145–9156, Nov. 2024, ISSN: 1939-9367.